U.PORTO
FACULDADE DE CIÊNCIAS
UNIVERSIDADE DO PORTO

FACULDADE DE
CIÊNCIAS E TECNOLOGIA
UNIVERSIDADE NOVA DE LISBOA

universidade
de aveiro

Nanobioconjugates of Gold and Silver Nanoparticles for Biosensors

Miguel Peixoto de Almeida
PhD thesis submitted to
Faculdade de Ciências da Universidade do Porto,
Faculdade de Ciências e Tecnologia da Universidade Nova de Lisboa,
Universidade de Aveiro
Chemistry
2018

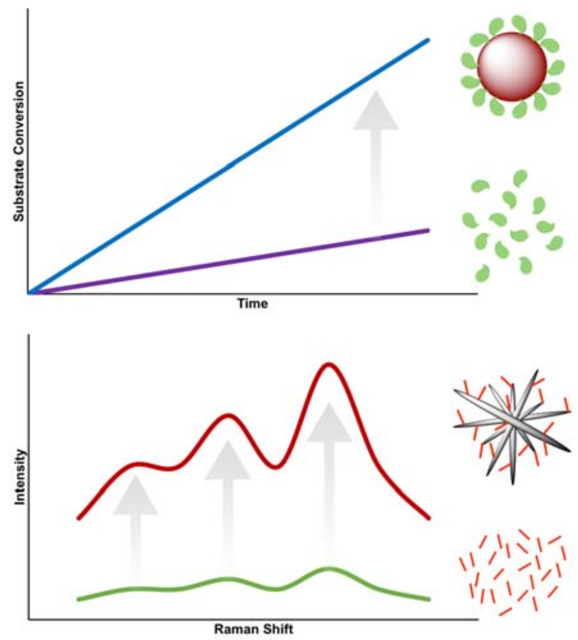

Nanobioconjugates of Gold and Silver Nanoparticles for Biosensors

Miguel Peixoto de Almeida
Doutoramento em Química Sustentável
Departamento de Química e Bioquímica
2018

Orientador
Eulália Fernanda Alves de Carvalho Pereira, Professor Auxiliar
Faculdade de Ciências

Coorientador
Baltazar Manuel Romão de Castro, Professor Catedrático
Faculdade de Ciências

Acknowledgements

To *Fundação para a Ciência e a Tecnologia* for the fellowship SFRH/BD/95983/2013, in context of the *Programa Operacional Capital Humano*, funded by European Union (European Social Fund) and national funds.

To *Programa Doutoral em Química Sustentável* board of directors, together with *Universidade de Aveiro*, *Universidade Nova de Lisboa* and *Universidade do Porto*, for giving me the opportunity of being part of this program.

To *REQUIMTE* that assured the technical conditions to develop this scientific work.

To *ICETA* team and *Gabinete de Pós-Graduação FCUP*, namely Paula Marques, for always helping me in all the administrative processes.

To *Faculdade de Ciências da Universidade do Porto,* in particular *Departamento de Química e Bioquímica*, for having me as a PhD student.

To Prof. Dr. Eulália Pereira, for all the commitment in my supervision, available to help at any time with her outstanding teaching and scientific skills.

To Prof. Dr. Baltazar de Castro, for his best efforts to assure that the doctoral programme and my work went flawlessly.

To Prof. Dr. Ricardo Franco, for all the interesting discussions about diverse scientific topics and for being an excellent liaison with *FCTUNL*.

To Prof. Dr. Nicolae Leopold and *Universitatea Babeş-Bolyai* for welcoming me in Cluj-Napoca and assuring that I had everything I need, inside and outside the university.

To Prof. Dr. Agostinho Moreira e Prof. Dr. Abílio Almeida for introducing me to Raman spectroscopy and making the *IFIMUP* Raman laboratory open for me.

To Dr. Pedro Quaresma for TEM imaging and for teaching me a lot about nanoparticles.

To Dr. Peter Eaton for SEM imaging and for teaching me a lot about microscopy.

To Prof. Dr. Hugo Águas and other *CENIMAT|i3N* members for their cooperation, namely Maria João Oliveira for SERS measurements and SEM imaging and Dr. Andreia Cardoso Araújo for preparing silver nanoparticle-coated surfaces.

To Prof. Dr. Luísa Peixe and her team members Dr. Ângela Novais, Dr. Carla Rodrigues and Dr. Filipa Grosso, for the all microbiologic work.

To Dr. Lucinda Bessa for the fruitful discussions about microbiology.

To my co-authors in articles published in this period.

To my school teachers that made me realize my interest in science, namely Jorge Pacheco and Rosalino Moura.

To my fellow colleagues, to Prof. Dr. Paula Gameiro and her team for all the good moments inside and outside the laboratory.

To *FCUP* students that helped me in my work, namely Catarina Pelicano, Emma Calle, Marta Belda and Patrícia Soares.

To my grandparents, parents and brother for all the support.

To my wife for the patience, for the help, for everything and more.

FCT Fundação para a Ciência e a Tecnologia
MINISTÉRIO DA CIÊNCIA, TECNOLOGIA E ENSINO SUPERIOR
POCH
COMPETE 2020
PORTUGAL 2020
UNIÃO EUROPEIA
Fundos Europeus Estruturais e de Investimento

Contents

Acknowledgements iii
Contents v
Abstract ix
Resumo xi
List of figures xiv
List of tables xxv
List of abbreviations xxvii
1. General Introduction 1
  1.1. Nanotechnology and nanoparticles 3
  1.2. Gold and silver nanoparticles 5
    1.2.1. Synthesis of gold nanoparticles 5
    1.2.2. Synthesis of silver nanoparticles 6
  1.3. Gold nanoparticles nanobioconjugates in sensing 8
    1.3.1. Colorimetric Assays 8
    1.3.2. Lateral Flow Assays 11
    1.3.3. Electrochemical Assays 14
    1.3.4. Other Assays 17
  1.4. Interaction of gold nanoparticles and proteins 19
  1.5. Surface-enhanced Raman spectroscopy (SERS) 23
    1.5.1. Principal component analysis (PCA) 24
  1.6. Silver nanoparticles nanobioconjugates in sensing by surface-enhanced Raman spectroscopy 25
    1.6.1. Surface-enhanced Raman spectroscopy in immunoassays 25
    1.6.2. Surface-enhanced Raman spectroscopy and proteins 26
    1.6.3. Surface-enhanced Raman spectroscopy and nucleic acids 27
    1.6.4. Surface-enhanced Raman spectroscopy and multiple biomolecules 30
    1.6.5. Surface-enhanced Raman spectroscopy and chemometric methods for sample discrimination 30
  1.7. Thesis objectives and outline 32
  1.8. References 34
2. Nanobioconjugates of Gold Nanoparticles and Laccase in Solution 51
  2.1. Introduction 55
    2.1.1. Laccases 55
  2.2. Published Article 57
    Abstract 57
    Introduction 57
    Results and Discussion 59
    Materials and Methods 70
    Conclusions 73
    Acknowledgements 75

Notes and references 75
2.3. Article's supporting information 79
2.4. Final remarks 87
2.5. References 88
3. Immobilized Nanobioconjugates of Gold Nanoparticles and Laccase 91
3.1. Introduction 93
3.1.1. Laccase from *Trametes versicolor* 93
3.1.2. Immobilization of *Trametes versicolor* laccase 93
3.1.3. Membrane-like support materials 94
3.1.4. Immobilization of gold nanoparticles 96
3.2. Methods 97
3.2.1. Synthesis of gold nanoparticles 99
3.2.1.1. Synthesis of 15 nm gold nanospheres (AuNPs15) 100
3.2.1.2. Synthesis of 40 nm gold nanospheres (AuNPs40) 100
3.2.1.3. Synthesis of gold nanostars (AuNSs) 100
3.2.2. Nanobioconjugation in solution 101
3.2.3. Support impregnation with gold nanoparticles 101
3.2.4. Gold nanoparticles loading and stability assessment 102
3.2.5. Sample preparation for scanning electron microscopy 102
3.2.6. Nanobioconjugates assembly 102
3.2.7. Enzymatic activity assays 105
3.3. Results and Discussion 107
3.3.1. Synthesis of gold nanoparticles 107
3.3.2. Nanobioconjugation in solution 113
3.3.3. Impregnation of the supports with gold nanoparticles 116
3.3.4. Nanobioconjugates assembling 124
3.3.5. Disks enzymatic activity 125
3.4. Conclusions 129
3.5. References 130
4. Nanobioconjugates for Wine Fingerprinting by Surface-Enhanced Raman Spectroscopy 137
4.1. Introduction 139
4.1.1. Wine characterization 139
4.1.2. Wine fingerprinting 140
4.1.3. Portuguese wines 141
4.2. Methods 142
4.2.1. Synthesis of silver nanostars (AgNSs) 142
4.2.2. Wines 143
4.2.3. Silver nanostars functionalization with wine molecules 144
4.2.3.1. Silver nanostars synthesised in wine with added reducing agents 144
4.2.3.2. Silver nanostars synthesised in wine without added reducing agents 146
4.2.3.3. Silver nanostars functionalization by wine compounds with incubation 147
4.2.3.4. Silver nanostars functionalization by wine compounds without incubation 147
4.2.3.5. Data collection for principal component analysis of three protocols 149
4.2.4. Raman/SERS measurements 150
4.2.5. Principal component analysis 150
4.3. Results and Discussion 151

4.3.1. Synthesis of silver nanostars (AgNSs) 151
4.3.2. Nanobioconjugation 152
4.3.2.1. Silver nanostars synthesised in wine with added reducing agents 153
4.3.2.2. Silver nanostars synthesised in wine without added reducing agents ... 156
4.3.2.3. Silver nanostars functionalization by wine compounds with incubation . 162
4.3.2.4. Silver nanostars functionalization by wine compounds without incubation 169
4.3.3. Wine fingerprinting 172
4.3.4. Band assignments 180

4.4. Conclusions 182

4.5. References 184

5. Nanobioconjugates for Bacteria Fingerprinting by Surface-Enhanced Raman Spectroscopy 187

5.1. Introduction 189
5.1.1. Antibiotic-resistant bacteria 189
5.1.2. Common method for bacteria identification 190
5.1.3. Raman spectroscopy for bacteria identification. 190

5.2. Methods 192
5.2.1. Synthesis of silver nanostars 192
5.2.2. Microbiologic material 192
5.2.3. Nanobioconjugation between silver nanostars and bacteria 193
5.2.4. Preparation of the nanobioconjugates for SERS measurements 195
5.2.5. SERS measurements 195
5.2.6. Data analysis 195

5.3. Results and Discussion 196
5.3.1. Nanobioconjugation protocols 196
5.3.2. Interspecies bacteria discrimination 200
5.3.2.1. Laser selection 200
5.3.2.2. Selection of nanobioconjugation media 203
5.3.2.3. Protocol selection 208
5.3.3. Intraspecies discrimination 213
5.3.3.1. Laser selection 214

5.4. Conclusions 220

5.5. References 222

6. Nanostructured surfaces for Surface-Enhanced Raman Spectroscopy 225

6.1. Introduction 227
6.1.1. Nanostructured silver surfaces for SERS 227
6.1.2. Amine-functionalized glass supports 228

6.2. Methods 229
6.2.1. Synthesis of silver nanostars 229
6.2.2. Decorated silicon-based supports 229
6.2.3. Functionalized glass-based supports 230
6.2.4. Decorated cardboard-based supports 232
6.2.5. Silver mirror-based supports 233
6.2.6. Zinc oxide nanorods-based supports 234
6.2.7. SERS measurements and data analysis 235

6.3. Results and Analysis 237
6.3.1. Silicon-based supports 237
6.3.1.1. Influence of silver nanostars concentration 237

6.3.1.2. Influence of the shaking method 238
6.3.2. Glass-based supports 240
6.3.2.1. Influence of the concentration 241
6.3.2.2. Influence of shaking 247
6.3.2.3. Influence of media pH 248
6.3.3. Other supports..249
6.3.3.1. Cardboard-based surfaces..250
6.3.3.2. Silver mirror-based surfaces 251
6.3.3.3. Zinc oxide nanorods-based surfaces 253

6.4. Conclusions...255

6.5. References..257

7. General Conclusion...261

Abstract

In the scope of the study of the interaction of metal nanoparticles with biomolecules, gold nanoparticles were used as a scaffold for nanobioconjugates with laccases (phenol oxidases) from two different species – *Toxicodendron verniciflua* and *Trametes versicolor*. Nanobioconjugates between spherical gold nanoparticles and laccase from *T. verniciflua* readily form in solution. The formation of the nanobioconjugates was studied by Dynamic Light Scattering, Electrophoretic Light Scattering, Agarose Gel Electrophoresis and fluorescence quenching. Adsorption constants were determined in the range $6.8 < \log K < 8.9$, highlighting the strong interaction between gold nanoparticles and this enzyme. The enzymatic activity of the adsorbed enzyme was found to be ca. 9 times higher than the activity of this laccase in solution. In addition, the pH profile of enzymatic activity of the nanobioconjugates shows increased activity in the pH range 6.5–8.5 in comparison with the free enzyme, showing that the use of these nanobioconjugates extends the useful pH range for this enzyme. For the laccase from *T. versicolor*, no significant interaction with gold nanoparticles was detected in solution using Dynamic Light Scattering and Nanoparticle Tracking Analysis. Instead, co-adsorption of gold nanoparticles and this laccase in several supports (hydrophilic mixed cellulose esters, polytetrafluoroethylene, hydrophilic polyvinylidene fluoride, regenerated cellulose, nitrocellulose, filter paper and office paper) was studied, with promising results for nitrocellulose. The enzymatic activity of gold nanoparticles-enriched supports exceeded the enzymatic performance of the same supports only with laccase. These results show that the increase in enzymatic activity does not depend on a strong interaction between the enzyme and the nanoparticles, indicating that the role of the nanoparticles is probably related to facilitating electron transfer, and not to structural changes on the protein upon adsorption at the gold nanoparticles.

In the scope of applications of the localized surface plasmon resonance (LSPR) phenomenon, silver nanostars were studied as enhancers for Raman spectroscopy, due to their ability of creating a strong localized electric field upon interaction with electromagnetic radiation. This enhanced localized electric field strongly increases the Raman signal of adsorbed molecules, a phenomenon that is used in surface-enhanced Raman spectroscopy (SERS). Two different approaches were studied in this work: use of silver nanostars/SERS for sample fingerprinting and for “ready to read” nanostructured surfaces for SERS analysis. Star-shaped silver nanoparticles (AgNSs) were selected due to the large number of corners and edges typical of this shape, which are known to be hotspots where Raman enhancement is particularly strong.

Fingerprinting with SERS was applied to two different types of samples: wines from three different regions in Portugal (Minho, Douro and Alentejo) and resistant bacterial strains. In both cases, the procedure for the preparation of the sample was first optimized. SERS spectra were analysed by Principal Component Analysis (PCA) to evaluate the discrimination potential of the technique. Using this approach, it was possible to properly discriminate three different white wines representing three different wine regions in Portugal. The results point to the possibility of using this quick and easy method for wine identification. In addition, four of the top priority resistant bacterial species indicated by World Health Organization (WHO) were properly discriminated with a similar method. The method developed is able of interspecies discrimination, but it was also able to discriminate different sequence types from the same species. This could be a fast method to identify bacteria, and especially low cost when compared to the golden standard for bacteria routine identification – mass spectrometry.

Finally, "ready to read" nanostructured surfaces for SERS analysis were prepared by deposition of silver nanostars in silicon wafers with a silver nanospheres layer, cardboard with a silver nanospheres layer, APTES-functionalised glass, silver mirror, zinc oxide nanorods and zinc oxide nanorods with a silver nanospheres layer. The deposition method was optimized in order to obtain a homogeneous surface with a high density of hotspots. The surface with these characteristics was found to be an APTES-functionalised glass with AgNSs deposited under orbital agitation using a concentration of 0.2 nM and pH not adjusted with buffer, that provide up to 10^4 enhancement factors. Among several compounds that can be measured on this substrate, are also biomolecules, therefore these supports can be considered "ready for nanobioconjugation".

Keywords

nanoparticles; gold; silver; enzyme; laccase; nanobioconjugates; membranes; SERS; surface-enhanced Raman spectroscopy; bacteria; wine; principal component analysis

Resumo

No âmbito do estudo da interação entre nanopartículas metálicas e biomoléculas, nanopartículas de ouro foram utilizadas como suporte para a formação de nanobioconjugados com lacases (fenol oxidases) de duas espécies diferentes - *Toxicodendron verniciflua* e *Trametes versicolor*. Nanobioconjugados entre nanopartículas esféricas de ouro e lacase de T. verniciflua formam-se facilmente em solução. A formação dos nanobioconjugados foi estudada por dispersão de luz dinâmica (*dynamic light scattering*, *DLS*), dispersão de luz eletroforética (*electrophoretic light scattering*, *ELS*), eletroforese em gel de agarose e *quenching* de fluorescência. As constantes de adsorção determinadas situam-se no intervalo $6,8 < \log K < 8,9$, destacando a forte interação entre as nanopartículas de ouro e esta enzima. Verificou-se que a atividade enzimática da lacase adsorvida era *ca.* 9 vezes maior que a atividade desta em solução. Além disso, o perfil de pH da atividade enzimática dos nanobioconjugados mostra atividade aumentada na faixa de pH de 6,5 a 8,5 em comparação com a enzima livre, mostrando que o uso destes nanobioconjugados amplia a faixa de pH útil para esta enzima. Para a lacase de *T. versicolor*, nenhuma interação significativa com nanopartículas de ouro foi detetada em solução usando a dispersão de luz dinâmica e a análise por seguimento de nanopartículas (*nanoparticle tracking analysis*, *NTA*). Em vez disso, a co-adsorção de nanopartículas de ouro e esta lacase em vários suportes (ésteres de celulose mistos hidrofílicos, politetrafluoretileno, fluoreto de polivinilideno hidrofílico, celulose regenerada, nitrocelulose, papel de filtro e papel de escritório) foi estudada, com resultados promissores para a nitrocelulose. A atividade enzimática dos suportes enriquecidos com nanopartículas de ouro excedeu o desempenho enzimático dos mesmos suportes apenas com lacase. Estes resultados mostram que o aumento na atividade enzimática não depende de uma forte interação entre a enzima e as nanopartículas, indicando que o papel das nanopartículas está provavelmente relacionado com a facilitação da transferência de eletrões, e não a mudanças estruturais na proteína após a adsorção em nanopartículas de ouro.

No âmbito das aplicações do fenómeno de ressonância plasmónica localizada de superfície (*localised surface plasmon resonance*, *LSPR*), as nanoestrelas de prata foram estudadas como potenciadores para a espetroscopia Raman, devido à sua capacidade de criar um campo elétrico forte localizado dada a interação com a radiação eletromagnética. Este campo elétrico localizado aumenta fortemente o sinal Raman de moléculas adsorvidas, um fenómeno que é usado na espetroscopia Raman amplificada por superfície (*surface-enhanced Raman spectroscopy*, *SERS*). Duas abordagens diferentes foram estudadas neste trabalho: uso de nanoestrelas de prata e SERS para identificação (*fingerprinting*) de amostras e de superfícies nanoestruturadas “prontas para leitura” para análise via SERS. Nanopartículas de prata em forma de estrela (AgNSs) foram selecionados devido ao grande número de arestas e vértices típicos desta forma, que são conhecidos por serem *hotspots* onde a amplificação do sinal de Raman é particularmente intensa.

O processo de *fingerprinting* via SERS foi aplicado a dois tipos diferentes de amostras: vinhos de três regiões diferentes em Portugal (Minho, Douro e Alentejo) e estirpes bacterianas resistentes. Em ambos os casos, o procedimento para a preparação da amostra foi primeiro otimizado. Os espetros de SERS foram analisados por análise de componentes principais (*principal component analysis*, *PCA*) para avaliar o potencial de discriminação da técnica. Utilizando esta abordagem, foi possível discriminar adequadamente três vinhos brancos diferentes, representando três regiões vinícolas em Portugal. Os resultados apontam para a possibilidade de utilizar este método rápido e fácil para identificação de vinhos. Além disso, quatro das espécies bacterianas resistentes de elevada prioridade indicadas pela Organização Mundial da Saúde (OMS) foram devidamente discriminadas por um método semelhante. O método desenvolvido é capaz de discriminar interespécies, mas também foi capaz de discriminar diferentes tipos de sequências da mesma espécie. Este poderia ser um método rápido para identificar bactérias, e especialmente de baixo custo, quando comparado com o padrão para identificação de rotina de bactérias - espetrometria de massa.

Finalmente, as superfícies nanoestruturadas “prontas para leitura” para análise via SERS foram preparadas pela deposição de nanoestrelas de prata em *wafers* de silício com uma camada de nanoesferas de prata, cartão com uma camada de nanoesferas de prata, vidro funcionalizado por APTES, espelho de prata, nanobastonetes de óxido de zinco e de óxido de zinco com uma camada de nanoesferas de prata. O método de deposição foi otimizado para obter uma superfície homogénea com alta densidade de *hotspots*. Verificou-se que a superfície com essas características é um vidro funcionalizado por APTES com AgNSs depositadas sob agitação orbital usando uma concentração de 0,2 nM e pH não ajustado com tampão, que garantem um fator de amplificação de até 10^4. Entre vários compostos que podem ser medidos neste substrato, estão também biomoléculas, portanto estes suportes podem ser considerados “prontos para a nanobioconjugação”.

Palavras-chave

nanopartículas; ouro; prata; enzima; lacase; nanobioconjugados; membranas; SERS; espetroscopia de Raman amplificada por superfície; bactérias; vinho; análise de componentes principais

List of figures

Chapter 1

Figure 1.1 – Schematic representation of the localized surface plasmon resonance (LSPR) phenomenon in metal nanoparticles. **|** ***4***

Figure 1.2 – Scheme of the basic structure of a lateral flow assay – adapted. **|** ***11***

Chapter 2

Figure 2.1 – Schematic representation of a substrate (Subs) redox reaction catalysed by laccase (Lac), in presence of molecular oxygen. **|** ***55***

Figure 1 – Variation of hydrodynamic volumes for bionanoconjugates produced with different laccase concentrations, determined by DLS. Variations are relative to the hydrodynamic volume measured for CALNN-functionalized AuNPs alone in solution. Bionanoconjugates were produced with AuNPs at 1 nM (black squares); 3 nM (red circles); 5 nM (blue triangles); and 7 nM (purple inverted triangles). Data points are from three independent measurements; lines correspond to fitting to a Langmuir type equation, with fitting parameters shown in Table 1. **|** ***61***

Figure 2 – Variation of electrophoretic mobility, determined by ELS, of the bionanoconjugates relative to the parent AuNPs, for increasing concentration of laccase, and the corresponding Langmuir fit. **|** ***63***

Figure 3 – Photograph of the agarose gel electrophoresis for bionanoconjugates at the indicated concentration of laccase (left). Fitting of the relative electrophoretic mobility to a Langmuir curve (right, see details in ESI). **|** ***65***

Figure 4 – Oxidase activity of laccase alone as a control (“LAC”, blue), and in the presence of AuNPs 5 nM (AuNP+LAC, red), for several total concentrations of laccase. The dashed red line for laccase with gold nanoparticles is a guide to the eye. The dotted blue line for laccase only corresponds to the linear regression obtained for laccase concentration between 15 and 250 nM (Figure S7, ESI). Error bars represent the standard deviation of the activity measurements. **|** ***67***

Figure 5 – Scheme of the model used to calculate the increase in hydrodynamic volume of bionanoconjugates per laccase molecule. The hydrodynamic diameter of AuNPs (dAuNP) was obtained by DLS, the diameter of laccase (dLAC) was calculated from its

molecular weight and the maximum diameter of bionanoconjugates (dBNC) was determined by fitting DLS data to a Langmuir isotherm. **| *68***

Figure 6 – Oxidase activity of laccase alone as a control ((“LAC”, blue) and in the presence of AuNPs 5 nM (AuNP+LAC, red grid) for pH range 6.5-8.5. **| *70***

Figure S1 – TEM micrograph of a representative area of the TEM grid and resulting size histogram showing an average diameter of 13.6 nm with a standard deviation of 2.2 nm. **| *80***

Figure S2 – XPS analysis of AuNP-CALNN, showing the areas corresponding to Au, N and S. **| *80***

Figure S3 – Variation of 1/KL as a function of the concentration of AuNPs. Bars are the standard error calculated from the fitting of DLS data. Linear fitting of these data is 1/KL = 30.7 [AuNP], with R2=0.990. **| *81***

Figure S4 – Processed digital image of the gel and migration quantification. The black lines show the average brightness intensity measured along each lane. The red lines show the fitted Gaussian curves and the peak positions for each lane, with lane 1 corresponding to the leftmost lane on the gel. The horizontal scale is in image pixels. **| *82***

Figure S5 – Langmuir isotherm plot, obtained by fitting µmin and Keq to the band migration values at different concentrations of laccase. **| *83***

Figure S6 – Fluorescence emission spectra for laccase fluorescence quenching (excitation at 280 nm) by increasing concentrations of AuNPs (A); and respective Stern-Volmer plot (emission at 330 nm) (B). **| *84***

Figure S7 – Enzymatic activity of laccase solutions in the concentration range 15-250 nM. The inset contains the results of the linear correlation. Data in red corresponds to the experimental points in Figure 4. **| *86***

Figure S8 – UV/vis spectra of a solution containing bionanoconjugates in the experimental conditions for the enzymatic assay. Curve in green is the spectrum before addition of the substrate syringaldazine, and the curve in blue is after 5 minutes of reaction. The increase in absorbance at 530 nm arises from the oxidation product of syringaldazine and it was used to follow enzymatic kinetics. **| *86***

Chapter 3

Figure 3.1 – Chemical structure of cellulose (A), nitrocellulose (B), cellulose acetate (C), polytetrafluoroethylene (D) and polyvinylidene fluoride (E). **|** ***95***

Figure 3.2 – Schematic representation of assembly process of a bioactive disk: main preparation steps (top) and representation of main changes on the support (bottom). A – Disk-shaped support (t = 0); B – Support enriched with gold nanoparticles; C – Support enriched with thiol functionalized gold nanoparticles; D – Support with nanobioconjugates; E – Stored disk for activity measurements. **|** ***103***

Figure 3.3 – Scheme summarizing the activity assay conditions, performed in a UV-Visible spectroscopy quartz cell (1 cm path, 1 ml total volume). **|** ***106***

Figure 3.4 – UV-Visible spectra for small gold nanospheres (AuNPs15, red line), big gold nanospheres (AuNPs40, green line) and gold nanostars (AuNSs, blue line). **|** ***108***

Figure 3.5 – Transmission electron microscopy (TEM) micrograph of gold nanostars. **|** ***109***

Figure 3.6 – Diameter distribution (histogram) for gold stars. Average diameter (analysis of 120 particles) in TEM micrographs: 60.4 ± 12.1 nm. **|** ***109***

Figure 3.7 – Hydrodynamic diameter distribution for gold nanostars, obtained by NTA. Average diameter: 82.6 ± 5.2 nm. Mode diameter: 85.6 ± 15.6 nm. **|** ***110***

Figure 3.8 – Transmission electron microscopy (TEM) micrograph of gold nanospheres. **|** ***111***

Figure 3.9 – Diameter distribution (histogram) for 40 nm gold nanospheres. Average diameter (analysis of 514 particles) in TEM micrographs: 40.4 ± 5.6 nm. **|** ***111***

Figure 3.10 – Hydrodynamic diameter distribution for 40 nm gold nanospheres, obtained by NTA. Average diameter: 53.0 ± 5.2 nm. Mode diameter: 42.9 ± 2.8 nm. **|** ***112***

Figure 3.11 – Zeta potential values for different molar ratios between laccase (*Trv*L) and 1 nM 15 nm gold nanoparticles (AuNPs15) – measurements in 10 mM pH 7.0 phosphate buffer (blue dots –electrostatic conjugation; red dots – covalent conjugation) . **|** ***114***

Figure 3.12 – Hydrodynamic diameter for AuNPs-MUA-BSA nanobioconjugates (red dots) and tentative AuNPs40-MUA-*Trv*L nanobioconjugates (blue dots), determined by nanoparticle tracking analysis. **|** ***115***

Figure 3.13 – Size comparison, at the same scale, between the three nanoparticle types, individualized (A) and overlapping (B), on top of a locally flat zone. **|** ***120***

Figure 3.14 – Scanning electron microscopy (backscattered electrons detection mode) microphotographs of filter paper impregnated (right) and not impregnated (left) with small gold nanospheres. **|** ***121***

Figure 3.15 – Scanning electron microscopy (backscattered electrons detection mode) microphotographs of hydrophilic mixed cellulose esters membrane impregnated (right) and not impregnated (left) with small gold nanospheres. **|** ***122***

Figure 3.16 – Scanning electron microscopy (backscattered electrons detection mode) microphotographs of nitrocellulose membrane impregnated (right) and not impregnated (left) with small gold nanospheres. **|** ***123***

Figure 3.17 – Schematic representations of two hypothesis for *Trametes versicolor* laccase immobilization onto nanoparticles-enriched support, via support away from nanoparticles influence (blue, in both A and B), via support under nanoparticle influence (green, in both A and B) and via electrostatic interaction with nanoparticle capping (red, just in B). **|** ***125***

Figure 3.18 – Laccase enzymatic activities (blue columns) and respective standard deviation (black lines) for nitrocellulose disks (6 mm diameter) with no AuNPs15 (A.00.000.L) and with AuNPs functionalised with 11-MUTMA (A.Au.MUT.L), 11-MUA (A.Au.MUA.L) and 4-MBA (A.Au.MBA.L). **|** ***126***

Figure 3.19 – Laccase enzymatic activities (blue columns) and respective standard deviation (black lines) for nitrocellulose disks (3 mm diameter) with no AuNPs15 (B.00.000.L), with non-functionalised AuNPs15 (B.Au.000.L) and with AuNPs functionalised with 11-MUTMA (B.Au.MUT.L), 11-MUA (B.Au.MUA.L) and 4MBA (B.Au.MBA.L). **|** ***127***

Figure 3.20 – Representation of *Trametes versicolor* laccase crystal structure, showing a 499 amino acids chain, N-Acetyl-D-Glucosamine molecules and water molecules (hydrogen atoms omitted), obtained using UCSF Chimera software54 and PDB entry 1GYC51. **|** ***128***

Chapter 4

Figure 4.1 – Silver nanostars UV-visible spectrum. **|** ***151***

Figure 4.2 – Hydrodynamic diameter distribution for silver nanostars, obtained by NTA. **|** ***152***

Figure 4.3 – Spectra obtained for the white wine MWA (left) and the red wine MRA (right), for all the tested conditions listed in table 4.2. Collected using a 633 nm laser. **|** ***153***

Figure 4.4 – Spectra for samples with silver nitrate added to silver nanostars in white wine. Yellow trace represents the sample with twice the amount of silver nitrate relatively to the other sample (grey trace). Collected using a 633 nm laser. **|** ***154***

Figure 4.5 – Spectra for samples using the reagents (all or part) for silver nanostars synthesis in wine. Collected using a 633 nm laser. **|** ***155***

Figure 4.6 – Spectra obtained for the white wine MWA, for all the tested conditions listed in table 4.2. Collected using a 785 nm laser. **|** ***155***

Figure 4.7 – Spectra for all samples reacted for 20 hours listed in table 4.3. Collected using a 442 nm laser. **|** ***157***

Figure 4.8 – Spectra for Douro white wine (top left), green wine (top right), both wines and silver nanostars without silver nitrate addition (bottom left) and silver nanostars (bottom right). Collected using a 532 nm laser. **|** ***158***

Figure 4.9 – Spectra for Douro white wine (top left), green wine (top right), both wines and silver nanostars without silver nitrate addition (bottom left) and silver nanostars (bottom right). Collected using a 633 nm laser. **|** ***160***

Figure 4.10 – Spectra for Douro white wine (top left), green wine (top right), both wines and silver nanostars without silver nitrate addition (bottom left) and silver nanostars (bottom right). Collected using a 785 nm laser. **|** ***161***

Figure 4.11 – Spectra collected with the green (top), red (middle) and infrared (bottom) lasers for Douro white wine (left), green wine (middle) and silver nanostars (right) . **|** ***162***

Figure 4.12 – SERS spectra for MWD (top left) and VWN (top right) wines incubated with different amounts of AgNSs; for MWA, MWD and VWN wines incubated with same amount of AgNSs (bottom left) and Raman spectra for MWA, MWD and VWN wines in absence of AgNSs. Collected with 442 nm laser. **|** ***163***

Figure 4.13 – SERS spectra for MWD (top left) and VWN (top right) wines incubated with different amounts of AgNSs; for MWA, MWD and VWN wines incubated with same amount of AgNSs (bottom left) and Raman spectra for MWA, MWD and VWN wines in absence of AgNSs. Collected with 532 nm laser. **|** ***164***

Figure 4.14 – SERS spectra for MWD (top left) and VWN (top right) wines incubated with different amounts of AgNSs; for MWA, MWD and VWN wines incubated with same

amount of AgNSs (bottom left) and Raman spectra for MWA, MWD and VWN wines in absence of AgNSs. Collected with 633 nm laser. **| *165***

Figure 4.15 – SERS spectra for MWD (top left) and VWN (top right) wines incubated with different amounts of AgNSs; for MWA, MWD and VWN wines incubated with same amount of AgNSs (bottom left) and Raman spectra for MWA, MWD and VWN wines in absence of AgNSs. Collected with 785 nm laser. **| *166***

Figure 4.16 – SERS spectra for MWD (top), VWN (middle) and MWA (bottom) wines, acquired with four lasers. **| *167***

Figure 4.17 – Raman spectra for water and sample support (tin foil) obtained with 442 nm (top left), 532 nm (top right), 633 nm (bottom left) and 785 nm (bottom right) lasers. **| *168***

Figure 4.18 – Spectra for MWA (top left), MWD (top right) and VWN (bottom left) mixed in different proportions of wine to nanostars and for the three wines under the same conditions (bottom right). Acquired with 532 nm laser. **| *169***

Figure 4.19 – Spectra for MWA (top left), MWD (top right) and VWN (bottom left) mixed in different proportions of wine to nanostars and for the three wines under the same conditions (bottom right). Acquired with 633 nm laser. **| *170***

Figure 4.20 – Spectra for MWA (top left), MWD (top right) and VWN (bottom left) mixed in different proportions of wine to nanostars and for the three wines under the same conditions (bottom right). Acquired with 785 nm laser. **| *171***

Figure 4.21 – Spectra of the three wines (AB*, DB* and VV*) prepared by the three different protocols (grouped as **1, **2 or **3 samples). Data collected with 532 nm laser. **| *173***

Figure 4.22 – Scores plot depicting PC1 and PC2 (top) and loadings plot for the two PC (bottom). Applied to protocol 1, with data pre-treatment by BLC. **| *174***

Figure 4.23 – Scores plot depicting PC1 and PC2 (top) and loadings plot for the two PC (bottom). Applied to protocol 1, with data pre-treatment by SNV. **| *175***

Figure 4.24 – Scores plot depicting PC1 and PC2 (top) and loadings plot for the two PC (bottom). Applied to protocol 2, with data pre-treatment by BLC. **| *176***

Figure 4.25 – Scores plot depicting PC1 and PC2 (top) and loadings plot for the two PC (bottom). Applied to protocol 2, with data pre-treatment by SNV. **| *177***

Figure 4.26 – Scores plot depicting PC1 and PC2 (top) and loadings plot for the two PC (bottom). Applied to protocol 3, with data pre-treatment by BLC. **| *178***

Figure 4.27 – Scores plot depicting PC2 and PC3 (top) and loadings plot for the two PC (bottom). Applied to protocol 3, with data pre-treatment by BLC. **| *179***

Figure 4.28 – Scores plot depicting PC1 and PC2 (top) and loadings plot for the two PC (bottom). Applied to protocol 3, with data pre-treatment by SNV. **| *180***

Figure 4.29 – Raman spectra for the three different wines, with some proposed assignments for common wine components. Black arrows: exclusive peaks; White arrows: relevant missing peaks. **| *181***

Chapter 5

Figure 5.1 – Molecular structures of citrate (left) and cysteamine (right). **| *194***

Figure 5.2 – Micrographs of the original filter paper support (left) and of the nanobioconjugates spot (right) – 50x magnification. **| *197***

Figure 5.3 – SEM micrographs of *Enterococcus spp*. (bacteria D) prepared for SERS, accordingly to protocols 1-5 (from top to bottom rows), shown in 1000x (left) and 25000x (right) magnifications. **| *198-199***

Figure 5.4 – PCA score plot for nanobioconjugates with *Acinetobacter baumannii* (◆) and with *Klebsiella pneumoniae* (■), prepared in UW – data collected with the 532 nm laser. **| *201***

Figure 5.5 – PCA score plot for nanobioconjugates with *Acinetobacter baumannii* (●) and with *Klebsiella pneumoniae* (◆), prepared in UW – data collected with the 633 nm laser. **| *202***

Figure 5.6 – PCA score plot for nanobioconjugates with *Acinetobacter baumannii* (◆) and with *Klebsiella pneumoniae* (■), prepared in UW – data collected with the 785 nm laser. **| *203***

Figure 5.7 – Spectra of cysteamine-capped AgNSs (red), free *Acinetobacter baumannii* (blue) and nanobioconjugates with *Acinetobacter baumannii* prepared in PBS (purple) and UW (yellow) – acquired with 633 nm laser. **| *204***

Figure 5.8 – Spectra of cysteamine-capped AgNSs (red), free *Klebsiella pneumoniae* (blue) and nanobioconjugates with *Klebsiella pneumoniae* prepared in PBS (purple) and UW (red) – acquired with 633 nm laser. **| *205***

Figure 5.9 – PCA score plot for nanobioconjugates with *Acinetobacter baumannii* prepared in PBS (■) and UW (◆) and with *Klebsiella pneumoniae* prepared in PBS (▼) and UW (▲). **|** ***206***

Figure 5.10 – PCA score plot for nanobioconjugates with *Acinetobacter baumannii* (◆) and with *Klebsiella pneumoniae* (■), prepared in PBS – data collected with the 633 nm laser. **|** ***207***

Figure 5.11 – PCA score plot for nanobioconjugates with *Acinetobacter baumannii* (◆) and with *Klebsiella pneumoniae* (■), prepared in PBS – data collected with the 785 nm laser. **|** ***207***

Figure 5.12 – PCA score plot for *Klebsiella pneumoniae* (▼), *Salmonella enterica* (●) and *Enterococcus spp.* (▲ and ■) samples, prepared accordingly protocol 1. **|** ***209***

Figure 5.13 – PCA score plot for *Klebsiella pneumoniae* (▼), *Salmonella enterica* (●) and *Enterococcus spp.* (▲ and ■) samples, prepared accordingly protocol 2. **|** ***210***

Figure 5.14 – PCA score plot for *Klebsiella pneumoniae* (▼), *Salmonella enterica* (●) and *Enterococcus spp.* (▲ and ■) samples, prepared accordingly protocol 3. **|** ***211***

Figure 5.15 – PCA score plot for *Klebsiella pneumoniae* (▼), *Salmonella enterica* (●) and *Enterococcus spp.* (▲ and ■) samples, prepared accordingly protocol 4. **|** ***212***

Figure 5.16 – PCA score plot for *Klebsiella pneumoniae* (▼), *Salmonella enterica* (●) and *Enterococcus spp.* (▲ and ■) samples, prepared accordingly protocol 5. **|** ***213***

Figure 5.17 – PLS-DA score plot for nanobioconjugates with *Acinetobacter baumannii* sequence types 98 (●), 103 (■), 208 (▲), 218 (▼), 515 (★) and 1000 (◆), prepared in UW – data collected with the 633 nm laser. **|** ***214***

Figure 5.18 – PLS-DA score plot for nanobioconjugates with *Acinetobacter baumannii* sequence types 98 (●), 103 (■), 208 (▲), 218 (▼), 515 (★) and 1000 (◆), prepared in UW – data collected with the 785 nm laser. **|** ***215***

Figure 5.19 – PLS-DA score plot for nanobioconjugates with *Klebsiella pneumoniae* sequence types 14 (◆), 15 (▲), and 147 (■), prepared in UW – data collected with the 633 nm laser. **|** ***216***

Figure 5.20 – PLS-DA score plot for nanobioconjugates with *Klebsiella pneumoniae* sequence types 14 (◆), 15 (▲), and 147 (■), prepared in UW – data collected with the 785 nm laser. **|** ***216***

Figure 5.21 – PLS-DA score plot for nanobioconjugates with *Klebsiella pneumoniae* sequence types 14 (◆), 15 (▲), and 147 (■), prepared in PBS – data collected with the 633 nm laser. **| *217***

Figure 5.22 – PLS-DA score plot for nanobioconjugates with *Klebsiella pneumoniae* sequence types 14 (◆), 15 (▲), and 147 (■), prepared in PBS – data collected with the 785 nm laser. **| *218***

Figure 5.23 – PLS-DA score plot for nanobioconjugates with *Klebsiella pneumoniae* sequence types 11 (■), 14 (▲), 15 (★), 101 (◆), 147 (▼) and 258 (●), prepared in UW – data collected with the 633 nm laser. **| *219***

Chapter 6

Reaction Scheme 6.1 – APTES hydrolysis followed by condensation for silica surface amination. **| *228***

Figure 6.1 – Raman (blue trace) and SERS (orange trace) spectra of rhodamine 6G (10-3 M and 10-6 M, respectively). **| *235***

Figure 6.2 – Enhancement factors (blue columns) and standard error (black lines) for samples prepared using 0.05 nM (SS.05.UU), 0.10 nM (SS.10.UU) and no (SS.C1 and SS.C2) silver nanostars solutions. Calculated based on R6G 1360 cm^{-1} band. **| *237***

Figure 6.3 – Enhancement factors (blue columns) and standard error (black lines) calculated from the 1360 cm^{-1} (left) and 1509 cm^{-1} (right) bands, for samples prepared without shaking (SS.05.UUd–f) and assisted by ultrasounds (SS.05.US). **| *239***

Figure 6.4 – Scanning electron microscopy micrographs of samples SS.05.UUd (top), with an undisturbed adsorption process and SS.05.USa (bottom), with the adsorption process assisted by ultrasounds. **| *240***

Figure 6.5 – Enhancement factors (blue columns) and standard error (black lines) calculated from the 1360 cm^{-1} (left) and 1509 cm^{-1} (right) bands, for samples prepared using 0.10 nM (GS.10.OS.60.085) and 0.20 nM (GS.20.OS.60.085) silver nanostars solutions. **| *241***

Figure 6.6 – Samples prepared over orbital shaking for 60 minutes at pH 8.5, using immersion solutions with silver nanostars concentrations of 0.1 nM, 0.2 nM, 0.3 nM, 0.5 nM, 0.8 nM and 0.1 + 0.1 nM (two 30 minutes cycles at 0.1 nM) – samples

GS.10.OS.60.085, GS.20.OS.60.085, GS.30.OS.60.085, GS.50.OS.60.085, GS.80.OS.60.085, and GS.1010.OS.3030.085, respectively. **|** ***243***

Figure 6.7 – SEM micrograph of fragmented silver nanostars representing the set samples GS.10.OS.60.085, GS.20.OS.60.085, GS.30.OS.60.085, GS.50.OS.60.085, GS.80.OS.60.085, and GS.1010.OS.3030.085. **|** ***243***

Figure 6.8 – SEM micrographs obtained in two different regions from samples GS.80.OS.60.085 (left) and GS.1010.OS.3030.085 (right). **|** ***244***

Figure 6.9 – Enhancement factors (blue columns) and standard error (black lines) calculated from the 1360 cm^{-1} (left) and 1509 cm^{-1} (right) bands, for samples using immersion solutions with silver nanostars concentrations of 0.1 nM, 0.2 nM, 0.3 nM, 0.5 nM, 0.8 nM and 0.1 + 0.1 nM (two 30 minutes cycles at 0.1 nM) – samples GS.10.OS.60.085, GS.20.OS.60.085, GS.30.OS.60.085, GS.50.OS.60.085, GS.80.OS.60.085, and GS.1010.OS.3030.085, respectively. **|** ***245***

Figure 6.10 – SEM micrographs using immersion solutions with silver nanostars concentrations 0.1 nM, 0.2 nM, 0.1 + 0.1 nM, 0.1 + 0.2 nM and 0.2 + 0.1 nM (two 60 minutes cycles) – samples GS.10.OS.120.00, GS.20.OS.120.00, GS.1010.OS.6060.00, GS.1020.OS.6060.00, and GS.2010.OS.6060.00, respectively. **|** ***246***

Figure 6.11 – Enhancement factors (blue columns) and standard error (black lines) calculated from the 1360 cm^{-1} (left) and 1509 cm^{-1} (right) bands, for samples using immersion solutions with silver nanostars concentrations of 0.1 nM, 0.2 nM, 0.1 + 0.1 nM, 0.1 + 0.2 nM and 0.2 + 0.1 nM (two 60 minutes cycles) – samples GS.10.OS.120.00, GS.20.OS.120.00, GS.1010.OS.6060.00, GS.1020.OS.6060.00, and GS.2010.OS.6060.00, respectively. **|** ***247***

Figure 6.12 – Enhancement factors (blue columns) and standard error (black lines) calculated from the 1360 cm^{-1} (left) and 1509 cm^{-1} (right) bands, for samples prepared with orbital shaking (GS.10.OS.60.085) and assisted by ultrasounds (GS.10.OS.60.085). **|** ***248***

Figure 6.13 – Enhancement factors (blue columns) and standard error (black lines) calculated from the 1360 cm^{-1} (left) and 1509 cm^{-1} (right) bands, for samples prepared at pH 6.0 (GS.10.OS.60.060), pH 8.5 (GS.10.OS.60.085), and pH 11.0 (GS.10.OS.60.110). **|** ***249***

Figure 6.14 – Enhancement factors (blue columns) and standard error (black lines) calculated from the 1360 cm^{-1} (left) and 1509 cm^{-1} (right) bands, for samples CBa–c. **|** ***250***

Figure 6.15 – SEM micrographs obtained from sample CBc. **| *250***

Figure 6.16 – Enhancement factors calculated from the 1360 cm^{-1} (left) and 1509 cm^{-1} (right) bands, for samples using a silver mirror and controls. **| *251***

Figure 6.17 – SEM micrographs for samples (SM.05.60.50.N, top) and (SM.C2, bottom). **| *252***

Figure 6.18 – SEM micrographs of silver nanospheres-decorated zinc oxide nanorods tentatively decorated with silver nanostars. **| *253***

Figure 6.19 – SEM micrographs of bare zinc oxide nanorods tentatively decorated with silver nanostars. **| *254***

List of tables

Chapter 2

Table 1 – Fitting parameters for the hydrodynamic volume of the bionanoconjugates as a function of laccase concentration, to a Langmuir adsorption curve. Results are presented for four different AuNPs concentrations (see Figure 1). **|** ***62***

Chapter 3

Table 3.1 – Membrane composition for enzymatic activity tests – set of experiments A. **|** ***104***

Table 3.2 – Membrane composition for enzymatic activity tests – set of experiments B. **|** ***105***

Table 3.3 – Summary of characterization data for all synthesised nanoparticles. **|** ***113***

Table 3.4 – Photographs of the support materials impregnated with gold nanoparticles – 15 nm gold nanospheres (AuNPs15), 40 nm gold nanospheres (AuNPs40) and gold nanostars (AuNSs). **|** ***117***

Chapter 4

Table 4.1 – Key for wine samples codes. **|** ***143***

Table 4.2 – Sample composition for extra silver nanostars synthesised in wine, with additional reducing agents. **|** ***145***

Table 4.3 – Sample composition for extra silver nanostars synthesised in wine, without additional reducing agents. **|** ***146***

Table 4.4 – Sample composition for SERS measurements using silver nanostars decorated with wine molecules. **|** ***147***

Table 4.5 – Tubes composition for SERS measurements of wines, enhanced by silver nanostars. **|** ***148***

Table 4.6 – Sample codification, grouped by protocol. **|** ***149***

Chapter 5

Table 5.1 – *Acinetobacter baumannii* and *Klebsiella pneumoniae* sequence types. **|** ***193***

Table 5.2 – *Klebsiella pneumoniae* sequence types. **|** ***193***

Table 5.3 – Silver nanostars and bacteria nanobioconjugation protocols. **|** ***194***

Chapter 6

Table 6.1 – Silicon based supports. **|** ***230***

Table 6.2 – Functionalised glass-based supports. **|** ***232***

Table 6.3 – Silver mirror-based supports. **|** ***233***

Table 6.4 – Zinc oxide nanorods-based supports. **|** ***234***

List of abbreviations

11-MUA 11-mercaptoundecanoic acid

11-MUTMA (11-mercaptoundecyl)-*N*,*N*,*N*-trimethylammonium chloride

2D Two-dimensional / two dimensions

3D Three-dimensional / three dimensions

4-MBA 4-mercaptobenzoic acid

Ab Antibody

Ag Antigen

AGE Agarose Gel Electrophoresis

AgNS Silver nanostar (AgNSs for plural)

ALP Alkaline phosphatase

APTES (3-aminopropyl)triethoxysilane

ATP Adenosine triphosphate

AuE Gold electrode

AuNP Gold nanosphere (AuNPs for plural)

AuNPs15 Gold nanosphere with a diameter of 15 nm

AuNPs40 Gold nanosphere with a diameter of 40 nm

AuNS Gold nanostar (AuNSs for plural)

BLC Baseline linear correction

BSA Bovine serum albumin

BSE Backscattered electrons

BSED Backscattered electrons detector

CALNN Pentapeptide Cysteine-Alanine-Leucine-Asparagine-Asparagine

CCD Charge-coupled device

CTAB Cetyltrimethylammonium bromide

CTAC Cetyltrimethylammonium chloride

CYS Cysteine

DET Direct electron transfer

DLS Dynamic light scattering

DNA Deoxyribonucleic acid

DTNB 5,5′-dithiobis(2-nitrobenzoic acid)

EDC 1-Ethyl-3-(3-dimethylaminopropyl)carbodiimide

EF Enhancement factor

EGFR Epidermal growth factor receptor

ELISA Enzyme-linked immunosorbent assay

ELS Electrophoretic light scattering

ESEM Environmental scanning electron microscope

FCTUNL *Faculdade de Ciências e Tecnologia da Universidade Nova de Lisboa*

FCUP *Faculdade de Ciências da Universidade do Porto*

FFUBB *Facultatea de Fizică* from *Universitatea Babeș-Bolyai*

FFUP *Faculdade de Farmácia da Universidade do Porto*

FP Filter paper

GCE Glassy carbon electrode

GN Gram-negative

GP Gram-positive

HAS Human serum albumin

HMCE Hydrophilic mixed cellulose esters

HPLC High-performance liquid chromatography

HPVDF Hydrophilic polyvinylidene fluoride

HRP Horseradish peroxidase

ICP-MS Inductively coupled plasma mass spectrometry detection

IR Infrared

LC-MS Liquid chromatography coupled to mass spectrometry

LDA Linear discriminant analysis

LFA Lateral flow assays

LSPR Localized surface plasmon resonance

LV Latent variables

MALDI Matrix-assisted laser desorption/ionization

MALDI–MS Matrix-assisted laser desorption/ionization mass spectrometry

MALDI–TOF–MS Matrix-assisted laser desorption/ionization time-of-flight mass spectrometry

MIR Mid-infrared

miRNA Micro ribonucleic acid

MRA *Maduro* red wine from *Alentejo* region

MRD *Maduro* red wine from *Douro* region

MS Mass spectrometry

MWA *Maduro* white wine from *Alentejo* region

MWD *Maduro* white wine from *Douro* region

NBC Nanobioconjugate (NBCs for plural)

NC Nitrocellulose

NHS *N*-Hydroxysuccinimide

NIR Near-infrared

NP Nanoparticle (NPs for plural)

NTA Nanoparticle tracking analysis

OP Office paper

PARAFAC Parallel factor analysis

PBS Phosphate buffer saline

PC Principal component

PCA Principal component analysis

PDB Protein Data Bank

PLS-DA Partial least squares discriminant analysis

PSA Prostate-specific antigen

PTFE Polytetrafluoroethylene

PVD Physical vapour deposition

PVDF Polyvinylidene fluoride

PVP Polyvinylpyrrolidone

RC Regenerated cellulose

RCF Relative centrifugal force

RI Refractive index

RNA Ribonucleic acid

RSD Relative standard deviation

SAM Self-assembled monolayer

SD Standard deviation

SEM Scanning electron microscopy

SERRS Surface-enhanced resonance Raman spectroscopy

SERS Surface-enhanced Raman spectroscopy

SI Similarity index

SNV Standard normal variate

TEM Transmission electron microscopy

TOF Time-of-flight

***Tov*L** *Toxicodendron vernicifluum* laccase

Trv *Trametes versicolor*

***Trv*L** *Trametes versicolor* laccase

UV–Vis Ultraviolet-visible spectroscopy

UW Ultrapure water

VMN Green (*Verde*) wine

ZP Zeta potential

General Introduction

1

This thesis, fitting in nanotechnology and sustainable chemistry fields, is centred in nanobioconjugation with different components – enzymes (chapters 2 and 3), and chemical and biochemical compounds from wine (chapter 4) and bacteria (chapter 5) – and for different purposes – nanoparticle–protein adsorption studies (chapter 2), enzymatic activity enhancement (chapters 2 and 3) and sample fingerprinting (chapters 4 and 5). Chapter 6 does not describe a nanobioconjugation process, but nanobioconjugation-ready substrates. Despite the use of several techniques, such as Raman and SERS, and data processing methods, such as PCA, they were always used with the main focus on nanobioconjugates.

This general introduction starts with a brief contextualisation of the nanotechnology field and nanoparticles' properties that make them so unique, followed by a panorama of the state of the art in the biosensing field using gold and silver nanoparticles.

1.1. Nanotechnology and nanoparticles

The gap between macroscale and nanoscale is big enough to completely turn the table regarding material properties. These all-new properties of the nanomaterials have been object of fundamental research since some decades now. Nowadays, with an already considerable accumulated knowledge concerning these properties, they are put into good use in several applications, in multiple fields. Nanotechnology, with its name disseminated since 1986 after K. Eric Drexel's book "*Engines of Creation: The Coming Era of Nanotechnology*",[1] is nowadays a transversal science and it is often deeply connected to chemistry, physics and materials science, with ultimate applications in relevant and current fields than can go, for example, from health[2] to catalysis, clean energy[3] or information technology.

Being in the field of nanotechnology is synonym of producing or using materials with a size, or the size of its components, that falls in the often-accepted range between one nanometre and one hundred nanometres. Typical examples of these materials are carbon nanotubes (with a section diameter usually with a few nanometres), graphene (that can even go to a sub-nanometre thickness) and a huge variety of nanoparticles (with a broader range of sizes within the nanoscale). Regarding this last type of nanomaterial, there is a lot of research dealing with metal nanoparticles (both magnetic and non-magnetic), although other non-metal types, like mesoporous silica nanoparticles, are also popular in research and literature.

Due to their size, nanoparticles in general have a huge ratio between surface area and volume. As can be seen in equation 1.1 for a sphere, the most common nanoparticle shape, the lower the particle radius (r), the higher is the ratio between surface area and volume (R_{SV}).

$$R_{SV} = \frac{Surface\ Area}{Volume} = \frac{4\pi \cdot r^2}{\frac{4}{3}\pi \cdot r^3} = \frac{3}{r} \qquad \text{(Eq. 1.1)}$$

This high proportion of atoms at the surface imparts new and size dependent properties to nanoparticles, in a way that does not occur in the respective macroscopic bulk material. One of these new properties relates to the interaction of metal nanoparticles with incident light. The electric field of the incident light causes a collective oscillation of the electrons at the nanoparticle, a phenomenon called localized surface plasmon resonance (LSPR), and it is represented in figure 1.1.

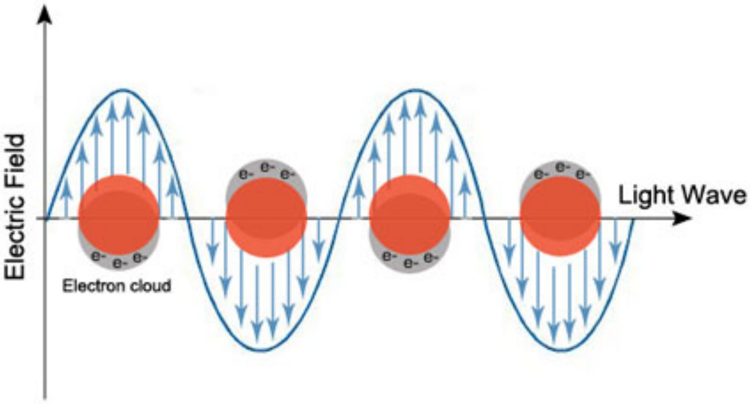

Figure 1.1 – Schematic representation of the localized surface plasmon resonance (LSPR) phenomenon in metal nanoparticles. *Image reproduced with no changes in context of Creative Commons licence.*

This phenomenon imparts useful optic properties, strongly dependent of their size and shape, that have been explored in multiple applications.[4-5]

1.2. Gold and silver nanoparticles

Under the metal nanoparticles (NPs) category, gold nanoparticles (AuNPs) are probably the most explored in research, namely in biosensors field[6] – further explored in section 1.3. Characteristics like (i) their plasmonic properties, with special consequences at the color level[4], in response to size and shape changes[5] (ii) the possibility of having their surface tuned with a variety of chemical compounds, taking special advantage of the high affinity of sulphur compounds to AuNPs surface[4, 7], (iii) high thermic and electric conductivities[5], (iv) fluorescence quenching properties[5] and (v) high resistance to oxidation[5], makes AuNPs particularly adequate for numerous applications.

Silver nanoparticles are also been the object of numerous studies, with typical uses in research as bactericidal agents[8-9] and as enhancers for Raman spectroscopy[10]. In the case of Raman spectroscopy, silver nanoparticles are typically not the focus, but the adjuvants for the measurement. This role is however quite important, since it allows the detection and quantification of trace analytes in samples where, even at trace amounts, they can have serious implications. Food safety[11-12], pharmaceuticals purity[13] and biosensors – further explored in section 1.4 – are examples were trace detection is critical.

1.2.1. Synthesis of gold nanoparticles

The synthesis of citrate-stabilized AuNPs based on the aqueous reduction of tetrachloroauric acid ($HAuCl_4$) by sodium citrate, was developed by Turkevich *et al.*[14] and modified by Frens *et al.*[15], and it still is the most commonly employed synthesis method in aqueous solution.[16] Several improvements on this method have been reported[17-21], and, in the best cases, the reproducibility between batches regarding the average size of particles is quite high (relative standard deviation < 3%). The obtained size dispersion is acceptable for the majority of the work where these AuNPs are applied.

For bigger sizes, especially bigger than 40 nm nanospheres, seed-mediated synthesis strategies, based on the temporal separation of nucleation and growth processes, are considered to be very efficient methods to control the AuNPs size and shape.[16] In a seeded growth strategy for the synthesis of size-controlled large citrate-stabilized spherical AuNPs, based on the classical Turkevich–Frens reaction system, the critical step is the inhibition of secondary nucleation during the growth process, allowing the enlargement of AuNPs via the surface-catalysed reduction of Au^{3+} by sodium citrate.[16]

In gold nanoparticle synthesis, it is also possible to tune the final shape of the nanoparticle, using director agents which lead to a preferential growth starting from a specific facet. Shapes like rods[22], octahedrons[23], triangles[24] or stars[25-26] were already described in literature. This directed growth is favoured by polymers like polyvinylpyrrolidone (PVP)[25-26] or surfactants like cetyltrimethylammonium bromide (CTAB)[23, 27] and cetyltrimethylammonium chloride (CTAC)[24]. All of these directed growth agents have drawbacks. CTAB and CTAC are toxic and PVP forms a strong capping around the newly-synthesised gold nanoparticles, weakening the interaction between (bio)molecules and the particles.

Recently, star-shaped gold nanoparticles were synthesised using silver as director agent.[28] This synthesis is based on the growth of seeds obtained by the Turkevich–Frens[14-15] method. The critical difference is the addition of silver nitrate. Silver nitrate will deposit only on some facets at the AuNPs seeds surface. These seeds will be like “silver stained gold nanoparticles” and newly available gold (via $HAuCl_4$) will not deposit evenly across the AuNPs surface, but only at these spots. The inhomogeneous growth yields several tips growing from a common spherical core, giving rise to star-like nanoparticles (multipod). All of this happens in a few seconds and, besides fast, is also an easy synthesis to perform. Comparing this synthesis with the ones using PVP[26], the possibility of tuning the size and morphology is lost, however the fact of being citrate-capped is a major advantage. Since this capping agent can be easily replaced, citrate-capped AuNSs are easily to be functionalised with other capping of interest (typically thiols) or allow better interaction AuNSs–analyte.

1.2.2. Synthesis of silver nanoparticles

Like gold nanoparticles, silver nanoparticles can be synthesised with different shapes – spheres[29], rods[30], cubes[29, 31], and stars[32]. These synthesis are made using silver nitrate as precursor and using different reducing agents – hydroxylamine[32], citrate[32], ethylene glycol[31], sodium borohydride[30, 33] or even light[34] – with final capping agents like PVP[29, 31], poly(vinyl alcohol)[35], citrate[30, 32] or *L*-cysteine[36]. One major difference between the synthesis of gold and silver nanoparticles is that, for silver, synthesis methods using biological materials as the reducing source are extensively used, being a hot topic at the moment[34-35, 37-40]. However, the size and shape are much more difficult to control in these cases.

From all the shapes, silver nanostars (AgNSs) are probably the most interesting regarding plasmonic properties. The multiplicity of number or arms, arm's length and resulting global size basically enables interaction with light across all the visible spectra, but more importantly on the ~400 nm region.[32] One of the most important applications for these AgNSs in surface-enhanced Raman spectroscopy (SERS), due to their remarkable capacity to form hotspots, (see section 1.5.1). These nanoparticles tick all the boxes regarding the typical morphology that favours hotspots: rough surface, sharp tips, intraparticle and interparticle nanogaps.[41]

1.3. Gold nanoparticles nanobioconjugates in sensing

Nanoparticles are very useful in the development of sensors nowadays, in particular metal nanoparticles and, in this category, spherical gold nanoparticles (AuNPs). As mentioned in the beginning of the section 1.2, this type of nanoparticles encompasses several advantages, such as well-known and reproductible synthesis protocols, stability to oxidation, easy functionalization with a wide range of thiols and excellent optical/electronic properties. Given the properties and advantages enlisted above, AuNPs are often used in colorimetric assays, lateral flow assays and electrochemical assays, reviewed in sections 1.3.1 to 1.3.3.

1.3.1. Colorimetric Assays

The localized surface plasmon resonance (LSPR) wavelength of spherical gold nanoparticles (AuNPs) strongly depends on their size and their aggregation state. These changes are translated into different colors of gold nanoparticles and this is one of their properties more commonly used in sensors.[5, 42-43] A typical approach is in the detection of analytes that are able to aggregate or crosslink (covalently or non-covalently) AuNPs, by acting as linkers between nanoparticles or by decreasing the surface charge that assures the electronic repulsion between particles, triggering a clearly visible change in the color of AuNPs in solution. The opposite process, where the aggregation is reversed, is also monitored for some tests. Several sensors were developed taking advantage of these processes, namely for detection of analytes such as DNA and proteins. In this section, some typical examples of the application of AuNPs in optical sensing are described.

Chuang *et al.*[44] used AuNPs for measuring proteinase activity. 15 nm gold nanospheres were capped with gelatine, a proteinase substrate, and with 6-mercaptohexan-1-ol (HSOH), a non-charged thiol. When these AuNPs–(HSOH/gelatine) are in the presence of proteinases such as trypsin or gelatinases, gelatine is digested, the shell that ensured AuNPs individualization is lost and these non-charged nanoparticles aggregate. This has been used as qualitative method for the presence of the enzyme, since the color change from red to blue upon aggregation is readily detected by the naked eye. In addition, it is possible to quantify the enzymatic activity by measuring the absorbance at 625 nm (Abs_{625}) and at 525 nm (Abs_{525}) and plotting the ratio between these two values (Abs_{625}/Abs_{525}) against time. The detection limit of trypsin activity obtained in this test was 1.25 x 10^{-2} U and the reaction took 10 minutes. The method has the potential to be developed as a system for point-of-care biosensor, however, it cannot distinguish between different proteases (e.g. from gelatinase A and gelatinase B).

A two-in-one method based on the color change of gold nanoparticles was described by Ou *et al.*[45] for detection of exonucleases or DNA-binding proteins. In this case, two groups of AuNPs, functionalised with two different DNA sequences, are crosslinked by DNA hybridization, which lead to their aggregation. When an exonuclease is present in the medium, this hybridization is destroyed, and the AuNPs revert from blue to the original red color, typical of individualized AuNPs. Moreover, in the presence of a DNA-binding protein specific for that sequence, the hybridization is not affected by an exonuclease, *i.e.* using the same DNA-functionalised AuNPs, it is possible to detect the presence of a sequence-specific DNA-binding protein because it blocks the effect of an exonuclease added to the medium. The main advantage of this method is the possibility to implement it for high-throughput assays (e.g. microplate format) and it is even suitable for two types of analytes. The authors tested the method for exonuclease III, achieving a detection limit of 10 nM, using the correlation between the ratio between absorbances at 700 nm and 525 nm (A_{700}/A_{525}) and the exonuclease concentration.

Amini *et al.*[46] used a similar principle to detect a target DNA, in this case *P. aeruginosa* exotoxin A (ETA) gene. Gold nanoparticles functionalised with a DNA fragment capable of hybridizing with the ETA gene, are mixed with this target DNA. After that, *BamHI* endonuclease starts to fragment the hybridized DNA (both strands), which leaves part of the gold nanoparticles without capping, so they can easily aggregate. The amount of target DNA is directly proportional to the extent of aggregation, quantified by ratio between absorbances at 600 nm and 525 nm (A_{600}/A_{525}), and it was possible to detect the DNA down to 10 ng/mL. As in other methods here described, this method can be the base of a hand-held DNA diagnostic device, capable to detect pathogenic microorganisms at point-of-care.

Other example of using the disaggregation of AuNPs for quantifying DNA at a nanomolar level was given by Liu *et al.*[47] Here, larger DNA sequences are cleaved in residual DNA, in the presence of exonuclease III. These residual DNA molecules will functionalise the gold nanoparticles in solution, providing resistance to salt induced aggregation. It was possible to linearly correlate their aggregation state, through a ratio between the absorbances at 525 nm and 625 nm (A_{525}/A_{625}), to the initial DNA concentration in a 10–150 nM range.

AuNPs–protein nanobioconjugates were used to monitor pH or the presence of mono-, di- or trivalent metal ions in solution.[48] AuNPs were capped with insulin, and these nanobioconjugates can undergo reversible aggregation at low pH. At pH 7.0, 9.0 and 11.0 there was no evidence of aggregation, whereas at pH 1.8, 3.6 and 4.3 aggregation occurred, especially for the lowest pH. Regarding the metals, the following ions destabilized the AuNPs–insulin colloidal dispersion, in ionic concentrations of 100–200 µM, with the following strength: Fe^{3+} > Al^{3+}, Cr^{3+}, La^{3+} ≥ Au^{3+} ≥ Pb^{2+}, Hg^{2+} > Cu^{2+} > Fe^{2+} > Ag^{+} > Cd^{2+} > Zn^{2+} > Ni^{2+}. These ions did not show any influence: Na^{+}, Ca^{2+}, Mg^{2+}, Mn^{2+}, Co^{2+}. In other work, AuNPs–papain nanobioconjugates were used to detect metal ions – Hg^{2+}, Pb^{2+} and Cu^{2+}.[49] Papain is a protein with seven cysteine residues, which selectively bind these ions, promoting the aggregation of the AuNPs–papain nanobioconjugates. The nanobioconjugates showed a strong response to mercury ions in water and a moderate response to lead and copper ions. Other nine more ions were tested, with no noticeable change in the aggregation state of the nanobioconjugates. The sensitivity of the detection system was influenced by the pH, the concentration of nanobioconjugates and the size of gold nanoparticles. Despite the common use of smaller AuNPs (~15 nm diameter), it was found that larger (42 nm diameter) gold nanoparticles provide for a better sensitivity, with a detection limit as low as 200 nM of Hg^{2+}, Pb^{2+} or Cu^{2+}. The underlying principles of this work can be applied to water monitoring in developing regions, where waters are often contaminated and the resources for chemical analysis are scarce.

Using gold nanoparticles functionalized with cholesterol oxidase, Nirala *et al.*[50] developed a method capable of linearly correlate the amount of free cholesterol in solution with the aggregation state of the AuNPs using the absorbance decrease of the SPR peak. Cholesterol was quantified in the 25–300 mg/dL range and the authors even created a color wheel as a key to translate test color into cholesterol concentration. This way, the test was easy to perform and its results were easy to read.

Other colorimetric assay[51], this time assisted by an external electric field, was used to concentrate AuNPs on top of a membrane to evaluate their aggregation state. The detection of human serum albumin (HSA) in simulated urine is made by HSA nanobioconjugation with AuNPs. The formation of these nanobioconjugates protect AuNPs from aggregation when exposed to the electric field, in opposition to non-conjugated AuNPs that readily aggregate. It was also possible to find a linear correlation between the logarithm of HSA concentration and the adjusted red level in pictures of the membrane, captured with a digital camera. The method was able to quantify HSA in the 0.1–20 µM range. It is important to notice that in this case the nanobioconjugate was not previously assembled to detect other analyte, but the nanobioconjugation itself worked as a method to detect and quantify the biomolecule forming the nanobioconjugate. The fact of the reading is made after AuNPs concentration reduces the number of nanoparticles needed, however the need to apply an electric field adds an extra task and more material, that are not typically in the aim of these tests.

All of these example represent tests that are typically developed with the objectives of (i) detecting the presence of an analyte by the naked eye (although is often possible to quantify the analyte by following absorbance values using UV-Vis), (ii) obtaining immediate or quick results, (iii) producing hand-held devices or reaction kits and (iv) making a low cost test to become widely available. All of this makes these methods perfect candidates to point-of-care detection. However, not a lot of them already made the leap to assays with real samples or to a prototype. Those are crucial steps for real-world applications.

1.3.2. Lateral Flow Assays

Other type of assays that use the plasmonic properties of gold nanoparticles are lateral flow assays (LFA). These assays have a physical structure very similar between them and it is generically schematized in figure 1.2.

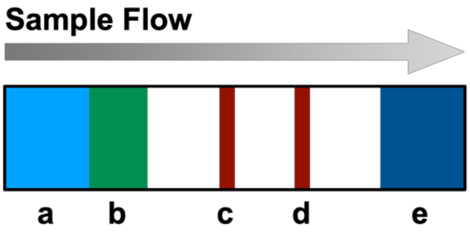

Figure 1.2 – Scheme of the basic structure of a lateral flow assay – adapted[52]. a – sample pad; b – conjugate pad; c – test line; d – control line; e – absorption pad.

An LFA is a sequence of elements (a–e, figure 1.2) intercalated with a nitrocellulose membrane (white regions, figure 1.2) assembled on a strip support with a few square centimetres. A liquid sample deposited in one end of the strip (a) goes through a series of structures towards the other end (e) that, with its absorption properties, assures that the sample properly contacts with all the other elements (b–d). In the conjugate pad (b), there are labelled (e.g. with AuNPs) biomolecules (e.g.

antibodies, DNA) that will specifically bind the analyte, if present. These labelled biomolecules migrate to the next structure – the test line (c) – that also contains biomolecules (immobilized, non-labelled) selective to the analyte. In the presence of the analyte, it will work as a bridge between the non-labelled and labelled biomolecules, so the label will be detectable at this line. The subsequent structure – the control line (d) – contains biomolecules (immobilized, non-labelled) capable of binding the labelled biomolecules that left the conjugate pad (b) in the beginning. The control line always binds the labelled biomolecules and assures that the sample already crossed the test line. In sum, both test and control line will have detectable labels in a positive test, whereas in a negative test only the control line will have the labels.

Lateral flow assays are often used for clinical diagnosis[53] and show advantages like their low cost and easy production – especially relevant to bring diagnosis to regions with low resources –, rapid results, little interferences and they can be used by non-specialized users by simply adding the sample to the test.[52] The sample can be as easy to collect as saliva.[54] Several of LFA are already available in the market, namely the well-known pregnancy tests.[52]

For LFA, spherical gold nanoparticles are typically conjugated with biomolecules such as DNA or antibodies and, less often, proteins. Typical examples will be discussed in the following paragraphs. The major assembling strategies and working mechanism for these tests are (i) antibody-based sandwich format, (ii) antibody-based competitive format, (iii) DNA-based hybridization format and (iv) DNA-based aptamer format.[52] Recently, this last format is replacing the use of antibodies, because aptamers have molecular recognition features similar to antibodies but they can be easily edited and tuned to a particular biomolecular target.[55-56]

The antibody-based sandwich format is very popular. Antibodies are well-known by their high affinity with the antigen. A recent example of this format describes the detection of *Staphylococcus aureus* enterotoxin A (SaEA) in milk.[57] This involves two different types of anti-SaEA – one labelled with AuNPs (red color), that is kept in the conjugate pad, and the other is immobilized in the test line with no labelling. In addition, one anti-(anti-SaEA) antibody is immobilized in the control line. If SaEA is present in the sample, it is captured by anti-SaEA-AuNPs, which are then captured by anti-SaEA immobilized in the test line, with SaEA working as bridge between the two antibodies (sandwich). Due to the presence of the AuNPs in the sandwich complex, the test line becomes red. Anti-SaEA-AuNPs in excess keep migrating and are captured by the antibodies immobilized in control line. Control line also becomes red. In absence of the

SaEA, there is no formation of the sandwich complex, so anti-SaEA-AuNPs keep migrating and are only captured in the control line. So, for a negative test, only the control line turns red. The same approach was also employed to staphylococcal enterotoxin B.[58] Shiga toxins (from E. coli), together with enterotoxins are the main microbial toxins targeted by LFA research.[59-61]

The antibody-based competitive format, an alternative to the sandwich format, uses immobilized analyte in the test line, instead of anti-analyte antibodies like the sandwich format. In the conjugate pad are available anti-analyte antibodies labelled with AuNPs (like the sandwich format). If the sample contains the analyte, it will block the anti-analyte–AuNPs conjugates before they get to the test line. With them blocked, they will not be able to bind to the analyte in test line, and they keep migrating to the control line where they will be captured (again, like the sandwich format). In sum, the difference resides in the test line, here containing analyte (usually associated with BSA to avoid unspecific binding), and a positive test is translated by the absence of red color at this line. This format avoids the use of one type of antibodies, which are often more expensive and harder to obtain than the analyte itself.

A recent example is the test developed by Dou *et al.*[62] to detect furazolidone as a model analyte, with a detection limit of 1 ng/mL. In this test, only a test line was used, but typically there is a control line, with an antibody capable of binding the anti-analyte antibody even if blocked. This was the case of the LFA for detecting tenofovir in urine developed by Pratt *et al.*[63], with results down to 1 µg/mL.

In the case of other binding type with high affinity and selectivity – DNA hybridization – a sandwich-like method can also be employed. He *et al.*[64] developed a lateral flow strip biosensor using 15 nm gold nanospheres, capable of detecting a DNA sequence of interest, down to a 0.01 pM concentration. The labelled probes are AuNPs functionalized with DNA capable of partial hybridization with the target DNA. Upon sample addition, the target DNA will firstly hybridize with the labelled probes available in the conjugate pad. The new conjugates keep migrating towards the test line, that contains immobilized DNA also capable of hybridizing with the target DNA. In case of the positive test, the target DNA will act as a bridge between the DNA immobilized on the test line and the probes, giving a red color to the line. The DNA on the test line is not able to hybridize directly with the DNA bound to the AuNPs, in opposition to the one immobilized in the control line, that captures directly the AuNPs–DNA probes. This method is also valid for target RNA.[65] Hu *et al.*[66] followed a similar strategy, but functionalizing the probes additionally with DNA capable of hybridizing with other DNA-functionalised AuNPs in order to enhance the signal. The aggregates formed have molecular extinction coefficients that increase exponentially with the particle size, thus providing a more intense color and lower detection limits.[67]

Finally, the assays where the affinity arises from an aptamer–protein interaction, share some similarities to antibody-based LFA, namely the competitive essays. In these cases, AuNPs are typically functionalized with an aptamer, specific for the protein to be detected (analyte). At the test line, this same protein is immobilized and at the control line an oligonucleotide complementary to the aptamer is immobilized. In the absence of analyte, the AuNPs–aptamer conjugates will bind the protein at the test line and the oligonucleotide at the control line. In the presence of the analyte, AuNPs–aptamer will be blocked by the analyte, so the probes will not bind to the test line. However, given the high affinity between the aptamer and its complementary immobilized oligonucleotide, some proteins are displaced from the probes and make free aptamers to bind in the control line. This was the case of the LFA for detection of β-conglutin with a detection limit of 55 pM proposed by Jauset-Rubio *et al.*[68]

The research around these LFA is still very active, with this type of point-of-care tests still being explored for a vast variety of analytes. This continuous interest arises from the huge advantage in having all the material and reagents needed in one single small strip that only has to be putted in contact with the sample. This automatically leads to the already mentioned strongest points of method, such as, low cost, easiness of transportation, namely to remote and low resources areas, and no need of technical expertise to manipulate the test.

1.3.3. Electrochemical Assays

Gold nanoparticles are often used in order to improve electrode performance, even without any kind of bioconjugation involved[69-72], especially due to its direct electron transfer (DET) properties and the capacity to increase the electrode surface area given the (nano)roughness they add to the surface.[73-74]

Direct electron transfer is an important phenomenon for electrochemistry and laccases enable DET in bioelectrodes because it makes possible to couple their enzymatic activity to electric current production when conveniently linked to an electrode.[75-76] This phenomenon is the opposite of mediated electron transfer (MET) that requires redox mediators, which complicate the enzyme electrode design stability and is frequently toxic.[76] DET avoids all of these drawbacks. The first allusion to direct electron transfer with a redox protein (cytochrome *c*) were published in 1977 by two independent groups. In the following years other reports showed evidence that DET was also possible for larger redox proteins with enzymatic activity (oxidoreductases), namely laccase. As mentioned before, DET is especially important for electrochemical applications, such as bioelectrodes, and even long-range electron transfer between redox enzymes and electrodes is possible.[77]

Metal nanoparticles, namely gold nanoparticles (AuNPs), can help in bioelectrodes either by favouring the DET phenomenon[76] and also by an increase of the enzymatic activity itself[78]. For example, some enzyme molecules with an organized immobilization on adequately functionalized AuNPs establish very fast DET with the electrode via their Type 1 copper site.[76] AuNPs incorporation in electrodes is performed by multiple drop cast of a concentrated AuNPs solution on top of the electrode[79] or by *in situ* electrochemical synthesis, with electrode immersion in a gold precursor solution[80].

In order to evaluate the impact of careful nanobioconjugation on an electrode, Huerta-Miranda *et al.*[82], gold nanoparticles were electrodeposited on a glassy carbon electrode (GCE), however in a ordered way. The electrodeposition was made with the GCE covered by a polymer film that was removed after the AuNPs were formed. This assured that the AuNPs for enzyme bioconjugation with horseradish peroxidase were spread across the electrode surface with some gaps between them. The assembling of the nanobioconjugates continued with the functionalization with an aminothiol followed by the enzyme conjugation (intermediate washing steps were performed). The controlled orientation and packaging of enzymes on the electrodes was essential to a good performance of the system. A good and reversible electrochemical behaviour of the heme prosthetic group was obtained, in opposition to a random distribution of the nanobioconjugates (starting with AuNPs electrodeposition with no film) that showed a modest redox response, with lower sensitivity regarding to H_2O_2 quantification. The preservation of the protein original folding and the lack of steric impediments seem crucial to the electrode efficiency.

A specific class of proteins immobilized in electrodes decorated with gold nanoparticles is antibodies. This type of electrodes is usually carefully assembled, especially given the high cost of some of the antibodies that brings a need of a high reactivity with a low quantity. This is the case of the electrodes assembled by Elshafey *et al.*[80], where gold electrodes with electrodeposited AuNPs (AuNPsE) were sequentially immersed in solutions containing cysteamine, *p*-phenylene diisothiocyanate, protein G and finally antibody, with intermediate washing steps. Cysteamine binds to the AUNPs in the electrode, through its thiol group, providing a well-organized monolayer. *p*-phenylene diisothiocyanate is then bound to the electrode through binding to amine groups of cysteamine, also providing additional functional groups for binding amine groups from the next component of protein G. The high affinity of antibodies to protein G is then used to finally immobilize the desired antibody. This electrode with a layer-by-layer assembly was able to detect epidermal growth factor receptor (EGFR), a cancer biomarker, often quantified using time-consuming conventional approaches. The final electrode layer-by-layer composition was then AuNPsE–cyst–PDITC–pG–anti-EGFR and enabled the detection of EGFR down to 0.34 pg/mL in PBS and 0.88 pg/mL in human plasma. Hasanzadeh *et al.*[83] also described the use gold nanoparticles bioconjugated with antibodies for tumour suppressor protein p53, immobilized on an electrode. A quantification limit for p53 in the femtomolar range was achieved in this work.

Finally, is worth to mention cases where AuNPs, previously incorporated in nanobioconjugates, will only be part of the electrode in case of the presence of the analyte. This can be used to detect biomolecules such as proteins[84] or DNA/RNA[85]. An example for protein detection is the use of this method for mucin 1 protein (MUC1), a tumour biomarker.[84] The electrode, besides other modifications, has a layer of streptavidin, well-known for its ability to bind biotin. On the nanobioconjugate with AuNPs two main components are present: a hairpin oligonucleotide with a thiol group in one end and biotin in the other end – these two ends will bind to AuNPs surface – and horseradish peroxidase (HRP). Part of the hairpin oligonucleotide is MUC1 aptamer so, in the presence of this analyte, MUC1 will open the hairpin and release the biotin end from the AuNP surface, now free to bind to streptavidin. In this way, the nanobioconjugate, also containing HRP, will be immobilized onto the electrode, contributing to the enhancement of the electrochemical signal upon reaction of this enzyme with an appropriate substrate.

Other example, this time to micro RNA (miRNA) detection, was developed by Lin *et al.*[85] As the starting point, DNA probes were immobilized on a gold electrode (AuE), capable to hybridize with the target miRNA, other cancer biomarker. Separate nanobioconjugates with AuNPs functionalized with biotin and 3-aminophenylboronic acid (APBA –AuNP–biotin), capable to bind one end of the miRNA, were prepared. In the presence of miRNA, an assembly of AuE–(DNA/miRNA)–(APBA–AuNP–biotin) is obtained. In the next step, a protein dimer, comprised by streptavidin and alkaline phosphatase (ALP) is added to the electrode. Streptavidin is captured by biotin and a final AuE–(DNA/miRNA)–(APBA–AuNP–biotin)–(streptavidin–ALP) assembly is formed in the presence of the analyte. As in the previous example, AuNPs enhance the electrochemical signal upon reaction of the enzyme with an appropriate substrate.

1.3.4. Other Assays

Besides the major groups of applications of gold nanospheres mentioned in the previous three sections – colorimetric, lateral flow and electrochemical assays –, there are other reports about the usefulness of AuNPs for sensing purposes. The ability of enhancing Raman spectroscopy signal of strongly bound compounds trough a sulphur atom, or of enhancing enzymatic activity, can also be explored for nanobiosensing. The following examples list other several applications and strategies found in the literature.

Conjugation of the envelope protein of West Nile virus (WNV) with AuNPs (AuNPs-pWNV), allowed the detection of antibodies against this antigen in serum, as described by Neng *et al.*[86]. Besides the preparation of AuNPs–pWNV, a Raman molecular probe (malachite green) was conjugated with protein A/G, producing a probe capable of binding to antibodies. In the presence of WNV antibodies, they will work as a bridge the nanobioconjugates containing AuNPs and the probe containing malachite green. The last will be under the influence of surface enhanced Raman scattering effect originated by the close AuNPs. This is an example of nanobioconjugation for WNV (or other diseases) diagnostic in solution.

Other example of using gold nanoparticles as sensors was given by Yi *et al.*[87], using the zeta potential of AuNPs as a measure of the concentration of an enzyme in solution. These authors proposed the conjugation of a specific peptide to gold nanoparticles, through a thiolated polyethylene glycol. This peptide contains a tyrosine residue, so it is a perfect target for protein tyrosine kinases, such as Abelson murine leukemia viral oncogene kinase, used as analyte in this study. Since the action of this enzyme, in the presence of adenosine triphosphate (ATP), phosphorylates the peptide, the negative charge of the peptide increase, resulting in a decrease of the zeta potential of the nanobioconjugates. A linear correlation was found between zeta potential values and kinase concentration, in the range from 1 to 40 nM.

AuNPs were also found to improve well-stablished methods such as enzyme-linked immunosorbent assay (ELISA).[88] The use of 10 nm gold nanoparticles nanobioconjugated with horseradish peroxidase labelled anti-C reactive protein, enabled the detection of 0.1 ng/mL of C reactive protein with only 30 s of incubation, in opposition to 10 ng/mL for the ELISA performed in the absence of AuNPs. This detection limit of 0.1 ng/mL was also achieved in capillary ELISA, using the same nanobioconjugates, with its maximum absorbance reached in 2.5 min, while it took 13.5 min for the typical well-plate ELISA. The focus in this same analyte, granted other several publications in this decade but most of them are the electrochemical, colorimetric and lateral-flow assays using the same AuNPs–anti-C reactive protein antibodies nanobioconjugates, with similar assembles and mechanisms described before.[89]

In another work, the most common marker for prostate cancer – prostate-specific antigen (PSA) – was detected down to 1 pg/µL using AuNPs.[90] Biotin-functionalized gold nanoparticles were able to bind biotin-functionalized anti-PSA antibodies trough streptavidin molecules. PSA molecules were previously captured by anti-PSA antibodies immobilized on array surfaces. So, in a positive test, the assembly is (surface–anti-PSA)–PSA–(anti-PSA–biotin)–streptavidin–(biotin–AuNP). In this particular case[90] the assembly is further treated with $HAuCl_4$ that will cover the AuNPs, for a better signal in array imaging. The reduction of the added $HAuCl_4$ will grow the existing AuNPs, so the intensity of the scattered light hitting the detector (on a 633 nm laser array scanner) is exponentially higher. In a similar fashion, AuNPs were used to detect human α-thrombin in western blots.[91] AuNPs were functionalized with an aptamer specific for human α-thrombin, initially protected with a complementary DNA strand with a polyA tail. In the presence of the protein (comprising one of the bands in a western blot), the protective complementary strand is released and the AuNPs are captured via an aptamer–protein bond. Further enhancement of the AuNPs using $HAuCl_4$ as the previous method, also with the objective of increasing the light scattering signal for easier visualization (in this case with an office scanner), enables a lower detection limit for this technique. There are other cases where the signal enhancement is done using silver instead of gold.[92]

1.4. Interaction of gold nanoparticles and proteins

In order to further develop the use of bionanoconjugates of protein and gold nanoparticles in sensing applications, it is important to understand the process of nanobioconjugation itself, and also to characterize the changes in structure/reactivity of the proteins and in the physical properties of the gold nanoparticles upon nanobioconjugation. Proteins usually show a high-affinity for gold nanoparticles. This high affinity has even been used in protein isolation, such as solid-phase extraction, that can be improved by the introduction of gold nanoparticles in the stationary phase.[93]

Regarding the opportunities given by the synergy created upon conjugation of AuNPs with proteins, it is known that, for example, enzymes highly benefit from their nanobioconjugation with AuNPs. The conjugation of enzymes with AuNPs can lead to (i) the retention or even to an increase of their biological stability/activity, (ii) a facilitation of electron transfer between the catalytic sites of immobilised enzymes and the electrode materials, improvement of the analytical sensitivity and selectivity of biosensors and (iii) to often obviating the need for enzyme mediators.[94]

More than 37000 kinds of proteins are present in the human body[95] that together with many more proteins of interest, make the AuNPs–proteins nanobioconjugation a research field that deserve to be comprehensively explored. Two major concerns regarding nanobioconjugation, due to an eventual loss of biological function, are the changes in protein structure upon conjugation and nanoparticles and/or nanobioconjugates colloidal stability. Aggregation is typically undesired in nanobioconjugation but, for example, Neupane *et al.*[96] showed that the aggregation mechanism of AuNPs triggered by T4 lysozyme does not affect this enzyme's integrity. This not necessarily implies that the total enzymatic activity is not affected, since part of the enzyme molecules are entrapped in aggregates with lower accessibility for the substrate. If no aggregation is verified but the protein undergoes partial or total denaturation due to the way it bounds to the AuNPs, the nanobioconjugates are also compromised. Therefore, these two main aspects – colloidal and conformational stability – are crucial for an effective nanobioconjugate. In the other hand, there are cases that AuNPs positively interfere with proteins structure and proteins that increase the colloidal stability. The functionalization of AuNPs with bovine serum albumin (BSA) is a well-known method to improve colloidal stability of AuNPs.[97] There are also cases where AuNPs are responsible for improving the stability of bounded proteins, especially noticeable by an improved resistance to changes in the medium, such as changes in pH, temperature, or the introduction of organic solvents.

Interaction between gold nanoparticles and proteins, and even between the resultant nanobioconjugates, depends on the particle size and shape and also on the protein itself. Gagner *et al.* studied the interaction between gold nanospheres and nanorods with lysozyme and α-chymotrypsin.[98] Under saturating conditions, both enzymes were adsorbed with a higher surface density on nanorods when compared to nanospheres. In the case of lysozyme, adsorption on nanospheres and nanorods resulted in a 10% and 15% loss of secondary structure, respectively, leading to conjugate aggregation and reduced enzymatic activity. α-Chymotrypsin retained most of its structure and activity on nanospheres and nanorods at low surface coverages, but for high coverages on nanorods, 40% loss in secondary structure and 86% loss of activity was observed. This high-density packaging can originate protein–protein interactions that are typically absent when there is a bigger distance between them. An example of these interprotein interactions that led to conformational changes, are the hydrophobic interactions between lipophilic residues that in normal conditions are unexposed on the protein's core (only intraprotein interactions). Subsequent adsorption of α-chymotrypsin in multilayers on the nanorods surface allowed the conjugates to recover activity and remain stable. It was clear that nanoparticles morphology does affect this adsorbed protein structure. Each protein–nanoparticle association has to be studied individually given, on the nanoparticles side, the type and the proportion between crystalline facets of the surface metal atoms in different type of nanoparticles, different curvatures between nanospheres of different sizes or even also between different spots of the same nanoparticle for anisotropic particles. On the proteins side, there also different sizes and shapes that will interfere in the physical interaction particle–protein and also protein–protein but also a variety of outer residues and their locations that will also influence the chemical interactions.[99]

The dependence of shape and size, surface functionalization, protein-to-nanoparticle molar ratio, and incubation time in nanobioconjugation was recently studied by capillary electrophoresis with inductively coupled plasma mass spectrometry detection (CE–ICP–MS).[100] As expected, all these factors affect nanobioconjugation, but at different levels for the two proteins used in this study, albumin and transferrin, highlighting the difficulty to generalize optimal conditions for nanobioconjugation. This work stresses out the aforementioned fact that this phenomenon should be studied for each different protein to gather more information about this complex process.

The interface between the AuNPs or nanobioconjugates with a target in these biological systems will be the protein corona – a protein dense coating on nanoparticles, that, when formed in biological fluids, can also include a small fraction of electrolytes, lipids, and metabolites also able to adsorb (by electrostatic, hydrophobic, van der Waals, and dispersive forces) onto the nanoparticle.[101] Piella *et al.* explored the formation of a corona on AuNPs.[101] Three steps were identified: (i) AuNPs-protein complexes (partial corona), (ii) near-single dense protein corona layer on AuNPs, and (iii) multilayer corona on AuNPs. Using BSA as a model, it was found that nanoparticles with diameters of ~3 nm can bind 1–2 protein molecules, whereas ~30 nm nanoparticles can bind hundreds of proteins. These protein-to-nanoparticle ratios indicate that small AuNPs yield a low-density protein coating due to geometric constrains, while bigger nanoparticles form a full protein corona with high density protein coating, where cooperative effects, either positive or negative, are expected.

Most of the studies reported, evaluate the dynamic behaviour of the nanoparticles or nanobioconjugates in solution either based on measuring hydrodynamic size or zeta potential. Electrophoretic methods like the already mentioned capillary electrophoresis[100] or gel electrophoresis[102], are also able to provide information about the nanobioconjugate size and charge based on the different migration rate in the capillary or gel. However, these techniques do not provide any information about the uniformity of the protein corona. A recent report[103] shows that it is possible to visualize the protein corona by transmission electron microscopy (TEM). AuNPs decorated with human serum albumin (HSA), where typically only the core metal is visible on TEM images, were stained with uranylacetate or phosphotungstic acid, which made it possible to visualise the presence of the protein corona and conclude about is uniformity.

Finally, it is important to stress out that nanobioconjugation between AuNPs and proteins goes beyond the application in biosensors. For example, AuNPs can accelerate the nucleation step, facilitating crystallization of proteins. The presence of AuNPs in the protein crystal does not compromise data collection by X-ray diffractometry and structure determination.[104] The usefulness of AuNPs protein binding properties have also been applied to amyloid destruction and/or characterization, that may prove useful to understand and treat neurodegenerative diseases. AuNPs were proven to eliminate human islet amyloid polypeptide toxicity, facilitating their X-ray destruction, and allowing dark-field imaging of pathogenic amyloids and their immunogenic response by human T cells.[105] Other application of nanobioconjugation is as potent anti-metastatic drugs, as described for AuNPs conjugated with the cytotoxic protein NKCT1, a snake venom protein toxin, and their effect in cancer cells.[106] This nanobioconjugation also assures that NKCT1 is not as toxic for normal cells as in its free form.[107]

1.5. Surface-enhanced Raman spectroscopy (SERS)

Raman spectroscopy is based on inelastic scattering of a photon by molecules, which was first theoretically proposed by Smekal[108] in 1923 and experimentally observed by Raman[109-110] and Krishnan[110] in 1928. In this scattering process, vibrational or rotational modes of molecules are excited or relaxed leading to a change in wavelength of the photons.[111] Raman spectroscopy provides rich information about the molecular structure of the sample. Data analysis techniques based on multivariate analysis have made possible to extract full information content from Raman spectra and to draw conclusions about the chemical structure and composition of very complex systems such as biological materials.[112]

Surface-enhanced Raman spectroscopy (SERS) is a technique providing sensitive, selective and non-destructive chemical information, which is highly desirable in several fields such as medical diagnostics, environmental protection, food safety, etc.[111] During the last decade research was focused in the fabrication of SERS-active materials and also to adapt SERS methods for real life applications.[111]

Raman signal enhancement is originated by an electrical field magnification through excitation of localized surface plasmon resonances. The rougher is a surface, more probable is that SERS occurs. Surface roughness or curvature is required for the excitation of surface plasmons by light.[113] These specific regions where the electromagnetic field is extremely strong for amplifying Raman scattering are called hotspots. Many efforts have been made to construct such hotspots, typically by synthesizing gold or silver nanoparticles with rough surface, sharp tips, and inter- or intraparticle nanogaps.[41]

Given the signal increase provided by SERS, it is even possible to detect one single molecule, so it can be an interesting tool for sensing molecules in trace amounts within the fields of chemical and biochemical analytics.[114] Most of the recent applications (real samples) of SERS are mainly within the fields of food safety – detection of an herbicide residue in milk[115], pesticide residues on fruit peels[116-117], juice[117-118]and water[119] – or health – determination of zwitterionic morphine in human urine[120], cardiac biomarkers[121] and synthetic cannabinoids[122].

Also, several SERS supports were recently reported, like silver dendrites and graphene oxide composite membranes[123], titanium dioxide and gold nanoparticles on reduced graphene oxide nanosheets[124], gold film on cicada wings[116], gold nanorods–poly(methyl methacrylate) films[125], silver nanosponges[126], silver nanolenses[127]. Although these supports are new, gold or silver nanoparticles are used to take advantage of their LSPR properties.

1.5.1. Principal component analysis (PCA)

As stated in section 1.5, there are multivariate analysis processes that allow to deeply explore the data contained in Raman/SERS spectra.[112] Principal component analysis (PCA) is one of them. Principal component analysis is a statistical analysis technique which produce score plots for analytes or samples. These score plots consist of a coordinate system with axes in a two (or higher) dimensionality space, showing a coordinate system in which analytes or samples under analysis are best discriminated.[128]

The first step is always to organize the raw data in a matrix with a $n \times v$ dimension, where n is the number of samples and v is the number of variables evaluated per sample.[129] For example, for spectra analysis every single point of the spectra is an entry in that matrix.

The main goal of PCA is to transduce a high number of eventually correlated variables into quite less uncorrelated variables – the principal components. It can be considered as data compression method. To interpret high volumes of data, like the individual values that comprise several spectra, it is useful to reduce the number of variables to a few interpretable linear combinations of the data. Each linear combination will correspond to a principal component (PC).[130]

Each sample has scores for each one of these principal components. These scores can be plotted in a 2D (or higher dimension) chart, confronting scores from two different PC (*e.g.* PC1 *vs.* PC2). The more samples are similar, closer scores they have (therefore closer points on the score plot describe them). It can be said that groups of similar samples will originate groups of points in the score plot. This clustering phenomenon enables the discrimination of samples that were indiscriminate before the PCA.[131].

1.6. Silver nanoparticles nanobioconjugates in sensing by surface-enhanced Raman spectroscopy

Surface-enhanced Raman spectroscopy (SERS) has becoming an interesting technique for rapid chemical analysis, with high specificity and a sensitivity down to one molecule.[132] With this technique, Raman intensity is amplified by a localized electromagnetic field in certain point of a surface (hotspot) in several orders of magnitude. Silver nanoparticles (AgNPs), specially tips and edges of anisotropic silver nanoparticles that are quite prone to become hotspots[133-136], are generically the type of nanoparticles that work as better enhancers.[127]

Although gold nanoparticles are also used in SERS[137], since the work presented in this thesis is focused at silver nanoparticles in SERS-related chapters, recent works using AgNPs for SERS are explored in the following sections. Most of analytes of interest herein explored, comprising or detected by nanobioconjugates, are directly responsible for diseases or are diseases' biomarkers, and, as stated before, SERS can be very helpful regarding the low detection limits, without compromising the speed of the analysis or the ability of reading several targets in a single biological sample.[138-139]

1.6.1. Surface-enhanced Raman spectroscopy in immunoassays

A recent report combines an LFA (immunologic sandwich type), comprising three test lines, with surface-enhanced Raman spectroscopy (SERS).[121] The analytes detected in the three test lines were three cardiac biomarkers: myoglobin (Myo), cardiac troponin I (cTnI), and creatine kinase-MB isoenzymes (CK-MB). As SERS enhancers and part of the immunologic nanobioconjugates, silver nanoparticles (AgNPs), covered with a gold shell, were used. Besides the functionalization of these nanoparticles with antibodies (one type per particle), they incorporate the Raman probe Nile blue A (NBA) in the interface between the silver core and the gold shell. The authors were able to correlate the amount of the analyte in the sample with the intensity of the most intense peak in NBA SERS spectra, with limits of detection down to <10 pg/mL.

A similar work was described by Rong *et al.*[140], also using an LFA, but this time designed for the detection of C-reactive protein (CRP) at levels down to 10 pg/mL. The reservoir only comprises one type of nanobioconjugates. These nanobioconjugates are AgNPs with a gold core, with 5,5′-dithiobis(2-nitrobenzoic acid) (DTNB) as a probe in the core-shell interface, functionalized with anti-CRP antibodies. In the test line the nanobioconjugates are captured in a sandwich fashion in the presence of CRP, and a SERS signal is acquired in that LFA region. The correlation between the peak intensity and CRP was stablished and worked as a calibration curve.

Other case where SERS was coupled to an immunoassay was reported by Yang *et al.*[141], although this time AgNPs are not bioconjugated but are instead deposited on graphene oxide that will be in the end the composite analysed by SERS. The test was designed to detect and quantify prostate-specific antigen (PSA) using an immobilized anti-PSA antibody, that in the presence of PSA will form a sandwich with another anti-PSA antibody labelled with biotin. This biotinylated antibody captured glucose oxidase (GOx) conjugated with streptavidin. So, in the presence of PSA, the assembling adopts the following format: anti-PSA–PSA–(anti-PSA–biotin)–(streptavidin–GOx). The more PSA in the medium, more GOx is immobilized and, upon addition of glucose to the system, more H_2O_2 is produced, and bigger is the extent of AgNPs degradation (introduced in the system under the form of an AgNPs – graphene oxide composite). In the SERS measurements in the end of the test, the less intense is the signal of the graphene oxide, the higher the original PSA concentration. With this intricated assay, the authors reported a limit of detection of 0.23 pg/mL.

1.6.2. Surface-enhanced Raman spectroscopy and proteins

The use of antibodies, as in the examples in the previous section, can be considered a drawback due to their cost. Therefore, the possibility of directly detect proteins – often measured as diseases' biomarkers[142] – by SERS is welcomed.

The use of silver nanocuboids, with a gold rod core, allows an ultrasensitive detection of single-point mutations of TDP-43 proteins, at 10 pM.[133] The nanoparticles were deposited on top of silicon surface, ready to later accept the analyte. The SERS spectra obtained from a dried drop for this DNA-binding protein associated to amyotrophic lateral sclerosis, clearly discriminated the wild type and two different mutants, with no labelling. This is a typical case of a measurement on top of pre-assembled nanostructured surface. In the following example, the processes occur in solution.

Also focusing in a protein closely associated to degenerative diseases (diabetes mellitus type II and Alzheimer's), D'Urso *et al.*[143] described the detection of amyloidogenic proteins – human islet amyloid polypeptide (hIAPP), amyloid Aβ(1–40) and their equimolar mixture – by SERS. For this work, Raman signal was enhanced by the often used chemically synthesised AgNPs, but the authors also describe the production of AgNPs by laser. This last method consists in irradiating bulk silver, submerged in water, with a nanosecond pulsed laser. Despite the detection of the isolated proteins at 10 nM levels, the most interesting data arises from the 1:1 mixture of both. SERS spectra showed that hIAPP and Aβ(1–40) forms oligomeric aggregates with a nucleus rich in hIAPP and an outer shell rich in Aβ(1–40).

Other methods are mentioned in the literature for protein detection and discrimination, like adding AgNPs to samples of human glycated and non-glycated albumin, with the possibility to discriminate between the two groups based on their SERS spectra.[144]

1.6.3. Surface-enhanced Raman spectroscopy and nucleic acids

One of the most important types of biomolecules are the nucleic acids, such as DNA and RNA, often used as diseases' biomarkers. Besides worthy reports of SERS being able to detect very low levels of these molecules, they can also be used in SERS to detect other analytes, by changes induced in its hybridization status or working as aptamers. This explains the profusion of reports about SERS and nucleic acids in the most recent years.

A way of using nucleic acids for SERS is by monitoring their Raman signal, or the signal from a linked molecular probe, after conformational changes induced by the analyte. These conformational changes can bring the probe closer or away from the metal nanoparticle with noticeable implication in spectra intensity, since the signal enhancement factor can change several orders of magnitude within a few nanometres range.[113] The use of silver nanoparticles, conjugated with DNA strands capable of selectively detect Hg^{2+} and Pb^{2+}, enable the simultaneous detection of these hazardous heavy metal ions down to 168 ppt and 19.8 ppt, respectively.[145] AgNPs grown on top of a silicon wafer were functionalized with two different DNA sequences (linked to the particles trough a thiol end). Each one of these DNA fragments change their conformation in presence of its specific ion, and the changes in the intensity of specific peaks in the SERS spectra were linearly correlated to the $\log_{10}$ of the ion concentration. Liu *et al.* described a very similar work, but only for Hg^{2+} ion.[146]

In the previous method the nanobioconjugation AgNPs–DNA was meant to detect an analyte external to the nanobiosystem, but in the following cases targets are the oligonucleotides themselves. Using silicon nanowires decorated with silver nanoparticles, He *et al.*[147] were able to detect DNA at ~1 fM, by a sandwich method. The AgNPs on the nanowires were functionalized with capture DNA able of hybridizing with a portion of the target DNA sequence; other DNA fragment, labelled with a Raman molecular probe, hybridizes with other portion of the DNA target, so, in the presence of the analyte, the Raman probe will be conjugated to the AgNPs trough the following fashion: (nanowire–AgNPs)–capture DNA–target DNA–(DNA–probe). This detection method was designed for a single target, but nowadays, taking advantage of the high selectivity of the hybridization process, the focus is going to multiple target detection methods.

Zhou *et al.*[148] used SERS to simultaneously detect different microRNA liver cancer biomarkers. Silver hollow microparticles, functionalized with capture DNA, were used to capture target microRNA molecules, and also capture nanoprobes containing DNA capable of hybridizing with the target microRNA, *i.e.*, microRNA hybridizes with both immobilized DNA, working as a linker between the silver particles and the nanoprobes. These nanoprobes consist of three different batches (to detect three different microRNA molecules) of gold nanoparticles functionalized with a specific DNA fragment (complementary to the respective microRNA target) and a specific molecular Raman probe. The SERS spectra showed peaks for one, two or three molecular probes, allowing to identify which microRNA targets are present in the sample and even quantify them through an established correlation between peak intensities and concentration of each one of the microRNA molecules, down to 10 fM. A similar work, also for detecting DNA targets, was developed by Su *et al.*[149], where the target oligonucleotide links both a nanoprobe and superparamagnetic microparticles functionalized with capture DNA, in this case immobilized in a silicon wafer. Again, three different nanoprobes were produced for detecting three different targets – DNA from hepatitis A virus, hepatitis B virus and human immunodeficiency virus. The nanoprobes are gold nanospheres functionalized with DNA complementary to the targets and different molecular Raman probes. The silver responsible for SERS effect is introduced in the system as a partial and asymmetrical shell grown onto the AuNPs. Peak intensities were correlated to the target DNA concentrations, ranging from 1 pM to 10 nM for all the targets.

Also focusing in the detection of multiplexed disease biomarkers, but this time via aptamer–protein reactions, Xu *et al.*[150] developed nanopyramids, where the vertices are AgNPs and the edges are DNA strands, with special attention to three of these edges that contain three different aptamers. Those aptamers are specific for PSA, thrombin and mucin-1 proteins. Regarding the four AgNPs, one of them is not functionalized except for the conjugation with three DNA–aptamer partially hybridized strands; the remaining three AgNPs are functionalised with a different Raman molecular probe. If the target protein is present, the edge with the respective aptamer collapses and brings the non-functionalised AgNP closer to the functionalised AgNP, enhancing the signal of the respective molecular probe. The same is applied to the presence of two or three target proteins that equally collapse the DNA–aptamer strands, *i.e.*, for example, if all three analytes are present, the top AgNP is brought down to the centre of the pyramid base and the signals of all the probes are enhanced. The intensities of the main peak of each compound were correlated with analyte concentrations, down to aM levels. Yet in the category of the aptamers, Nie *et al.*[151] used a negatively charged aptamer, specific for malathion, able to bind AgNPs functionalized with spermine (positively charged). When the analyte malathion is present, it will decorate the AgNPs through the aptamer and it becomes under the influence of the AgNSs, and consequently its spectrum is enhanced. The authors were able to quantify malathion even in a mixture with other similar compounds, achieving a linear correlation between analyte concentration and peak intensities, in a range down to 500 nM.

Like in section 1.3.1, that SERS was combined with immunologic lateral flow assays, it is also possible to combine SERS-ready surfaces and/or methods and microfluidics. Using AgNPs on a graphene oxide (GO) surface, Han *et al.*[152] developed a reusable microfluidic SERS sensor for DNA detection. After the deposition of AgNPs–GO on a DVD, a laser scribing process was made in order to exfoliate a region of the DVD with the same design of the microfluidic channels. The exfoliated region was transferred to a polydimethylsiloxane slide and other slide of the same material with the engraved microfluidic channels was fitted to the AgNPs–GO drawing. This surface is able to bind biomolecules such as a DNA (e.g. 10^{-6} M for 30-base single strand), with an easy cleaning process based in hybridization of a complementary strand, making the device reusable for other samples. Other carbon materials, like carbon nanotubes, were already described as effective support for metal nanoparticles aimed at SERS applications.[153]

Finally, it is worth mentioning the possibility to follow a real-time PCR using SERS to monitor the process.[154] A small DNA fragment coupled with a Raman dye (e.g. rhodamine 6G) hybridizes with one of the DNA strands accessible after denaturation. This labelled DNA fragment is degraded upon primer extension and the dye, now linked with a very small DNA fragment, and it is able to cross a membrane and interact with AgNSs available in the medium. This way, by monitoring the SERS peak intensity, it is possible to monitor the progress of the PCR.

1.6.4. Surface-enhanced Raman spectroscopy and multiple biomolecules

There are cases where the analyte is not just one or a group of one type of biomolecules, so they do not fit in just one of the previous sub-sections. This is the case of the incubation of AgNPs with a cell lysate, rich in several types of biomolecules.[155] An example is the work of Hassoun *et al.*[156] where it was possible to quantify the percentage of monocytic leukaemia cells in a monocytes population. The ratios between intense spectral contributions of proteins and of nucleic acids were correlated with the larger cytoplasm to nucleus ratios of leukaemia cells when compared to control monocytes.

The SERS analysis of these complex matrixes, with different compositions or different proportions between their compounds, can lead to obtaining a unique spectra per sample. However, similar samples typically originate similar spectra. This is the basic principle that allows sample fingerprinting.

1.6.5. Surface-enhanced Raman spectroscopy and chemometric methods for sample discrimination

In some cases, sample fingerprinting by SERS is assisted by chemometric methods, such as principal component analysis (PCA).[112] There are examples in the literature that use Raman spectroscopy and chemometric methods but with no need to using SERS. Successful differentiation between colorectal cancer[157] cell lines and between head and neck cancer[158] and esophageal squamous cell carcinoma[159] malignant and healthy tissues were already obtained by this protocol. Four different bacteria species were also successfully discriminate with no need of using SERS.[160] There also cases of sample fingerprinting by SERS but without data treatment by chemometric methods, lacking this useful way of traducing the data to scores and doing instead overall raw spectra analysis.[161] Although there is a lack of reports of SERS experiments, with silver nanoparticles as the enhancer, and with their data analysed by chemometric methods, in the following paragraphs are selected examples of types of biologic samples discriminated by this procedure.

Dina *et al.* have synthesised silver nanoparticles in the presence of different fungus – *A. fumigatus s.s.*, *A. fumigatus sp.* and *R. pusillus* – in the synthesis media.[162] After a short period of incubation (3 minutes), Raman spectra from the three fungi soaked in the AgNPs colloidal suspension were individually collected. Although peaks from ubiquitous molecules like carbohydrates, lipids and proteins were present in all samples, their Raman shifts and relative intensities were unique from species to species. This, together with some peaks exclusive for one species, allowed, by applying PCA and other chemometric methods – fuzzy principal component analysis (FPCA) in combination with linear discriminant analysis (LDA) –, to clear discriminate between groups of spectra obtained for the different species. Since these three fungi are clinically relevant, this is a promising method, given the advantages of being a quick and simple detection method to execute.

Other area where SERS fingerprinting can be successfully used is bacteria differentiation. As in fungal infections, a detailed and quick identification of an infection-causing species is highly desired, since it can be the key for successful treatment. With the objective to differentiate one Gram positive and one Gram negative bacteria using SERS and PCA, Wang *et al.*[163] differentiated *Salmonella enterica* from *Escherichia coli*, mixed with silver dendrites for SERS fingerprinting. Colonies were collected from bacteria cultures, grown in liquid media and, after separation from the medium, mixed with silver dendrites. The resultant suspension (few μl) was deposited in glass and dried. SERS spectra were collected from a random square region of the sample, using an infrared laser, and it was possible to identify in the surface spots with *Salmonella enterica*, spots with *Escherichia coli* and bare silver dendrites. Species differentiation on a surface with adhered bacteria, can be very helpful for example for biofilm characterization.

Besides fungi and bacteria, the other main infectious agents are virus. Hoang *et al.*[164] used silver nanorods for genotyping of the RNA measles virus (MV). The substrate was then silver nanorods grown directly on a glass surface. The virus samples were simply diluted in methanol and drop-casted into the substrate. After drying, SERS spectra were collected using an infrared laser and four genotypes – A, D4, D9 and H1 – were differentiated in three distinct groups consisting in A, H1 and D type genotypes. The differentiation between the most equivalent genotypes (D4 and D9) was not possible, which opens the door to system optimization in order to get a better discrimination, even between similar genotypes. However, this method can substitute for more expensive and time-consuming stablished protocols, such as immunoassays.

Finally, is worth to acknowledge that despite the usefulness of the differentiation methods described above, Raman spectroscopy can also be a great non-invasive method to monitor cell invasion by pathogens, with spatial and temporal information. This kind of information is not typically available in commonly-used techniques such as electron microscopy.[165]

1.7. Thesis objectives and outline

The transversal objective of this thesis is to improve several processes by introducing gold or silver nanoparticles in that process. By producing nanobioconjugates, or creating the best conditions for their formation, is the proposed way to include the nanoparticles in the systems. These novel nanobioconjugates should be able to behave as biosensors on their own or prepared in way that make them usable as key part of a biosensor.

The work described herein can be grouped in two main themes: (i) nanobioconjugates of gold nanoparticles and enzymes – chapters 2 and 3 – and (ii) silver nanostars capable of nanobioconjugation for surface-enhance Raman spectroscopy applications – chapters 4, 5 and 6.

Chapter 2 presents an article published in Physical Chemistry Chemical Physics[78] about nanobioconjugation of 15 nm gold nanoparticles with *Toxicodendron vernicifluum* laccase. The article reports adsorption constants determined by four different techniques (Dynamic Ligth Scattering, Electrophoretic Ligth Scattering, Agarose Gel Electrophoresis and fluorescence quenching) and a study of the enzymatic activity enhancement in the nanobioconjugates.

Chapter 3 describes the use of gold nanoparticles for nanobioconjugation with a different laccase, this time from *Trametes versicolor*. After attempts of nanobioconjugation in solution, a nanobioconjugate immobilization process was studied. The immobilization procedure provided a simple method to prepare enzymatic disks with improved activity that may be useful in electrochemical sensors and other applications.

Chapter 4 reports the use of silver nanostars for wine fingerprinting. Using three Portuguese wines, from three different regions, the best way to achieve a good discrimination of SERS data when evaluated by principal component analysis was studied.

Chapter 5 describes a similar approach to that used in chapter 4 for bacteria fingerprinting. Different bacteria species with high importance regarding their antibiotic resistance, conjugated with silver nanostars in different ways were discriminated by principal component analysis. Besides the interspecies discrimination, intraspecies discrimination was also studied.

Chapter 6 reports the study of the best nanostructured surfaces prepared using silver nanostars, immobilized in different surfaces – silicon wafers, silver mirrors, aluminium-covered cardboard, and glass – using different strategies for their immobilization – covalent linking *vs.* drop cast, pH control, agitation *vs.* sonication and range of concentrations.

Finally, chapter 7 compiles all the main conclusions from the previous five chapters.

1.8. References

1. KE Drexler, *Engines of Creation: The Coming Era of Nanotechnology*. 1986.

2. DJ de Aberasturi, AB Serrano-Montes, LM Liz-Marzán. Modern Applications of Plasmonic Nanoparticles: From Energy to Health. *Advanced Optical Materials* **2015,** *3* (5), 602-617.

3. WR Erwin, HF Zarick, EM Talbert, R Bardhan. Light trapping in mesoporous solar cells with plasmonic nanostructures. *Energy & Environmental Science* **2016,** *9* (5), 1577-1601.

4. Y Chen, Y Xianyu, X Jiang. Surface Modification of Gold Nanoparticles with Small Molecules for Biochemical Analysis. *Accounts of Chemical Research* **2017,** *50* (2), 310-319.

5. E Priyadarshini, N Pradhan. Gold nanoparticles as efficient sensors in colorimetric detection of toxic metal ions: A review. *Sensors and Actuators B: Chemical* **2017,** *238*, 888-902.

6. M Peixoto de Almeida, E Pereira, P Baptista, I Gomes, S Figueiredo, L Soares, R Franco, Gold Nanoparticles as (Bio)Chemical Sensors. In *Gold Nanoparticles in Analytical Chemistry*, 2014; Vol. 66, pp 529-567.

7. L Vigderman, ER Zubarev. Therapeutic platforms based on gold nanoparticles and their covalent conjugates with drug molecules. *Advanced Drug Delivery Reviews* **2013,** *65* (5), 663-76.

8. TM Abdelghany, AMH Al-Rajhi, MA Al Abboud, MM Alawlaqi, A Ganash Magdah, EAM Helmy, AS Mabrouk. Recent Advances in Green Synthesis of Silver Nanoparticles and Their Applications: About Future Directions. A Review. *BioNanoScience* **2017,** *8* (1), 5-16.

9. N Duran, M Duran, MB de Jesus, AB Seabra, WJ Favaro, G Nakazato. Silver nanoparticles: A new view on mechanistic aspects on antimicrobial activity. *Nanomedicine* **2016,** *12* (3), 789-799.

10. MV Canamares, JV Garcia-Ramos, S Sanchez-Cortes, M Castillejo, M Oujja. Comparative SERS effectiveness of silver nanoparticles prepared by different methods: a study of the enhancement factor and the interfacial properties. *Journal of Colloid and Interface Science* **2008,** *326* (1), 103-9.

11. T Janči, L Mikac, M Ivanda, N Marušić Radovčić, H Medić, S Vidaček. Optimization of parameters for histamine detection in fish muscle extracts by surface-enhanced Raman spectroscopy using silver colloid SERS substrates. *Journal of Raman Spectroscopy* **2017,** *48* (1), 64-72.

12. T Janci, D Valinger, J Gajdos Kljusuric, L Mikac, S Vidacek, M Ivanda. Determination of histamine in fish by Surface Enhanced Raman Spectroscopy using silver colloid SERS substrates. *Food Chemistry* **2017,** *224*, 48-54.

13. A Lanzarotta, L Lorenz, JS Batson, C Flurer. Development and implementation of a pass/fail field-friendly method for detecting sildenafil in suspect pharmaceutical tablets using a handheld Raman spectrometer and silver colloids. *Journal of Pharmaceutical and Biomedical Analysis* **2017,** *146*, 420-425.

14. J Turkevich, PC Stevenson, J Hillier. A study of the nucleation and growth processes in the synthesis of colloidal gold. *Discussions of the Faraday Society* **1951,** *11*.

15. G Frens. Controlled Nucleation for the Regulation of the Particle Size in Monodisperse Gold Suspensions. *Nature Physical Science* **1973,** *241* (105), 20-22.

16. NG Bastús, J Comenge, V Puntes. Kinetically controlled seeded growth synthesis of citrate-stabilized gold nanoparticles of up to 200 nm: size focusing versus Ostwald ripening. *Langmuir* **2011,** *27* (17), 11098-11105.

17. M Wuithschick, A Birnbaum, S Witte, M Sztucki, U Vainio, N Pinna, K Rademann, F Emmerling, R Kraehnert, J Polte. Turkevich in New Robes: Key Questions Answered for the Most Common Gold Nanoparticle Synthesis. *ACS Nano* **2015,** *9* (7), 7052-71.

18. K Zabetakis, WE Ghann, S Kumar, M-C Daniel. Effect of high gold salt concentrations on the size and polydispersity of gold nanoparticles prepared by an extended Turkevich–Frens method. *Gold Bulletin* **2012,** *45* (4), 203-211.

19. J Kimling, M Maier, B Okenve, V Kotaidis, H Ballot, A Plech. Turkevich method for gold nanoparticle synthesis revisited. *The Journal of Physical Chemistry B* **2006,** *110* (32), 15700-7.

20. F Schulz, T Homolka, NG Bastus, V Puntes, H Weller, T Vossmeyer. Little adjustments significantly improve the Turkevich synthesis of gold nanoparticles. *Langmuir* **2014,** *30* (35), 10779-84.

21. H Xia, Y Xiahou, P Zhang, W Ding, D Wang. Revitalizing the Frens Method To Synthesize Uniform, Quasi-Spherical Gold Nanoparticles with Deliberately Regulated Sizes from 2 to 330 nm. *Langmuir* **2016,** *32* (23), 5870-80.

22. B Nikoobakht, MA El-Sayed. Preparation and Growth Mechanism of Gold Nanorods (NRs) Using Seed-Mediated Growth Method. *Chemistry of Materials* **2003,** *15* (10), 1957-1962.

23. D Kim, J Heo, M Kim, YW Lee, SW Han. Size-controlled synthesis of monodisperse gold nanooctahedrons and their surface-enhanced Raman scattering properties. *Chemical Physics Letters* **2009,** *468* (4-6), 245-248.

24. L Scarabelli, M Coronado-Puchau, JJ Giner-Casares, J Langer, LM Liz-Marzan. Monodisperse gold nanotriangles: size control, large-scale self-assembly, and performance in surface-enhanced Raman scattering. *ACS Nano* **2014,** *8* (6), 5833-42.

25. CG Khoury, T Vo-Dinh. Gold Nanostars For Surface-Enhanced Raman Scattering: Synthesis, Characterization and Optimization. *The Journal of Physical Chemistry C* **2008,** *112* (48), 18849-18859.

26. P Senthil Kumar, I Pastoriza-Santos, B Rodriguez-Gonzalez, F Javier Garcia de Abajo, LM Liz-Marzan. High-yield synthesis and optical response of gold nanostars. *Nanotechnology* **2008,** *19* (1), 015606.

27. NR Jana, L Gearheart, CJ Murphy. Wet Chemical Synthesis of High Aspect Ratio Cylindrical Gold Nanorods. *The Journal of Physical Chemistry B* **2001,** *105* (19), 4065-4067.

28. H Yuan, CG Khoury, H Hwang, CM Wilson, GA Grant, T Vo-Dinh. Gold nanostars: surfactant-free synthesis, 3D modelling, and two-photon photoluminescence imaging. *Nanotechnology* **2012,** *23* (7), 075102.

29. B Wiley, Y Sun, B Mayers, Y Xia. Shape-controlled synthesis of metal nanostructures: the case of silver. *Chemistry* **2005,** *11* (2), 454-63.

30. NR Jana, L Gearheart, CJ Murphy. Wet chemical synthesis of silver nanorods and nanowires of controllable aspect ratio. *Chemical Communications* **2001,** *0* (7), 617-618.

31. Y Sun, Y Xia. Shape-controlled synthesis of gold and silver nanoparticles. *Science* **2002,** *298* (5601), 2176-9.

32. A Garcia-Leis, JV Garcia-Ramos, S Sanchez-Cortes. Silver Nanostars with High SERS Performance. *The Journal of Physical Chemistry C* **2013,** *117* (15), 7791-7795.

33. A Lustosa, AC de Jesus Oliveira, PV Quelemes, A Placido, FV da Silva, IS Oliveira, M Peixoto de Almeida, A Amorim, C Delerue-Matos, RCM de Oliveira, DA da Silva, P Eaton, JRS de Almeida Leite. *In Situ* Synthesis of Silver Nanoparticles in a Hydrogel of

Carboxymethyl Cellulose with Phthalated-Cashew Gum as a Promising Antibacterial and Healing Agent. *International Journal of Molecular Sciences* **2017,** *18* (11), 2399.

34. CRB Lopes, LC Courrol. Green synthesis of silver nanoparticles with extract of Mimusops coriacea and light. *Journal of Luminescence* **2018,** *199*, 183-187.

35. P Mandal, S Ghosh. Green synthesis of poly(vinyl alcohol)–silver nanoparticles hybrid using Palash (Butea monosperma) flower extract and investigation of antibacterial activity. *Polymer Bulletin* **2017,** *75* (5), 1949-1955.

36. S Panhwar, SS Hassan, RB Mahar, A Canlier, Sirajuddin, M Arain. Synthesis of l-Cysteine Capped Silver Nanoparticles in Acidic Media at Room Temperature and Detailed Characterization. *Journal of Inorganic and Organometallic Polymers and Materials* **2017,** *28* (3), 863-870.

37. S Shah, Su Din, A Khan, Rehmanullah, SA Shah. Green Synthesis and Antioxidant Study of Silver Nanoparticles of Root Extract of Sageretia thea and Its Role in Oxidation Protection Technology. *Journal of Polymers and the Environment* **2017,** *26* (6), 2323-2332.

38. R Mythili, T Selvankumar, S Kamala-Kannan, C Sudhakar, F Ameen, A Al-Sabri, K Selvam, M Govarthanan, H Kim. Utilization of market vegetable waste for silver nanoparticle synthesis and its antibacterial activity. *Materials Letters* **2018,** *225*, 101-104.

39. SS Sana, LK Dogiparthi. Green synthesis of silver nanoparticles using Givotia moluccana leaf extract and evaluation of their antimicrobial activity. *Materials Letters* **2018,** *226*, 47-51.

40. D Bharathi, S Vasantharaj, V Bhuvaneshwari. Green synthesis of silver nanoparticles using Cordia dichotoma fruit extract and its enhanced antibacterial, anti-biofilm and photo catalytic activity. *Materials Research Express* **2018,** *5* (5), 55404.

41. K Liu, Y Bai, L Zhang, Z Yang, Q Fan, H Zheng, Y Yin, C Gao. Porous Au-Ag Nanospheres with High-Density and Highly Accessible Hotspots for SERS Analysis. *Nano Letters* **2016,** *16* (6), 3675-81.

42. H Chen, K Zhou, G Zhao. Gold nanoparticles: From synthesis, properties to their potential application as colorimetric sensors in food safety screening. *Trends in Food Science & Technology* **2018,** *78*, 83-94.

43. G Yue, S Su, N Li, M Shuai, X Lai, D Astruc, P Zhao. Gold nanoparticles as sensors in the colorimetric and fluorescence detection of chemical warfare agents. *Coordination Chemistry Reviews* **2016,** *311*, 75-84.

44. Y-C Chuang, J-C Li, S-H Chen, T-Y Liu, C-H Kuo, W-T Huang, C-S Lin. An optical biosensing platform for proteinase activity using gold nanoparticles. *Biomaterials* **2010,** *31* (23), 6087-6095.

45. L-J Ou, P-Y Jin, X Chu, J-H Jiang, R-Q Yu. Sensitive and Visual Detection of Sequence-Specific DNA-Binding Protein via a Gold Nanoparticle-Based Colorimetric Biosensor. *Analytical Chemistry* **2010,** *82* (14), 6015-6024.

46. B Amini, M Kamali, M Salouti, P Yaghmaei. Spectrophotometric, colorimetric and visually detection of Pseudomonas aeruginosa ETA gene based gold nanoparticles DNA probe and endonuclease enzyme. *Spectrochimica Acta Part A: Molecular and Biomolecular Spectroscopy* **2018,** *199*, 421-429.

47. Q Liu, L Li, Y Zhao, Z Chen. Colorimetric detection of DNA at the nanomolar level based on enzyme-induced gold nanoparticle de-aggregation. *Microchimica Acta* **2018,** *185* (6).

48. M Chanana, MA Correa-Duarte, LM Liz-Marzan. Insulin-Coated Gold Nanoparticles: A Plasmonic Device for Studying Metal-Protein Interactions. *Small* **2011,** *7* (18), 2650-2660.

49. Y Guo, Z Wang, W Qu, H Shao, X Jiang. Colorimetric detection of mercury, lead and copper ions simultaneously using protein-functionalized gold nanoparticles. *Biosensors and Bioelectronics* **2011,** *26* (10), 4064-4069.

50. NR Nirala, PS Saxena, A Srivastava. Colorimetric detection of cholesterol based on enzyme modified gold nanoparticles. *Spectrochimica Acta Part A: Molecular and Biomolecular Spectroscopy* **2018,** *190*, 506-512.

51. T-S Lai, T-C Chang, S-C Wang. Gold nanoparticle-based colorimetric methods to determine protein contents in artificial urine using membrane micro-concentrators and mobile phone camera. *Sensors and Actuators B: Chemical* **2017,** *239*, 9-16.

52. EB Bahadır, MK Sezgintürk. Lateral flow assays: Principles, designs and labels. *TrAC Trends in Analytical Chemistry* **2016,** *82*, 286-306.

53. K Mohd Hanafiah, N Arifin, Y Bustami, R Noordin, M Garcia, D Anderson. Development of Multiplexed Infectious Disease Lateral Flow Assays: Challenges and Opportunities. *Diagnostics* **2017,** *7* (3).

54. O Miocevic, CR Cole, MJ Laughlin, RL Buck, PD Slowey, EA Shirtcliff. Quantitative Lateral Flow Assays for Salivary Biomarker Assessment: A Review. *Front Public Health* **2017,** *5*, 133.

55. M Jauset-Rubio, MS El-Shahawi, AS Bashammakh, AO Alyoubi, CK O'Sullivan. Advances in aptamers-based lateral flow assays. *TrAC Trends in Analytical Chemistry* **2017,** *97*, 385-398.

56. T Schüling, A Eilers, T Scheper, J Walter. Aptamer-based lateral flow assays. *AIMS Bioengineering* **2018,** *5* (2), 78-102.

57. N Upadhyay, S Nara. Lateral flow assay for rapid detection of Staphylococcus aureus enterotoxin A in milk. *Microchemical Journal* **2018,** *137*, 435-442.

58. S Rong-Hwa, T Shiao-Shek, C Der-Jiang, H Yao-Wen. Gold nanoparticle-based lateral flow assay for detection of staphylococcal enterotoxin B. *Food Chemistry* **2010,** *118* (2), 462-466.

59. KH Ching, X He, LH Stanker, AV Lin, JA McGarvey, R Hnasko. Detection of shiga toxins by lateral flow assay. *Toxins* **2015,** *7* (4), 1163-73.

60. T Yonekita, R Ohtsuki, E Hojo, N Morishita, T Matsumoto, T Aizawa, F Morimatsu. Development of a novel multiplex lateral flow assay using an antimicrobial peptide for the detection of Shiga toxin-producing Escherichia coli. *Journal of Microbiological Methods* **2013,** *93* (3), 251-6.

61. Y Terao, K Takeshita, Y Nishiyama, N Morishita, T Matsumoto, F Morimatsu. Promising Nucleic Acid Lateral Flow Assay Plus PCR for Shiga Toxin-Producing Escherichia coli. *Journal of Food Protection* **2015,** *78* (8), 1560-8.

62. L Dou, B Zhao, T Bu, W Zhang, Q Huang, L Yan, L Huang, Y Wang, J Wang, D Zhang. Highly sensitive detection of a small molecule by a paired labels recognition system based lateral flow assay. *Analytical and Bioanalytical Chemistry* **2018,** *410* (13), 3161-3170.

63. GW Pratt, A Fan, B Melakeberhan, CM Klapperich. A competitive lateral flow assay for the detection of tenofovir. *Analytica Chimica Acta* **2018,** *1017*, 34-40.

64. Y He, S Zhang, X Zhang, M Baloda, AS Gurung, H Xu, X Zhang, G Liu. Ultrasensitive nucleic acid biosensor based on enzyme-gold nanoparticle dual label and lateral flow strip biosensor. *Biosensors and Bioelectronics* **2011,** *26* (5), 2018-2024.

65. BA Rohrman, V Leautaud, E Molyneux, RR Richards-Kortum. A lateral flow assay for quantitative detection of amplified HIV-1 RNA. *PLoS One* **2012,** *7* (9), e45611.

66. J Hu, L Wang, F Li, YL Han, M Lin, TJ Lu, F Xu. Oligonucleotide-linked gold nanoparticle aggregates for enhanced sensitivity in lateral flow assays. *Lab on a Chip* **2013,** *13* (22), 4352-7.

67. W Haiss, NT Thanh, J Aveyard, DG Fernig. Determination of size and concentration of gold nanoparticles from UV-vis spectra. *Analytical Chemistry* **2007,** *79* (11), 4215-21.

68. M Jauset-Rubio, M Svobodova, T Mairal, C McNeil, N Keegan, MS El-Shahawi, AS Bashammakh, AO Alyoubi, CK O'Sullivan. Aptamer Lateral Flow Assays for Ultrasensitive Detection of beta-Conglutin Combining Recombinase Polymerase Amplification and Tailed Primers. *Analytical Chemistry* **2016,** *88* (21), 10701-10709.

69. H Jeong, DM Nguyen, MS Lee, HG Kim, SC Ko, LK Kwac. N-doped graphene-carbon nanotube hybrid networks attaching with gold nanoparticles for glucose non-enzymatic sensor. *Materials Science & Engineering C: Materials for Biological Applications* **2018,** *90*, 38-45.

70. M Hasanzadeh, HN Baghban, N Shadjou. Non-enzymatic Determination of L-Proline Amino Acid in Unprocessed Human Plasma Sample Using Hybrid of Graphene Quantum Dots Decorated with Gold Nanoparticles and Poly Cysteine: A Novel Signal Amplification Strategy. *Analytical Sciences* **2018,** *34* (3), 355-362.

71. G Bolat, S Abaci. Non-Enzymatic Electrochemical Sensing of Malathion Pesticide in Tomato and Apple Samples Based on Gold Nanoparticles-Chitosan-Ionic Liquid Hybrid Nanocomposite. *Sensors* **2018,** *18* (3).

72. S Berbec, S Zoladek, A Jablonska, B Palys. Electrochemically reduced graphene oxide on gold nanoparticles modified with a polyoxomolybdate film. Highly sensitive non-enzymatic electrochemical detection of H2O2. *Sensors and Actuators B: Chemical* **2018,** *258*, 745-756.

73. P Bollella, G Fusco, D Stevar, L Gorton, R Ludwig, S Ma, H Boer, A Koivula, C Tortolini, G Favero, R Antiochia, F Mazzei. A Glucose/Oxygen Enzymatic Fuel Cell based on Gold Nanoparticles modified Graphene Screen-Printed Electrode. Proof-of-Concept in Human Saliva. *Sensors and Actuators B: Chemical* **2018,** *256*, 921-930.

74. G Chang, H Shu, K Ji, M Oyama, X Liu, Y He. Gold nanoparticles directly modified glassy carbon electrode for non-enzymatic detection of glucose. *Applied Surface Science* **2014,** *288*, 524-529.

75. S Shleev, J Tkac, A Christenson, T Ruzgas, AI Yaropolov, JW Whittaker, L Gorton. Direct electron transfer between copper-containing proteins and electrodes. *Biosensors and Bioelectronics* **2005,** *20* (12), 2517-54.

76. C Gutierrez-Sanchez, M Pita, C Vaz-Dominguez, S Shleev, AL De Lacey. Gold nanoparticles as electronic bridges for laccase-based biocathodes. *Journal of the American Chemical Society* **2012,** *134* (41), 17212-20.

77. A Christenson, N Dimcheva, EE Ferapontova, L Gorton, T Ruzgas, L Stoica, S Shleev, AI Yaropolov, D Haltrich, RNF Thorneley, SD Aust. Direct Electron Transfer Between Ligninolytic Redox Enzymes and Electrodes. *Electroanalysis* **2004,** *16* (1314), 1074-1092.

78. M Peixoto de Almeida, P Quaresma, S Sousa, C Couto, I Gomes, L Krippahl, R Franco, E Pereira. Measurement of adsorption constants of laccase on gold nanoparticles to evaluate the enhancement in enzyme activity of adsorbed laccase. *Physical Chemistry Chemical Physics* **2018,** *20* (24), 16761-16769.

79. X Wang, M Falk, R Ortiz, H Matsumura, J Bobacka, R Ludwig, M Bergelin, L Gorton, S Shleev. Mediatorless sugar/oxygen enzymatic fuel cells based on gold nanoparticle-modified electrodes. *Biosensors and Bioelectronics* **2012,** *31* (1), 219-225.

80. R Elshafey, AC Tavares, M Siaj, M Zourob. Electrochemical impedance immunosensor based on gold nanoparticles-protein G for the detection of cancer marker epidermal growth factor receptor in human plasma and brain tissue. *Biosensors and Bioelectronics* **2013,** *50*, 143-149.

81. PA Rasheed, N Sandhyarani. Electrochemical DNA sensors based on the use of gold nanoparticles: a review on recent developments. *Microchimica Acta* **2017,** *184* (4), 981-1000.

82. GA Huerta-Miranda, AA Arrocha-Arcos, M Miranda-Hernandez. Gold nanoparticles/4-aminothiophenol interfaces for direct electron transfer of horseradish peroxidase: Enzymatic orientation and modulation of sensitivity towards hydrogen peroxide detection. *Bioelectrochemistry* **2018,** *122*, 77-83.

83. M Hasanzadeh, HN Baghban, N Shadjou, A Mokhtarzadeh. Ultrasensitive electrochemical immunosensing of tumor suppressor protein p53 in unprocessed human plasma and cell lysates using a novel nanocomposite based on poly-cysteine/graphene quantum dots/gold nanoparticle. *International Journal of Biological Macromolecules* **2018,** *107*, 1348-1363.

84. R Hu, W Wen, Q Wang, H Xiong, X Zhang, H Gu, S Wang. Novel electrochemical aptamer biosensor based on an enzyme-gold nanoparticle dual label for the ultrasensitive detection of epithelial tumour marker MUC1. *Biosensors and Bioelectronics* **2014,** *53*, 384-389.

85. L Liu, N Xia, H Liu, X Kang, X Liu, C Xue, X He. Highly sensitive and label-free electrochemical detection of microRNAs based on triple signal amplification of multifunctional gold nanoparticles, enzymes and redox-cycling reaction. *Biosensors and Bioelectronics* **2014,** *53*, 399-405.

86. J Neng, MH Harpster, H Zhang, JO Mecham, WC Wilson, PA Johnson. A versatile SERS-based immunoassay for immunoglobulin detection using antigen-coated gold nanoparticles and malachite green-conjugated protein A/G. *Biosensors and Bioelectronics* **2010,** *26* (3), 1009-1015.

87. F Yi, XY Huang, JC Ren. Simple and Sensitive Method for Determination of Protein Kinase Activity Based on Surface Charge Change of Peptide-Modified Gold Nanoparticles As Substrates. *Analytical Chemistry* **2018,** *90* (6), 3871-3877.

88. W-J Kim, HY Cho, B Jeong, S Byun, J Huh, YJ Kim. Synergistic Use of Gold Nanoparticles (AuNPs) and "Capillary Enzyme-Linked Immunosorbent Assay (ELISA)" for High Sensitivity and Fast Assays. *Sensors* **2018,** *18* (1).

89. M Antonio, J Nogueira, R Vitorino, AL Daniel-da-Silva. Functionalized Gold Nanoparticles for the Detection of C-Reactive Protein. *Nanomaterials* **2018,** *8* (4), 21.

90. AW Scott, V Garimella, CM Calabrese, CA Mirkin. Universal Biotin-PEG-Linked Gold Nanoparticle Probes for the Simultaneous Detection of Nucleic Acids and Proteins. *Bioconjugate Chemistry* **2017,** *28* (1), 203-211.

91. F Li, J Li, Y Tang, C Wang, X-F Li, XC Le. Targeted Enlargement of Aptamer Functionalized Gold Nanoparticles for Quantitative Protein Analysis. *Proteomes* **2017,** *5* (1).

92. GB Kim, JO Lee, Y-P Kim. Graying the self-assembly of gold nanoparticles for improved enzyme activity assays. *Sensors and Actuators B: Chemical* **2017,** *246*, 271-277.

93. I Ten-Domenech, E Francisco Simo-Alfonso, J Manuel Herrero-Martinez. Isolation of human milk whey proteins by solid phase extraction with a polymeric material modified with gold nanoparticles. *Microchemical Journal* **2017,** *133*, 320-326.

94. J Cortez, E Vorobieva, D Gralheira, I Osório, L Soares, N Vale, E Pereira, P Gomes, R Franco. Bionanoconjugates of tyrosinase and peptide-derivatised gold nanoparticles for biosensing of phenolic compounds. *Journal of Nanoparticle Research* **2010,** *13* (3), 1101-1113.

95. L Tian, A Chang, MP Melancon. Exploring gold nanoparticle interactions with proteins and the tumor microenvironment in biological systems. *Translational Cancer Research* **2017,** *6*, S309-S312.

96. S Neupane, Y Pan, S Takalkar, K Bentz, J Farmakes, Y Xu, B Chen, G Liu, SY Qian, Z Yang. Probing the Aggregation Mechanism of Gold Nanoparticles Triggered by a Globular Protein. *The Journal of Physical Chemistry C* **2017,** *121* (2), 1377-1386.

97. SH Brewer, WR Glomm, MC Johnson, MK Knag, S Franzen. Probing BSA binding to citrate-coated gold nanoparticles and surfaces. *Langmuir* **2005,** *21* (20), 9303-7.

98. JE Gagner, MD Lopez, JS Dordick, RW Siegel. Effect of gold nanoparticle morphology on adsorbed protein structure and function. *Biomaterials* **2011,** *32* (29), 7241-7252.

99. SR Saptarshi, A Duschl, AL Lopata. Interaction of nanoparticles with proteins: relation to bio-reactivity of the nanoparticle. *Journal of Nanobiotechnology* **2013,** *11*, 26.

100. J Legat, M Matczuk, A Timerbaev, M Jarosz. CE Separation and ICP-MS Detection of Gold Nanoparticles and Their Protein Conjugates. *Chromatographia* **2017,** *80* (11), 1695-1700.

101. J Piella, NG Bastus, V Puntes. Size-Dependent Protein-Nanoparticle Interactions in Citrate-Stabilized Gold Nanoparticles: The Emergence of the Protein Corona. *Bioconjugate Chemistry* **2017,** *28* (1), 88-97.

102. K Ranoszek-Soliwoda, E Czechowska, E Tomaszewska, G Celichowski, T Kowalczyk, T Sakowicz, J Szemraj, J Grobelny. Catalase-modified gold nanoparticles: Determination of the degree of protein adsorption by gel electrophoresis. *Colloids and Surfaces B: Biointerfaces* **2017,** *159*, 533-539.

103. IA Pyshnaya, KV Razum, AS Dolodoev, VV Shashkova, EI Ryabchikova. Surprises of electron microscopic imaging of proteins and polymers covering gold nanoparticles layer by layer. *Colloids and Surfaces B: Biointerfaces* **2017,** *150*, 23-31.

104. S Ko, HY Kim, I Choi, J Choe. Gold Nanoparticles as Nucleation-Inducing Reagents for Protein Crystallization. *Crystal Growth & Design* **2017,** *17* (2), 497-503.

105. I Javed, Y Sun, J Adamcik, B Wang, A Kakinen, EH Pilkington, F Ding, R Mezzenga, TP Davis, PC Ke. Cofibrillization of Pathogenic and Functional Amyloid Proteins with Gold Nanoparticles against Amyloidogenesis. *Biomacromolecules* **2017,** *18* (12), 4316-4322.

106. T Bhowmik, A Gomes. Down-regulation of cyclin-dependent kinase-4 and MAPK through estrogen receptor mediated cell cycle arrest in human breast cancer induced by gold nanoparticle tagged toxin protein NKCT1. *Chemico-Biological Interactions* **2017,** *268*, 119-128.

107. T Bhowmik, PP Saha, A Sarkar, A Gomes. Evaluation of cytotoxicity of a purified venom protein from Naja kaouthia (NKCT1) using gold nanoparticles for targeted delivery to cancer cell. *Chemico-Biological Interactions* **2017,** *261*, 35-49.

108. A Smekal. Zur Quantentheorie der Dispersion. *Die Naturwissenschaften* **1923,** *11* (43), 873-875.

109. CV Raman. A new radiation. *Indian Journal of Physics* **1928,** *2*, 387-398.

110. CV Raman, KS Krishnan. A new class of spectra due to secondary radiaton. *Indian Journal of Physics* **1928,** *2*, 399-419.

111. G Demirel, H Usta, M Yilmaz, M Celik, HA Alidagi, F Buyukserin. Surface-enhanced Raman spectroscopy (SERS): an adventure from plasmonic metals to organic semiconductors as SERS platforms. *Journal of Materials Chemistry C* **2018,** *6* (20), 5314-5335.

112. K Kneipp, H Kneipp, I Itzkan, RR Dasari, MS Feld. Ultrasensitive Chemical Analysis by Raman Spectroscopy. *Chemical Reviews* **1999,** *99* (10), 2957-2976.

113. S Schlucker. Surface-Enhanced Raman Spectroscopy: Concepts and Chemical Applications. *Angewandte Chemie International Edition* **2014,** *53* (19), 4756-4795.

114. D Cialla, A Marz, R Bohme, F Theil, K Weber, M Schmitt, J Popp. Surface-enhanced Raman spectroscopy (SERS): progress and trends. *Analytical and Bioanalytical Chemistry* **2012,** *403* (1), 27-54.

115. MZ Hua, S Feng, S Wang, X Lu. Rapid detection and quantification of 2,4-dichlorophenoxyacetic acid in milk using molecularly imprinted polymers-surface-enhanced Raman spectroscopy. *Food Chemistry* **2018,** *258*, 254-259.

116. G Shi, M Wang, Y Zhu, Y Wang, W Ma. Synthesis of flexible and stable SERS substrate based on Au nanofilms/cicada wing array for rapid detection of pesticide residues. *Optics Communications* **2018,** *425*, 49-57.

117. J Sun, L Gong, Y Lu, D Wang, Z Gong, M Fan. Dual functional PDMS sponge SERS substrate for the on-site detection of pesticides both on fruit surfaces and in juice. *Analyst* **2018,** *143* (11), 2689-2695.

118. Z Xiong, M Lin, H Lin, M Huang. Facile synthesis of cellulose nanofiber nanocomposite as a SERS substrate for detection of thiram in juice. *Carbohydrate Polymers* **2018,** *189*, 79-86.

119. S Fateixa, M Raposo, HIS Nogueira, T Trindade. A general strategy to prepare SERS active filter membranes for extraction and detection of pesticides in water. *Talanta* **2018,** *182*, 558-566.

120. B Yu, C Cao, P Li, M Mao, Q Xie, L Yang. Sensitive and simple determination of zwitterionic morphine in human urine based on liquid-liquid micro-extraction coupled with surface-enhanced Raman spectroscopy. *Talanta* **2018,** *186*, 427-432.

121. D Zhang, L Huang, B Liu, HB Ni, LD Sun, EB Su, HY Chen, ZZ Gu, XW Zhao. Quantitative and ultrasensitive detection of multiplex cardiac biomarkers in lateral flow assay with core-shell SERS nanotags. *Biosensors and Bioelectronics* **2018,** *106*, 204-211.

122. SK Islam, YP Cheng, RL Birke, O Green, T Kubic, JR Lombardi. Rapid and sensitive detection of synthetic cannabinoids AMB-FUBINACA and α-PVP using surface enhanced Raman scattering (SERS). *Chemical Physics* **2018,** *506*, 31-35.

123. C Chen, O Oladele, Y Tang, F Yan. Freestanding silver dendrite/graphene oxide composite membranes as high-performance substrates for surface-enhanced Raman scattering. *Materials Letters* **2018,** *226*, 83-86.

124. LL Qu, N Wang, G Zhu, TP Yadav, X Shuai, D Bao, G Yang, D Li, H Li. Facile fabrication of ternary TiO2-gold nanoparticle-graphene oxide nanocomposites for recyclable surface enhanced Raman scattering. *Talanta* **2018,** *186*, 265-271.

125. N Yang, TT You, YK Gao, CM Zhang, PG Yin. Rapid fabrication of flexible and transparent gold nanorods/poly (methyl methacrylate) membrane substrate for SERS nanosensor application. *Spectrochimica Acta Part A: Molecular and Biomolecular Spectroscopy* **2018,** *202*, 376-381.

126. Q Huang, W Wei, L Wang, H Chen, T Li, X Zhu, Y Wu. Synthesis of uniform Ag nanosponges and its SERS application. *Spectrochimica Acta Part A: Molecular and Biomolecular Spectroscopy* **2018,** *201*, 300-305.

127. C Heck, Y Kanehira, J Kneipp, I Bald. Placement of Single Proteins within the SERS Hot Spots of Self-Assembled Silver Nanolenses. *Angewandte Chemie International Edition* **2018,** *57* (25), 7444-7447.

128. S Stewart, MA Ivy, EV Anslyn. The use of principal component analysis and discriminant analysis in differential sensing routines. *Chemical Society Reviews* **2014,** *43* (1), 70-84.

129. R Bro, AK Smilde. Principal component analysis. *Analytical Methods* **2014,** *6* (9), 2812-2831.

130. TPS University Lesson 11: Principal Components Analysis (PCA). https://onlinecourses.science.psu.edu/stat505/node/49/ (accessed 12 June 2018).

131. K Dunn 6.5. Principal Component Analysis (PCA). https://learnche.org/pid/latent-variable-modelling/principal-component-analysis/index (accessed 12 June 2018).

132. RY Shi, XJ Liu, YB Ying. Facing Challenges in Real-Life Application of Surface-Enhanced Raman Scattering: Design and Nanofabrication of Surface-Enhanced Raman Scattering Substrates for Rapid Field Test of Food Contaminants. *Journal of Agricultural and Food Chemistry* **2018,** *66* (26), 6525-6543.

133. GP Tu, N Deogratias, M Xu, XW Li, JJ Liu, L Jiang, YL Yang, JT Zhang. Sharp-featured Au@Ag core/shell nanocuboid synthesis and the label-free ultrasensitive SERS detection of protein single-point mutations. *Materials Chemistry Frontiers* **2018,** *2* (9), 1720-1724.

134. H Wei, HX Xu. Hot spots in different metal nanostructures for plasmon-enhanced Raman spectroscopy. *Nanoscale* **2013,** *5* (22), 10794-10805.

135. MW Li, YY Qiu, CC Fan, K Cui, YM Zhang, ZY Xiao. Design of SERS nanoprobes for Raman imaging: materials, critical factors and architectures. *Acta Pharmaceutica Sinica B* **2018,** *8* (3), 381-389.

136. P Matteini, M Cottat, F Tavanti, E Panfilova, M Scuderi, G Nicotra, MC Menziani, N Khlebtsov, M de Angelis, R Pini. Site-Selective Surface-Enhanced Raman Detection of Proteins. *ACS Nano* **2017,** *11* (1), 918-926.

137. L Fabris. Gold-based SERS tags for biomedical imaging. *Journal of Optics* **2015,** *17* (11), 114002.

138. S Laing, K Gracie, K Faulds. Multiplex in vitro detection using SERS. *Chemical Society Reviews* **2016,** *45* (7), 1901-1918.

139. M Kahraman, ER Mullen, A Korkmaz, S Wachsmann-Hogiu. Fundamentals and applications of SERS-based bioanalytical sensing. *Nanophotonics* **2017,** *6* (5), 831-852.

140. Z Rong, R Xiao, S Xing, GL Xiong, ZY Yu, LM Wang, XF Jia, KL Wang, YW Cong, SQ Wang. SERS-based lateral flow assay for quantitative detection of C-reactive protein

as an early bio-indicator of a radiation-induced inflammatory response in nonhuman primates. *Analyst* **2018,** *143* (9), 2115-2121.

141. L Yang, SJ Zhen, YF Li, CZ Huang. Silver nanoparticles deposited on graphene oxide for ultrasensitive surface-enhanced Raman scattering immunoassay of cancer biomarker. *Nanoscale* **2018,** *10* (25), 11942-11947.

142. JR Li, J Wang, YS Grewal, CB Howard, LJ Raftery, S Mahler, YL Wang, M Trau. Multiplexed SERS Detection of Soluble Cancer Protein Biomarkers with Gold-Silver Alloy Nanoboxes and Nanoyeast Single-Chain Variable Fragments. *Analytical Chemistry* **2018,** *90* (17), 10377-10384.

143. L D'Urso, M Condorelli, O Puglisi, C Tempra, F Lolicato, G Compagnini, C La Rosa. Detection and characterization at nM concentration of oligomers formed by hIAPP, A(1-40) and their equimolar mixture using SERS and MD simulations. *Physical Chemistry Chemical Physics* **2018,** *20* (31), 20588-20596.

144. JY Lin, XL Lin, CR Hu, PG Bai, HS Yang, YT Dai, HJ Qiu, M Lin, SY Feng, JJ Pan, R Chen, JQ Lin, XC Zhang. Silver nanoparticle based surface-enhanced Raman spectroscopy for label-free discrimination of diabetic albumin under near-infrared laser excitation. *Laser Physics Letters* **2018,** *15* (9), 9.

145. Y Shi, N Chen, YY Su, HY Wang, Y He. Silicon nanohybrid-based SERS chips armed with an internal standard for broad-range, sensitive and reproducible simultaneous quantification of lead(II) and mercury(II) in real systems. *Nanoscale* **2018,** *10* (8), 4010-4018.

146. XJ Liu, MM Liu, YD Lu, CJ Wu, YC Xu, D Lin, DC Lu, T Zhou, SY Feng. Facile Ag-Film Based Surface Enhanced Raman Spectroscopy Using DNA Molecular Switch for Ultra-Sensitive Mercury Ions Detection. *Nanomaterials* **2018,** *8* (8), 12.

147. Y He, S Su, TT Xu, YL Zhong, JA Zapien, J Li, CH Fan, ST Lee. Silicon nanowires-based highly-efficient SERS-active platform for ultrasensitive DNA detection. *Nano Today* **2011,** *6* (2), 122-130.

148. W Zhou, YF Tian, BC Yin, BC Ye. Simultaneous Surface-Enhanced Raman Spectroscopy Detection of Multiplexed MicroRNA Biomarkers. *Analytical Chemistry* **2017,** *89* (11), 6121-6129.

149. J Su, DF Wang, L Norbel, JL Shen, ZH Zhao, YZ Dou, TH Peng, JY Shi, S Mathur, CH Fan, SP Song. Multicolor Gold Silver Nano-Mushrooms as Ready-to-Use SERS Probes for Ultrasensitive and Multiplex DNA/miRNA Detection. *Analytical Chemistry* **2017,** *89* (4), 2531-2538.

150. LG Xu, WJ Yan, W Ma, H Kuang, XL Wu, LQ Liu, Y Zhao, LB Wang, CL Xu. SERS Encoded Silver Pyramids for Attomolar Detection of Multiplexed Disease Biomarkers. *Advanced Materials* **2015,** *27* (10), 1706-1711.

151. YH Nie, YJ Teng, P Li, WH Liu, QW Shi, YC Zhang. Label-free aptamer-based sensor for specific detection of malathion residues by surface-enhanced Raman scattering. *Spectrochimica Acta Part A: Molecular and Biomolecular Spectroscopy* **2018,** *191*, 271-276.

152. B Han, YL Zhang, L Zhu, XH Chen, ZC Ma, XL Zhang, JN Wang, W Wang, YQ Liu, QD Chen, HB Sun. Direct laser scribing of AgNPs@RGO biochip as a reusable SERS sensor for DNA detection. *Sensors and Actuators B: Chemical* **2018,** *270*, 500-507.

153. XJ Wang, C Wang, L Cheng, ST Lee, Z Liu. Noble Metal Coated Single-Walled Carbon Nanotubes for Applications in Surface Enhanced Raman Scattering Imaging and Photothermal Therapy. *Journal of the American Chemical Society* **2012,** *134* (17), 7414-7422.

154. SM Restaino, IM White. Real-time multiplexed PCR using surface enhanced Raman spectroscopy in a thermoplastic chip. *Lab on a Chip* **2018,** *18* (5), 832-839.

155. E Genova, M Pelin, G Decorti, G Stocco, V Sergo, A Ventura, A Bonifacio. SERS of cells: What can we learn from cell lysates? *Analytica Chimica Acta* **2018,** *1005*, 93-100.

156. M Hassoun, N Kose, R Kiselev, T Kirchberger-Tolstik, IW Schie, C Krafft, J Popp. Quantitation of acute monocytic leukemia cells spiked in control monocytes using surface-enhanced Raman spectroscopy. *Analytical Methods* **2018,** *10* (23), 2785-2791.

157. JG de Pablo, FJ Armistead, SA Peyman, D Bonthron, M Lones, S Smith, SD Evans. Biochemical fingerprint of colorectal cancer cell lines using label-free live single-cell Raman spectroscopy. *Journal of Raman Spectroscopy* **2018,** *49* (8), 1323-1332.

158. S Holler, E Mansley, C Mazzeo, MJ Donovan, M Sobrero, BA Miles. Raman Spectroscopy of Head and Neck Cancer: Separation of Malignant and Healthy Tissue Using Signatures Outside the "Fingerprint" Region. *Biosensors* **2017,** *7* (2).

159. JF Wang, K Lin, W Zheng, KY Ho, M Teh, KG Yeoh, ZW Huang. Simultaneous fingerprint and high-wavenumber fiber-optic Raman spectroscopy improves in vivo diagnosis of esophageal squamous cell carcinoma at endoscopy. *Scientific Reports* **2015,** *5*.

160. U Munchberg, P Rosch, M Bauer, J Popp. Raman spectroscopic identification of single bacterial cells under antibiotic influence. *Anal Bioanal Chem* **2014,** *406* (13), 3041-50.

161. E Prado, A Colin, L Servant, S Lecomte. SERS Spectra of Oligonucleotides as Fingerprints to Detect Label-Free RNA in Microfluidic Devices. *The Journal of Physical Chemistry C* **2014,** *118* (25), 13965-13971.

162. NE Dina, AMR Gherman, V Chis, C Sarbu, A Wieser, D Bauer, C Haisch. Characterization of Clinically Relevant Fungi via SERS Fingerprinting Assisted by Novel Chemometric Models. *Analytical Chemistry* **2018,** *90* (4), 2484-2492.

163. P Wang, S Pang, J Chen, L McLandsborough, SR Nugen, M Fan, L He. Label-free mapping of single bacterial cells using surface-enhanced Raman spectroscopy. *Analyst* **2016,** *141* (4), 1356-62.

164. V Hoang, RA Tripp, P Rota, RA Dluhy. Identification of individual genotypes of measles virus using surface enhanced Raman spectroscopy. *Analyst* **2010,** *135* (12), 3103-9.

165. C Grosse, N Bergner, J Dellith, R Heller, M Bauer, A Mellmann, J Popp, U Neugebauer. Label-free imaging and spectroscopic analysis of intracellular bacterial infections. *Anal Chem* **2015,** *87* (4), 2137-42.

Nanobioconjugates of Gold Nanoparticles and Laccase in Solution

2

This chapter is comprised of the following article:

Miguel Peixoto de Almeida, Pedro Quaresma, Susana Sousa, Cláudia Couto, Inês Gomes, Ludwig Krippahl, Ricardo Franco and Eulália Pereira

Measurement of adsorption constants of laccase on gold nanoparticles to evaluate the enhancement in enzyme activity of adsorbed laccase (**2018**) Physical Chemistry Chemical Physics, **20**, 16761–16769.

DOI: 10.1039/C8CP03116A

The first author contributions for the article were:

- Gold nanoparticle synthesis and capping agent exchange;
- Preparation of bionanoconjugates of laccase and gold nanoparticles;
- Dynamic light scattering (DLS) and electrophoretic light scattering (ELS) measurements;
- Determination of adsorption constants based on DLS and ELS data;
- Assays of laccase enzymatic activity;
- Data plotting;
- Data compilation for the paper;
- Writing and editing of the manuscript in cooperation with the co-authors.

Since sections 2.2 and 2.3 are integral transcripts of the published article and supplementary information in their final version, section 2.1 was added as a brief introduction to the class of enzymes used in this work. Other enzymes from this class were also used in the work described in chapter 3.

Section 2.4 includes final remarks complementary to the paper information. The references in section 2.5 are independent from the article and are related to sections 2.1 and 2.4.

2.1. Introduction

2.1.1. Laccases

These enzymes fits in the Enzyme Commission number 1.10.3.2, *i.e.*, belongs to the Oxidoreductases class (1), catalysing redox type reactions, acting on diphenols and related substances as donors (1.10), with oxygen as acceptor (1.10.3) and finally classified as a laccase (1.10.3.2).[1-6]

Laccases are multi-nuclear copper-containing enzymes. They are considered eco-friendly enzymes since they catalyse the one-electron oxidation of substrates with molecular oxygen (*e.g.* present in the air) as reducing agent and water as the only by-product.[7] They are useful in many industrial processes (*e.g.* paper), food applications, bioremediation and bioconversion processes[8] and more recently, biofuel cells.[9-11] They can also be used as catalysts in organic synthesis, where their typical substrates (phenols and amines), give origin to products like dimers and oligomers by coupling reactive radical intermediates. The main application nowadays is still the enzymatic dye decolorization (biobleaching),[10] however very recently, laccases from different fungal species have shown applications in health, like the ability to inhibit HIV–I reverse transcriptase and antiproliferative and cytotoxic effects on tumour cells.[12]

The typical laccase catalytic reaction is schematised in figure 2.1.

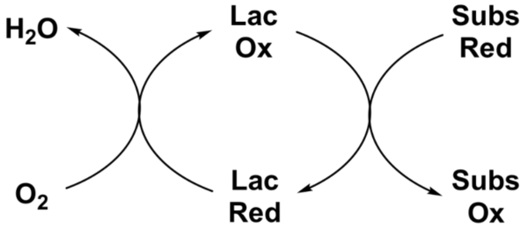

Figure 2.1 – Schematic representation of a substrate (Subs) redox reaction catalysed by laccase (Lac), in presence of molecular oxygen.

These enzymes are quite ubiquitous in nature and are typically found in higher plants and fungi. The very first report of an enzyme from this group was a laccase from the lacquer tree *Rhus vernicifera* (now *Toxicodendron vernicifluum*).[9]

Given the several industrial applications, laccase immobilization attempts have been reported in the past years.[13] The interest of the immobilization of this (and other) enzymes, arises from the possibility of reusing them and of applying them to continuous flow processes.[14] Together with these two main advantages of the whole system, there also advantages in the performance of the enzyme itself. For example, for one of the major applications of laccase – pollutants degradation in wastewaters – higher activity and stability in a uncontrolled medium (composition, pH, ionic strength, etc.) is very important.[15] One possible way to achieve this purpose, is to conjugate enzymes with metal nanoparticles[16].

It is important to remember that each conjugation process between the several sizes, shapes and composition of metal nanoparticles and the several enzymes from several species is almost a unique process, so they must be studied individually.[17]

Nanobioconjugation between laccase from *Toxicodendron vernicifluum* and gold nanoparticles has not been studied before, regarding the adsorption process and the enzymatic activity implications of the nanobioconjugation, so this was the focus of the work reported in the article that follows.

2.2. Published Article

Abstract

Adsorption of enzymes to nanoparticles and the mechanisms responsible for enzyme activity modulation of adsorbed enzymes are not well understood. In this work, gold nanoparticles were used for electrostatic adsorption of a plant-derived laccase. Adsorption constants were determined by four independent techniques: dynamic light scattering, electrophoretic light scattering, agarose gel electrophoresis and fluorescence quenching. Stable bionanoconjugates were formed with log K in the range 6.8-8.9. An increase in enzyme activity was detected, in particular at acidic and close to neutral pH values, a feature that expands the useful pH range of the enzyme. A model for the adsorption was developed, based on geometrical considerations and volume increase data from dynamic light scattering. This indicates that enzymes adsorbed to gold nanoparticles are ca. 9 times more active than the free enzyme.

Introduction

Gold nanoparticles (AuNPs) have been widely used in the development of biosensors and bioremediation systems due to their unique properties, including high surface area, size-dependent physical properties, and ease of synthesis and functionalization.[1] AuNPs provide a suitable scaffold for the immobilization of biomolecules, namely enzymes, retaining or even increasing their stability and biological activity.[2-4] The synergy between AuNPs and enzymes has implications in many areas, namely in electrochemical sensors, where AuNPs facilitate electron transfer between the catalytic center of the immobilized enzyme and its redox partner, improving analytical sensitivity and selectivity and often avoiding the need for chemical mediators.[5-7]

A key approach to influence the formation of conjugates between AuNPs and enzyme is the modification of the AuNPs surface using selected capping agents. For example, formation of monolayers of alkanethiols on the surface of AuNPs is a convenient, adaptable, and simple way to prepare a “biologically friendly” environment for the adsorption of proteins, while minimizing unfavourable interactions between the protein and the metal surface.[8-9] Peptides also have great potential as capping agents for the preparation of bionanoconjugates with proteins. They provide a surface environment chemically similar to proteins, favourable for protein binding, while maintaining or enhancing bioactivity.[10], [11] Binding of proteins to peptide functionalized nanoparticles can be either covalent, using well-known bioconjugation procedures, or non-covalent, relying on electrostatic interactions with charged residues, hydrogen bonds, hydrophobic interactions, etc. Usually, higher enzymatic activities are obtained for enzymes that are non-covalently adsorbed relative to covalently bound enzymes, possibly due to conformational changes and to undesired side reactions occurring in the chemical process of covalent conjugation.[12] We have previously shown the formation of stable bionanoconjugates of tyrosinase and AuNPs functionalized with the peptide CALNN.[3] This pentapeptide was designed to present a thiol group (from the N-terminal cysteine, C) for binding to AuNPs, a hydrophobic region (AL) to promote self-assembly at the AuNP surface, and two uncharged and hydrophilic asparagine residues (NN), at the C-terminal, for interaction with the enzyme and to promote colloidal stability in water.[10] AuNP-CALNN-tyrosinase bionanoconjugates showed increased enzymatic activity in comparison with the free enzyme in solution, as high as ca. 40% in the pH range 5.5-8.0.[3]

To further understand the influence of nanoparticles on proteins, it is critical to obtain reliable data on adsorption of proteins on nanoparticles. Nevertheless, the number of studies reporting adsorption constants is still very limited. In addition, the special properties of nanoparticles and their inherent poor colloidal stability can impair the reliable determination of adsorption constants. It is thus fundamental to study protein-nanoparticle interactions using different techniques, to evaluate possible artefacts and interferences specific to this type of systems.

In this work, we have selected laccase, a multi-copper oxidase, for conjugation with AuNPs. Laccases are a group of enzymes found in plants, fungi and microorganisms that catalyse the oxidation of phenols by dioxygen. Laccases contain one catalytic trinuclear copper cluster, where reduction of dioxygen to water takes place, and one type 1 copper centre responsible for electron transfer from the phenolic substrate. Laccases have numerous biotechnological applications in the textile, food processing, pharmaceutical and chemical industries.[12-15] A key feature of these enzymes is their ability to catalyse one-electron oxidations of a broad variety of substrates. In addition, dioxygen is the co-substrate, avoiding the use of environmental unfriendly oxidizing agents. Due to these properties, laccases have been widely used, for example, in electrochemical sensing of a variety of phenolic substrates and in the construction of cathodes for fuel cells.[16-17] For the aforementioned electrochemical applications, conjugation of laccase to AuNPs can result in significant advantages, because the direct electron transfer between the enzyme copper centre and the electrode can be facilitated by AuNPs.[18] We have prepared enzymatically active bionanoconjugates using the enzyme laccase from the Japanese lacquer tree *Toxicodendron vernicifluum* (formerly *Rhus vernicifera*), and CALNN-capped AuNPs, by a non-covalent binding approach. Binding of the enzyme to AuNPs was studied using four different techniques: Dynamic Light Scattering, Electrophoretic Light Scattering, Agarose Gel Electrophoresis and fluorescence quenching. The results obtained by these techniques were similar, showing a high affinity of the enzyme for the CALNN-AuNPs. The resulting bionanoconjugates have enhanced enzymatic performance over an extended pH-range, thus showing that these new bionanoconjugates can advantageously replace laccase in biotechnological applications.

Results and Discussion

Spherical gold nanoparticles were synthesized by a modification of the Turkevich method.[19] The citrate capping agent was exchanged with the pentapeptide CALNN by incubation at room temperature with a 1000x excess of this new capping agent. TEM analysis of the gold nanoparticles shows an average diameter of (13.6 ± 2.2) nm for the gold core (ESI, Figure S1). The exchange of the capping agent was assessed by XPS after extensive washing of the nanoparticles. In addition to the Au peak, XPS shows peaks for N and S (ESI, Figure S2), most probably arising from CALNN, since the capping agent used in the synthesis (citrate) does not contain either of these elements. Successful CALNN functionalization of the nanoparticles was further assessed by Dynamic Light Scattering (DLS), with citrate-AuNPs increasing from an average hydrodynamic diameter of 11.75 nm, to 14.54 nm for CALNN-AuNPs. Bionanoconjugates were prepared by incubation of laccase with a solution of CALNN-AuNPs (hereafter “AuNPs”). Formation of bionanoconjugates was studied by Dynamic Light Scattering (DLS), Electrophoretic Light Scattering (ELS), Agarose Gel Electrophoresis (AGE) and fluorescence quenching. All the techniques used provided evidence for the formation of stable bionanoconjugates.

Binding of Laccase to Gold Nanoparticles Functionalized with the Pentapeptide CALNN

Dynamic Light Sccattering (DLS)

Binding of laccase to AuNPs was studied by DLS, by adding increasing amounts of laccase to solutions of AuNPs and measuring the hydrodynamic diameter of the resulting conjugates. Four different concentrations of AuNPs were studied. The results show an increase of the hydrodynamic diameter with the concentration of laccase in a typical Langmuir adsorption curve (Figure 1, Table 1). We have used the hydrodynamic volume to fit a Langmuir isotherm equation:

$$\Delta V_H = \Delta V_{H,max} \frac{K_L[\mathrm{LAC}]}{1+K_L\mathrm{LAC}]} \qquad (1)$$

where ΔV_H is the difference in hydrodynamic volume between the bionanoconjugates and CALNN-AuNPs, $\Delta V_{H,max}$ is the maximum value of ΔV_H, K_L is the Langmuir adsorption constant and [LAC] is the total concentration of laccase. To derive this equation, we have assumed that the increase in the hydrodynamic volume is directly proportional to the increase in the number of laccase molecules adsorbed to AuNPs; thus, the ratio between the increase in hydrodynamic volume (ΔV_H) and the maximum increase in hydrodynamic volume ($\Delta V_{H,max}$) is a suitable approximation for the fractional occupancy of adsorption sites. In this model, we have assumed that the hydration sphere of the nanoparticles does not appreciably change for different number of laccase molecules adsorbed to AuNPs. We have used DLS data resulting from distributions of number of particles, in order to have a reliable evaluation of the increase of the average number of laccase molecules adsorbed per AuNP. Note that DLS data resulting from distributions of number of particles are slightly different from those obtained by the more common intensity distribution, since in the latter case there is a bias towards bigger nanoparticles, which contribute more than small nanoparticles to the intensity of light dispersed.

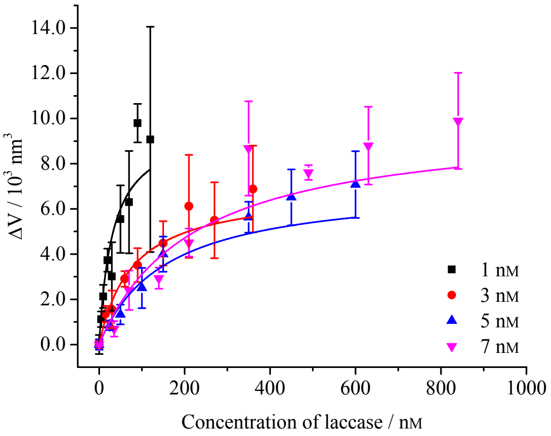

Figure 1. Variation of hydrodynamic volumes for bionanoconjugates produced with different laccase concentrations, determined by DLS. Variations are relative to the hydrodynamic volume measured for CALNN-functionalized AuNPs alone in solution. Bionanoconjugates were produced with AuNPs at 1 nm (black squares); 3 nm (red circles); 5 nm (blue triangles); and 7 nm (purple inverted triangles). Data points are from three independent measurements; lines correspond to fitting to a Langmuir type equation, with fitting parameters shown in Table 1.

The Langmuir model is valid for the adsorption of molecules to solids, and the application of this model to the binding of molecules to AuNPs assumes that the ensemble of AuNPs in solution is equivalent to a bulk solid phase. The calculated binding constant is thus only applicable to the particular solution of nanoparticles used, *i.e.* the same size, the same size distribution and the same concentration of nanoparticles. For different amounts of nanoparticles, the number of available adsorption sites will increase linearly with the number of nanoparticles, leading to a decrease in the value of K_L. According to the Langmuir model, the inverse of the binding constant is the concentration of laccase necessary for half-saturation of the adsorption sites, and thus should increase linearly with the amount of AuNPs in solution.[3, 20] We confirmed this behaviour in our system, with 31 ± 2 laccase molecules in solution per AuNP necessary for half-saturation (ESI, Figure S3). In contrast, the maximum increase in the hydrodynamic volume does not change considerably for varying concentrations of AuNPs in the range 1-7 nm, showing an average value of (8.4 ± 1.7) x 10^3 nm^3. This value can be interpreted as the volume of the protein corona for maximum saturation. Using the hydrodynamic volume of the AuNPs in the absence of laccase and the maximum changes in hydrodynamic volume, the maximum increases in radii were calculated ($\Delta r_{H,max}$, Table 1), corresponding to an average radius increase of (6.5 ± 0.6) nm. This value is close to the diameter calculated from the protein molecular mass (110 kD) of 6.3 nm,[21] a strong indication that the full protein corona corresponds to one monolayer of laccase molecules.

Table 1. Fitting parameters for the hydrodynamic volume of the bionanoconjugates as a function of laccase concentration, to a Langmuir adsorption curve. Results are presented for four different AuNPs concentrations (see Figure 1).

[AuNP] [nM]	$\Delta V_{H,max}$ [nm^3] [a]	K_L [10^6 M^{-1}][b]	R^2 [c]	$\Delta r_{H,max}$ [nm] [d]
1.0	9.8 x 10^3	32 ± 5	0.918	6.8
3.0	6.9 x 10^3	13 ± 1	0.986	6.0
5.0	7.1 x 10^3	6.4 ±0.8	0.959	6.0
7.0	9.9 x 10^3	4.7 ± 0.7	0.974	7.2

[a] Maximum variation of the hydrodynamic volume. [b] Langmuir adsorption constant. [c] Coefficient of determination. [d] Maximum variation of the hydrodynamic radius.

Electrophoretic Light Scattering (ELS) and Agarose Gel Electrophoresis (AGE)

Two techniques for measuring the electrophoretic mobility, electrophoretic light Scattering (ELS) and Agarose Gel Electrophoresis (AGE), were applied to bionanoconjugates obtained with increasing laccase concentrations in the range 0 to 600 nM, with a AuNPs concentration of 5 nM, at pH 7.0 (10 mM phosphate buffer). Figure 2 shows the results obtained by electrophoretic light scattering. As laccase concentration increases, the electrophoretic mobility becomes less negative, from a starting value of (-2.3 ± 0.2) x 10^{-8} m2 V^{-1} s^{-1} until a saturation plateau is reached at (-0.8 ± 0.1) x 10^{-8} m^2 V^{-1} s^{-1} for a laccase concentration around 250 nM. This variation of the electrophoretic mobility corresponds to a change in the zeta potential from (-29.8 ± 0.3) mV to (-10.7 ± 1.3) mV. This behaviour can be explained by the change in surface charge of AuNPs as more protein molecules bind to the AuNPs through electrostatic interactions of the negatively charged terminal carboxylate groups from the capping agent (CALNN), with oppositely charged residues on the protein. Variation of electrophoretic mobility of the bionanoconjugates relative to that of AuNPs alone ($\Delta\mu$) was plotted against laccase concentration (Figure 2), and a Langmuir-type equation was fitted to the experimental data:[20]

$$\Delta\mu = \Delta\mu_{max} \frac{K_L[LAC]}{1+K_L[LAC]} \qquad (2)$$

where $\Delta\mu$ is the difference in electrophoretic mobility between the bionanoconjugates and the parent AuNPs, $\Delta\mu_{max}$ is the maximum value of $\Delta\mu$, K_L is the Langmuir adsorption constant and [LAC] is the total concentration of laccase. K_L was (9.4 ± 1.9) x 10^{7} M^{-1} and $\Delta\mu_{max}$ was (1.58 ± 0.05) x 10^{-8} m2 V^{-1} s^{-1}. It should be noted that the binding constant obtained by this method is one order of magnitude higher than the binding constant obtained by DLS (Table 1). However, the change in electrophoretic mobility may not be a good assessment of the occupancy of the adsorption sites on the AuNPs by protein molecules. In fact, electrophoretic mobility of a single BNC depends not only on the number of protein molecules adsorbed, but also on the orientation of the adsorbed protein molecule, exposing different charged residues to the solvent. For proteins containing highly charged patches with an opposite charge relative to the AuNP surface, such as cytochrome c, it is expected that most of the proteins will adsorb with a similar orientation, maximizing the interaction between the charged patch and the AuNP;[20] but for proteins such as laccase, where the positively charged residues are distributed over large areas of the protein surface, orientation of adsorbed molecules may vary considerably. In this case, the changes in electrophoretic mobility will reflect not only the number of adsorbed proteins, but also the orientation of the adsorbed molecules. In contrast, the increase in hydrodynamic volume of the bionanoconjugates measured by DLS is expected to be less dependent of the orientation of the proteins adsorbed and is thus a better measure of the occupancy of the adsorption sites.

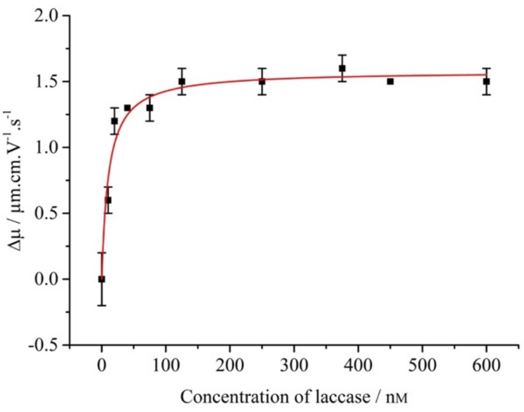

Figure 2. Variation of electrophoretic mobility, determined by ELS, of the bionanoconjugates relative to the parent AuNPs, for increasing concentration of laccase, and the corresponding Langmuir fit.

To further examine adsorption of laccase to the AuNP surface, Agarose Gel Electrophoresis (AGE) was used (Figure 3). This technique has been previously applied to study the interaction between nanoparticles and biomolecules, and explores nanoparticles and bionanoconjugates separation according to differences in their electrophoretic mobility in agarose gel.[22-25] It should be noted that the electrophoretic mobility measured in gels depends not only on the charge of the particles, but also on their size because the structure of the gel opposes the free movement of particles, with bigger particles having their movement more delayed that smaller particles. This is to be contrasted with ELS, where the measured electrophoretic mobility in free solution is independent of size. Figure 3 shows a typical AGE gel obtained with bionanoconjugates prepared with the same laccase and AuNPs concentrations as in the ELS experiments. Bands for AuNPs alone (corresponding to [laccase] = 0) and bionanoconjugates are clearly discernible without using any developing dye, due to the strong red colour of the AuNPs. A profile similar to that observed in the ELS measurements was obtained, with a progressive decrease of electrophoretic mobility with increasing laccase concentration, up to a saturation plateau for a concentration of laccase around 250 nM. A considerable band smearing effect is noticeable in lanes below this plateau, indicating a broad distribution in the number of laccase molecules per AuNP. This behaviour, arising from the multiple equilibria established between laccase and AuNPs, results in a random distribution of the number of bound proteins around an average value.[24] An innovative computer program was used for data analysis, based on the presented photograph. Program outputs are the relative electrophoretic mobility data, that were then adjusted to the Langmuir equation (2). (see full description in ESI, Figures S4 and S5). In this case, the binding constant K_L was (6±1) x 10^7 M^{-1}, very close to the value obtained by ELS. The excellent agreement between the constants derived by the measurement of electrophoretic mobility by ELS and by AGE seems to imply that, in this case, the effects of change of size are not very important for the electrophoretic mobility values obtained by AGE.

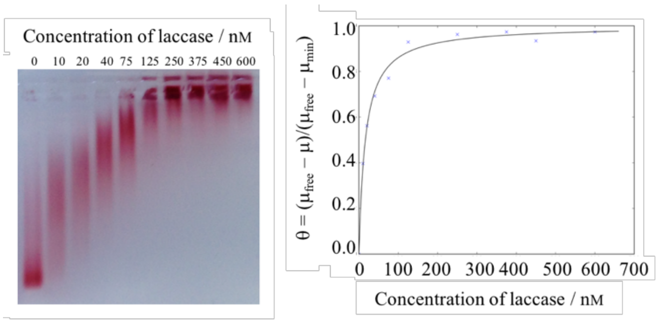

Figure 3. Photograph of the agarose gel electrophoresis for bionanoconjugates at the indicated concentration of laccase (left). Fitting of the relative electrophoretic mobility to a Langmuir curve (right, see details in ESI).

Fluorescence Quenching of Laccase by Gold Nanoparticles

To further characterize the binding of laccase to CALLN-functionalized AuNPs, fluorescence quenching experiments were performed, taking advantage of the quenching properties of gold nanoparticles[26] and the fluorescence of the aromatic residues of laccase (ESI, Figure S4). A Stern-Volmer equation:

$$\frac{F_0}{F} = 1 + K_{SV}[\mathrm{AuNPs}] \qquad (3)$$

in which F_0 is the fluorescence intensity of laccase in the absence of the quencher (AuNPs), and F is the fluorescence emission intensity for bionanoconjugates prepared with varying AuNP concentrations, was used to fit the experimental values, yielding K_{SV} of (8.4 ± 0.5) x 10^8 M^{-1}. AuNPs are known to be very effective fluorescence quenchers, with values of K_{SV} as high as 1.16 x 10^{10} M^{-1} reported for the quenching of fluorescence of bovine serum albumin and AuNPs.[26] These high values are typical of a static quenching mechanism, with a strong association between protein and nanoparticle. In this case, the Stern-Volmer constant can be taken as the binding constant between laccase and AuNPs. We have also evaluated the possible existence of cooperative effects by adjusting the experimental values to the modified equation:

$$log\frac{F_0-F}{F} = n[\mathrm{AuNPs}] - logK \qquad (4)$$

where n is the Hill coefficient for cooperative binding and K is the association constant. In our case log K = 9.6 ± 0.6, and n=1.08 ± 0.06, indicative of a very slight positive cooperativity. The association constant determined by fluorescence quenching is higher than those determined by the other methods used in this study, but it also indicates a strong interaction between laccase and gold nanoparticles. It should also be noted, that in this particular method, the concentration of laccase is kept constant, varying the concentration of AuNPs, whereas in the other techniques used, it is the concentration of laccase that was varied, keeping the concentration of AuNPs constant. In addition, the range of concentrations of laccase and gold nanoparticles was also different between the fluorescence determination and the other three methods. For the fluorescence studies, the concentration of free laccase must be high enough to provide a measurable fluorescence intensity and this is only achieved by having the binding sites on gold nanoparticles almost completely occupied. In contrast, for the other techniques used, the binding constant is determined by the part of the Langmuir curve corresponding to 0-75% of occupancy. It is surprising that the binding constant determined by fluorescence, where there is always a large excess of laccase, is higher than those determined by DLS, ELS and AGE, where there is an excess of gold nanoparticles. This seems to indicate that binding of laccase to gold nanoparticles covered by laccase is stronger than binding of laccase to bare gold nanoparticles, in other words that there is a positive cooperativity effect on laccase binding. Nevertheless, the slight cooperativity detected in the fluorescence studies ($n=1.08 \pm 0.06$) is not high enough to justify the difference in the binding constants. Overall, our results stress out the need to use different techniques to determine protein binding constants to nanoparticles, in order to better understand the complex interaction between them.

Enzyme Activity of Bionanoconjugates of Laccase and Gold Nanoparticles

Effect of Gold Nanoparticles on the Enzymatic Activity of Laccase

The enzymatic activity of the laccase in the presence and in the absence of AuNPs was measured by UV/vis spectrophotometry, with syringaldazine as the substrate (Figure 4 and Figure S7, ESI). Syringaldazine was chosen as substrate due to its high specificity for laccases (as opposed to other oxidases)[13] and lower susceptibility to auto-oxidation than most other laccase substrates[27]. For all laccase concentrations studied, the activity in the presence of AuNPs was remarkably increased relative to the enzyme alone at the same concentration. These values were reproducible for the same batch of enzyme but varied between batches. Batch variation of enzymatic activity is quite common for glycosylated enzymes, which can present different degrees and patterns of glycosylation between different batches. It is also known that enzymatic activity can decrease during manipulation due to loss of copper from the active centre. Nevertheless, for all the different batches of enzyme assessed, the enzyme was invariably more active in the presence of AuNPs. For the sake of clarity, all results shown here were obtained with the same batch of enzyme.

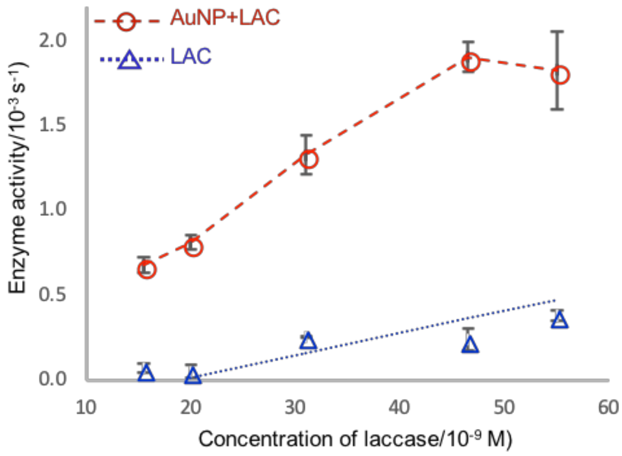

Figure 4. Oxidase activity of laccase alone as a control (“LAC”, blue), and in the presence of AuNPs 5 nM (AuNP+LAC, red), for several total concentrations of laccase. The dashed red line for laccase with gold nanoparticles is a guide to the eye. The dotted blue line for laccase only corresponds to the linear regression obtained for laccase concentration between 15 and 250 nM (Figure S7, ESI). Error bars represent the standard deviation of the activity measurements.

The relative increase in activity of solutions containing AuNPs decreased for higher concentrations of laccase. This behaviour can be explained by an increase in the fraction of enzyme that is not bound to AuNPs in the BNC solutions, as the total concentration of laccase added to the AuNPs increases. Therefore, enzyme activities determined for the solutions of bionanoconjugates have two contributions: the activity of laccase adsorbed to the AuNPs and the activity of free enzyme remaining in solution.

To evaluate the relative contribution of these two components to the measured enzyme activity, it is necessary to assess the amount of AuNP-bound laccase for each total concentration of laccase. For that purpose, we have used data from DLS measurements and a simple geometric model (compact packing of small spheres on the surface of a larger sphere[28]) to calculate the maximum number of laccase molecules that can be adsorbed to the surface of a AuNP (see detailed description in ESI). In this model, we have assumed that both the AuNP and the enzyme are spherical (Figure 5), and that the void space between protein molecules is occupied by the solvent. The diameter of the central, larger sphere was taken as the hydrodynamic diameter obtained from DLS measurements of AuNPs alone (12.9 ± 0.6 nm, number distribution). The surrounding spheres are laccase, considered as a globular protein, with a radius that can be calculated from its molecular weight (110 kDa), of 3.16 nm.[21] This value is very close to 3.0 nm as measured for the *Trametes versicolor* laccase crystallographic structure (PDB file 1GYC, using UCSF Chimera 1.10.1).[29] Using these two sphere sizes for the central AuNP larger sphere and the surrounding smaller laccase spheres, respectively, a maximum value of 30 laccase molecules per AuNP was calculated. This value was then used to calculate the average contribution to the increase in hydrodynamic volume per laccase molecule due to formation of the protein corona. The difference in hydrodynamic volume between the AuNPs alone and the maximum hydrodynamic volume obtained from fitting the experimental DLS data (number distribution) to a Langmuir adsorption isotherm was taken as the volume of the protein corona. Assuming that the protein corona is due to one single layer of protein molecules, *i.e.* to 30 protein molecules, the average contribution of one protein molecule to the protein corona is then 7077 nm3/30 = 236 nm3. This value seems reasonable in comparison to the volume as calculated from laccase molecular weight (132 nm3),[21] since the protein corona also includes solvent and other adsorbed species.

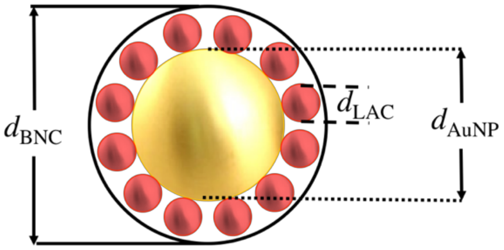

Figure 5. Scheme of the model used to calculate the increase in hydrodynamic volume of bionanoconjugates per laccase molecule. The hydrodynamic diameter of AuNPs (dAuNP) was obtained by DLS, the diameter of laccase (dLAC) was calculated from its molecular weight and the maximum diameter of bionanoconjugates (dBNC) was determined by fitting DLS data to a Langmuir isotherm.

Using the average contribution of one single laccase molecule to the volume of the protein corona and the volume of the protein corona (from DLS data fitting) for each concentration of laccase used, it is possible to calculate the average number of bound proteins per AuNP for the different concentrations of laccase used. The concentration of laccase adsorbed to the AuNPs is then calculated by multiplying the average number of bound proteins per AuNP by the total concentration of nanoparticles (5 nM). The total oxidase activity determined in the bionanoconjugate solutions can then be decomposed in the activity deriving from free laccase (calculated from the molar activity of free laccase from the control experiments and the concentration of free laccase in bionanoconjugates solutions), and the activity deriving from the AuNP-CALNN-bound laccase. The molar activity of laccase alone was (5.4 ± 2.2) x 10^3 M^{-1} s^{-1}, whereas for AuNP-bound laccase the molar activity was (4.9 ± 0.4) x 10^4 M^{-1} s^{-1}, *i.e.* the bound enzyme is ca. 9 times more active than the free enzyme. This model indicates that, within the concentration range studied, 88%-71% of laccase is adsorbed to AuNPs, and that this corresponds to 99%-94% of the enzymatic activity measured. It is also interesting to note that for the highest laccase concentration, the molar activity of bound laccase slightly decreases, being 10% lower than the average. Such observation can be due to protein crowding at the AuNP, that can hinder substrate diffusion, and thus enzyme activity. Nevertheless, this effect is within the experimental error except for very high total concentration of laccase (data not shown), for which DLS measurements indicate aggregation of the AuNPs. For the other concentrations studied, no aggregation was detected either before or after the assay for enzymatic activity (Figure S8, ESI).

Activity increase of enzymes when bound to AuNPs were demonstrated in multiple cases in the literature.[30-32] The reasons for this increase can be diverse and range from a simple stabilization effect on the bound enzyme, due to a decrease in conformational freedom that might impair activity; to more complex changes in the microenvironment of the enzyme,[33] substrate binding mode,[34] or both. An interesting possibility, that takes into account the properties of AuNPs, is an increase in electron transfer rates facilitated by the metal nanoparticle. This phenomenon is common in AuNPs-enzyme systems when immobilized in electrodes and could play an important role in the observed activity enhancement.[18, 35]

The influence of pH on the oxidase activity of the bionanoconjugates was evaluated and compared with the pH-dependent activity profile for the enzyme alone in solution (Figure 6). The pH for the formation of bionanoconjugates and the respective activity measurements was varied between 6.5-8.5 and the concentration of laccase (15.5 nM) was in a range where more than 85% of the total enzyme is bound to the AuNPs, corresponding to 99% of activity coming from laccase bound to AuNPs (according to the calculations described above). This pH range was chosen based on the fact that plant laccases, such as the one used here from the Japanese lacquer tree *Toxicodendron vernicifluum*, have optimal pH in the range 6.8-7.4.[13, 15] In pH range 6.5-8.5, bionanoconjugates were always more active than the free enzyme (Figure 6). In fact, in the presence of AuNPs, enzyme activity at this pH range was 1.5-5.2 times higher than the enzyme activity at optimum pH. This was especially relevant for pH between 6.5-7.5, in which bionanoconjugates were ca. 10 times more active than the free enzyme at the same pH value. For pH 8.0 and 8.5 the activity increase is lower, ca. 3 and 6 times, respectively. Laccase has a pI of 8.2-9.1,[15] so this lower increase in activity may be due to a decrease in adsorption of laccase to the negatively charged AuNP, due to the lower positive overall charge of the enzyme. The considerable increase in oxidase activity at lower pH has important implications at the industrial level, as it opens the possibility to use this plant-type laccase at lower and close to neutral pH values, filling a pH gap on the industrial use of laccases.[13, 15]

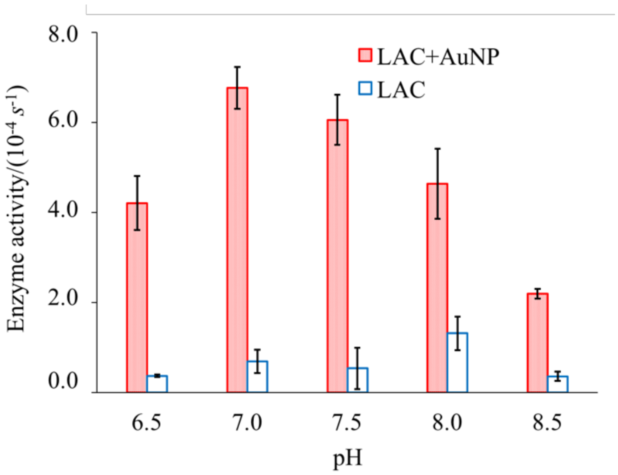

Figure 6. Oxidase activity of laccase alone as a control ((“LAC”, blue) and in the presence of AuNPs 5 nm (AuNP+LAC, red grid) for pH range 6.5-8.5.

Materials and Methods

Chemicals and Reagents

Laccase from *Toxicodendron vernicifluum* (formerly, *Rhus vernicifera*) was purchased as a crude acetone powder from Sigma (≥50 U/mg solid). Syringaldazine (3,5-dimethyl-4-hydroxybenzaldazine), the substrate for laccase used in enzymatic experiments, was purchased from Sigma. Stock solutions were prepared by dissolving the powder in methanol (Sigma, 99.8% pure). The pentapeptide CALNN was obtained from CASLO Laboratory (Lyngby, Denmark) and dissolved in deoxygenated water (Water for Molecular Biology, Sigma). The concentration of protein was determined by the bicinchoninic acid method using a kit (Sigma). UltraPure agarose for agarose gels was from Invitrogen. Bovine

Serum Albumin protein standard was purchased from Sigma, as a stock solution (1 mg/ml). All other chemicals and reagents were from Sigma Aldrich or Fluka and were of the highest purity available. Unless otherwise stated, all aqueous solutions were prepared with MilliQ water (18 MΩ cm^{-1}).

Gold Nanoparticle Synthesis and Capping Agent Exchange

Gold nanoparticles (AuNPs) were synthesized by the Turkevich method, with minor changes, using $HAuCl_4$ solution (30%) and citrate as the reducing and capping agent.[19] Transmission Electron Microscopy (TEM) analysis of a representative sample is shown in Figure S5 (ESI). AuNP concentration was determined by the method of Haiss *et al.*[36] Exchange of citrate for the pentapeptide CALNN was performed by addition of an aqueous solution of CALNN (1000x molar excess) to the AuNPs, followed by incubation at room temperature for 24 hours. AuNPs were then centrifuged at 10,000 g for 20 min and re-suspended in milliQ water. For XPS analysis, the sample was thoroughly washed by repeated centrifugation and resuspension cycles to remove any traces of unbound peptide, before deposition on carbon disks (ESI, Figure S6). XPS was performed at CEMUP (Faculdade de Ciências da Universidade do Porto, Portugal), in a VG Scientific ESCALAB 200A spectrometer using non-monochromatized Al Kα radiation (1486.6 eV). XPS spectra were deconvoluted with the XPSPEAK 4.1 software, using non-linear least squares fitting routine after a Shirley-type background subtraction.

Preparation of Bionanoconjugates of Laccase and Gold Nanoparticles

Laccase from *Toxicodendron vernicifluum* (20 mg) acetone powder was dissolved in potassium phosphate buffer (10 ml, 10 mM), with vortex stirring for 10 minutes. The solution was centrifuged at 8000 rpm for 20 minutes to remove insoluble material,[37] and the supernatant containing laccase was filtered with an Acrodisc syringe filter with HT Tuffryn membrane (0.45 μm, 25 mm, Sigma). The resulting clear solution was stored in aliquots at -20 °C. SDS-PAGE and UV-Vis spectroscopy analyses revealed a homogenous protein preparation. Bionanoconjugates of AuNPs and laccase were prepared by overnight incubation, at 4 °C, of AuNP solution in phosphate buffer (10 mM, pH 7.0), with the required volume of laccase solution.

UV-Vis Spectrophotometry

UV-Vis spectrophotometry was performed in quartz cells with 1 cm path length (Hellma, Germany), using an UV-Vis spectrophotometer Varian, model Cary 50, version 3.0). Temperature control was achieved using a Cary single cell Peltier accessory.

Dynamic Light Scattering and Electrophoretic Light Scattering

DLS and ELS were performed in a Malvern Zetasizer Nano ZS (Malvern, Worcestershire, UK), at 25 °C, with light detection at 173° (DLS) and at 17° using the backscatter mode (ELS). Bionanoconjugates with [AuNP] =1, 3, 5 and 7 nM (DLS) and 5 nM (ELS) and ratios [laccase]:[AuNPs] of 0-200 (pH 7.0; 10 mM phosphate buffer) were studied. Each sample was measured at least 3 times; each measurement was the average of 75 submeasurements. Hydrodynamic volumes (V_H) were obtained from number distributions. Zeta-potentials were calculated from the electrophoretic mobility measured using the Henry equation with the Smoluchowski approximation, using the software provided by the manufacturer. Fitting of the experimental data to a Langmuir-type equation was performed using OriginPro9 software.

Fluorescence spectrophotometry

Bionanoconjugates with a constant concentration of laccase (13.5 nM) and different concentrations of AuNPs in the range 0-2 nM were prepared in phosphate buffer, (10 mM, pH 7.0), by overnight incubation at 4 °C. Fluorescence emission was measured using a Cary Eclipse Spectrophotometer (Agilent Technologies, USA). The excitation wavelength was 280 nm and the emission wavelength was 330 nm. The fluorescence emission intensities were measured within the scanning wavelength ranging from 290 nm to 450 nm. Excitation and emission slits were set at 5 nm and 10 nm, respectively. Measurements were carried out at 25 °C.

Agarose Gel Electrophoresis

Agarose gels were prepared in Tris-Acetate-EDTA (TAE) buffer (0.125 X, pH 8). All AuNP-containing samples were centrifuged (15,000 x g, 4 °C, 25 min) on Centurion Scientific K3 Series centrifuge (Norleq), re-suspended in phosphate buffer (13.5 μL, 10 mM, pH 7.0) and mixed with glycerol (1.5 μL, 87%) prior to loading. Gel electrophoresis of bionanoconjugates was performed in agarose gel (0.5 %), and the mini-protean system Power source from BioRad was used with a running time of 30 min and an applied electric field of 10 V/cm. Digital pictures were taken with a Nikon COOLPIX L16 digital camera, with 7.1 Mega Pixels resolution and processed with linear contrast adjustments. Analysis of the gels was as described in the ESI (Figures S3 and S4), with electrophoretic mobility (μ) of the bionanoconjugates calculated as previously described.[25]

Essay of Laccase Enzymatic Activity

Laccase activity was determined using a modification of the procedure of Ride *et al.*[27] with syringaldazine as the substrate. Assays were carried out at 30 °C, by mixing phosphate buffer (1100 μl, 10 mM, pH 7.0) with of laccase or bionanoconjugates solutions (250 μl) in a glass cuvette. After 10 min in a pre-heated Peltier cell holder for temperature equilibration, syringaldazine solution in methanol (150 μl, 0.432 mM) was added and mixed by cell inversion. The activity of the enzyme was measured by UV-Vis spectrophotometry at 530 nm (5 min. with data collection every 5 sec.) in a spectrophotometer Varian, model Cary 50, version 3.0, with a Peltier temperature control. The procedure was the same for studies at different values of pH, but using phosphate buffer (10 mM) at the selected pH (6.5-8.5). The activity values reported are the initial rates of absorbance increase per second, obtained from the linear zone of the Abs vs *t* curve. All measurements were performed in triplicate. Molar enzyme activity was calculated by dividing the experimental activity values by the concentration of protein determined by the bicinchoninic acid method.

Conclusions

An increase in enzymatic activity mediated by nanoparticle conjugation has been reported for many enzymes and it is an important research subject in biotechnology, due to the possible impact in many industrial processes and biotechnological applications. The interaction of enzymes with AuNPs is very complex, especially because of the difficulty in separating various contributing factors. Therefore, more fundamental studies on the interaction of enzymes with AuNPs are needed. In this work, bionanoconjugates of AuNPs and laccase were prepared using a simple electrostatic conjugation method, with peptide-functionalized AuNPs. This approach allows for a biocompatible surface for the conjugation, mimicking the weak interaction forces typically present in protein-protein associations. Binding of laccase to AuNPs was characterized using different techniques, namely Dynamic Light Scattering measuring the increase in hydrodynamic volume; Electrophoretic Light Scattering and Agarose Gel Electrophoresis for assessing the change in surface charge; and fluorescence quenching of laccase by AuNPs. Analysis of data from these four different techniques, based on a simple Langmuir adsorption model (or on a simple Stern-Volmer quenching model for fluorescence data), provided binding constants in the range $6.8 < \log K < 8.9$, indicating a strong association between AuNPs and laccase. The significant difference between the binding constants determined by the four different techniques used, also suggests the need to use different techniques to further understand binding between proteins and nanoparticles.

More importantly, a considerable increase in enzyme activity of laccase in the presence of AuNPs was observed, in comparison to laccase alone in solution. This increase in activity upon interaction with AuNPs has been previously observed for oxidases, and it is possibly due to favourable conformation of the adsorbed proteins.[33] Using data from the binding studies and a simple geometric model, it was possible to evaluate the independent contributions of free laccase and bound laccase to the total enzymatic activity. Our model indicates that, within the concentration range studied, 88%-71% of laccase is adsorbed to AuNPs, and that this corresponds to 99%-94% of the enzymatic activity measured in solution. Furthermore, it was found that bound laccase (in bionanoconjugates) was *ca.* 9 times more active than free laccase. Finally, comparison of the pH profile of activity for bionanoconjugates and free laccase showed that bionanoconjugates are always more active in the pH range studied (pH = 6.5-8.5), with the highest increases in activity observed at lower pH values. Lowering the workable pH range for this laccase has important implications at the industrial level and will allow the utilization of this plant-type laccase at close to neutral pH values, filling a pH gap to fungal laccases, that are more active at more acidic pH values. The results presented here are useful not only for a better understanding of enzyme-AuNP interactions, but also the laccase-based bionanoconjugates can be used as building blocks for more complex bionanotechnology systems, namely in electrodes and biocathodes.[18, 38-39]

Conflicts of interest

There are no conflicts of interest to declare.

Acknowledgements

Marta Giza is acknowledged for expert utilization of the UCSF Chimera package. Chimera is developed by the Resource for Biocomputing, Visualization, and Informatics at the University of California, San Francisco (supported by NIGMS P41-GM103311). This work was supported by a) Unidade de Ciências Biomoleculares Aplicadas-UCIBIO which is financed by Portuguese national funds from FCT/MEC (UID/Multi/04378/2013) and co-financed by the ERDF under the PT2020 Partnership Agreement (POCI-01-0145-FEDER-007728); and NOVA LINCS UID/CEC/04516/2013; and b) European Union (FEDER funds through COMPETE) and National Funds (FCT, Fundação para a Ciência e Tecnologia), under the Partnership Agreement PT2020 through project UID/QUI/50006/2013-POCI/01/0145/FEDER/007265 (LAQV/REQUIMTE), Programa Operacional Regional do Norte (ON.2 - O Novo Norte), under the Quadro de Referência Estratégico Nacional (QREN) and funded by Fundo Europeu de Desenvolvimento Regional NORTE-01-0145-FEDER-000011. PQ, SS and IG acknowledge their post-doctoral fellowships (SFRH/BPD/84018/2012, SFRH/BPD/103788/2014 and SFRH/BPD/63850/2009, respectively), and MPA acknowledges his doctoral fellowship (SFRH/BD/95983/2013); all fellowships are financed by Fundação para a Ciência e a Tecnologia, Portugal.

Notes and references

1. M. Peixoto de Almeida, E. Pereira, P. Baptista, I. Gomes, S. Figueiredo, L. Soares and R. Franco, Chapter 13 - gold nanoparticles as (bio)chemical sensors. In *Comprehensive analytical chemistry*, Miguel, V; IL-L Ángela, Eds. Elsevier: 2014; Vol. Volume 66, pp 529-567.

2. P. V. Baptista, G. Doria, P. Quaresma, M. Cavadas, C. S. Neves, I. Gomes, P. Eaton, E. Pereira and R. Franco, Chapter 11 - nanoparticles in molecular diagnostics. In *Progress in molecular biology and translational science*, Antonio, V, Ed. Academic Press: 2011; Vol. Volume 104, pp 427-488.

3. J. Cortez, E. Vorobieva, D. Gralheira, I. Osório, L. Soares, N. Vale, E. Pereira, P. Gomes and R. Franco, *Journal of Nanoparticle Research,* 2011**, 13**, 1101-1113.

4. B. Pelaz, S. Jaber, D. J. de Aberasturi, V. Wulf, T. Aida, J. M. de la Fuente, J. Feldmann, H. E. Gaub, L. Josephson, C. R. Kagan, N. A. Kotov, L. M. Liz-Marzán, H. Mattoussi, P. Mulvaney, C. B. Murray, A. L. Rogach, P. S. Weiss, I. Willner and W. J. Parak, *ACS Nano,* 2012**,** **6**, 8468-8483.

5. G.-Y. Kim, J. Shim, M.-S. Kang and S.-H. Moon, *Journal of Hazardous Materials,* 2008**,** **156**, 141-147.

6. D. W. Kimmel, G. LeBlanc, M. E. Meschievitz and D. E. Cliffel, *Analytical Chemistry,* 2011**,** **84**, 685-707.

7. J. M. Pingarron, P. Yanez-Sedeno and A. Gonzalez-Cortes, *Electrochimica Acta,* 2008**,** **53**, 5848-5866.

8. K. M. Harkness, B. N. Turner, A. C. Agrawal, Y. Zhang, J. A. McLean and D. E. Cliffel, *Nanoscale,* 2012**,** **4**, 3843-3851.

9. J. C. Love, L. A. Estroff, J. K. Kriebel, R. G. Nuzzo and G. M. Whitesides, *Chemical Reviews,* 2005**,** **105**, 1103-69.

10. R. Levy, Z. Wang, L. Duchesne, R. C. Doty, A. I. Cooper, M. Brust and D. G. Fernig, *Chembiochem,* 2006**,** **7**, 592-4.

11. M. De, C.-C. You, S. Srivastava and V. M. Rotello, *Journal of the American Chemical Society,* 2007**,** **129**, 10747-10753.

12. M. Fernandez-Fernandez, M. Angeles Sanroman and D. Moldes, *Biotechnology Advances,* 2013**,** **31**, 1808-1825.

13. V. Madhavi and S. S. Lele, *Laccase: Properties and applications*. 2009; Vol. 4.

14. S. Rodríguez Couto and J. L. Toca Herrera, *Biotechnology Advances,* 2006**,** **24**, 500-513.

15. Y. Y. Wan, Y. M. Du, F. X. Yang, Y. Xu, R. Z. Chen and J. F. Kennedy, *International Journal of Biological Macromolecules,* 2006**,** **38**, 232-240.

16. M. Pita, D. M. Mate, D. Gonzalez-Perez, S. Shleev, V. M. Fernandez, M. Alcalde and A. L. De Lacey, *J Am Chem Soc,* 2014**,** **136**, 5892-5.

17. O. Schaetzle, F. Barriere and U. Schroeder, *Energy & Environmental Science,* 2009**,** **2**, 96-99.

18. C. Gutierrez-Sanchez, M. Pita, C. Vaz-Dominguez, S. Shleev and A. L. De Lacey, *Journal of the American Chemical Society,* 2012**,** **134**, 17212-17220.

19. J. Kimling, M. Maier, B. Okenve, V. Kotaidis, H. Ballot and A. Plech, *Journal of Physical Chemistry B,* 2006**, 110**, 15700-15707.

20. I. Gomes, M. Feio, N. Santos, P. Eaton, A. Serro, B. Saramago, E. Pereira and R. Franco, *Journal of Nanoparticle Research,* 2012**, 14**.

21. H. P. Erickson, *Biological Procedures Online,* 2009**, 11**, 32-51.

22. R. Franco and E. Pereira, Gold nanoparticles and proteins, interactions. In *Encyclopedia of metalloproteins.*, Kretsinger, RHU, V.N.; Permyakov, E.A. , Ed. Springer Science+Business Media New York, 2013; pp 908-915.

23. L. Piantanida, D. Naumenko and M. Lazzarino, *Rsc Advances,* 2014**, 4**, 15281-15287.

24. U. Pyell, *Electrophoresiss,* 2010**, 31**, 814-831.

25. D. Zanchet, C. M. Micheel, W. J. Parak, D. Gerion, S. C. Williams and A. P. Alivisatos, *The Journal of Physical Chemistry B,* 2002**, 106**, 11758-11763.

26. S. K. Vaishanav, K. Chandraker, J. Korram, R. Nagwanshi, K. K. Ghosh and M. L. Satnami, *Journal of Molecular Structure,* 2016**, 1117**, 300-310.

27. J. P. Ride, *Physiological Plant Pathology,* 1980**, 16**, 187-196.

28. D. Kottwitz, *Acta Crystallographica Section A,* 1991**, 47**, 158-165.

29. E. F. Pettersen, T. D. Goddard, C. C. Huang, G. S. Couch, D. M. Greenblatt, E. C. Meng and T. E. Ferrin, *Journal of Computational Chemistry,* 2004**, 25**, 1605-1612.

30. J. Deka, A. Paul and A. Chattopadhyay, *Rsc Advances,* 2012**, 2**, 4736-4745.

31. D. Pankratov, R. Sundberg, D. B. Suyatin, J. Sotres, A. Barrantes, T. Ruzgas, I. Maximov, L. Montelius and S. Shleev, *Rsc Advances,* 2014**, 4**, 38164-38168.

32. C.-S. Wu, C.-C. Lee, C.-T. Wu, Y.-S. Yang and F.-H. Ko, *Chemical Communications,* 2011**, 47**, 7446-7448.

33. D. Zaramella, P. Scrimin and L. J. Prins, *Journal of the American Chemical Society,* 2012**, 134**, 8396-8399.

34. B. J. Johnson, W. Russ Algar, A. P. Malanoski, M. G. Ancona and I. L. Medintz, *Nano Today,* 2014**, 9**, 102-131.

35. X. J. Han, W. L. Cheng, Z. L. Zhang, S. J. Dong and E. K. Wang, *Biochimica Et Biophysica Acta-Bioenergetics,* 2002**, 1556**, 273-277.

36. W. Haiss, N. T. K. Thanh, J. Aveyard and D. G. Fernig, *Analytical Chemistry,* 2007**, 79**, 4215-4221.

37. R. Lu and T. Miyakoshi, *Enzyme Research,* 2012**, 2012**.

38. M. Govindhan, B.-R. Adhikari and A. Chen, *Rsc Advances,* 2014**, 4**, 63741-63760.

39. M. Pita, C. Gutierrez-Sanchez, D. Olea, M. Velez, C. Garcia-Diego, S. Shleev, V. M. Fernandez and A. L. De Lacey, *Journal of Physical Chemistry C,* 2011**, 115**, 13420-13428.

2.3. Article's supporting information

The following pages are the supporting information for the article included in the previous section, as published online and available on:

http://www.rsc.org/suppdata/c8/cp/c8cp03116a/c8cp03116a1.pdf

1. Transmission electron microscopy and size histogram of the as-synthesized AuNPs

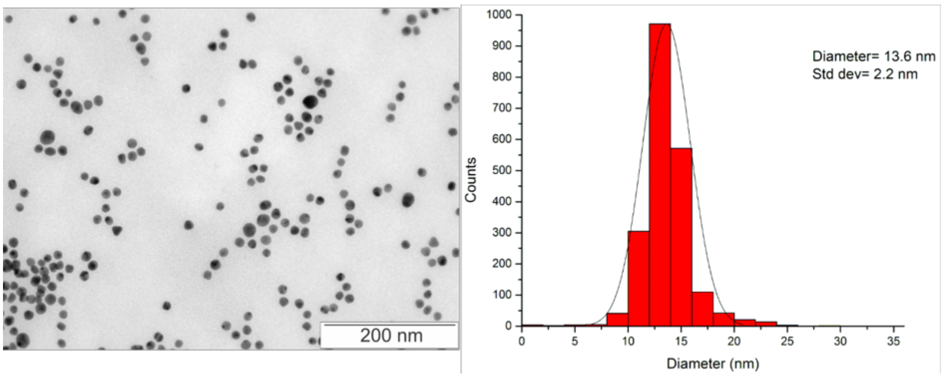

Figure S1. TEM micrograph of a representative area of the TEM grid and resulting size histogram showing an average diameter of 13.6 nm with a standard deviation of 2.2 nm.

2. XPS of AuNP-CALNN

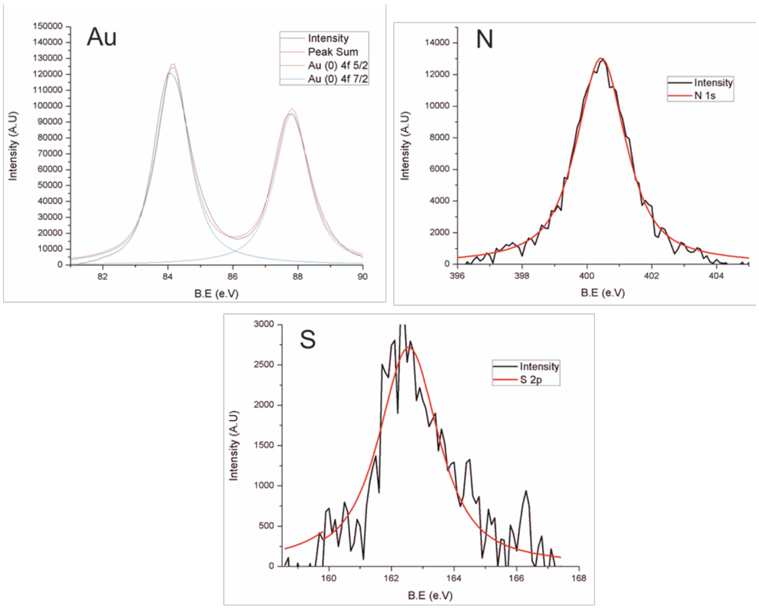

Figure S2. XPS analysis of AuNP-CALNN, showing the areas corresponding to Au, N and S.

3. Dynamic Light Scattering (DLS) measurements for BNC at different AuNP concentrations

Binding constants of laccase to CALNN-functionalized AuNPs (obtained by DLS) are proportional to AuNP concentration **(**Figure S3**)**, whereas the volumes of the fully packed bionanoconjugates are mostly independent on AuNP concentration (Table 1).

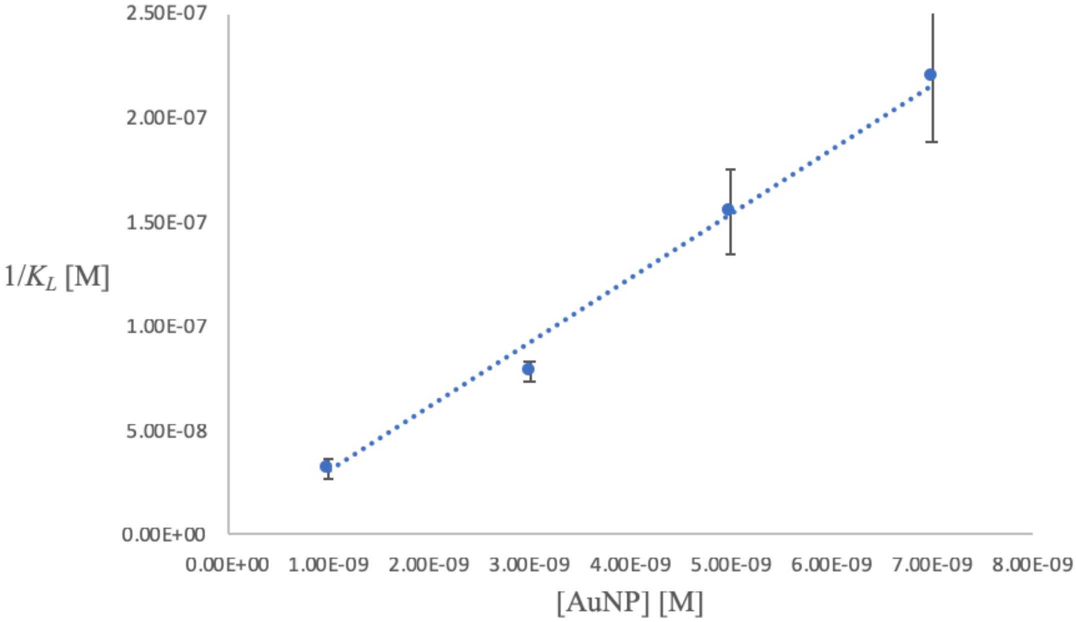

Figure S3. Variation of 1/K_L as a function of the concentration of AuNPs. Bars are the standard error calculated from the fitting of DLS data. Linear fitting of these data is 1/K_L = 30.7 [AuNP], with R^2=0.990.

4. Analysis of Agarose Gel Electrophoresis data

The migration distances for each concentration ratio were computed from the digital image of the electrophoresis gel by fitting Gaussian curves to the image intensity profiles averaged for each lane. This allowed a more reliable quantification of band migration, since the most relevant bands were quite broad.

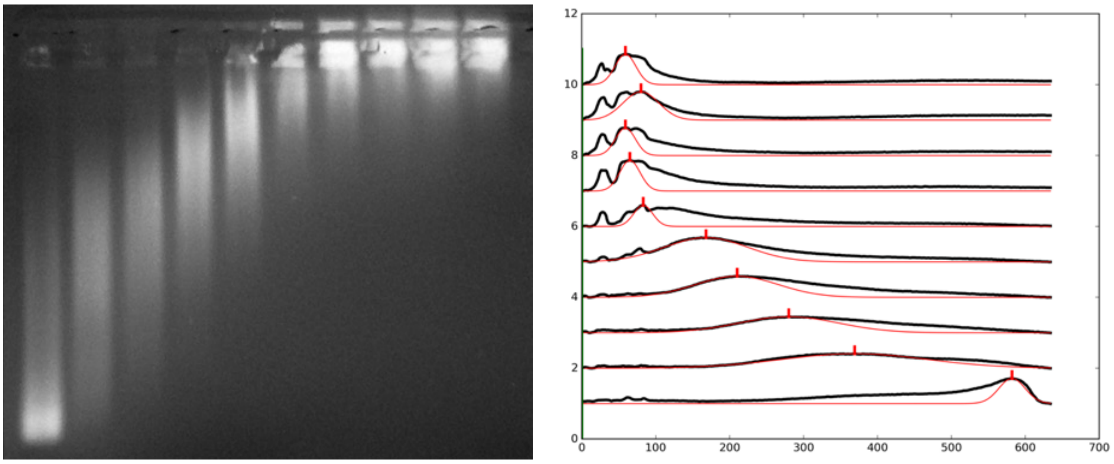

Figure S4. Processed digital image of the gel and migration quantification. The black lines show the average brightness intensity measured along each lane. The red lines show the fitted Gaussian curves and the peak positions for each lane, with lane 1 corresponding to the leftmost lane on the gel. The horizontal scale is in image pixels.

The Langmuir equation was fit considering that the occupation factor is:

$$\Theta = \frac{\mu_{free} - \mu}{\mu_{free} - \mu_{min}} \qquad \text{(S1)}$$

where μ is the mobility of each peak; μ_{free} is the maximum mobility, obtained directly from the position of the peak at ratio 0; and μ_{min} is the minimum mobility at full occupation, obtained from the fitting of the curve. The reason for fitting μ_{min} instead of measuring it directly is that a direct measure would make this value too sensitive to the exact placement of the last bands. The curve fitted is the Langmuir isotherm:

$$\Theta = \frac{K_L\,[LAC]}{1 + K_L\,[LAC]} \qquad \text{(S2)}$$

where K_L is the binding constant and [LAC] the concentration of laccase. Fitting the curve to both μ_{min} and K_L gave a K_L of (0.6 ± 0.1) x 10^8 M^{-1}, with a 95% confidence interval determined by residual bootstrapping using 500 replicas.

This analysis was done using eReuss, a gel analysis application currently under development and freely available at https://github.com/lkrippahl/eReuss

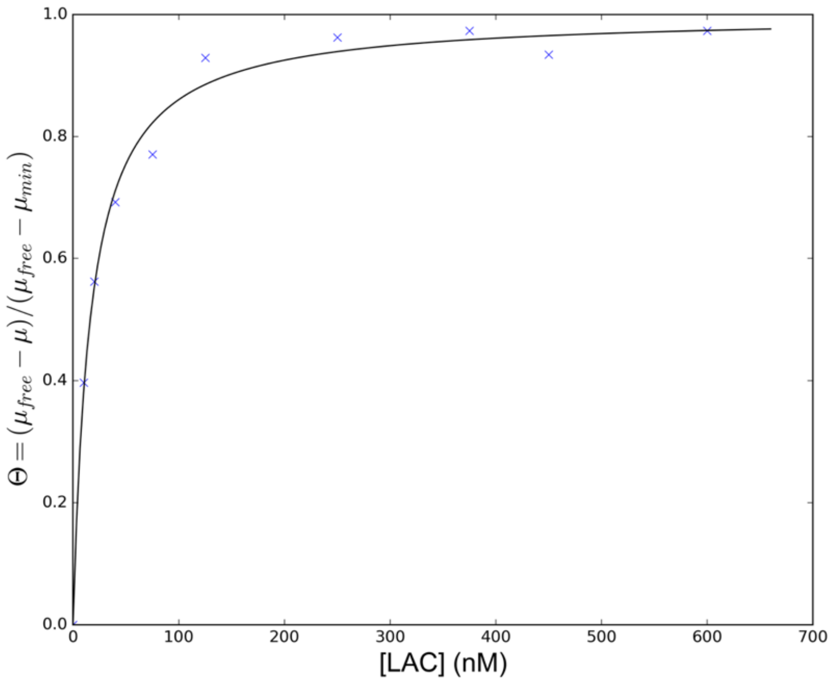

Figure S5. Langmuir isotherm plot obtained by fitting μ_{min} and K_{eq} to the band migration values at different concentrations of laccase.

5. Fluorescence quenching

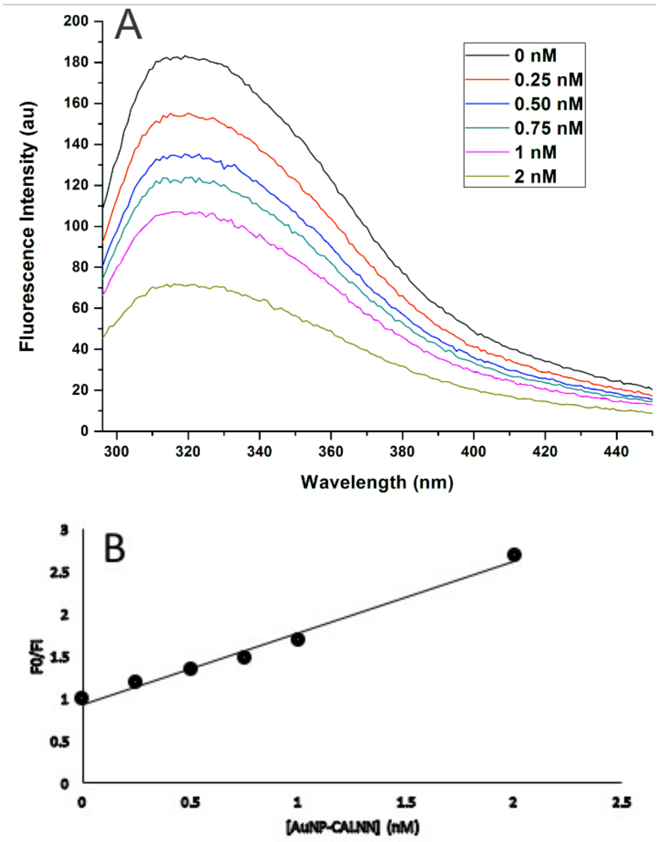

Figure S6. Fluorescence emission spectra for laccase fluorescence quenching (excitation at 280 nm) by increasing concentrations of AuNPs (A); and respective Stern-Volmer plot (emission at 330 nm) (B).

6. Calculation of the contributions to the enzyme activity of laccase in solution and adsorbed laccase in the bionanoconjugates

In order to evaluate the molar activity of free laccase and adsorbed laccase, it is necessary to evaluate the concentration of free laccase in the BNC solution. We started by using a simple geometrical model of packing of spheres on a sphere (D. Kottwitz, *Acta Crystallographica Section A* **1991,** *47* (3), 158). Using the hydrodynamic diameter of the AuNPs and the diameter of a globular protein with the laccase molecular weigth, a maximum of 30 protein molecules per particle was calculated (see main text). We then calculated the contribution of each laccase adsorbed to the increase in the hydrodynamic volume of bionanoconjugates as:

$$V_{LAC} = \frac{\Delta V_{H,max}}{30} \qquad \text{(S3)}$$

where $\Delta V_{H,max}$ is the maximum increase in hydrodynamic volume obtained by fitting DLS data to a Langmuir equation (Table 1, main text). The average number of laccase bound per AuNP (N) was then calculated, for each bionanoconjugate studied, using the equation:

$$V_{H,BNC} = V_{H,AuNPs} + N \times V_{LAC} \qquad \text{(S4)}$$

where is the hydrodynamic volume of the bionanoconjugates calculated from fitting of the experimental DLS data to **equation 1** (main text); $V_{H,AuNPs}$ is the hydrodynamic volume of the parent AuNPs alone.

The amount of laccase adsorbed was then calculated by:

$$n_{LAC,ads} = N \times [AuNP] \times V_{sol} \qquad \text{(S5)}$$

where [AuNP] is the concentration of AuNPs and V_{sol} is the volume of the solution.

The amount of free laccase was calculated by:

$$n_{LAC,free} = n_{LAC,total} - n_{LAC,ads} \qquad \text{(S6)}$$

where $n_{LAC,total}$ is the total amount of laccase in solution.

The contribution of free laccase to the enzymatic activity was then calculated by:

$$act_{LAC,free} = act_{LAC,control} \times \frac{n_{LAC,free}}{n_{LAC,total}} \qquad \text{(S7)}$$

where $act_{LAC,control}$ is the enzymatic activity in the control with laccase only.

The enzymatic activity of adsorbed laccase was calculated as follows:

$$act_{LAC,ads} = act_{BNC} - act_{LAC,free} \quad \text{(S8)}$$

where act_{BNC} is the experimental enzymatic activity of solutions containing bionanoconjugates and free laccase.

7. Enzymatic assay

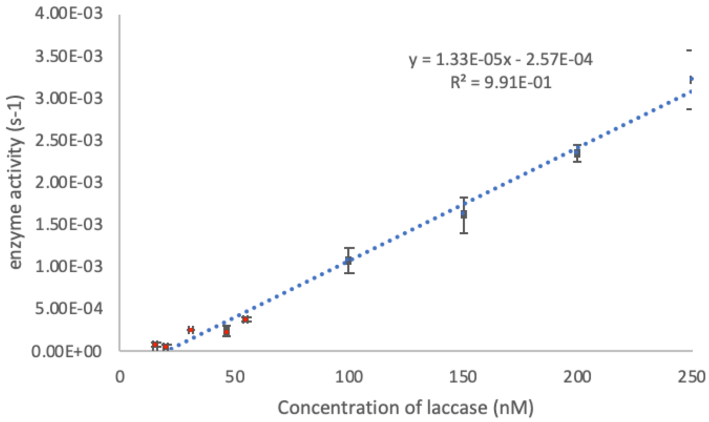

Figure S7. Enzymatic activity of laccase solutions in the concentration range 15-250 nM. The inset contains the results of the linear correlation. Data in red corresponds to the experimental points in Figure 4.

To evaluate the colloidal stability of the nanoparticles during the enzymatic assay, we have taken UV/vis spectra (Figure S8) and determined the hydrodynamic diameter of the bionanoconjugates before and after the enzymatic essay. The hydrodynamic diameter before the assay was (21.6 ± 6.2) nm and after the assay was (19.8 ± 6.0) nm, showing no evidences for significant aggregation. UV/vis spectra shown in Figure S8 show an increase of the absorbance at 530 nm, due to the formation of the oxidation product of syringaldazine, but no major increase of the bandwidth, nor increase of light scattering at lower wavelengths, the two major changes expected in case of aggregation of the gold nanoparticles.

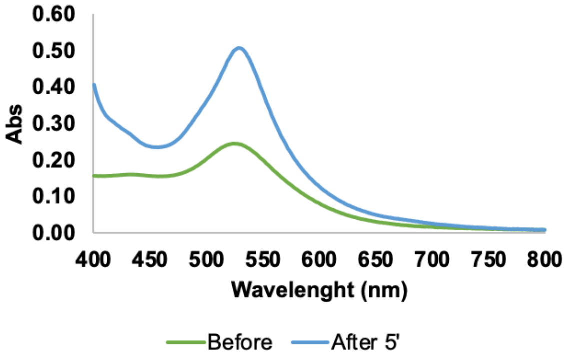

Figure S8. UV/vis spectra of a solution containing bionanoconjugates in the experimental conditions for the enzymatic assay. Curve in green is the spectrum before addition of the substrate syringaldazine, and the curve in blue is after 5 minutes of reaction. The increase in absorbance at 530 nm arises from the oxidation product of syringaldazine and it was used to follow enzymatic kinetics.

2.4. Final remarks

The conclusions obtained from this work can be good clues from what can happen in other nanobioconjugates, comprised by other elements, however case-by-case studies are desirable. It was demonstrated that a variety of techniques can be used for these studies and the combination of the data obtained from all of them can give solid information about the nanobioconjugation process and nanobioconjugates' stability.

It is known that the protein corona formed on gold nanoparticles and their physical properties depends on the size and on the shape of the nanoparticles, mainly because the local curvatures and crystalline facets on the nanoparticles' surface. However, most of the studies are carried out with spherical nanoparticles which is the simpler shape model.[18-19] Other shapes deserve to be further studied since they present different curvatures and crystalline facets than gold nanospheres.

Studies with AuNPs:protein ratios <1, like using small nanoparticles that will decorate the proteins, are also interesting to see which domains of a protein are more prone to work as nanobioconjugation interfaces.[20] This kind of studies are quite important for the use of AuNPs in biologic media, namely serum.[19]

2.5. References

1. Nomenclature Committee of the International Union of Biochemistry and Molecular Biology. *Enzyme Nomenclature 1992*. Academic Press: San Diego, California, 1992.

2. Nomenclature Committee of the International Union of Biochemistry and Molecular Biology. Enzyme Nomenclature. Recommendations 1992. Supplement: Corrections and Additions. *European Journal of Biochemistry* **1994,** *223* (1), 1-5.

3. Nomenclature Committee of the International Union of Biochemistry and Molecular Biology. Enzyme Nomenclature. Recommendations 1992. Supplement 2: Corrections and Additions (1994). *European Journal of Biochemistry* **1995,** *232* (1), 1-1.

4. Nomenclature Committee of the International Union of Biochemistry and Molecular Biology. Enzyme Nomenclature. Recommendations 1992. Supplement 3: Corrections and Additions (1995). *European Journal of Biochemistry* **1996,** *237* (1), 1-5.

5. Nomenclature Committee of the International Union of Biochemistry and Molecular Biology. Enzyme Nomenclature. Recommendations 1992. Supplement 4: Corrections and Additions (1997). *European Journal of Biochemistry* **1997,** *250* (1), 1-6.

6. Nomenclature Committee of the International Union of Biochemistry and Molecular Biology. Enzyme Nomenclature. Recommendations 1992. Supplement 5: Corrections and Additions (1999). *European Journal of Biochemistry* **1999,** *264* (2), 610-650.

7. AI Canas, S Camarero. Laccases and their natural mediators: biotechnological tools for sustainable eco-friendly processes. *Biotechnology Advances* **2010,** *28* (6), 694-705.

8. C Sanchez. Lignocellulosic residues: biodegradation and bioconversion by fungi. *Biotechnology Advances* **2009,** *27* (2), 185-94.

9. S Riva. Laccases: blue enzymes for green chemistry. *Trends in Biotechnology* **2006,** *24* (5), 219-26.

10. RL Singh, PK Singh, RP Singh. Enzymatic decolorization and degradation of azo dyes – A review. *International Biodeterioration & Biodegradation* **2015,** *104*, 21-31.

11. C Ji, J Hou, K Wang, YH Ng, V Chen. Single-Enzyme Biofuel Cells. *Angewandte Chemie International Edition* **2017,** *56* (33), 9762-9766.

12. MD Cannatelli, AJ Ragauskas. Two Decades of Laccases: Advancing Sustainability in the Chemical Industry. *The Chemical Record* **2017,** *17* (1), 122-140.

13. M Fernandez-Fernandez, MA Sanroman, D Moldes. Recent developments and applications of immobilized laccase. *Biotechnol Adv* **2013,** *31* (8), 1808-25.

14. JB Costa, MJ Lima, MJ Sampaio, MC Neves, JL Faria, S Morales-Torres, APM Tavares, CG Silva. Enhanced biocatalytic sustainability of laccase by immobilization on functionalized carbon nanotubes/polysulfone membranes. *Chemical Engineering Journal* **2019,** *355*, 974-985.

15. P Kaushik, A Malik. Fungal dye decolourization: recent advances and future potential. *Environment International* **2009,** *35* (1), 127-41.

16. J Cortez, E Vorobieva, D Gralheira, I Osório, L Soares, N Vale, E Pereira, P Gomes, R Franco. Bionanoconjugates of tyrosinase and peptide-derivatised gold nanoparticles for biosensing of phenolic compounds. *Journal of Nanoparticle Research* **2010,** *13* (3), 1101-1113.

17. SR Saptarshi, A Duschl, AL Lopata. Interaction of nanoparticles with proteins: relation to bio-reactivity of the nanoparticle. *Journal of Nanobiotechnology* **2013,** *11*, 26.

18. R Garcia-Alvarez, M Hadjidemetriou, A Sanchez-Iglesias, LM Liz-Marzan, K Kostarelos. In vivo formation of protein corona on gold nanoparticles. The effect of their size and shape. *Nanoscale* **2018,** *10* (3), 1256-1264.

19. F Charbgoo, M Nejabat, K Abnous, F Soltani, SM Taghdisi, M Alibolandi, WT Shier, TWJ Steele, M Ramezani. Gold nanoparticle should understand protein corona for being a clinical nanomaterial. *Journal of Controlled Release* **2018,** *272*, 39-53.

20. AL Lira, RS Ferreira, RJS Torquato, H Zhao, MLV Oliva, SA Hassan, P Schuck, AA Sousa. Binding kinetics of ultrasmall gold nanoparticles with proteins. *Nanoscale* **2018,** *10* (7), 3235-3244.

Immobilized Nanobioconjugates of Gold Nanoparticles and Laccase

3

3.1. Introduction

The previous chapter addresses the interaction between gold nanoparticles and *Toxicodendron vernicifluum* laccase (*Tov*L), that showed a good ability to electrostatically bind to 15 nm diameter gold nanospheres. In this chapter, the focus goes to *Trametes versicolor* laccase (*Trv*L).

Giving the successful formation of nanobioconjugates AuNP-*Tov*L, the work moved towards the assessment of other laccases, especially those with higher activities, here represented by *Trv*L. The main objectives of the work described herein are to understand if *Trv*L enzymatic performance could equally benefit from its conjugation with gold nanoparticles, if nanobioconjugation between gold nanoparticles and *Trv*L occurs straightforwardly in solution like the nanobioconjugates (NBCs) reported in the previous chapter and to find a good support for these NBCs.

3.1.1. Laccase from *Trametes versicolor*

Trametes versicolor (*Trv*) is a white-rot fungus[1] and, as many other fungi, is capable of synthesising laccase, a type of enzyme introduced in chapter 1. *Trametes versicolor* laccase proved to be very active in the decomposition of phenolic compounds, in homogeneous biocatalysis, either by using its total biomass[1] or by using the purified enzyme. Its activity was also described in heterogeneous biocatalysis, *i.e.* with *TrvL* immobilized in different types of supports[2-5], as explored in the following section.

Like other laccases, *Trv*L is used for a long time now to degrade dyes in liquid media[6], but several more recent applications have been described such as degradation of endocrine-disrupting compounds[5, 7], biotransformation of lignocellulosic materials into value-added products[8] or as catalysts for macromolecular synthesis[9]. It is then of the major importance to continue optimizing the performance of this enzyme.

3.1.2. Immobilization of *Trametes versicolor* laccase

Enzyme immobilization brings several advantages, like (i) the possibility of recovery and reuse of this biomolecule by allowing an easy separation from the media, (ii) the prospect of implementing biotechnology to flow processes, and (iii) flexibility in the assembly of biosensors engineered for different purposes.[3]

There are several reports of immobilization of this enzyme, namely onto poly(glycidyl methacrylate)[10] and chitosan[11] microspheres or silica-coated magnetic nanoparticles[12], in a functionalization/decoration approach, in agar-agar, polyacrylamide and gelatin[13], in an entrapment approach, or simply by drop-casting in crosslinkable itaconic copolymers[14]. There is also a report of *Trv*L immobilization on other species, *Hippospongia communis*, sponges.[15]

It was demonstrated that laccase enzymes keep their stability and activity in larger ranges of pH and temperature upon immobilization[16-17], so this process can be helpful in the optimization of the several applications mentioned in the previous section and deserved to be explored in the work described in this chapter.

3.1.3. Membrane-like support materials

Between the several supports, the reports of the use of membranes for *Trv*L immobilization are very scarce. This enzyme was immobilized, for example, on a multi-channel ceramic membrane[5].

Guided by the evolution of this work, namely the results obtained from nanobioconjugation experiments in suspension, and the known advantages of immobilising enzymes, we decided to include a third main component in the system. Beside the (functionalized) gold nanoparticles and the *Trametes versicolor* laccase, solid supports were introduced as facilitators of the initially planned nanobioconjugation between the nanoparticles and the enzyme molecules.

There is a variety of surface chemistries that can be found in membrane or membrane-like supports. It is possible to find differences in hydrophobicity, charge and porosity in these materials. For this work, we used cellulose-based materials and also other polymeric materials with carbon and fluorine in its composition. Five common materials found in membranes – hydrophilic mixed cellulose esters (HMCE), polytetrafluoroethylene (PTFE), hydrophilic polyvinylidene fluoride (HPVDF), regenerated cellulose (RC), nitrocellulose (NC) – and two more simple options – filter paper (FP) and office paper (OP), provide the range of chemical structures shown in figure 3.1.

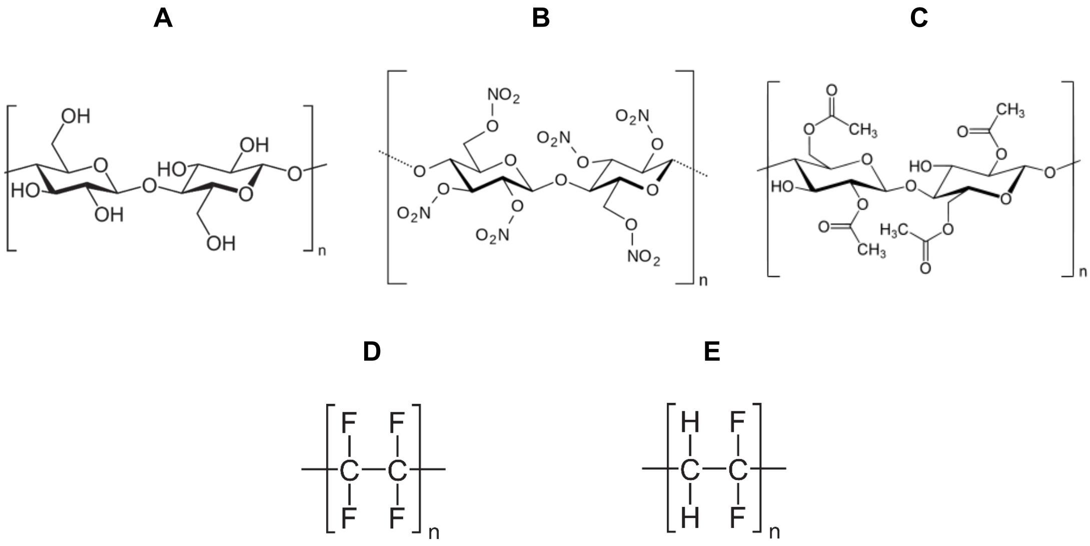

Figure 3.1 – Chemical structure of cellulose (A), nitrocellulose (B), cellulose acetate (C), polytetrafluoroethylene (D) and polyvinylidene fluoride (E).

The structure and porosity of these materials derive from their polymeric nature, both for those based on cellulose – 1,4-β-glucose dimers (cellobiose) represented in figure 3.1 A, B and C – and for those based on a fluorine-substituted carbon chain – represented in figure 3.1 D and E.

Regenerated cellulose (RC), filter paper (FP) and office paper (OP) are supports with the chemical structure shown in figure 3.1 A, *i.e.*, non-substituted cellulose – $(C_6H_{10}O_5)_n$. The differences between these materials are mainly density, presence of non-cellulosic compounds (like calcium carbonate in office paper[18-19]), and also cost.

Nitrocellulose (NC) – $(C_6H_7(NO_2)_3O_5)_n$, for completely nitrated cellulose, as shown in figure 3.1 B – is a derivatization of cellulose, where the hydrogen atom in the hydroxide groups (–OH) is replaced by a nitro (NO_2) group. These groups impart charge to cellulose and are considered electrophiles due to the nitrogen atom electron deficiency.

The last cellulose-based material is the membrane comprised by hydrophilic mixed cellulose esters (HMCE), *i.e.* it comprises both nitrocellulose (cellulose nitrate), with the chemical structure represented in figure 3.1 B, and cellulose acetate – $(C_6H_8(C_2H_3O)_2O_5)_n$ –, with the chemical structure shown in figure 3.1 C.

Some of the hydrophobic materials, like the polyvinylidene fluoride (PVDF), can undergo processes of hydrophilization[20], since the primary objective of this material is to be used as a membrane permeable to water, therefore the hydrophilic polyvinylidene fluoride (HPVDF) designation. However, the core PVDF material is still the same. It is a material similar to polytetrafluoroethylene (PTFE), but PVDF has every other carbon with one fluoro-substituent, in opposition to PTFE where all carbons have fluoro-substituents.

All of these materials were explored in this work as models of mechanic stability and affinity for gold nanoparticles and *Trametes versicolor* laccase.

3.1.4. Immobilization of gold nanoparticles

Most of the reports of gold nanoparticles immobilization are related to electrochemistry, namely for the enhancement of electrodes[21-27]. Some of the electrochemical applications of gold nanoparticles on electrodes, also involve enzymes, namely laccase from *Trametes versicolor*.[28-32] However, the increase of surface area and the direct electron transfer phenomenon are the main proposed explanations for the increase in electrochemical performance.

Regarding the nanoparticles used for the work described in this chapter, the focus goes here to this metal – gold – but factors like size and shape were evaluated. For this purpose, spherical gold nanoparticles and star-shaped gold nanoparticles were used.

Given the several fields that laccases, namely *Trametes versicolor* laccase, can be highly useful, the advantages of immobilizing these biomolecules and the enhancements in enzymatic activity assured by nanobioconjugation with gold nanoparticles, the preparation of bioactive disks that can merge all of these points was performed. There are no reports in the literature of this type of supported nanobioconjugates.

3.2. Methods

This section enlists the main equipment, the reagents and the experimental procedures. All the reagents were used as purchased, with no further steps of purification.

Centrifugations were done in a Sigma 30K centrifuge. Ultraviolet-visible spectroscopy (UV-Vis) was performed using a Varian Cary 50 Bio spectrophotometer equipped with a Varian Cary Dual Cell Peltier module with circulating water for temperature control.

Three different light scattering-based methods were used. Dynamic light scattering (DLS) and zeta potential (ZP) measurements were made in a Malvern Zetasizer Nano ZS equipment, with a 633 nm laser – results are an average of three measurements for the same sample, performed at 25 °C, with light detection at 173° (DLS) and at 17° using the backscatter mode (ZP). Nanoparticle tracking analysis (NTA) was done using a Malvern Nanosight NS300 equipped with a 642 nm (red) laser module.

Dynamic light scattering (DLS) technique is based on the Brownian motion of the particles in solution. This random motion of the particles is detected trough the light scattered by them. When the laser hits the sample, every particle scatters the light and, due to particles random movement, the scattered light path between the particle and the detector varies with time. With this information, it possible to determine the translational diffusion coefficient of the particles. For spherical particles, the hydrodynamic radius rh can be obtained from this coefficient (*D*) using the Stokes−Einstein equation:

$$D = \frac{k \cdot T}{6\pi \cdot \eta \cdot r_h} \qquad \text{(Eq. 3.1)}$$

where *k* is the Boltzmann's constant, η is the solvent viscosity, and *T* is the absolute temperature. If the particle is not spherical, r_h is often taken as the apparent hydrodynamic radius.[33]

This technique is the golden standard for monodisperse nanoparticle samples. For polydisperse samples and/or samples containing interferences like aggregates or microscopic contaminants, the calculated Z-average values are often unreliable. The high difference between water and gold or silver refractive indexes led DLS to have a good sensibility for these (and other) metal nanoparticles. The opposite happens to macromolecules (e.g. proteins), with their refractive indexes closer the one from water. They can be detected by DLS, but not in the presence of materials capable of high levels of light scattering, when DLS can become “blind” to these macromolecules, so they do not interfere with the measurements.

Electrophoretic light scattering (ELS) is a measurement often performed in an equipment that is capable of DLS and ELS measurements. The detection of nanoparticles’ movements is also based on the light scattered by them. In ELS, the diffusion coefficient (D) results from the movement of particles submitted to an electric potential difference, and not just from Brownian motion. This movement depends then on particle charge. The ELS equipment calculates directly the electrophoretic mobility (μ) of the particles. Only then a conversion from electrophoretic mobility (μ) to zeta potential (ζ) is done using the Henry’s equation below

$$\mu = \frac{2 \cdot \varepsilon \cdot \zeta}{3 \cdot \eta} \cdot f(kR) \qquad \text{(Eq. 3.2)}$$

Since zeta potential is related to electrophoretic mobility trough the dielectric constant (ε) and viscosity (η) from the solvent, the zeta potential is the same while electrophoretic mobility changes when media changes. *f(kR)* is Henry’s function and has values of 1.5 for aqueous media and 1 for non-aqueous systems. These values come from Smoluchowski and Huckel approximations, respectively.[34]

Besides the charge signal (positive or negative), zeta potential values can be translated to colloidal stability. If the zeta potential is 0 or close to 0, that colloidal dispersion is not stable, since particle will tend to aggregate due to the lack of charge on particles, capable of keep electrostatic repulsion and thus their individuality.

Nanoparticle tracking analysis (NTA) is the most recent technique between the all other light scattering-bases techniques mentioned in this section.[35] This method has some similarities with DLS. Both use the Stokes–Einstein equation (eq. 1.3), since they both register Brownian motion, determining then the diffusion coefficient and consequently the hydrodynamic radius. The nanoparticle tracking is done on a video that records the movements of the light scattered by the nanoparticles.

The three main advantages of this technique compared to DLS are the possibility of determining sample concentration (especially useful for anisotropic nanoparticles), the better capacity for distinguish populations with a very approximate size (higher resolution), and the small amount of sample needed for analysis (samples at picomolar concentrations).[36] One disadvantage of NTA is the narrower range of sizes that can be determined. Only a very clean sample (no aggregates) can be measured under 40 nm. The presence of two or more populations of particles with a big difference in size will difficult the video capture parameters. The amount of light scattered increases exponentially with size, so for capturing light scattered by big nanoparticles, the camera aperture has to be less open, which can originate the loss of the small amounts of light scattered by smaller nanoparticles.

Regarding electron microscopy, transmission electron microscopy (TEM) and scanning electron microscopy (SEM), used as external services, were performed using a Hitachi H8100 for TEM and a FEI Quanta 400 FEG environmental scanning electron microscope (ESEM), using a backscattered electrons detector (BSED). TEM was performed by Dr. Pedro Quaresma at *Instituto Superior Técnico*. SEM was performed by Dr. Peter Eaton at *Centro de Materiais da Universidade do Porto*.

3.2.1. Synthesis of gold nanoparticles

Gold nanoparticles with different shapes and sizes were synthesized. The following commercial reagents were used: gold (III) chloride solution 99.99% (Aldrich), trisodium citrate dihydrate 99.0% (Merck), silver nitrate 99.9999% (Aldrich) and ascorbic acid 99.9998% (Fluka).

All glassware was previously washed with *aqua regia* and rinsed abundantly with deionized water, followed by ultrapure water (18.2 MΩ·cm at 25 °C). All the solutions were prepared with ultrapure water.

3.2.1.1. Synthesis of 15 nm gold nanospheres (AuNPs15)

Spherical gold nanoparticles with 15 nm of average diameter were synthesised as described in chapter 2, in section 2.2.1.

3.2.1.2. Synthesis of 40 nm gold nanospheres (AuNPs40)

40 nm spherical gold nanoparticles were synthesised based on a protocol published by Bastús *et al.*[37].A volume of 140 mL of ultrapure water was heated in a three-neck round-bottom flask (central neck for a condenser, side neck for a thermometer and other side neck for the solution injections), submerged in a paraffin bath, until boiling and reflux were clearly visible. Then, 10 mL of a 33 mM sodium citrate solution was added. After 5 minutes, the boiling was again established and 1 mL of a 25 mM gold (III) chloride solution was added. After 10 minutes, the flask was removed from the bath and left to cool down to 90 °C. At this step, the suspension obtained was light red and contained the gold nanospheres (seeds, S0) that were subject to growth up to the desired size. For the first growth step, this solution was heated in the paraffin bath at 90 °C and, after temperature stabilization, 1 mL of 25 mM gold (III) chloride solution was added and after 30 minutes, the gold nanospheres have grown to size S1 (step A). Step A is repeated to obtain nanoparticles with size S2. For further growth, 55 mL of the nanoparticles solution S2 were removed from the three-neck round-bottom flask and were replaced by 55 mL 2.2 mM sodium citrate solution (step B). The growth step A was repeated (90 °C, 1 mL of 25 mM gold (III) chloride solution, 30-minute reaction) up to 3 times (S3-S5). For further growth, step B was performed in nanoparticles S5, followed by up to 3 consecutive growth steps A. Size was monitored by UV-Visible spectroscopy[38] (UV-Vis).

3.2.1.3. Synthesis of gold nanostars (AuNSs)

The star-shaped gold nanoparticles (~60 nm tip-to-tip diameter) were synthesised based on a protocol published by Yuan *et al.*[39].The reaction was performed at room temperature and under vigorous stirring. 84.3 mL of ultrapure water was added to an Erlenmeyer flask. Then, 3.0 mL of 5 nM 12 nm gold nanospheres (section 2.2.1) and 900 µl of 25 mM gold (III) chloride was added sequentially, followed by simultaneous addition of 900 µl of 2 mM silver nitrate and 900 µl of 50 mM ascorbic acid. The solution turns immediately blue, typical of gold nanostars.

Immediately after the synthesis, the suspension was centrifuged for 20 minutes at a relative centrifugal force (RCF) of 2500·g.

3.2.2. Nanobioconjugation in solution

Electrostatic nanobioconjugation in solution was performed very similarly to the procedure described in the previous chapter for *Tov*L. Briefly, *Trv*L was added to AuNPs15 in different molar ratios *Trv*L:AuNPs (final concentration of AuNPs was constant – 1 nM): 0, 10, 20, 30, 40 and 50. For the covalent nanobioconjugation, the procedure was the same, however there was an addition of 1-ethyl-3-(3-dimethylaminopropyl) carbodiimide hydrochloride (EDC) and *N*-hydroxysuccinimide (NHS) for a final concentration of 2 mM.

All samples were prepared in 10 mM pH 7.0 phosphate buffer. The samples were left overnight at 4 ºC before DLS and ZP analysis.

*Trv*L was prepared by dissolution of 10 mg of commercial powder in 10 mL of 10 mM pH 7.0 phosphate buffer. After filtration, *Trv*L in solution was then quantified by the bicinchoninic acid method[40].

3.2.3. Support impregnation with gold nanoparticles

The following materials were used as supports, in order to represent different structures (porosities) and surface chemistries: hydrophilic mixed cellulose esters (HMCE) Matricell, polytetrafluoroethylene (PTFE) Whatman, hydrophilic polyvinylidene fluoride (HPVDF) Millipore, regenerated cellulose (RC) Whatman, nitrocellulose (NC) Whatman Protran BA83, filter paper (FP) Whatman 2 and office paper (OP) Navigator Universal.

The supports have a micrometric thickness, and so they were easily cut with an office hole punch into ~6 mm diameter disks[41]. The disks were then submersed in 1 mL of gold nanoparticles (AuNPs15, AuNPs40 and AuNSs) solutions, in 1.5 mL microcentrifuge tubes, and were left 20 hours under orbital agitation at 200 rpm. The concentration of 15 nm nanospheres, 40 nm nanospheres and nanostars were 5 nM, 0.5 nM and 0.5 nM, respectively. After impregnation, the supports were washed twice by immersion in 1 mL of ultrapure water (figure 3.2, step A → B).

They were also used ~3 nm diameter disks for some of the final activity assays. In this case, one fourth of the volumes listed above were used.

3.2.4. Gold nanoparticles loading and stability assessment

The relative number of nanoparticles transferred to the supports was clearly distinguishable by naked eye, due to the different colour intensity (red for gold nanospheres, blue for gold nanostars) of the supports, which were all initially white. The disks were photographed to register their level of staining.

The degree of nanoparticle leaching from the support was assessed for selected combinations of material and gold nanoparticles type (the ones with the highest nanoparticle loadings) by UV-Vis and nanoparticle tracking analysis (NTA) of the solutions obtained after 20 hours of immersion of the gold nanoparticles-enriched supports in ultrapure water.

3.2.5. Sample preparation for scanning electron microscopy

In order to avoid material transference across the section and the introduction of microscopic defects, the supports were cryogenically fractured. The supports were dipped in liquid nitrogen for 30 seconds and then fractured with the help of tweezers. The support fragments were immobilized in SEM stainless steel supports using carbon tape. No sample coating was performed.

3.2.6. Nanobioconjugates assembly

The nanobioconjugates were assembled using thiolated compounds as nanoparticle capping agents, namely 11-mercaptoundecanoic acid (11-MUA) 95% (Aldrich), 4-mercaptobenzoic acid (4-MBA) 90% (Acros Organics) and (11-mercaptoundecyl)-*N*,*N*,*N*-trimethylammonium chloride (11-MUTMA) 95% (ProChimia). The enzyme in the nanobioconjugates was laccase from *Trametes versicolor* 10 U/mg (Sigma). The capping agents were dissolved in absolute ethanol 99.8% (Fisher). Ultrapure water was used for washing steps and as the solvent for acetate buffer prepared with acetic acid 99% (Sigma-Aldrich) and sodium acetate 99% (Merck).

Nanobioconjugates assembly, *i.e.* combining the enzyme with the gold nanoparticle trough a molecular linker, was performed with gold nanoparticles already supported. This overcomes possible aggregation problems since gold nanoparticles are immobilized onto the support and stabilized by its surface chemistry.

A schematic representation of the production of the support enriched with nanobioconjugates is shown below, in figure 3.2.

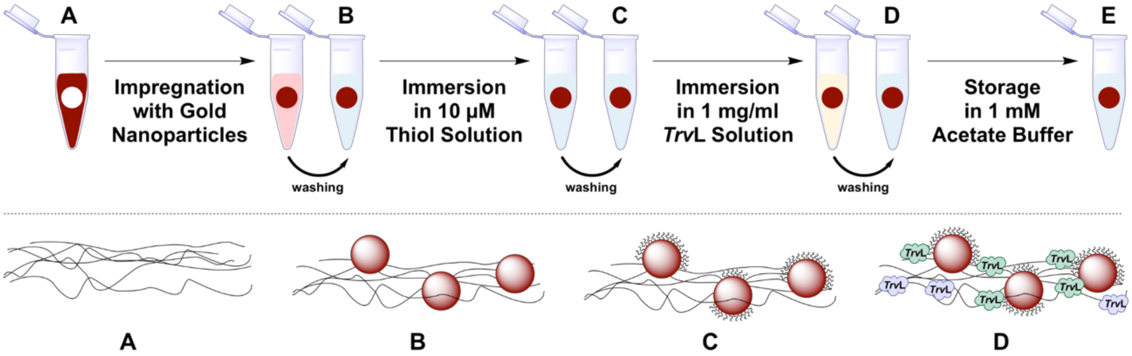

Figure 3.2 – Schematic representation of assembly process of a bioactive disk: main preparation steps (top) and representation of main changes on the support (bottom). A – Disk-shaped support (t = 0); B – Support enriched with gold nanoparticles; C – Support enriched with thiol functionalized gold nanoparticles; D – Support with nanobioconjugates; E – Stored disk for activity measurements.

After step A → B, (figure 3.2, described in section 3.2.4), disks were immersed in 10 µM thiol (4-MBA, 11-MUA or 11-MUTMA) solution for 1 hour. The step B → C finished after removing the thiol solution and washing the support with 1 mL of absolute ethanol and 1 mL of ultrapure water.

In step C → D disks were immersed in a solution of laccase from *Trametes versicolor*, prepared with 1 mg of commercial powder per mL of 1 mM pH 5.0 acetate buffer. The disks were kept immersed in the enzyme solution for 20 hours. Finally, they were washed with the same buffer and stored until activity measurements.

Described in table 3.1 and 3.2, are the tubes prepared for the final activity measurements.

Table 3.1 – Membrane composition for enzymatic activity tests – set of experiments A.

Sample Code	AuNPs15	Thiol			*Trv*L
		11–MUTMA	11–MUA	4–MBA	
A.Au.MUT.La–b	+	+	-	-	+
A.Au.MUA.La–b	+	-	+	-	+
A.Au.MBA.La–b	+	-	-	+	+
A.00.000.La–b	-	-	-	-	+
A.C1	+	+	-	-	-
A.C2	+	-	+	-	-
A.C3	+	-	-	+	-

+ : present; - : absent.

This type of enzymatic assays can be susceptible to external factors, like enzyme activation by temperature or evaporation of the solvent (methanol) from syringaldazine solution, with consequent substrate concentration. Although all precautions were made to avoid these situations, a new set of experiments (B) was performed, using triplicates instead of duplicates (except for controls) and with assays performed in a random order. In addition to the set of experiments A, they membranes with non-functionalised nanoparticles and laccase were tested.

Also, set of experiments B used nitrocellulose disks with 3 mm diameter, in order to reduce in 75% the reactants used for the active disks assembling.

Table 3.2 – Membrane composition for enzymatic activity tests – set of experiments B.

Sample Code	AuNPs15	Thiol			*Trv*L
		11–MUTMA	11–MUA	4–MBA	
B.00.000.La–c	-	-	-	-	+
B.Au.000.La–c	+	-	-	-	+
B.Au.MUT.La–c	+	+	-	-	+
B.Au.MUA.La–c	+	-	+	-	+
B.Au.MBA.La–c	+	-	-	+	+
B.C1	-	-	-	-	-
B.C2	+	-	-	-	-
B.C3	+	+	-	-	-
B.C4	+	-	+	-	-
B.C5	+	-	-	+	-

+ : present; - : absent.

These samples had their enzymatic activity determined (see section 3.2.7) in a random order. The assays were performed in the following order: B.C1-5, B.00.000.La, B.Au.000.La, B.Au.MUT.La, B.Au.MUA.La, B.Au.MBA.La, B.Au.MBA.Lb, B.Au.MUA.Lb, B.Au.MUT.Lb, B.Au.000.Lb, B.00.000.Lb, B.Au.000.Lc, B.Au.MUA.Lc, B.Au.MBA.Lc, B.00.000.Lc, B.Au.MUT.Lc.

3.2.7. Enzymatic activity assays

This task was performed with the help of Catarina Pelicano and Patrícia Soares during their extracurricular internship.

The enzymatic activity of the disks was assessed by the method[42] described in chapter 2, with slight modifications, in order to get a measurable variation of absorbance over time by UV-Visible spectroscopy. The concentration of substrate was chosen in order to enable the reading of at least 5 points in the v_0 phase.

The disks were immersed in 900 µl of 10 mM pH 5.0 acetate buffer in the UV-Vis cell. The cell was left in the UV-Vis spectrophotometer cell holder for 5 minutes, to assure a stable temperature of 30 °C. Buffer and water to wash were previously equilibrated at

30 °C in a water bath. After 5 minutes, 100 µl of 0.232 mM syringaldazine solution was added and absorbance at 525 nm was measured every 5 seconds, with an acquisition time of 1 second, for a total of 300 seconds. Between data collection (every 5 seconds), the solution was mixed with a micropipette (up and down liquid movement).

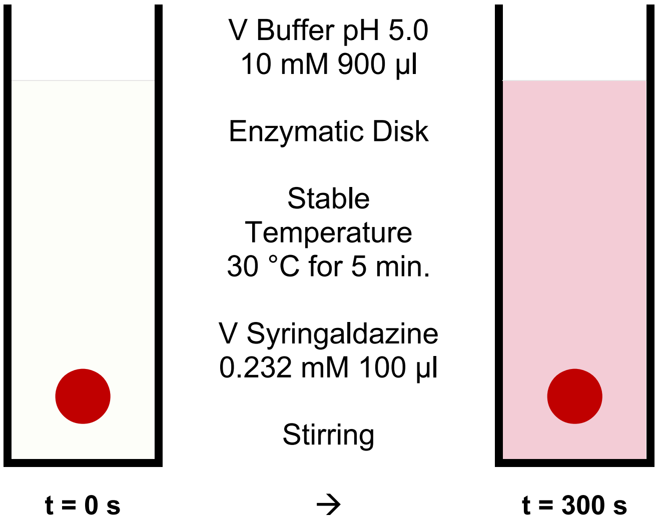

Figure 3.3 – Scheme summarizing the activity assay conditions, performed in a UV-Visible spectroscopy quartz cell (1 cm path, 1 mL total volume).

Initial reaction rate (v_0) was calculated as the slope of the plot absorbance *vs.* time, using the set of points with high linearity (first 10%-20%). Linear regression analysis was performed in Microsoft Excel software.

Several optimization steps regarding activity measurements were done before definitive activity assays in order to get reliable activity measurements. For the sake of simplicity, activity results reported in section 3.3.5 only show the two last sets of experiments, analysing the samples listed in the previous section.

3.3. Results and Discussion

3.3.1. Synthesis of gold nanoparticles

Disclosure: Part of the data in this section was already published in Emma Calle Serrano master's dissertation[43] *and Marta Belda Garrido bachelor's report*[44]*, who participated in this task.*

The 15 nm gold nanospheres (AuNPs15) were successfully synthesised, showing the typical red wine colour, UV-Visible spectrum, size distribution (*via* dynamic light scattering measurements) and zeta potential consistent with the literature[45-47]. Due to this protocol being well stablished among the scientific community, no further characterization was performed. All the experimental data support the morphology of these AuNPs15 is the same as for AuNPs discussed in chapter 1.

The 40 nm gold nanospheres (AuNPs40) showed the typical light red color after the nucleation process (S0) and then, after each growth step, the solution became darker and with slightly higher turbidity. This is in line with what is expected for progressively bigger gold nanoparticles, due to the red-shift of the plasmonic band and increase in light scattering as the size of the nanoparticles increases.

Finally, regarding the synthesis of star-shaped gold nanoparticles, the reaction solution showed the expected colour changes, starting colourless, changing to light red after seed addition, then orange (red from the seeds and yellow from the gold salt, no shift of the plasmonic band is observed) and finishing with a fast change to a dark blue colour, typical of AuNSs.

Figure 3.4 shows the UV-Visible spectra of the three types of nanoparticles synthesised in this work, all normalized to a maximum absorbance value of 1.

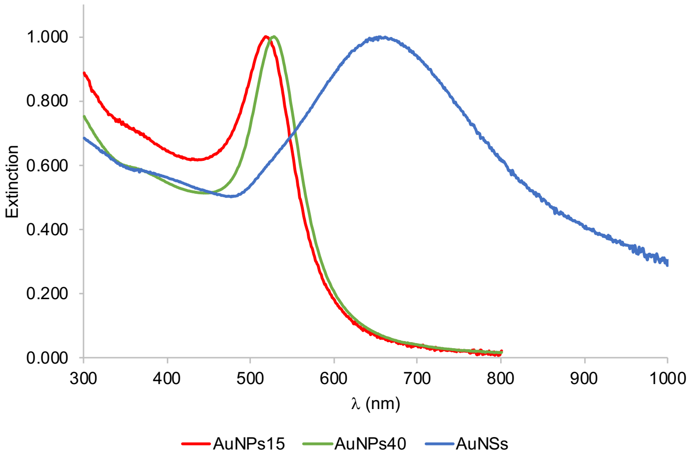

Figure 3.4 – UV-Visible spectra for small gold nanospheres (AuNPs15, red line), big gold nanospheres (AuNPs40, green line) and gold nanostars (AuNSs, blue line).

The spectra for gold nanospheres are quite similar, which is expected due to the similar shape. There is however a shift from 518 nm to 527 nm when 15 nm are compared to 40 nm gold nanospheres. There are some features in the nanospheres spectra that are important to highlight: (i) the peaks are quite narrow and well defined, which is expected since these are isotropic nanoparticles and present a low size dispersion; (ii) the right (blue) side of the LSPR band shows a sharp decrease in extinction, showing no evidence of the presence of aggregates or significant contamination with anisotropic shapes that usually absorb light at wavelengths closer to the blue region of the visible spectrum[39, 48].

The spectrum of the star-shaped gold nanoparticles is very different from the other two spectra, and the higher width of the peak is easily noticeable. The fact of the nanostars could have different number of tips, with different sizes and distributions across the seeds surface, gives many different ways for electrons to oscillate. The LSPR peak maximum absorption is observed for this batch at 655 nm (typically is 600 – 700 nm), with justifies the blue colour. It is also important to notice that this kind of anisotropic nanoparticles absorb light in the near-infrared (NIR) region. There is no noticeable contribution from gold seeds (equivalent to AuNPs15) in the spectrum so it is fair to assume that very high yields of conversion of the seeds into AuNSs are achieved.

Nanospheres are the most popular gold nanoparticle shape and they are widely used, so the information that can be extracted from UV-Vis spectra are well known and established. This includes size, shape, concentration and purity (regarding the presence of aggregates and other shapes). For star-shaped gold nanoparticles, although it is possible to say that a spectrum fits the typical spectra for that shape and estimated concentration, only with microscopy techniques like TEM and NTA is possible to have a more accurate information about their shape and concentration, respectively.

In figure 3.5 is shown a representative TEM micrograph for AuNSs, in figure 3.6 there is a histogram showing the distribution of tip-to-tip sizes (measured in TEM micrographs), and in figure 3.7 a hydrodynamic size distribution obtained by NTA.

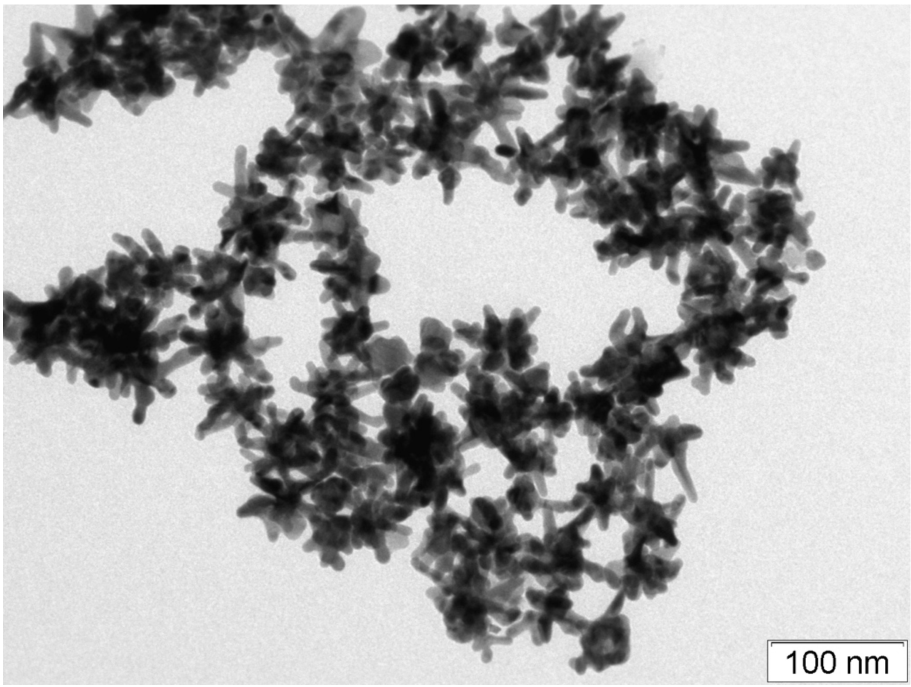

Figure 3.5 – Transmission electron microscopy (TEM) micrograph of gold nanostars.

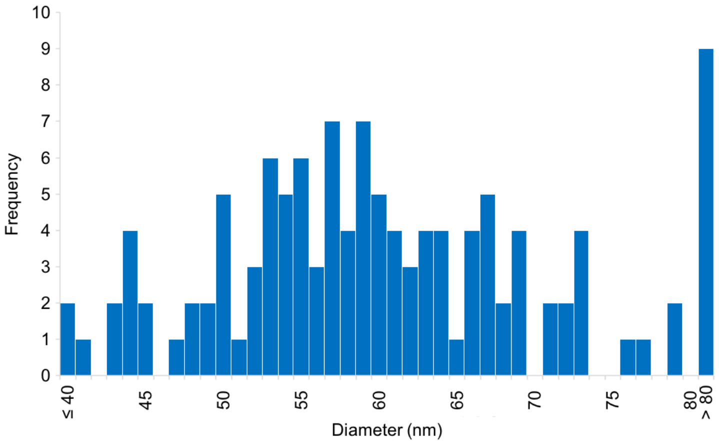

Figure 3.6 – Diameter distribution (histogram) for gold stars. Average diameter (analysis of 120 particles) in TEM micrographs: 60.4 ± 12.1 nm.

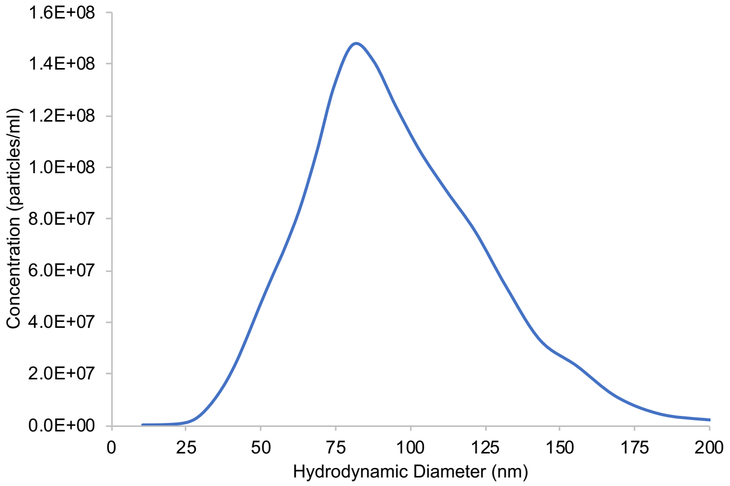

Figure 3.7 – Hydrodynamic diameter distribution for gold nanostars, obtained by NTA. Average diameter: 82.6 ± 5.2 nm. Mode diameter: 85.6 ± 15.6 nm.

Observing the TEM image of AgNSs (figure 3.5), is clearly visible the multiplicity of sizes, number of tips per star and their length. Each nanoparticle is quite unique, which explains the broad band in their UV-Vis spectrum depicted in figure 3.4.

This dispersion of sizes is also evident in figure 3.6 histogram (based on TEM micrographs from the same batch depicted in figure 3.5) and NTA data corroborates this high dispersion of sizes. However, there is a difference between the mean size determined by TEM (60.4 ± 12.1 nm) and NTA (82.6 ± 5.2 nm). It is expected that hydrodynamic radius is bigger than metallic radius but here the difference is considerable (~22 nm). However, the star shape can influence the hydrodynamic radius differently than what is often seen for spherical particles. DLS was also used to determine the hydrodynamic radius and the result – 85.0 ± 0.7 – corroborates the NTA result. From the TEM side, the manual measurement of the tip-to-tip distance can introduce an extra error, that can help to explain the difference.

The same characterization was done for AuNPs40. In figure 3.8 is shown a representative TEM micrograph for these nanoparticles, in figure 3.9 there is a histogram showing the distribution of the metallic diameter (measured in TEM micrographs), and in figure 3.10 a hydrodynamic size distribution obtained by NTA.

Together with the hydrodynamic size, that can be also obtained by DLS, the size distribution shown in figure 3.7 enables the possibility of determining the nanoparticle suspension concentration, which is a big advantage for anisotropic nanoparticles when compared to the other techniques[49].

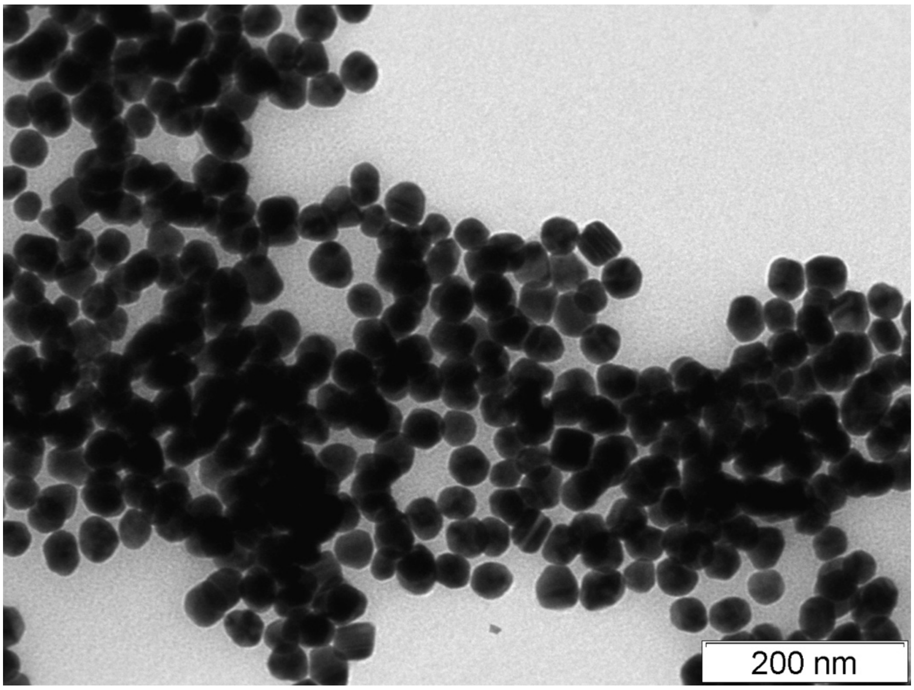

Figure 3.8 – Transmission electron microscopy (TEM) micrograph of gold nanospheres.

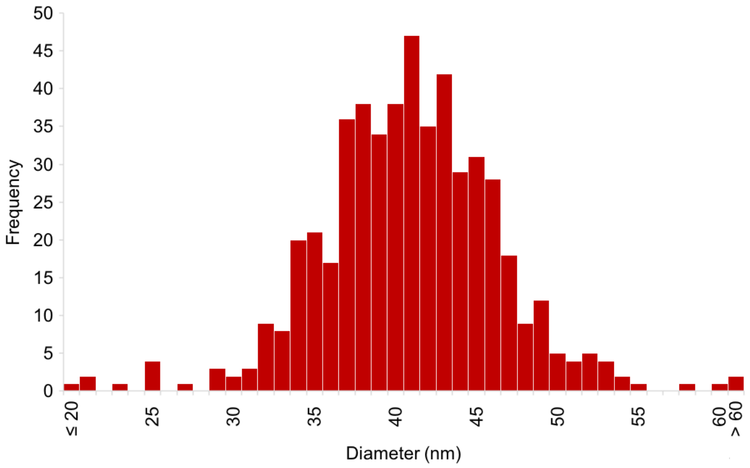

Figure 3.9 – Diameter distribution (histogram) for 40 nm gold nanospheres. Average diameter (analysis of 514 particles) in TEM micrographs: 40.4 ± 5.6 nm.

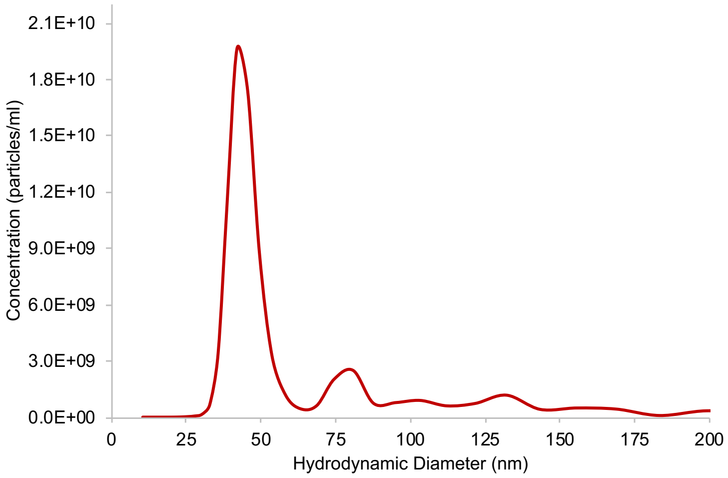

Figure 3.10 – Hydrodynamic diameter distribution for 40 nm gold nanospheres, obtained by NTA. Average diameter: 53.0 ± 5.2 nm. Mode diameter: 42.9 ± 2.8 nm.

For 40 nm gold nanospheres, TEM micrograph in figure 3.8 shows nanoparticles (2D) with high circularity. The dispersion shown in figure 3.9 histogram is not as high as for gold nanostars, with NTA data (figure 3.10) also showing a narrow peak when compared to the NTA distribution in figure 3.7. Here the difference between the mode diameter (main peak size) from NTA (42.9 ± 2.8 nm) and average metallic diameter from TEM (40.4 ± 5.6 nm) is only 2.5 nm.

Table 3.3 summarizes the sizes of all particles used in this work.

Table 3.3 – Summary of characterization data for all synthesised nanoparticles.

	DLS Size		**TEM**	**NTA**	**UV-Vis**[38]
	Z-Average (nm)[a]	**PdI**[a]	**Diameter (nm)**[b]	**Diameter (nm)**[e]	**Diameter (nm)**
AuNPs15	–[c]	–[c]	–[c]	–[f]	14
AuNPs40	–[c]	–[c]	40.4 ± 5.6	42.9 ± 2.8	39
AuNSs	85.0 ± 0.7	0.252 ± 0.004	60.4 ± 12.1[d]	85.6 ± 15.6	–[f]

Notes: a – the presented error value is the standard deviation of three measurements; b – the presented error value is the standard deviation from the calculated histogram; c – analysis not performed; d – the diameter is the distance between two opposite tips, determined with ImageJ software[50]; e – value for the main peak (mode), error value is the standard deviation of four measurements; f – technique not suitable to this parameter for this type of nanoparticles.

A group of three types of gold nanoparticles, representing different sizes and shapes, was then available to the next steps.

3.3.2. Nanobioconjugation in solution

Disclosure: Part of the data in this section was already published in Emma Calle Serrano master's dissertation[43] and Marta Belda Garrido bachelor's report[44], who participate in this task.

Following the work described in chapter 2, attempts were made to produce nanobioconjugates in solution, either using electrostatic interactions or covalent linking, in both cases trough 11-mercaptoundecanoic acid (MUA) as the capping agent. The formation of stable nanobioconjugates was assessed by measurement of zeta potential and the results obtained are shown in Fig. 3.11.

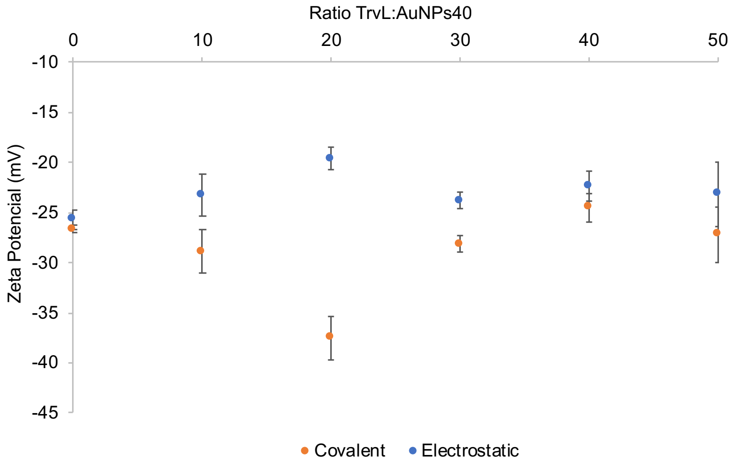

Figure 3.11 – Zeta potential values for different molar ratios between laccase (*Trv*L) and 1 nM 15 nm gold nanoparticles (AuNPs15) – measurements in 10 mM pH 7.0 phosphate buffer (blue dots –electrostatic conjugation; red dots – covalent conjugation).

The zeta potential values shown in figure 3.11 do not show a clear variation with increasing molar ratios. There is an initial decrease of ZP values for covalent conjugation, but for higher ratios the values are again identical to the one observed just for the AuNPs15 (ratio 0). Also, the standard deviation (SD) is much higher when both *Trv*L and AuNPs15 are present in solution. For the AuNPs15 with no *Trv*L in solution the ZP value is identical for both conjugation methods and present a small SD.

Even for these smaller ratios (0-50), there is no significant change in ZP with the increasing ratios for both covalent and electrostatic attempts of conjugating the enzyme with the nanoparticles. The variation of ZP values between ratios 0 and 20 do not seem relevant. This is the opposite to the observed for AuNPs15–*Tov*L conjugates in the previous chapter, where a curve with Langmuir fitting was observed.

Additionally, it was performed nanoparticle tracking analysis of nanobioconjugates using the same batch of gold nanoparticles (AuNPs40) and *Trv*L and, as a positive control for nanobioconjugation, bovine serum albumin (BSA), since it is known[51] its ability to efficiently conjugate with gold nanoparticles.

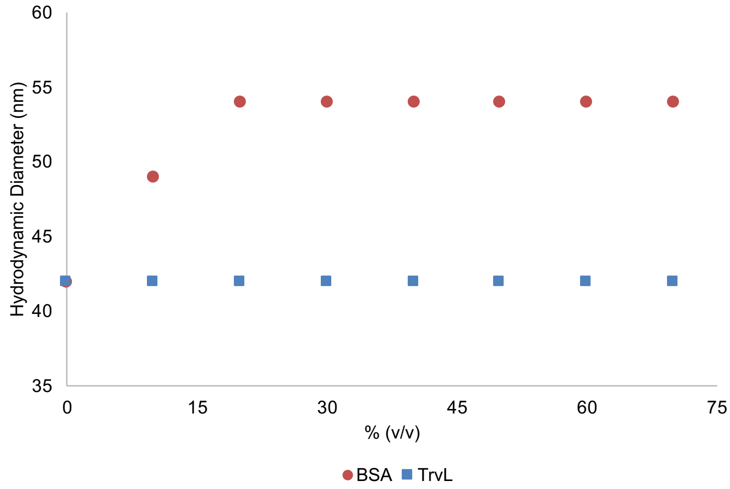

Figure 3.12 – Hydrodynamic diameter for AuNPs-MUA-BSA nanobioconjugates (red dots) and tentative AuNPs40-MUA-*Trv*L nanobioconjugates (blue dots), determined by nanoparticle tracking analysis.

It is clearly visible the increase of the hydrodynamic size for the AuNPs40-MUA-BSA nanobioconjugates, from an initial 42 nm diameter up to a 54 nm diameter step, in opposition to AuNPs40-MUA-*Trv*L nanobioconjugates that keep the 42 nm hydrodynamic diameter correspondent to the functionalized AuNPs40 with MUA, with presumably no *Trv*L conjugated. Bovine serum albumin has a 66.5 kDa size, that is similar to fungal laccases typical sizes (60–80 kDa range[52]), so the size and related constraints should be negligible.

The apparent impossibility of conjugating MUA-functionalized gold nanoparticles and *Trametes versicolor* laccase could be due to the enzyme having a negative net charge at the pH range studied. This pH range was selected based on the colloidal stability of the nanoparticles, that have a negative surface charge, due to deprotonated carboxylate group in the MUA terminal. The pKa of 11-mercaptoundecanoic acid in self-assembled monolayers is 4.8,[53] so it is necessary to keep the pH of the medium at least 1-2 pH units above this value to keep the carboxylic acid – carboxylate equilibrium strongly shifted towards the carboxylate form. Only under this condition it is possible to assure a strong negative charge at the NPs surface and keep a high electrostatic repulsion between the nanoparticles, assuring a stable colloidal dispersion. This has to be confronted to the enzyme net charge at these pH value where MUA is deprotonated (>6–7).

Marta Serra (from *Faculdade de Ciências e Tecnologia da Universidade Nova de Lisboa)* calculated the charge distribution of *Trametes versicolor* laccase at four pH values – 4, 5, 6 and 7, based on the *TrvL* crystal structure[54], available on Protein Data

Bank (PDB)[55]. At pH 4 and pH 5 several positive domains are shown, with no negative domains in sight. At pH 6, there are clearly negative domains on the protein's surface and some of the positive regions still present are very weakly charged. At pH 7 this behaviour is, as expected, even more noticeable.

There is a clear incompatibility between the pH ranges where MUA functionalized gold nanoparticles are negative and *Trv*L has positive domains available to interact with the carboxylates present in MUA self-assembled monolayer. Additionally, the pH range where these fungal laccases are typically more active is acidic (~5), is also incompatible with the range where MUA (or even other thiols with a carboxylate end) is deprotonated, which is necessary to avoid aggregation of the nanoparticles. If the nanoparticles are immobilized, no aggregation is expected, avoiding the problems associates with aggregation at pH values close to SAM pKa. This was the trigger to move on to a supported system of nanobioconjugates.

3.3.3. Impregnation of the supports with gold nanoparticles

Disclosure: Part of the data in this section was already published in Emma Calle Serrano master's dissertation[43] and Marta Belda Garrido bachelor's report[44], who participated in this task.

After being immersed for the same time (20 hours) in a nanoparticle suspension and washed as described, the disks were photographed. Table 3.4 shows photographs of 28 different combinations between support and nanoparticle type. No manipulation of the pictures shown in table 3.4 was performed.

Table 3.4 – Photographs of the support materials impregnated with gold nanoparticles – 15 nm gold nanospheres (AuNPs15), 40 nm gold nanospheres (AuNPs40) and gold nanostars (AuNSs).

Support	**No NPs**	**AuNPs15**	**AuNPs40**	**AuNSs**
Polytetrafluoroethylene (PTFE)				
Hydrophilic Polyvinylidene Fluoride (HPVDF)				
Regenerated Cellulose (RC)				
Office Paper (OP)		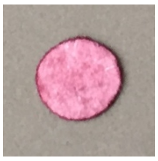		
Filter Paper (FP)				
Hydrophilic Mixed Cellulose Esters (HMCE)				
Nitrocellulose (NC)	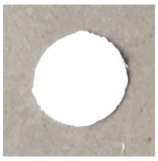			

Membranes with hydrophobic materials (PVDF or PTFE) in its constitution do not show a significant change in colour after immersion in gold nanoparticle solution. For the case of the PVDF-based material, HPVDF, it is only possible to see some light coloration especially where defects are present in the material, like in the borders of the disks. It is clear that a hydrophobic material is unfit to immobilize gold nanoparticles.

The remaining five supports are all cellulose-based. Regenerated cellulose and office paper present an intermediate degree of gold nanoparticles adsorption, however, more or less transversal to all of nanoparticles types and sizes, presenting even the best visible adsorption of gold nanostars. To use star-shaped gold nanoparticles, RC or OP would be the best choice, but with pros and cons for both cases. The cost of office paper is negligible when compared to regenerated cellulose membranes, however the last keeps its integrity better when immersed in water for long periods. Office paper is also a less pure material, with calcium carbonate in its composition aimed to fill the pores and giving a smooth and white finish[19], so it is a less controlled environment for immobilizing the gold nanoparticles and for further nanobioconjugation when compared to regenerated cellulose membrane, that is intended for laboratory use.

The other three cellulose-based materials, filter paper, hydrophilic mixed cellulose esters, and nitrocellulose, show clearly the higher loading for small gold nanospheres. Filter paper is even the support that shows higher loading in big spherical gold nanoparticles. Filter paper shares with office paper one main advantage, that is its low cost, which can be a huge step towards of a low cost final material, improving the possibility of its incorporation in cheap and disposable sensors. In the other hand, they also share the drawback of having a low resistance to manipulation in water. Regarding nitrocellulose and hydrophilic mixed cellulose esters membranes, they presented a high and homogenous loading of small gold nanospheres, however they also show poor loading of bigger nanoparticles, spheres or star-shaped. Concerning the manipulation in water, both NC and HMCE showed a good resistance, but nitrocellulose is a cheaper material, since its available in sheets or rolls, typically used for western blots.[56]

Cellulose is typically hydrophilic due its hydroxyl groups, which can undergo esterification giving place to nitro groups in nitrocellulose and both nitro and acetate groups in hydrophilic mixed cellulose esters material. The charges present in nitrocellulose and hydrophilic mixed cellulose esters membranes can help to stabilize the gold nanoparticles by replacing the citrate in the role of capping agent. This can explain the good results obtained for NC and HMCE materials regarding gold nanoparticle adsorption, especially for AuNPs15. The other non-modified cellulosic materials, RC, OP and FP, do not present charges on the surface, which can explain the apparent lower loading in gold nanoparticles. The exception is FP, that shows an intense red colour, although it is not clear an explanation for this according to the data discussed so far.

Regarding the type of gold nanoparticles and based on a visual inspection of the final supports, AuNPs15 show higher loading degrees; in contrast, it was not possible to achieve a high loading of gold nanostars in the supports. As discussed before, office paper and regenerated cellulose showed the best loadings for AuNSs, however with still visible white or light blue spots.

A lack of colour in supports treated with AuNSs does not mean that no AuNSs are immobilised. Part of AuNSs absorption spectrum is already on the infrared (IR) region, as depicted in figure 3.4. If some aggregation occurs, the localized surface plasmon resonance (LSPR) peak will red shift and enter in the near infrared (NIR) region, the AuNSs can become invisible to the naked eye. However, this was not the case, since the impregnation solution barely lost any absorbance (data not shown).

A similar behaviour was seen for big gold nanospheres, although a strong coloration is seen for theses nanoparticles in filter paper. It is important to notice that both gold nanostars and big gold nanospheres have molecular absorption coefficients (□) of a magnitude of 10^9 $M^{-1}\cdot cm^{-1}$ for their LSPR band (in water), while small gold nanospheres have a molecular absorption coefficient for LSPR of a magnitude of 10^8 $M^{-1}\cdot cm^{-1}$, in the same conditions. This one order of magnitude lower for AuNPs15 make the results observed for these nanoparticles even more noteworthy, since the most intense colorations were obtained for this type of nanoparticles (namely for FP, HMCE and NC), pointing to a significantly higher number of nanoparticles present in the materials.

The supports are microstructured, with pores and fibres with a size in the hundreds of nanometres range, therefore it was expected that any of these nanoparticle types could easily penetrate in the support. However, it is clear that the papers with higher colour intensities all were impregnated with small gold nanospheres. Since we did not apply pressure to force nanoparticles to penetrate the materials, it is expected that smaller particles will indeed diffuse more freely through the pores. Regarding the capacity of the support stabilizing the nanoparticle, the different sizes and shapes result in different nanoparticle-support interface areas. Big gold nanospheres are nanoparticles that can have a bigger nanoparticle-support interface area due its higher curvature radius when compared its smaller counterparts, however this also leaves a bigger area that is not stabilized by the support. For the star-shaped nanoparticles, the points of contact with the surface are the tips from the arms, which leaves even less contact area between the support and nanoparticle surfaces. For a better visualization of the nanoparticle-support interface, figure 3.9 shows two spheres with *r* and *2r* radii, and a star-like shape with a spherical core with a *r* radius, on top of a flat surface. The curvature of the support fibres was considered negligible for this model because their considerably higher size when compared to the gold nanoparticles, therefore the support is represented as a locally flat surface.

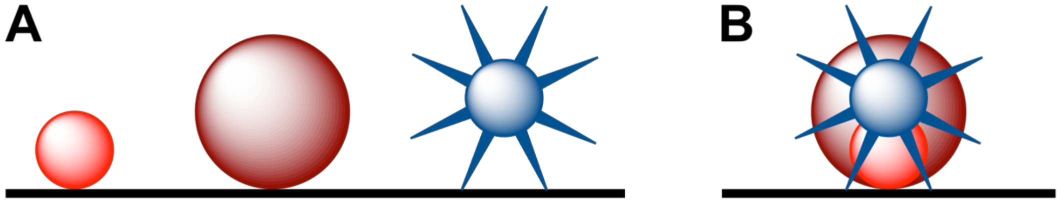

Figure 3.13 – Size comparison, at the same scale, between the three nanoparticle types, individualized (A) and overlapping (B), on top of a locally flat zone.

Considering the analysis done about nanoparticles loading and experience in manipulation of the supports, filter paper and hydrophilic mixed cellulose esters and nitrocellulose membranes loaded with small gold nanospheres were chosen for further characterization.

Scanning electron microscopy was performed in sections of the cryogenically fractured disks of these materials, either loaded with small gold nanospheres, or without any gold nanoparticle impregnation, as control. Figures 3.14, 3.15 and 3.16, show SEM micrographs obtained with a backscattered electrons detector (BSED), for FP, HMCE and NC, respectively, impregnated with gold nanoparticles and their respective controls. For each figure, the top pair of micrographs show the whole section height, at a 1 x 10^3 magnification, and presents on the bottom a pair of micrographs with a 5 x 10^4 magnification, necessary for visualization of individual small gold nanospheres. By capturing the SEM images using BSED, the conductive materials, such as metallic nanoparticles, give origin to bright (white) spots in the micrograph.

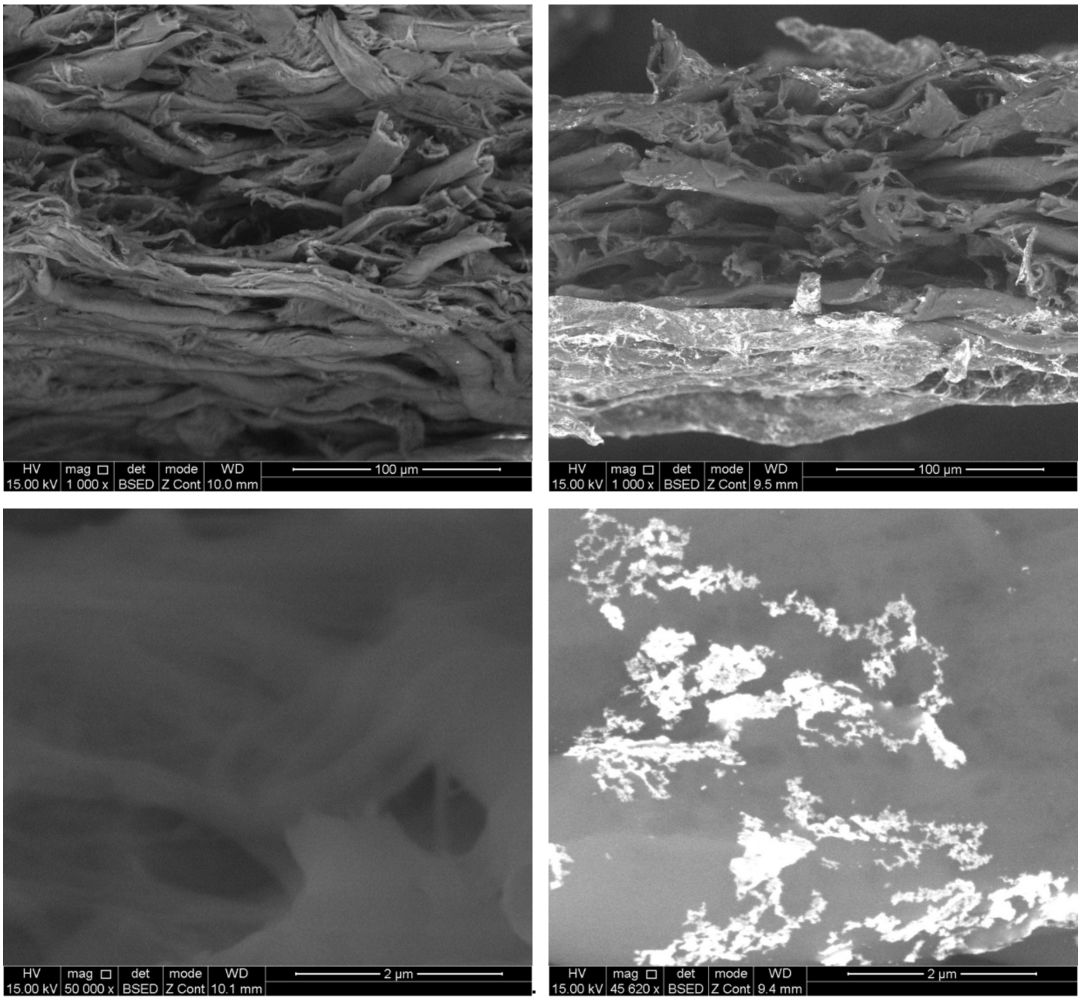

Figure 3.14 – Scanning electron microscopy (backscattered electrons detection mode) microphotographs of filter paper impregnated (right) and not impregnated (left) with small gold nanospheres.

Scanning electron microscopy images helped considerably to understand the gold nanoparticles distribution, namely for the small gold nanospheres. For filter paper under the lower magnification it is possible to see that the AuNPs15 are mainly distributed alongside the external part of support, with a negligible amount of these nanoparticles present across the paper section. Under the higher magnification it is clear that the nanoparticles are organized in aggregates. Aggregation is a major drawback since it is a phenomenon highly irreproducible, which can introduce several differences between batches and even between disks from the same batch, leading to responses with high variety. This accumulation of nanoparticles on the exterior, under the form of aggregates, can explain the strong red colour observed, despite having or not the highest effective loading of small gold nanospheres.

Regarding the support itself, the interlaced fibres morphology explains the fact that, upon repeated manipulation in water, the fibres start to become lose and disperse in the solvent, compromising the paper filter structure.

The SEM micrographs from hydrophilic mixed cellulose esters membrane shown below in figure 3.15 display a completely different structure compared to FP. The structure is alveolar, packed in a more compact way, that explains the better integrity of the material under repeated manipulation.

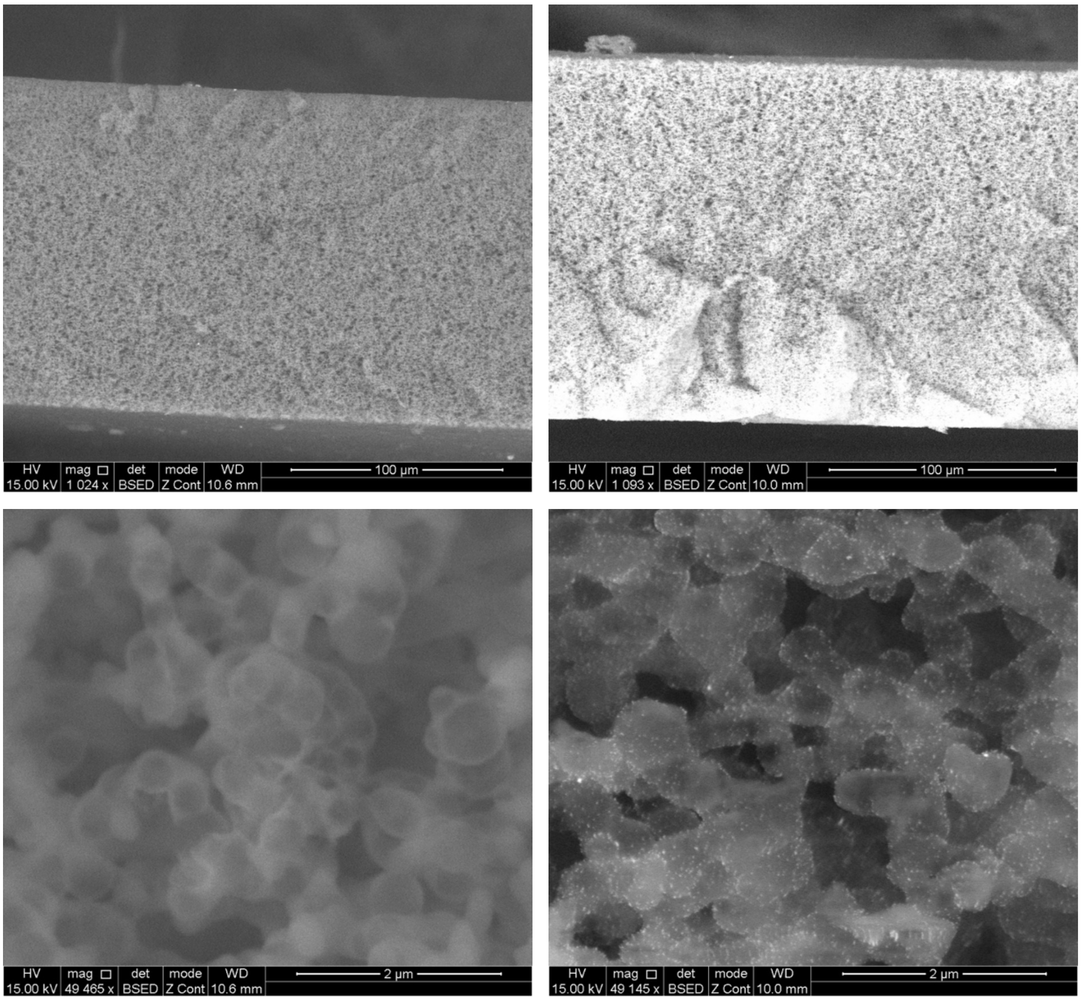

Figure 3.15 – Scanning electron microscopy (backscattered electrons detection mode) microphotographs of hydrophilic mixed cellulose esters membrane impregnated (right) and not impregnated (left) with small gold nanospheres.

At the lower magnification images, it is possible to see that the HMCE membrane enriched with gold nanoparticles (top right) shows a uniform bright appearance for the support section, indicating that an even distribution of the small gold nanoparticles was obtained all across the membrane. On the higher magnification, it is possible to see a homogeneous distribution of individual gold nanoparticles across the entire section, with a very scarce number of aggregates visible.

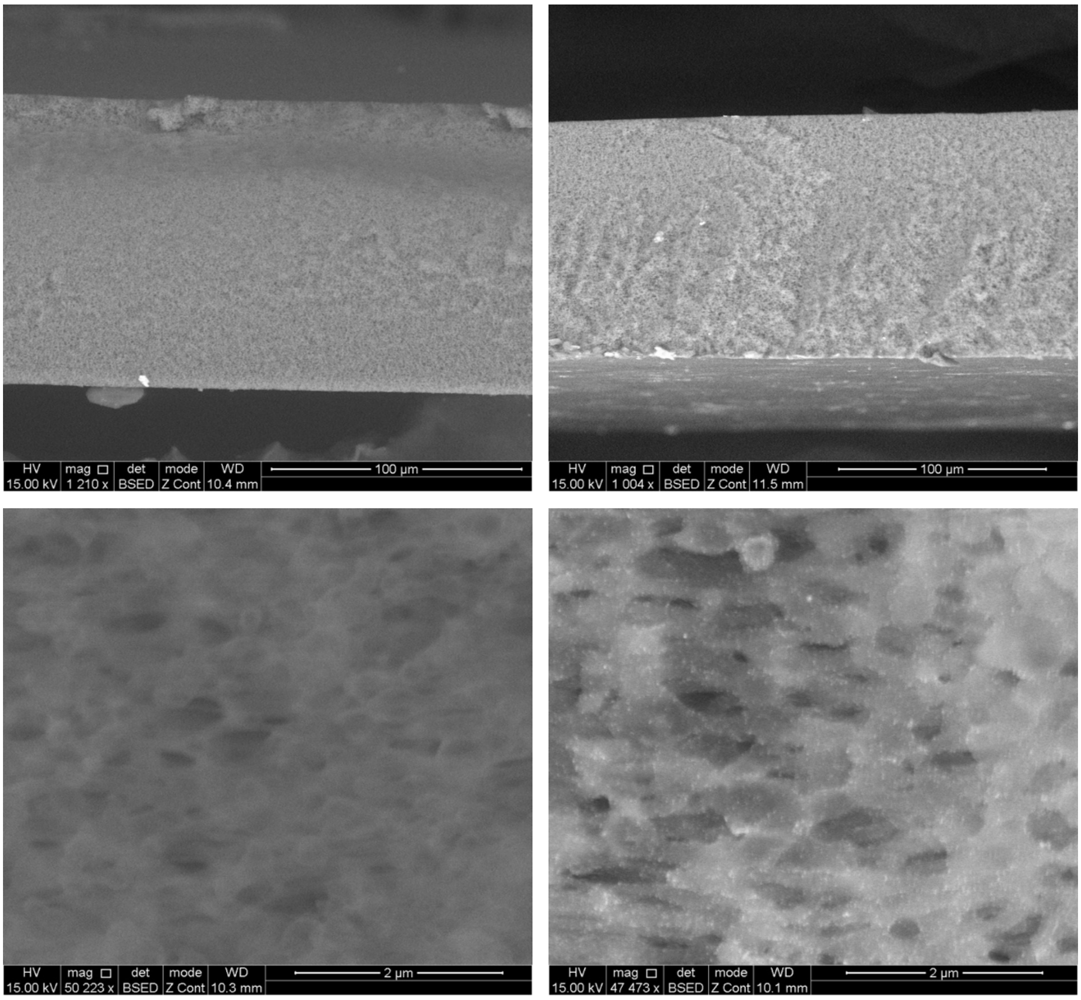

Figure 3.16 – Scanning electron microscopy (backscattered electrons detection mode) microphotographs of nitrocellulose membrane impregnated (right) and not impregnated (left) with small gold nanospheres.

For nitrocellulose disks the SEM images are quite similar to HMCE, both regarding structure and nanoparticle distribution. This indicates that the main contributor for nanoparticles stabilization in HMCE membrane could be the nitro groups rather that acetate groups.

Under the light of all the nanoparticle-enriched supports characterization results, hydrophilic mixed cellulose esters and nitrocellulose membranes impregnated with small gold nanospheres seem to be the best choice regarding support mechanical stability and nanoparticle loading quantity and distribution. Given the objective of developing materials that can be incorporated in low cost (eventually disposable) sensors, nitrocellulose revealed to be the best candidate to be used as the definitive support for further studies.

Finally, it was confirmed the ability of the supports to keep the nanoparticles stabilized into their structure. The ultrapure water where nanoparticle-enriched disks were left immersed for 20 hours showed a signal that could not be distinguished from the blank either by UV-Vis for the small gold nanospheres (with a limit of detection within the picomolar range), and by NTA for the big gold nanospheres and gold nanostars (with a sub-picomolar limit of detection).

3.3.4. Nanobioconjugates assembling

Given the already discussed failure in nanobioconjugates preparation in solution, nanobioconjugates were prepared in situ. The first step was impregnation of nitrocellulose, since this material shows a good distribution of the gold nanoparticles across the support. A formulation used and described on chapter 2 [nanoparticle (AuNPs15) – thiolated capping agent (CALNN) – enzyme (*TovL*)], had to be made with the AuNPs15 already supported, because, when these nanoparticles were already functionalized with a thiolated capping agent, no transference from the nanoparticles suspension to the supports was observed. This corroborates the hypothesis of the citrate replacement nanoparticles stabilization by the charged groups present on the microstructured support, which cannot happen when the citrate was already replaced by a thiol containing capping agent. A molecule with this chemical group is not so prone to be displaced from the particle due the great affinity of the sulphur to gold surfaces[57].

The second step of the assembling process, schematized as the step B → C in figure 3.2, is then this thiol functionalization. It was observed that there is an optimal time for incubation of thiol in ethanol solution with nanoparticle-enriched supports. Given the high affinity of the thiolated compounds to the gold nanoparticles[57], if the thiol solution is left for too long in contact with the disks, nanoparticles are released from the support into solution. A pink colour in solution was observed after 1 – 2 hours of contact. Taking into account that citrate-capped nanoparticles are easily captured and stabilized by the support, but thiol-capped nanoparticles are not, it is possible to propose the following order of crescent affinity to nanoparticles: citrate, support and thiol. When the supports with immobilized AuNPs15 are dipped in thiol solution, the remaining citrate, still present in nanoparticles surface regions not stabilized by the support, is replaced by the thiol in the first hour since citrate is a very labile capping. After this initial period, the competition between the thiol and the support surface is the main phenomenon going on, leading to nanoparticle release. Since all the phenomena are dynamic, this step B → C was stopped when most of the citrate is replaced but only a minor fraction of the nanoparticles left the support.

The next and final element of the bioactive disks is the *Trametes versicolor* laccase. If it is known that *Trv*L is incorporated in the supports since, as it can be seen in the following section, the supports are always active, it is not clear how the enzyme biomolecule is immobilized. The enzymatic activity results can give further details about what is going on the support, but two main scenarios are on the table. Nitrocellulose is known to be an excellent protein binding support[56], so it is safe to assume that enzyme biomolecules will adsorb directly to the support itself. In this process, some of these biomolecules are placed really close to the gold nanoparticles and can be under their influence. This scenario is illustrated by figure 3.17 A, with *Trv*L units under (green) and off (blue) the gold nanoparticles influence. In figure 3.17 B is included the representation of *Trv*L (red) electrostatically linked to the gold nanoparticle. This constitutes the second possible scenario that includes the presence of *Trv*L in a typical nanobioconjugates fashion, *i.e.*, nanoparticle – linker – biomolecule, like those described in chapter 2.

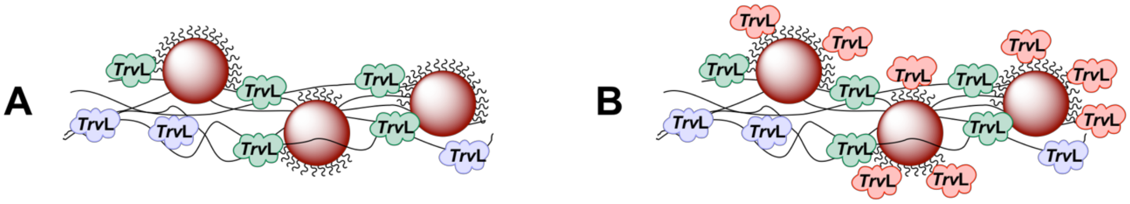

Figure 3.17 – Schematic representations of two hypothesis for *Trametes versicolor* laccase immobilization onto nanoparticles-enriched support, via support away from nanoparticles influence (blue, in both A and B), via support under nanoparticle influence (green, in both A and B) and via electrostatic interaction with nanoparticle capping (red, just in B).

3.3.5. Disks enzymatic activity

The enzymatic activity for the first set of experiments, detailed in table 3.1, is depicted in the following figure 3.18.

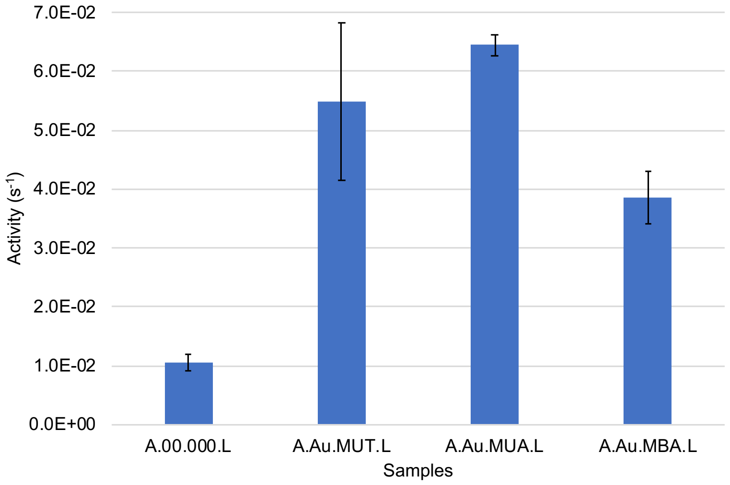

Figure 3.18 – Laccase enzymatic activities (blue columns) and respective standard deviation (black lines) for nitrocellulose disks (6 mm diameter) with no AuNPs15 (A.00.000.L) and with AuNPs functionalised with 11-MUTMA (A.Au.MUT.L), 11-MUA (A.Au.MUA.L) and 4-MBA (A.Au.MBA.L).

As can be seen in the figure above, laccase enzymatic activities of every single sample containing gold nanoparticles, capped by a thiol, are 4–6 times higher than the bare support with laccase. AuNPs15 functionalised with 11-MUA assure the higher activity, but the ones functionalised with 11-MUTMA are equivalent within the experimental error. Controls listed in table 3.1 were not active (data not shown).

The next set of results (B) – including now supports with not-functionalised AuNPs15, triplicates, smaller disks and randomly tested samples – are depicted below in figure 3.19.

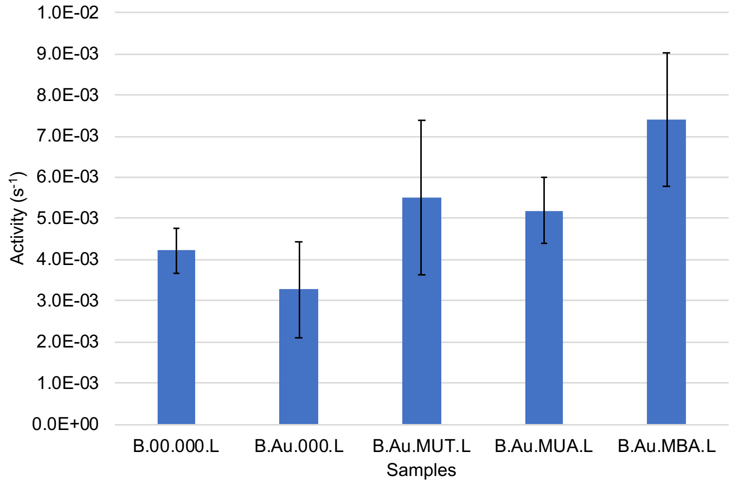

Figure 3.19 – Laccase enzymatic activities (blue columns) and respective standard deviation (black lines) for nitrocellulose disks (3 mm diameter) with no AuNPs15 (B.00.000.L), with non-functionalised AuNPs15 (B.Au.000.L) and with AuNPs functionalised with 11-MUTMA (B.Au.MUT.L), 11-MUA (B.Au.MUA.L) and 4-MBA (B.Au.MBA.L).

The activity results depicted in figure 3.19 a few folds lower than the activities measured in the previous experiments. This was expected since the disks have half the diameter and consequently 4 times less surface area (and volume). The active disks were made with 25% of the volumes of the previous samples, which is positive from the resources economy point of view, but the activity assays were less sensitive and prone to higher variations.

As seen before, the enzymatic activities of laccase supported on nitrocellulose membranes impregnated with functionalised gold nanoparticles are globally higher that the support with laccase alone. This time, it was introduced a sample (in triplicate) that used the support impregnated with unfunctionalised gold nanoparticles for laccase immobilization. Even the results can be considered equivalent due to the experimental error, it is not surprising this behaviour, giving an important role to nanoparticles functionalisation.

Despite the unclear role of the thiol linker regarding the interaction with the laccase biomolecule, there are advantages in having thiol functionalisation. Given the already discussed high affinity of molecules with thiol groups with gold surfaces, and the presence of five cysteine (CYS) amino acids (–CH_2–SH side chain) in *Trametes versicolor* laccase, if the gold nanoparticles exposed surface is not blocked with a thiolated compound, this can lead to adsorption of *Trv*L trough disulphide bonds, eventually breaking them, compromising the tertiary structure of this protein.

In figure 3.20 it is represented the tertiary structure of this laccase, based on the crystal structure available at Protein Data Bank[55] (PDB) where can be seen the five cysteine residues positions represented in black, delimited by a green line. The four residues indicated by the green double arrows are CYS 85 and CYS 488, covalently linked by a disulphide bond, that also happens for CYS 117 and CYS 205 residues. CYS 488 (top right residue in figure 3.20) is particularly exposed due to its external position and any reaction with the sulphur from its side chain can compromise the protein conformation, affecting eventually the active site. Other cysteine residue, CYS 453, has its sulphur atom directly stabilizing one of the three copper (II) ions, and it is highlighted in figure 3.20 by the dashed ellipse.

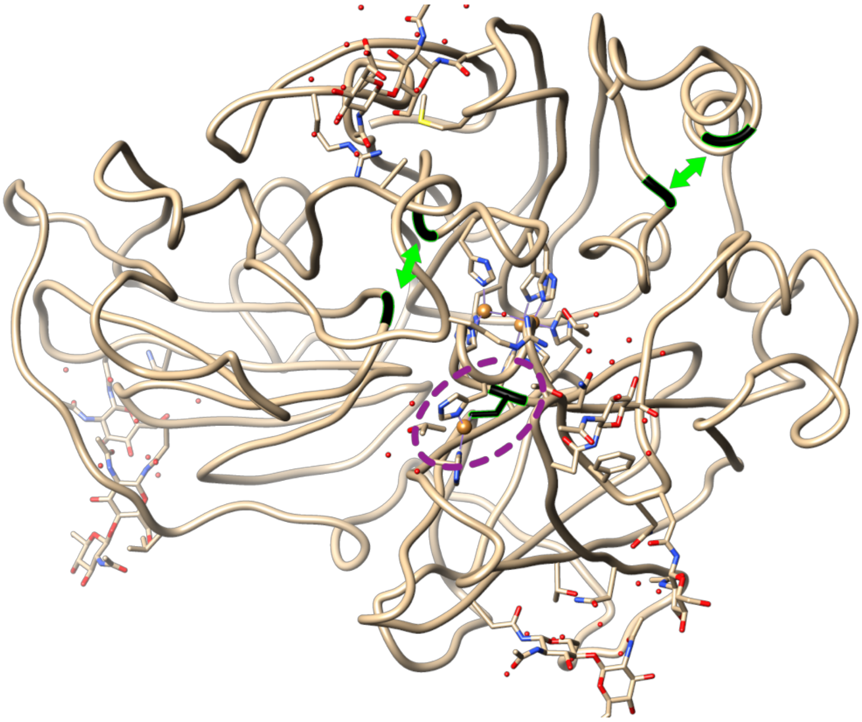

Figure 3.20 – Representation of *Trametes versicolor* laccase crystal structure, showing a 499 amino acids chain, N-Acetyl-D-Glucosamine molecules and water molecules (hydrogen atoms omitted), obtained using UCSF Chimera software[58] and PDB entry 1GYC[55].

3.4. Conclusions

The nanobioconjugation between *Trametes versicolor* laccase and gold nanoparticles revealed to be a difficult process, especially because the incompatibility between the net charge of the enzyme at pH values compatible with a charged capping.

This drawback opened doors towards a laccase immobilization system, comprised by a membrane-like support, gold nanoparticles and laccase. After a selection process regarding the nanoparticles shape and size and also support material, it was found that 15 nm gold nanoparticles deposited on nitrocellulose was a good choice. The 15 nm gold nanoparticles were the ones that better adsorbed onto the supports. The 40 nm gold nanoparticles and gold nanostars presented lower loadings, probably due to their size. From all the supports nitrocellulose revealed to be the better compromise between material resistance, loading in adsorbed nanoparticles, protein affinity and cost.

With nanoparticle immobilization was possible to functionalise them and yet not induce aggregation due to a low pH media. So, it is possible to have a support rich in individualised nanoparticles usable at *Trametes versicolor* laccase optimum pH.

Enzymatic activity tests revealed that every disk containing both laccase and functionalised gold nanoparticles performed better than disks with laccase alone, up to a six-fold increase. Is however important that gold nanoparticles are functionalised, so they do not covalently bind laccase molecules with consequent conformation changes and loss of activity.

Immobilised laccase with an enhanced activity due to the influence of gold nanoparticles in these active disks are promising building blocks for a nanobiosensor.

Some extra studies can be done regarding this work, such as, disk reutilization tests. The possibility of reusing a (bio)catalyst is one of the main advantages of immobilizing it. Additionally, since the purpose of developing these supports is a possible application in nanobiosensors, these gold-enriched supports can be tested in the future as electrodes. Some extra work is probably needed for optimizing the supports for this adaptation. Since the laccase (alone) disks turn from white to red in the presence of these substrate, maybe they can be adapted as an indicator for other compounds that can be substrates of this enzyme and change colour upon degradation/reaction.

3.5. References

1. Z Aksu, Aİ Tatlı, Ö Tunç. A comparative adsorption/biosorption study of Acid Blue 161: Effect of temperature on equilibrium and kinetic parameters. *Chemical Engineering Journal* **2008,** *142* (1), 23-39.

2. M Hartmann, D Jung. Biocatalysis with enzymes immobilized on mesoporous hosts: the status quo and future trends. *Journal of Materials Chemistry* **2010,** *20* (5), 844-857.

3. M Fernandez-Fernandez, MA Sanroman, D Moldes. Recent developments and applications of immobilized laccase. *Biotechnology Advances* **2013,** *31* (8), 1808-25.

4. M Bilal, M Asgher, R Parra-Saldivar, H Hu, W Wang, X Zhang, HMN Iqbal. Immobilized ligninolytic enzymes: An innovative and environmental responsive technology to tackle dye-based industrial pollutants - A review. *Science of the Total Environment* **2017,** *576*, 646-659.

5. C Barrios-Estrada, MJ Rostro-Alanis, AL Parra, MP Belleville, J Sanchez-Marcano, HMN Iqbal, R Parra-Saldivar. Potentialities of active membranes with immobilized laccase for Bisphenol A degradation. *International Journal of Biological Macromolecules* **2018,** *108*, 837-844.

6. P Kaushik, A Malik. Fungal dye decolourization: recent advances and future potential. *Environment International* **2009,** *35* (1), 127-41.

7. M Bilal, M Asgher, HM Iqbal, H Hu, X Zhang. Bio-based degradation of emerging endocrine-disrupting and dye-based pollutants using cross-linked enzyme aggregates. *Environmental Science and Pollution Research* **2017,** *24* (8), 7035-7041.

8. M Bilal, M Asgher, HM Iqbal, H Hu, X Zhang. Biotransformation of lignocellulosic materials into value-added products-A review. *International Journal of Biological Macromolecules* **2017,** *98*, 447-458.

9. S Shoda, H Uyama, J Kadokawa, S Kimura, S Kobayashi. Enzymes as Green Catalysts for Precision Macromolecular Synthesis. *Chemical Reviews* **2016,** *116* (4), 2307-413.

10. M Vera, BL Rivas. Immobilization of *Trametes versicolor* laccase on different PGMA-based polymeric microspheres using response surface methodology: Optimization of conditions. *Journal of Applied Polymer Science* **2017,** *134* (36).

11. M Asgher, S Noreen, M Bilal. Enhancing catalytic functionality of *Trametes versicolor* IBL-04 laccase by immobilization on chitosan microspheres. *Chemical Engineering Research and Design* **2017,** *119*, 1-11.

12. Y Moldes-Diz, M Gamallo, G Eibes, Z Vargas-Osorio, C Vazquez-Vazquez, G Feijoo, JM Lema, MT Moreira. Development of a Superparamagnetic Laccase Nanobiocatalyst for the Enzymatic Biotransformation of Xenobiotics. *Journal of Environmental Engineering* **2018,** *144* (3).

13. M Asgher, S Noreen, M Bilal. Enhancement of catalytic, reusability, and long-term stability features of *Trametes versicolor* IBL-04 laccase immobilized on different polymers. *International Journal of Biological Macromolecules* **2017,** *95*, 54-62.

14. F Müller, B Torger, PJ Allertz, K Jähnichen, S Keßler, M Müller, F Simon, K Salchert, H Mäurer, D Pospiech. Multifunctional crosslinkable itaconic acid copolymers for enzyme immobilization. *European Polymer Journal* **2018,** *102*, 47-55.

15. J Zdarta, K Antecka, R Frankowski, A Zgola-Grzeskowiak, H Ehrlich, T Jesionowski. The effect of operational parameters on the biodegradation of bisphenols by *Trametes versicolor* laccase immobilized on Hippospongia communis spongin scaffolds. *Science of the Total Environment* **2018,** *615*, 784-795.

16. A Apriceno, AM Girelli, FR Scuto. Design of a heterogeneous enzymatic catalyst on chitosan: investigation of the role of conjugation chemistry in the catalytic activity of a Laccase from *Trametes versicolor*. *Journal of Chemical Technology & Biotechnology* **2018,** *93* (5), 1413-1420.

17. E Jahangiri, I Thomas, A Schulze, B Seiwert, H Cabana, D Schlosser. Characterisation of electron beam irradiation-immobilised laccase for application in wastewater treatment. *Science of the Total Environment* **2018,** *624*, 309-322.

18. JMRCA Santos, MH Gil, A Portugal, JT Guthrie. Characterisation of the surface of a cellulosic multi-purpose office paper by inverse gas chromatography. *Cellulose* **2001,** *8* (3), 217-224.

19. X Wang, A Song, L Li, X Li, R Zhang, J Bao. Effect of calcium carbonate in waste office paper on enzymatic hydrolysis efficiency and enhancement procedures. *Korean Journal of Chemical Engineering* **2010,** *28* (2), 550-556.

20. DJ Brose, DT Friesen, JR Lowell, SB McCray, JM Radovich, Hydrophilic polyvinylidene fluoride membranes. Google Patents: 1995.

21. J Jia, B Wang, A Wu, G Cheng, Z Li, S Dong. A Method to Construct a Third-Generation Horseradish Peroxidase Biosensor: Self-Assembling Gold Nanoparticles to Three-Dimensional Sol−Gel Network. *Analytical Chemistry* **2002,** *74* (9), 2217-2223.

22. C Shan, H Yang, D Han, Q Zhang, A Ivaska, L Niu. Graphene/AuNPs/chitosan nanocomposites film for glucose biosensing. *Biosensors and Bioelectronics* **2010,** *25* (5), 1070-4.

23. MT Castañeda, S Alegret, A Merkoçi. Electrochemical Sensing of DNA Using Gold Nanoparticles. *Electroanalysis* **2007,** *19* (7-8), 743-753.

24. JM Pingarrón, P Yáñez-Sedeño, A González-Cortés. Gold nanoparticle-based electrochemical biosensors. *Electrochimica Acta* **2008,** *53* (19), 5848-5866.

25. W Putzbach, NJ Ronkainen. Immobilization techniques in the fabrication of nanomaterial-based electrochemical biosensors: a review. *Sensors* **2013,** *13* (4), 4811-40.

26. Y Wan, Y Su, X Zhu, G Liu, C Fan. Development of electrochemical immunosensors towards point of care diagnostics. *Biosensors and Bioelectronics* **2013,** *47*, 1-11.

27. M Holzinger, A Le Goff, S Cosnier. Nanomaterials for biosensing applications: a review. *Frontiers in Chemistry* **2014,** *2*, 63.

28. M Diaconu, SC Litescu, GL Radu. Laccase–MWCNT–chitosan biosensor—A new tool for total polyphenolic content evaluation from in vitro cultivated plants. *Sensors and Actuators B: Chemical* **2010,** *145* (2), 800-806.

29. C Lanzellotto, G Favero, ML Antonelli, C Tortolini, S Cannistraro, E Coppari, F Mazzei. Nanostructured enzymatic biosensor based on fullerene and gold nanoparticles: preparation, characterization and analytical applications. *Biosensors and Bioelectronics* **2014,** *55*, 430-7.

30. J Liu, J Niu, L Yin, F Jiang. In situ encapsulation of laccase in nanofibers by electrospinning for development of enzyme biosensors for chlorophenol monitoring. *Analyst* **2011,** *136* (22), 4802-8.

31. G Favero, G Fusco, F Mazzei, F Tasca, R Antiochia. Electrochemical Characterization of Graphene and MWCNT Screen-Printed Electrodes Modified with AuNPs for Laccase Biosensor Development. *Nanomaterials (Basel)* **2015,** *5* (4), 1995-2006.

32. G Fusco, L Chronopoulou, L Galantini, A Zerillo, ZM Rasik, R Antiochia, G Favero, A D'Annibale, C Palocci, F Mazzei. Evaluation of novel Fmoc-tripeptide based hydrogels

as immobilization supports for electrochemical biosensors. *Microchemical Journal* **2018,** *137*, 105-110.

33. PA Hassan, S Rana, G Verma. Making sense of Brownian motion: colloid characterization by dynamic light scattering. *Langmuir* **2015,** *31* (1), 3-12.

34. S Skoglund, J Hedberg, E Yunda, A Godymchuk, E Blomberg, I Odnevall Wallinder. Difficulties and flaws in performing accurate determinations of zeta potentials of metal nanoparticles in complex solutions-Four case studies. *PLoS One* **2017,** *12* (7), e0181735.

35. A Malloy, B Carr. NanoParticle Tracking Analysis - The Halo™ System. *Particle & Particle Systems Characterization* **2006,** *23* (2), 197-204.

36. V Filipe, A Hawe, W Jiskoot. Critical evaluation of Nanoparticle Tracking Analysis (NTA) by NanoSight for the measurement of nanoparticles and protein aggregates. *Pharmaceutical Research* **2010,** *27* (5), 796-810.

37. NG Bastús, J Comenge, V Puntes. Kinetically controlled seeded growth synthesis of citrate-stabilized gold nanoparticles of up to 200 nm: size focusing versus Ostwald ripening. *Langmuir* **2011,** *27* (17), 11098-11105.

38. W Haiss, NT Thanh, J Aveyard, DG Fernig. Determination of size and concentration of gold nanoparticles from UV-vis spectra. *Analytical Chemistry* **2007,** *79* (11), 4215-21.

39. H Yuan, CG Khoury, H Hwang, CM Wilson, GA Grant, T Vo-Dinh. Gold nanostars: surfactant-free synthesis, 3D modelling, and two-photon photoluminescence imaging. *Nanotechnology* **2012,** *23* (7), 075102.

40. PK Smith, RI Krohn, GT Hermanson, AK Mallia, FH Gartner, MD Provenzano, EK Fujimoto, NM Goeke, BJ Olson, DC Klenk. Measurement of protein using bicinchoninic acid. *Analytical Biochemistry* **1985,** *150* (1), 76-85.

41. ISO 838:1974. In *Paper - Holes for general filing purposes - Specifications*, 1974.

42. JP Ride. The effect of induced lignification on the resistance of wheat cell walls to fungal degradation. *Physiological Plant Pathology* **1980,** *16* (2), 187-196.

43. E Calle-Serrano. Preparation of membranes incorporating nanobioconjugates of laccase from *Trametes versicolor* and gold nanoparticles for the development of bisensors. MSc Thesis, Universidade do Porto, Porto, 2015.

44. M Belda-Garrido. Bionanoconjugados de nanopartículas de oro y lacasa para utilización en biosensores. BSc Report, Universidade do Porto, Porto, 2015.

45. J Turkevich, PC Stevenson, J Hillier. A study of the nucleation and growth processes in the synthesis of colloidal gold. *Discussions of the Faraday Society* **1951,** *11*.

46. J Kimling, M Maier, B Okenve, V Kotaidis, H Ballot, A Plech. Turkevich method for gold nanoparticle synthesis revisited. *The Journal of Physical Chemistry B* **2006,** *110* (32), 15700-7.

47. K Zabetakis, WE Ghann, S Kumar, M-C Daniel. Effect of high gold salt concentrations on the size and polydispersity of gold nanoparticles prepared by an extended Turkevich–Frens method. *Gold Bulletin* **2012,** *45* (4), 203-211.

48. H Chen, L Shao, Q Li, J Wang. Gold nanorods and their plasmonic properties. *Chemical Society Reviews* **2013,** *42* (7), 2679-724.

49. P Eaton, P Quaresma, C Soares, C Neves, M Peixoto de Almeida, E Pereira, P West. A direct comparison of experimental methods to measure dimensions of synthetic nanoparticles. *Ultramicroscopy* **2017,** *182*, 179-190.

50. CA Schneider, WS Rasband, KW Eliceiri. NIH Image to ImageJ: 25 years of image analysis. *Nature Methods* **2012,** *9* (7), 671-675.

51. SH Brewer, WR Glomm, MC Johnson, MK Knag, S Franzen. Probing BSA binding to citrate-coated gold nanoparticles and surfaces. *Langmuir* **2005,** *21* (20), 9303-7.

52. U Wollenberger, Third generation biosensors - integrating recognition and transduction in electrochemical sensors. In *Comprehensive Analytical Chemistry*, Elsevier: 2005; Vol. 44, pp 65-130.

53. Structure Dependence of the Surface pKa of Mercaptoundecanoic Acid SAM on Gold.

54. K Piontek, M Antorini, T Choinowski. Crystal structure of a laccase from the fungus *Trametes versicolor* at 1.90-A resolution containing a full complement of coppers. *Journal of Biological Chemistry* **2002,** *277* (40), 37663-9.

55. PDB Crystal Structure 1GYC. 2002.

56. WN Burnette. “Western Blotting”: Electrophoretic transfer of proteins from sodium dodecyl sulfate-polyacrylamide gels to unmodified nitrocellulose and radiographic detection with antibody and radioiodinated protein A. *Analytical Biochemistry* **1981,** *112* (2), 195-203.

57. MD Porter, TB Bright, DL Allara, CED Chidsey. Spontaneously organized molecular assemblies. 4. Structural characterization of n-alkyl thiol monolayers on gold by optical

ellipsometry, infrared spectroscopy, and electrochemistry. *Journal of the American Chemical Society* **1987,** *109* (12), 3559-3568.

58. EF Pettersen, TD Goddard, CC Huang, GS Couch, DM Greenblatt, EC Meng, TE Ferrin. UCSF Chimera – A visualization system for exploratory research and analysis. *Journal of Computational Chemistry* **2004,** *25* (13), 1605-1612.

Nanobioconjugates for Wine Fingerprinting by Surface-Enhanced Raman Spectroscopy

4

4.1. Introduction

This chapter starts a new approach on nanobioconjugation on this thesis. After the gold nanospheres were proven to improve enzymatic activity, in these new three chapters (4–6) the focus goes to star-shaped silver nanoparticles and their ability to improve Raman spectroscopy measurements, by means of the surface-enhancement phenomenon. Given the fact that nanoparticles in general and silver nanostars (AgNSs) in particular are capable of binding (bio)molecules that have affinity to their surfaces, surface-enhanced Raman spectroscopy (SERS) is here explored.

The main goal of this chapter is to use SERS for differentiating wines based on a statistic treatment – principal component analysis (PCA) – of the acquired spectra. This fingerprinting technique has the objective of avoiding laborious and/or costly sample analysis, including pre-treatment processes.

4.1.1. Wine characterization

The gold standards for wine characterization are chromatography methods, especially liquid chromatography. Methods like liquid chromatography coupled to mass spectrometry (LC–MS) and high-performance liquid chromatography (HPLC) are typically used, and efficient, but preliminary fractionation and purification steps are often needed before any analytical procedure.[1] The phenolic fraction is typically analysed by these chromatographic methods.

Phenolic composition is one of the most important quality parameters of wines. This composition is directly related to wine organoleptic characteristics such as colour, astringency, and bitterness.[2] They even show biological properties of interest, related to the antioxidant capacity. Major polyphenolic compounds occurring in wines are (+)–Catechin, (-)–Epicatechin, caftaric acid, coutaric acid, fertaric acid, *p*–coumaric acid, caffeic acid and gallic acid.[2] All of them can contribute to wine fingerprinting, especially for red wines which are richer in these compounds.

4.1.2. Wine fingerprinting

Several techniques were already described for wine discrimination based on the statistical analysis of their outputs (typically spectra). Red wines were analysed by fluorescence spectroscopy and data analysis by parallel factor analysis (PARAFAC) allowed to distinguish wines from different world regions (*e.g.* Australia, Chile, Spain, United States of America).[3] Also for red wines, fingerprinting based on similarity index (SI) analysis of mid-infrared (MIR) spectra was also reported.[4] Other described technique for red wine fingerprinting was matrix-assisted laser desorption/ionization mass spectrometry (MALDI–MS).[1] A group of four techniques were compared for the same batch of red wines (from only two different appellations): near infrared spectroscopy (NIR), ultraviolet-visible spectroscopy (UV-Vis), a headspace-mass "artificial nose" and a voltammetric "artificial tongue".[5] The best separation, determined by principal component analysis (PCA) and linear discriminant analysis (LDA), was achieved by the spectroscopic techniques, which is excellent, given their speed and ease of use. Chromatography techniques such as high-performance thin-layer chromatography (but with no sample pre-treatment) were also used to discriminate red wines, with the help of PCA.[6]

White wines are poorer in organic content (*e.g.* polyphenols), so the variety of compounds that can contribute for a fingerprint is much lower. Maybe because of this, most of the wine fingerprint reports are for red wines. A more complex analysis was described of Italian white wines, based on the determination of the ratio between the amounts of ^{87}Sr and ^{86}Sr.[7] This ^{87}Sr/^{86}Sr ratio is related to the geologic properties of vineyards terrain, however the relation between ^{87}Sr/^{86}Sr in soil and wines was not confirmed for all types of soil. This type of isotopic analysis was also used with a new set of white whites (together with a set of red wines).[8] White wines were also discriminated by MALDI–MS[9] and by a combination of NIR, MIR and Raman spectroscopies[10].

In sum, it was already demonstrated that is possible to differentiate wines from different continents[3], big countries like Australia[4] or from a specific region[5]. The aim of this work is to confirm if wine regions at Portugal mainland territory (only distance from each other a few hundreds of kilometres) can also be discriminated.

4.1.3. Portuguese wines

Portuguese wines can be organised in two main types: *Verde* and *Maduro*. Each one of these categories have white and red wines. Green wine (*Verde*) is typical from *Minho* Wine Region, on northwestern Portugal.[11] Across the remaining territory is essentially produced *Maduro* wine, original from areas like *Douro* (northeast) and *Alentejo* (south) wine regions. The main difference between *Verde* and *Maduro* wines is essentially the harvesting time, which is done at an earlier stage of maturation for green wine.[11]

This incomplete maturation stage influences the profile of compounds responsible for the organoleptic properties of wine. Between the several *Maduro* wine regions the main differences are due to the climate conditions. For example, *Douro* region has a lower average temperature and higher precipitation levels when compared to *Alentejo*.[11-13] This is also expected to influence the chemical composition of wines.

4.2. Methods

This section enlists the main equipment, the reagents and the experimental procedures. All the reagents were used as purchased, with no further steps of purification.

For the synthesis, a KD Scientific KDS 200 syringe pump, holding a BD 60 mL plastic syringe was used. Centrifugations were done in a Sigma 30K centrifuge, with a 19776H rotor. Ultraviolet-visible spectroscopy (UV-Vis) was performed using a Varian Cary 50 Bio spectrophotometer. Dynamic light scattering (DLS) and zeta potential (ZP) measurements were made in a Malvern Zetasizer Nano ZS equipment, with a 633 nm laser – results are an average of three measurements for the same sample, performed at 25 °C, with light detection at 173° (DLS) and at 17° using the backscatter mode (ZP). Nanoparticle tracking analysis (NTA) was done using a Malvern Nanosight NS300 equipped with a 642 nm (red) laser module, by acquisition of 5 videos of 1 minute each in different sample areas.

In surface-enhanced Raman spectroscopy measurements, a Renishaw InVia Raman microscope, coupled with 442 nm 80 mW (He-Cd), 532 nm 200 mW (diode), 633 nm 17 mW (He-Ne), 785/830 nm 300 mW (diode) lasers was used. Gratings of 1200 l/mm and 1800 l/mm were used, the first for 785 nm measurements and the second for 442 nm, 532 nm and 633 nm. The system is equipped with a CCD camera detector, with a 1040 x 256 resolution. The objective used had a 50x magnification. This equipment was operated at *Facultatea de Fizică* from *Universitatea Babeș-Bolyai* (*FFUBB*).

4.2.1. Synthesis of silver nanostars (AgNSs)

The star-shaped silver nanoparticles were synthesised based in a protocol from Garcia-Leis *et al.*[14].The following reagents were used: silver nitrate 99.9999% (Aldrich), hydroxylamine solution 50% wt. in water 99.999% (Aldrich), sodium hydroxide 98% (Fisher) and trisodium citrate dihydrate 99.0% (Merck). All the glass material was previously treated with *aqua regia* and rinsed abundantly with deionized water, followed by ultrapure water (18.2 MΩ·cm at 25 °C). All the solutions were prepared with ultrapure water.

For the synthesis reaction, 2.5 mL of a 50 mM sodium hydroxide solution (125 μM) and 2.5 of a 60 mM hydroxylamine solution (150 μM) were mixed in beaker and, immediately after, 45 mL of a 1 mM silver nitrate solution (45 μM) was added dropwise from a syringe, using a syringe pump at a 45 mL/min injection rate. After 90 seconds, 500 µl of a 1.5% wt. trisodium citrate (dihydrate) solution was added to the mixture. The reaction vessel was kept protected from light for a 3-hour reaction period.

After this 3-hour period, the content of the five beakers was mixed and the resultant batch (250 mL) of AgNSs suspension was centrifuged for 12 minutes at a relative centrifugal force (RCF) of 1600·g. The pellet was resuspended in ultrapure water (up to 10% of the initial volume) and stored in a glass vial.

4.2.2. Wines

For this work, five different Portuguese wines were chosen, three white and two red. *Portal de S. Braz* from *Alentejo* region (MWA), *Burmester* from *Douro* region (MWD), and *Amarante* from Portugal northwestern region (VWN), were the selected white wines. Red wines were also chosen from *Alentejo* and *Douro* regions, with the same brands: *Portal de S. Braz* from *Alentejo* region (MRA) and *Burmester* from *Douro* region (MRD). Four of the five wines are from a type called *Maduro*, the only exception is VWN, that is from the other type called *Verde* (green wine).

For simplification, the wines will be mentioned using a three-letter code based on their type, colour and origin. Table 4.1 summarizes the wine characteristics for this work.

Table 4.1 – Key for wine samples codes.

Wine Type 1st letter		Wine Colour 2nd letter		Portuguese Region 3rd letter	
M	Maduro	R	Red	A	Alentejo
V	Verde	W	White	D	Douro
				N	Norte Litoral

Wines were used as direct samples, with no further treatments.

4.2.3. Silver nanostars functionalization with wine molecules

Nanobioconjugation was performed by one of three main approaches:

A) synthesis of silver nanostars in wine, with extra reducing agents (section 4.2.3.1) and without extra reducing agents (section 4.3.2.2);

B) capping previously synthesised silver nanostars with wine molecules over an incubation period (section 4.3.2.3);

C) capping previously synthesised silver nanostars with wine molecules without an incubation period (section 4.3.2.4).

For data to be treated by principal component analysis, a fresh set of experiments is described in section 4.3.2.5, inspired in the results from approaches B and C listed above.

For simplicity, tables 4.2 to 4.6 only show parameters that are variable in the respective experiment.

4.2.3.1. Silver nanostars synthesised in wine with added reducing agents

For approach A, no reagents were directly dissolved in wine, *i.e.*, the reaction was made in wine, but the reagents were added as aqueous solutions. The final volume was also lower (1-2 mL), in order to reduce the volume of wine necessary for each analysis.

The first strategy from approach A started with just two wines, and the silver nanostars were tentatively synthesized with the necessary changes to the protocol described in section 4.2.1 in order to include the wine (50% of the total volume) in the system. In table 4.2 is summarized the experiment and the values are presented in function of concentration used in the original synthesis (described in section 4.2.1).

For example, for sample 03WSHBN0 that used 2.5x the concentrations of reagents used in the original synthesis, however here for a final volume of 2 mL, the tube was prepared with: 1000 µl of wine, 200 µl of AgNSs 0.1 nM, 50 µl of hydroxylamine 300 mM, 50 µl of sodium hydroxide 250 mM, 180 µl of silver nitrate 25 mM and the remaining volume (520 µl) of ultrapure water.

Table 4.2 – Sample composition for extra silver nanostars synthesised in wine, with additional reducing agents.

Sample Code	Wine	Silver Nanostars	Hydroxilamine	Sodium Hydroxide	Silver Nitrate	Citrate
01WS00N0	MWA	+	-	-	2.5x	-
02WS00N0		+	-	-	5x	-
03WSHBN0		+	2.5x	2.5x	2.5x	-
04WSHBN0		+	2.5x	2.5x + N	2.5x	-
05WSHBN0		+	1x	1x	1x	-
06W0HBN0		-	2.5x	2.5x	2.5x	-
07W0HBN0		-	5x	5x + N	5x	-
08W0HBNC		-	2.5x	2.5x	2.5x	2.5x
09RS00N0	MRA	+	-	-	5x	-
10RSHBN0		+	2.5x	2.5x + N	2.5x	-
11R0HBN0		-	5x	5x + N	5x	-
12R0HBNC		-	2.5x	2.5x	2.5x	2.5x

Notes +: present; -: absent; a – N: equimolar amount of hydroxylamine.

Table 4.2 summarizes then the first set of samples, prepared in 2 mL microcentrifuge tubes. It was added to the tubes 1000 µl of a red or a white wine, both from *Alentejo* region. Then, a volume of 200 µl of a 0.1 nM AgNSs suspension was added and dispersed into the wine. An adding sequence of hydroxylamine, sodium hydroxide, silver nitrate and sodium citrate was performed in similar timings to the ones described in silver nanostars synthesis, with concentrations equal (1x), 2.5 and 5 times higher than those used in the original synthesis. For the tubes that used the same concentration of the synthesis (1x), the volumes of 300 mM hydroxylamine hydrochloride solution, 250 mM sodium hydroxide solution, 25 mM silver nitrate solution and 60 mM trisodium citrate solution were, respectively, 20 µl, 20 µl, 72 µl and 20 µl. For the other cases, a correction factor of 2.5x or 5x was applied to these volumes. The entries with a minus signal (-) mean that the component/reagent was not included in that sample. For the sodium hydroxide, when "+ N" is shown in the table 4.2, it means that an extra volume was added to neutralize the hydrochloride introduced in the system by the hydroxylamine powder. Tubes were filled up to a 2000 µl final volume with ultrapure water. Reactions were performed for 20 hours, at room temperature and protected from light.

4.2.3.2. Silver nanostars synthesised in wine without added reducing agents

Other set of samples in line with approach A were analysed, replacing the previous wines by two different white wines, excluding external reducing agents, increasing the amount of silver nitrate added up to 10 times the amount used on AgNSs original synthesis and increasing the reaction time up to 44 hours. The samples were prepared in 2 mL microcentrifuge tubes, always with a 2000 µl total volume. It was added to the tubes 1000 µl of one of the two different white wines, or water for control. Then, a volume of 200 µl of a 0.1 nM AgNSs suspension was added and dispersed into the wine. Finally, 360 µl or 720 µl of a 25 mM silver nitrate solution was added, in order to introduce 5 or 10 times the amount proportionally found in AgNSs original synthesis, respectively. The reactions occurred overnight (20 hours) or for 44 hours, at room temperature. This is recapped in table 4.3.

Table 4.3 – Sample composition for extra silver nanostars synthesised in wine, without additional reducing agents.

Sample Code	Wine	Silver Nitrate	Time (h)
01WS01	MWD	-	20
02WSN1		5x	20
03WSN1		10x	20
04WSN2		10x	44
05VS01	VWN	-	20
06VSN1		5x	20
07VSN1		10x	20
08VSN2		10x	44
09CS01	-	-	20
10CSN1		5x	20
11CSN1		10x	20
12CSN2		10x	44

Note -: absent.

4.2.3.3. Silver nanostars functionalization by wine compounds with incubation

Going for approach B, the same wines used in 4.2.3.2 section were incubated with the same amount and proportion of AgNSs described in sections 4.2.3.1 and 4.2.3.2 (1x), with one quarter (0.25x) and twice (2x) the amount of AgNSs, always to 1000 µl of wine. There were also controls (wine replaced by ultrapure water) prepared in the same conditions. A sample with MWA wine was also included, however only prepared with AgNSs at the concentration already referred as 1x. All the tubes were filled with ultrapure water up to a 2000 µl final volume. This is summarised in table 4.4.

Table 4.4 – Sample composition for SERS measurements using silver nanostars decorated with wine molecules.

Sample Code	Wine	Silver Nanostars
01WS4	MWD	1x
02WS1		0.25x
03WS8		2x
04VS4	VWN	1x
05VS1		0.25x
06VS8		2x
07CS4	-	1x
08CS1		0.25x
09CS8		2x
10AS4	MWA	1x

Note -: absent.

4.2.3.4. Silver nanostars functionalization by wine compounds without incubation

The “mix and read” approach C was performed in small volumes, in a total volume of 20 µl. The proportions in volume of wine to 0.1 nM silver nanostars are listed in table 4.5 below. Sample components were mixed by “up and down” pipetting and immediately read.

Table 4.5 – Tubes composition for SERS measurements of wines, enhanced by silver nanostars.

Sample Code	Wine	Wine	:	Silver Nanostars
A1S0	MWA	1	:	0
A1S1		1	:	1
A1S3		1	:	3
A3S1		3	:	1
D1S0	MWD	1	:	0
D1S1		1	:	1
D1S3		1	:	3
D3S1		3	:	1
V1S0	VWN	1	:	0
V1S1		1	:	1
V1S3		1	:	3
V3S1		3	:	1
C0S1	-	0	:	1

Note -: absent.

4.2.3.5. Data collection for principal component analysis of three protocols

The final experiment aimed to collect 10 spectra per sample, to be assessed by principal component analysis. Three different wines were analysed by three different protocols:

Protocol 1: 1000 µl of wine and 100 µl 0.1 nM AgNS were incubated overnight;

Protocol 2: 10 µl of wine and 10 µl 0.1 nM AgNS were incubated overnight;

Protocol 3: 10 µl of wine and 10 µl 0.1 nM AgNS were mixed and read immediately.

All samples were prepared in duplicate.

The correspondences between sample code, wine and protocol are listed in table 4.6.

Table 4.6 – Sample codification, grouped by protocol.

Sample Code	Wine	Protocol
AB1	MWA	1
DB1	MWD	
VV1	VWN	
AB2	MWA	2
DB2	MWD	
VV2	VWN	
AB3	MWA	3
DB3	MWD	
VV3	VWN	

4.2.4. Raman/SERS measurements

Right before Raman/SERS measurements, samples containing nanoparticles were centrifuged for 5 minutes at a RCF of 1600·g, and then 99% of the supernatant volume was removed. The pellet rich in nanobioconjugates was dispersed in the remaining supernatant by “up and down” pipetting. From this volume 10 µl aliquots for analysis were taken. These steps were not applied to approach C protocols, *i.e.*, all section 4.2.3.4 and protocols 2 and 3 of section 4.2.3.5, where the final volume was 20 µl from the beginning, but all the measurements were performed also in 10 µl aliquots.

The aliquots were placed in a microscope glass slide, wrapped in one layer of tin foil. When justifiable, spectra of the external elements to the sample, like the tin foil, were acquired. This tin foil is in the origin of some peaks found in spectra collected with 633 nm and 785 nm lasers. This behaviour is depicted in figure 4.17.

Signal acquisition parameters like laser power and acquisition time changed accordingly the protocol, but the batches of spectra analysed together were acquired on the same conditions. The number of acquisitions was always two per sample and the acquisition times were between 4 and 10 seconds.

4.2.5. Principal component analysis

The principal component analysis (PCA) was performed using CAMO The Unscrambler® X 10.4.1 software. Before the PCA itself, spectra underwent a data pre-treatment process, either by baseline linear correction (BLC) or by standard normal variate (SNV).

For samples that had PCA applied to (section 4.2.3.5), ten spectra were collected per wine. Five spectra were collected in five different spots in both duplicates.

4.3. Results and Discussion

After the section depicting AgNSs characterisation (4.3.1), the SERS spectra results are organised by approach to AgNSs decoration method (section 4.3.2). Finally, data for principal component analysis and PCA results are described in section 4.3.3.

4.3.1. Synthesis of silver nanostars (AgNSs)

The assessment of this batch of silver nanostars was made using ultraviolet-visible spectroscopy (UV-Vis) and nanoparticle tracking analysis (NTA). Its spectrum can be seen in figure 4.1 and its size distribution is depicted in figure 4.2.

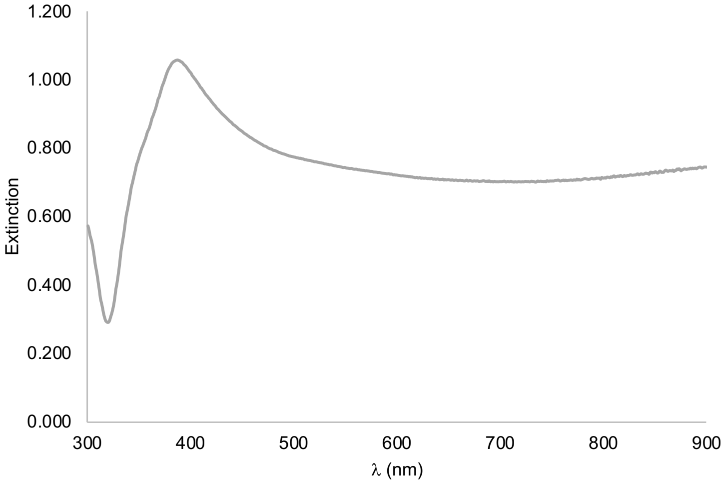

Figure 4.1 – Silver nanostars UV-visible spectrum.

The spectrum depicted in figure 4.1 is a typical spectrum for this type of nanoparticles. The spectrum has its maximum at a wavelength slightly below 400 nm, and the rest of the spectrum towards higher wavelength values, up to the near infrared region, keeps its intensity very high. This behaviour was the expected and it is due to the great multiplicity regarding the number of arms per star, the size of the arms and consequently the size of the final star-shaped nanoparticles.

Given the previous experience on AgNSs synthesis in our research group, it is known that concentration of silver nanostars is typically 0.01 nM after synthesis (on the

50 mL reaction volume). After centrifugation and resuspension into 10% of the initial volume (5 mL), the concentration is 0.1 nM. The centrifugation of the synthesised silver nanoparticles is practically lossless in terms of number of particles. This batch is no exception, with a concentration of 0.10 ± 0.01 nM, determined by NTA. Also determined by NTA, was the hydrodynamic diameter distribution depicted in figure 4.2.

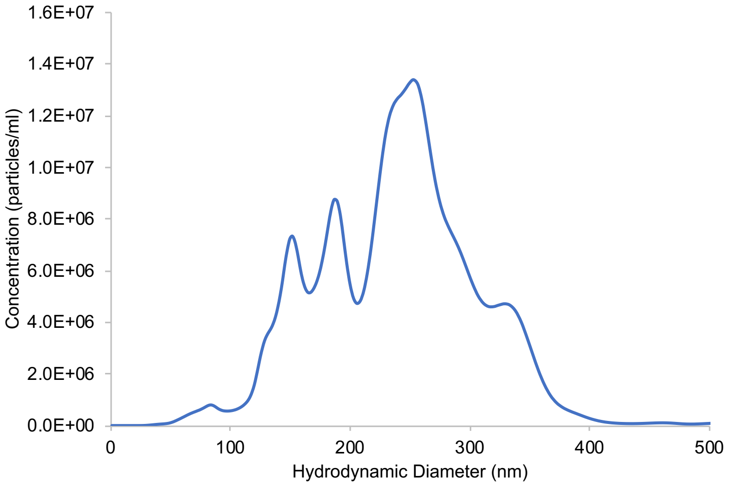

Figure 4.2 – Hydrodynamic diameter distribution for silver nanostars, obtained by NTA.

From the merged results of the five captured videos, it was determined a mean size of 217 nm, a mode of 253 nm and a standard deviation (SD) of 69 nm. This high SD value is in line with the multiplicity of sizes already discussed after UV-Vis analysis.

The synthesis was successfully performed, and the available characterization data is according to the literature[14]. Despite the lack of transmission electronic microscopy (TEM) and scanning electron microscopy (SEM) analysis for this batch, UV-Vis and NTA data showed that the morphology of the AgNSs is similar to the TEM and SEM micrographs shown in the two following chapters.

4.3.2. Nanobioconjugation

In this section, firstly are shown the results for AgNSs synthesis in wine, either with the help of external reductants (4.3.2.1) or without them (4.3.2.2). Then results for pre-synthesised AgNSs incubated in wine are shown (4.3.2.3). Results for pre-synthesised AgNSs conjugation without incubation time (“mix ad read”) are finally presented and discussed on section 4.3.2.4.

It is important to notice that all the spectra obtained in the presence of AgNSs showed a strong enhancement of the Raman signal. Later in section 4.3.2.4 there are depicted examples of the Raman spectra of the three wines and the respective SERS spectra, acquired under the influence of AgNSs.

4.3.2.1. Silver nanostars synthesised in wine with added reducing agents

The measurements related to experiments summarized on table 4.2 were performed only with the red (633 nm) and infrared (785 nm) lasers. Figures 4.3 to 4.6 show spectra obtained with the 633 nm laser and figure 4.7 shows spectra collected using the 785 nm laser.

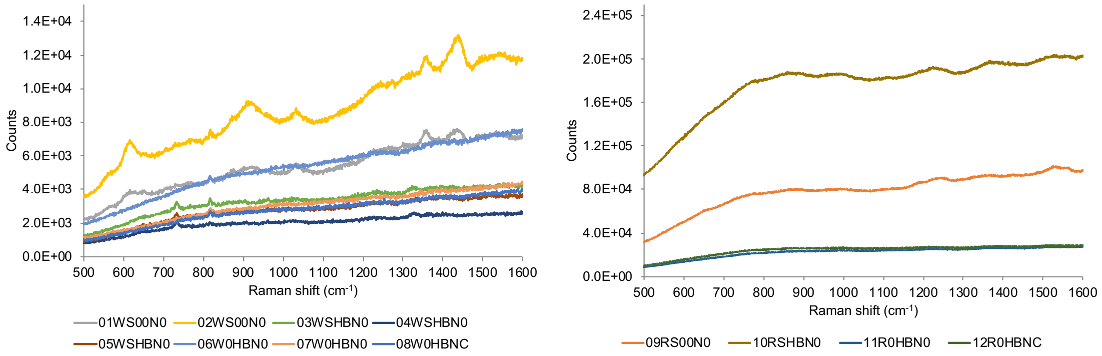

Figure 4.3 – Spectra obtained for the white wine MWA (left) and the red wine MRA (right), for all the tested conditions listed in table 4.2. Collected using a 633 nm laser.

Comparing the two groups of spectra shown in figure 4.3, it is clear that the spectra with well-defined peaks are on the group of the white wine (left), whereas the spectra from red wine present broad and less intense bands.

The profile seen in red wine spectra arises from the fluorescence effect due to phenolic compounds, like anthocyanins and tannins, abundantly found in red wines[3]. Since this phenomenon strongly compromises a proper signal acquisition, with a negative impact in the peak definition, the white wine samples were used to study the "synthesis in wine" approach.

SERS spectra of samples 01WS00N0 and 02WS00N0 – samples with pre-synthesized silver nanostars and silver nitrate, but the latter with twice the amount of the reagent – are shown in figure 4.4.

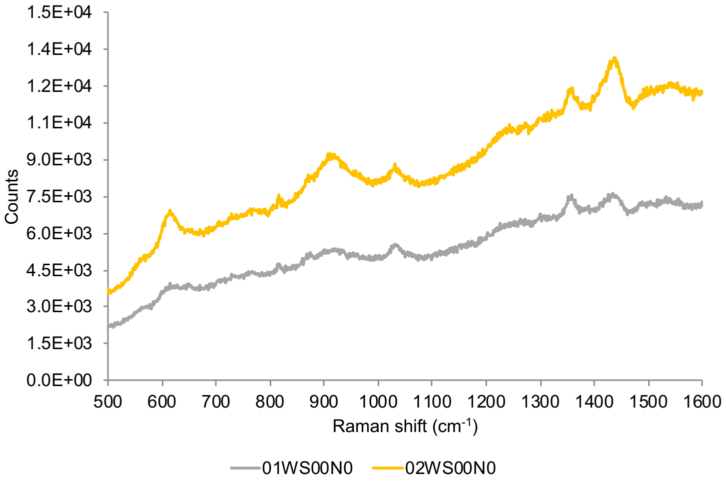

Figure 4.4 – Spectra for samples with silver nitrate added to silver nanostars in white wine. Yellow trace represents the sample with twice the amount of silver nitrate relatively to the other sample (grey trace). Collected using a 633 nm laser.

From all the spectra, those presented in figure 4.4 are the most structured. Nevertheless, bands detected at 1044 cm^{-1} and 1350 cm^{-1} are characteristic of nitrate.[15] Since the spectrum with the most intense signal corresponds to the sample with twice the amount of silver nitrate added, it is reasonable to assign the signal to nitrate ion coming from the silver nitrate. However, at least some of the peaks detected in the spectra can also arise from wine components, enhanced by new silver nanoparticles formed through reduction of silver (I) by reducing agents from the wine. This is also consistent with more intense signals for the sample where a higher amount of $AgNO_3$ was used, since in this case a higher final concentration of nanoparticles would be formed. This will be clarified later in section 4.3.2.2.

Other samples where silver nitrate is present, but together with the remaining reactants used for silver nanostars synthesis, the information is not so rich, with no gain in terms of producing spectra that can characterize wine, as seen in figure 4.4.

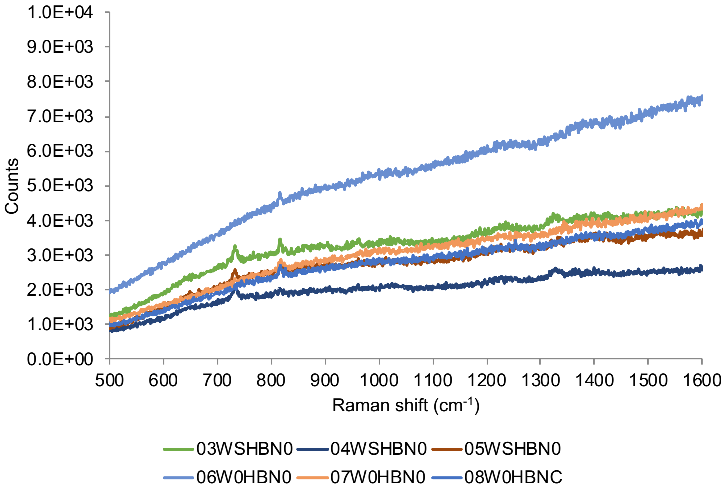

Figure 4.5 – Spectra for samples using the reagents (all or part) for silver nanostars synthesis in wine. Collected using a 633 nm laser.

Next, results obtained with a 785 nm laser are presented. Regarding the red wine, no useful information was retrieved due to fluorescence (omitted for simplicity), and regarding the white wine the results are shown below in figure 4.6.

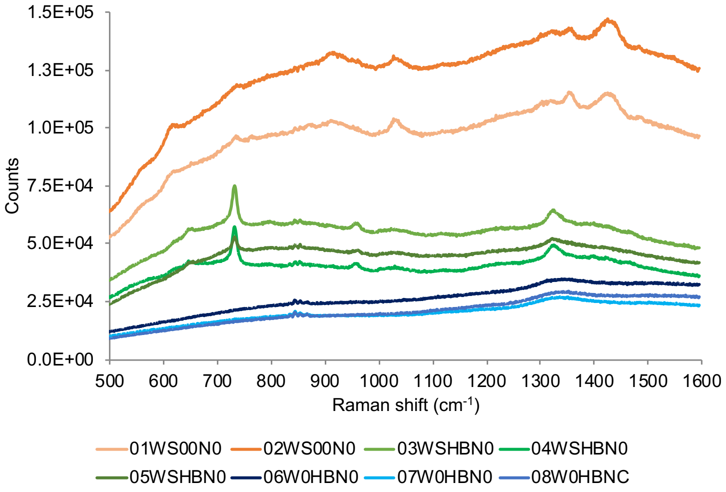

Figure 4.6 – Spectra obtained for the white wine MWA, for all the tested conditions listed in table 4.2. Collected using a 785 nm laser.

Three groups of spectra can be seen in figure 4.6. Each group is plotted in shades of blue, green or orange. Blue spectra are from samples lacking AgNSs. The spectra are barely a flat line, so very scarce information can be extracted from them. Green spectra are the ones where all the reagents necessary to AgNSs formation were available (in less quantity in 05WSHBN0 sample). The two orange spectra present a profile very similar to the ones shown in figure 4.4, exhibiting the highest number of peaks.

For the blue group, it was expected this absence of peaks, since, under the same acquisition conditions, there are no added AgNSs for a SERS effect. The peaks in green group seem to be related to the reagents, namely hydroxylamine and sodium hydroxide used in excess, since the peaks shown in the orange spectra (just silver nitrate added to wine, with no reductant) are missing, pointing to the full reduction of the silver nitrate.

The multiple peaks present around 850 cm^{-1} in all spectra come from the tin foil used as support, particularly noticeable with 785 nm laser.

4.3.2.2. Silver nanostars synthesised in wine without added reducing agents

Remembering what was attempted in this section, the aim is to get characteristic wine spectra, improved by the synthesis of silver nanostars in wine, that can use wine molecules as capping agents, *i.e.*, performing SERS of these molecules. So far, the red wine provided poor data, and the use of external reductants for silver (I) gave origin to very plain and uninformative spectra, therefore red wine samples and external reductants addition method for white wine samples were abandoned.

The best option from section 4.3.2.1 data were the samples using just silver nitrate in wine, already enriched with silver nanostars. Transferring the reduction role exclusively to the wines, we were looking for consequences in spectra coming from different reductant compound composition, characteristic of each wine. Given this information, the following data deals with two white wines, with different silver nitrate concentrations (starting on the maximum of the last experiment, up to twice this value) and using higher times for silver nanoparticles formation, since the reaction occurs at room temperature and the reducing agents available in white wines are in lower quantity (compared to red wines). Additionally, four lasers (blue, green, red and infrared) were used.

In figure 4.7 are depicted all spectra obtained with the 442 nm laser for the samples with overnight reaction.

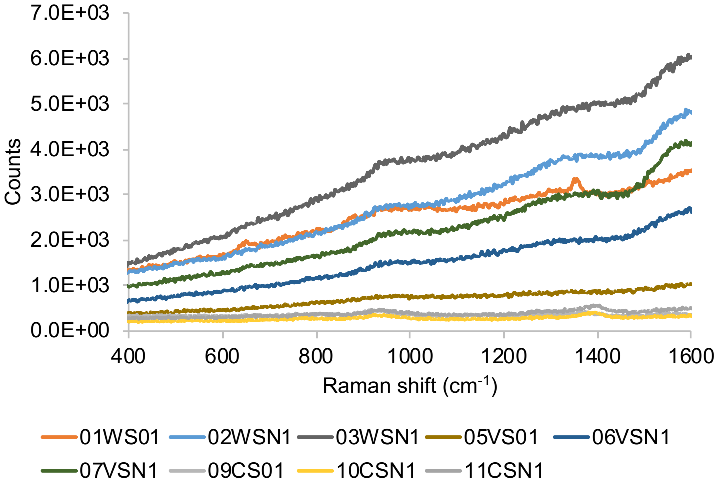

Figure 4.7 – Spectra for all samples reacted for 20 hours listed in table 4.3. Collected using a 442 nm laser.

Spectra shown in figure 4.7 are very noisy and uninformative, even though the data was collected at laser maximum power (80 mW). It is clear that the blue laser is not suitable for the samples. After this data, the blue laser data was not further analysed in this study.

Figures 4.8, 4.9 and 4.10 depict the spectra obtained for the samples left to react overnight, for green, red and infrared lasers, respectively.

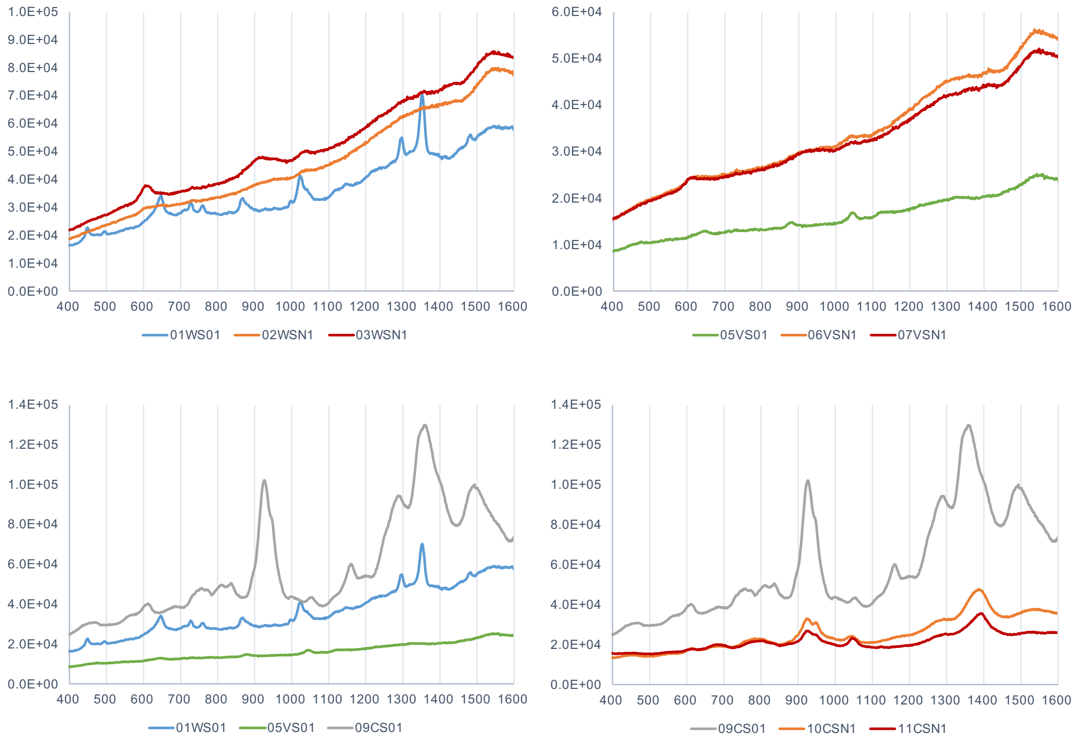

Figure 4.8 – Spectra for Douro white wine (top left), green wine (top right), both wines and silver nanostars without silver nitrate addition (bottom left) and silver nanostars (bottom right). Collected using a 532 nm laser.

Besides silver nanostars capped with citrate (09CS01), samples 01WS01 and 05VS01 – where only AgNSs were added to the wine – are the ones with more singular and defined spectra, especially the first.

Looking at the both top groups of spectra in figure 4.8, it is clear that samples where silver nitrate was introduced in the system (02WSN1 and 03WSN1, on the top left; 06VSN1 and 07VSN1, on the top right) leads to a loss of information when compared to wine spectra after 20 hours in the presence of silver nanostars only (01WS01, on the top left; 05VS01, on the top right). If any silver nanoparticles are formed, no positive effect is observed in SERS. In fact, the signal is quite worse, which possibly implies changes occurring directly on silver nanostars, with two possible explanations. Firstly, the presence of silver nitrate, together with reducing agents characteristically available in wine, leads to the distribution of silver atoms onto silver nanostars surface, however not in way that that allow them to keep their star shape and therefore their SERS performance. Secondly, given the affinity of oxygen atoms to silver, the nitrate ions, and eventually newly formed nitrite ions, can be adsorbed onto silver nanostars and work as a capping agent, that will not be easily replaced by wine compounds.

The second hypothesis seems to be supported by the fact that any sample containing wine and silver nitrate (orange and red traces in top charts in figure 4.8) mostly show the same bands, like, for example, the ones with Raman shifts of 610 cm^{-1}, 920 cm^{-1} and 1044 cm^{-1}, the last already mentioned to be assigned to nitrate. In the absence of wine (bottom right spectra), the samples with silver nitrate (10CSN1 and 11CSN1) seem also to attenuate the signal of citrate – AgNSs initial capping –, with a more noticeable effect for the sample with more silver nitrate (11CSN1).

Focusing on the wine samples and the water control that underwent 20 hours of incubation with silver nanostars and in absence of silver nitrate (bottom left spectra), the citrate (09CS01) peaks disappear for both wines, indicating that citrate is replaced by other components present in wine.

The competition phenomena between citrate, nitrate/nitrite and wine compounds, is not clear so far, however the following data collected with other lasers can eventually help to clarify this aspect.

In figure 4.9, for the samples prepared with Douro white wine (top left) is very clear that the main peaks in samples with silver nitrate (02WSN1 and 03WSN1), namely at 610 cm^{-1} and 920 cm^{-1} are not present in the sample without silver nitrate (01WS01). Like in the equivalent group of spectra for the 532 nm laser (figure 4.8, top left), the sample with twice the amount of silver nitrate (03WSN1) have more intense peaks, especially the ones with 610 cm^{-1} and 920 cm^{-1} Raman shifts.

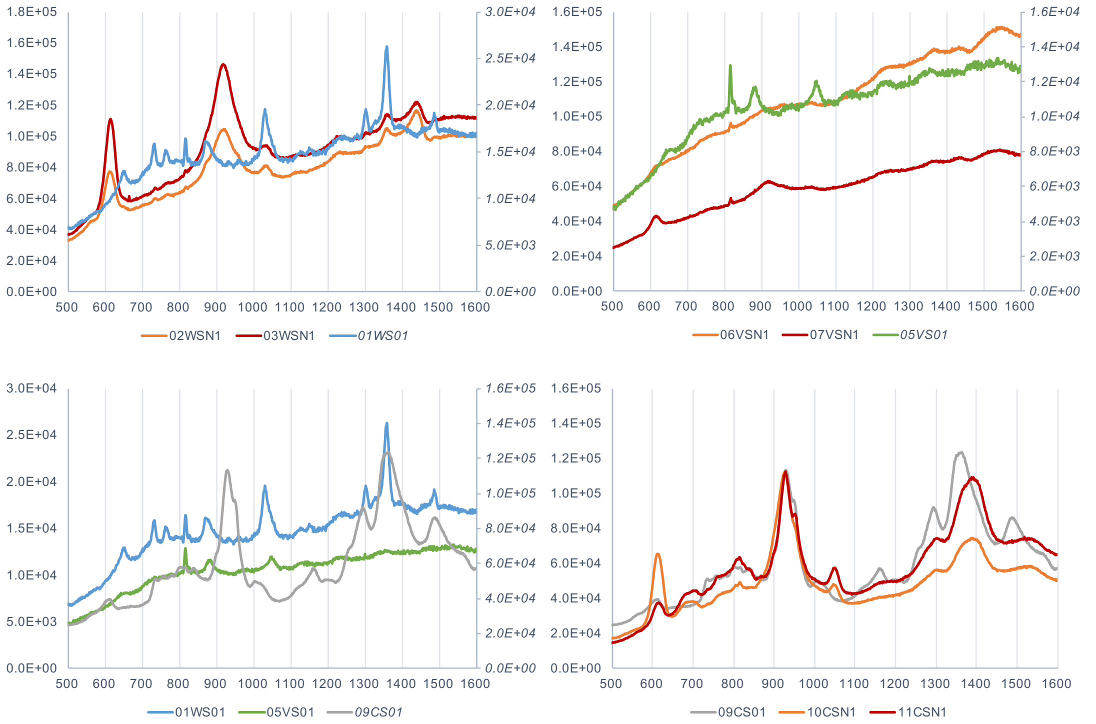

Figure 4.9 – Spectra for Douro white wine (top left), green wine (top right), both wines and silver nanostars without silver nitrate addition (bottom left) and silver nanostars (bottom right). Collected using a 633 nm laser.

In this case, the wines with just silver nanostars have a signal one order of magnitude below, and it is shown in this axis with the values in italic, for both top charts. For the green wine (top right) the signal is less structured for all samples, which is in line with the results from the 532 nm laser.

For the data obtained with the red laser, it is particularly clear that in spectra of samples including silver nitrate (***SN1 samples, with orange and red traces), for both wines and also the water control, there are peaks always present and with particularly high intensity (610 cm^{-1}, 920 cm^{-1} and 1044 cm^{-1}). This type of behaviour compromises the distinction of the samples, since the peaks from silver nitrate derivatives seem to overlap with those of the wine compounds.

Again, some bands present in the control sample (09CS01), completely disappear in the presence of wine, and new bands occur, as seen in bottom left chart of figure 4.9, confirming the citrate replacement by wine components.

Finally, for this section, data collected using the 785 nm laser is depicted in figure 4.10, with the same chart organization as figures presenting the data for 532 nm and 633 nm lasers.

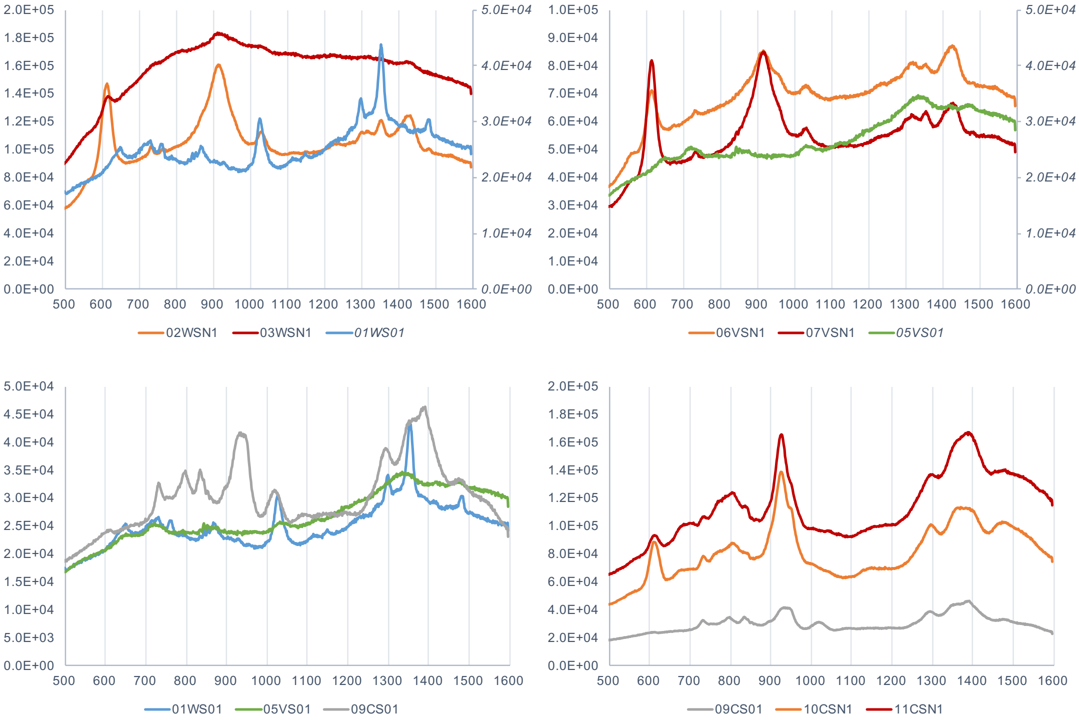

Figure 4.10 – Spectra for Douro white wine (top left), green wine (top right), both wines and silver nanostars without silver nitrate addition (bottom left) and silver nanostars (bottom right). Collected using a 785 nm laser.

The data collected with the near infrared laser and depicted in figure 4.10 does not provide significant additional information. The spectra globally present broader bands, especially noticeable for green wine (VWN) sample 05VS01. No further evidence or novelty can be extracted from data presented in figure 4.10.

In this round of experiments shown in table 4.3, three samples incubated for an extra 24 hours period (04WSN2, 08VSN2 and 12CSN2) were also included. The reaction occurs at room temperature, therefore the silver reduction into silver nanoparticles could be slower than expected, especially given that this time no other reductant was added to the sample. In figure 4.11, the spectra for these ***SN2 samples, are compared to the samples in the same conditions, except for the reaction time (03WSN1, 07VSN1 and 11CSN1, respectively). These last samples were already depicted in figures 4.8 to 4.10.

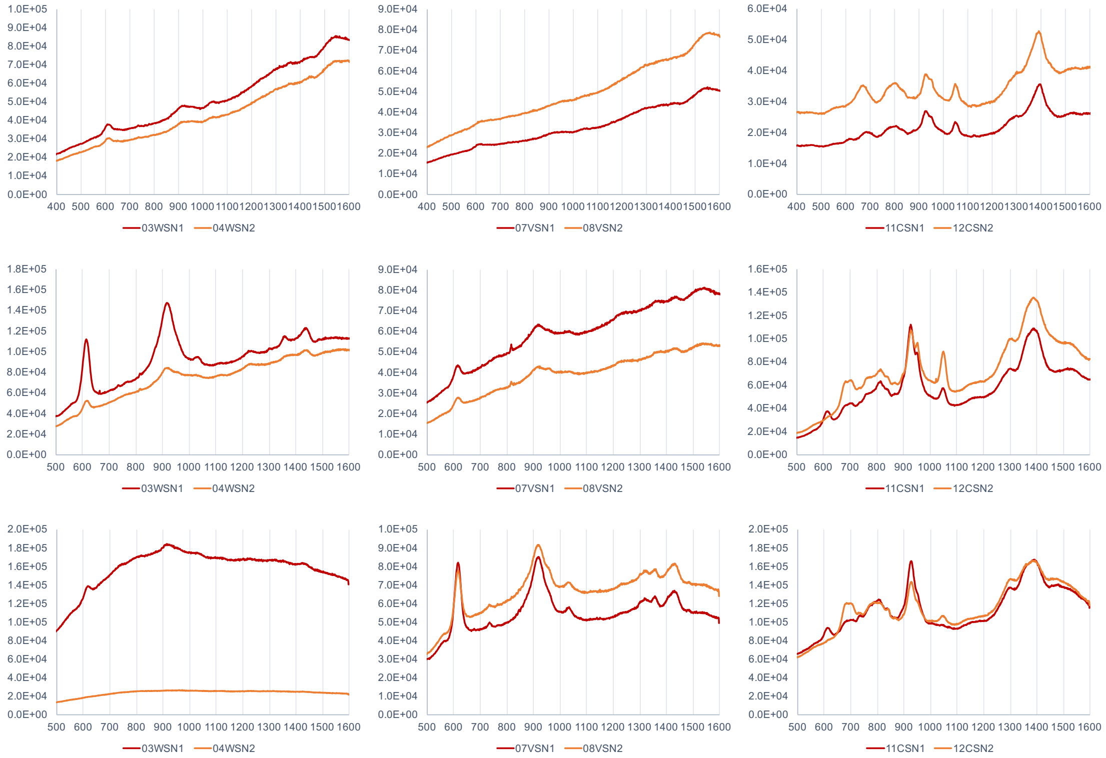

Figure 4.11 – Spectra collected with the green (top), red (middle) and infrared (bottom) lasers for Douro white wine (left), green wine (middle) and silver nanostars (right).

Data from blue laser was not included in figure 4.11 due its poor quality, already stated. Analysing the nine spectra pairs depicted in figure 4.11, it is obvious that globally no valuable changes are observed when the reaction time goes on for an extra 24 hours period. The majority of the spectra after 44 hours are equivalent or worse than the ones obtained just after 20 hours.

4.3.2.3. Silver nanostars functionalization by wine compounds with incubation

The following set of results, shown in figures 4.12 to 4.15, is focused on the functionalization of silver nanostars with wine molecules by enabling the contact of these nanoparticles with the different wines overnight.

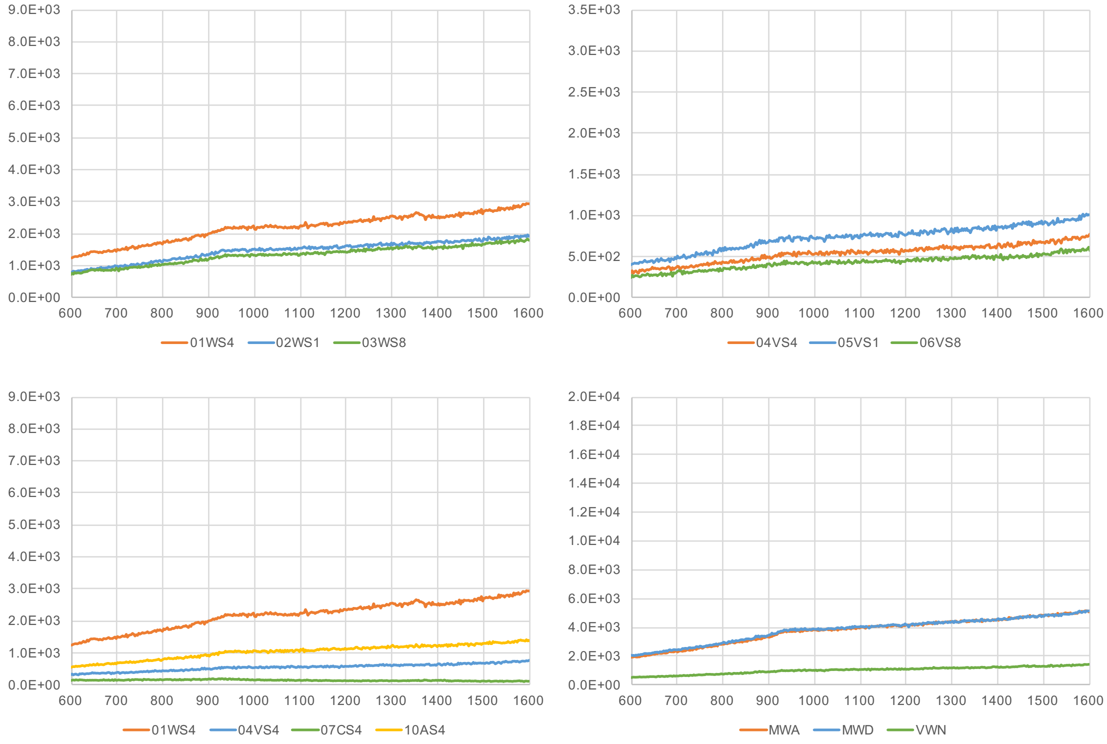

Figure 4.12 – Spectra collected for MWD (top left) and VWN (top right) wines incubated with different amounts of AgNSs; for MWA, MWD and VWN wines incubated with same amount of AgNSs (bottom left) and Raman spectra for MWA, MWD and VWN wines in absence of AgNSs. Collected with 442 nm laser.

Spectra collected with the blue laser, depicted above in figure 4.12, are poorly structured, which does not allow an easy fingerprinting of the wine samples. This is line with it was already showed in figure 4.8. Below, in figure 4.13, the presented spectra are much richer.

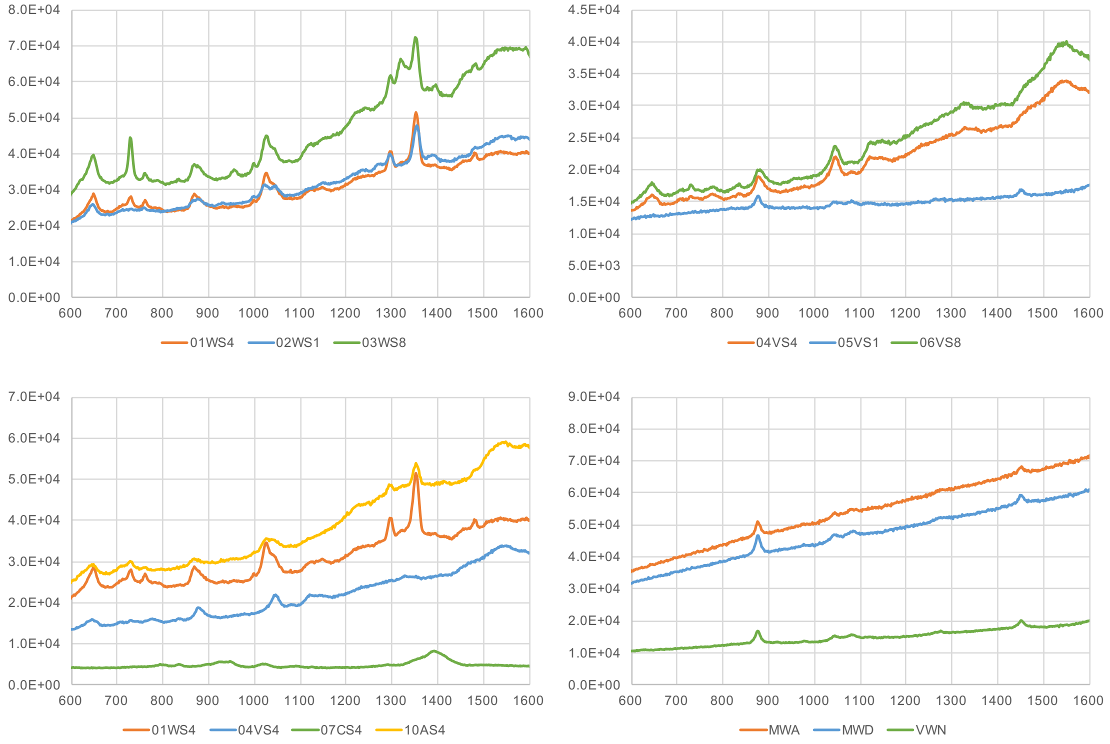

Figure 4.13 – SERS spectra for MWD (top left) and VWN (top right) wines incubated with different amounts of AgNSs; for MWA, MWD and VWN wines incubated with same amount of AgNSs (bottom left) and Raman spectra for MWA, MWD and VWN wines in absence of AgNSs. Collected with 532 nm laser.

When 532 nm laser was used to get SERS spectra of this set of samples, it was possible to observe well defined peaks that may be helpful to the fingerprinting.

Comparing the two top charts in figure 4.13, samples of MWD show a higher number of peaks than VWN samples, corroborating previous experiments. Regarding the AgNSs to wine volume ratios – ****1, ****4 and ****8 samples matching to 1:20, 4:20 and 8:20 ratios, respectively – the samples with the lowest ratio seem to lack some peaks for both MWD (02WS1) and VWN (05VS1) wines. Particularly for VWN, the spectrum is very similar to the presented in bottom right chart, which was obtained in absence of silver nanostars. For the samples representing the two highest ratios (04VS4 and 06VS8) the number of peaks is the same and no obvious differences between the spectra are found.

For MWD, the number of peaks clearly visible increase as the ratio AgNSs to wine increases. In opposition to what was observed for VWN, for MWD the two bigger ratios still have differences regarding the number of peaks, namely at 955 cm^{-1} and 1315 cm^{-1}. Regarding the *Maduro* wine type, a sample from Alentejo region (MWA) was also included, however only incubated with AgNSs in a 4:20 ratio (10AS4), in line with the amounts used in previous experiments.

As it can be seen in bottom left chart in figure 4.13, the three different wines have peaks in common, like the ones with the 650 cm^{-1} and 880 cm^{-1} Raman shifts. The remaining well-defined peaks are either exclusive for a specific wine or for a wine type. These similarities and differences are summarized in table 4.7 below, together with vibration frequency assignments.

In the bottom right chart of figure 4.13 are plotted the spectra for the three different wines used in this experiment, being clearly visible how equivalent they are, showing that these three wines cannot be easily identified by Raman under these conditions.

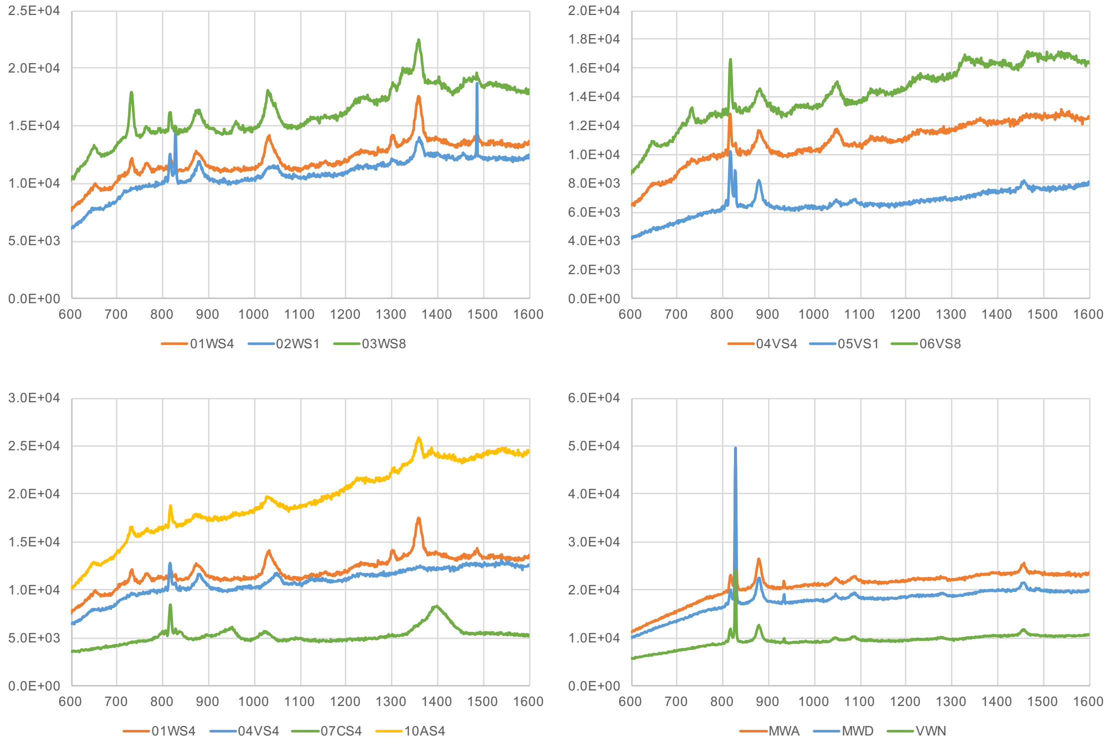

Figure 4.14 – SERS spectra for MWD (top left) and VWN (top right) wines incubated with different amounts of AgNSs; for MWA, MWD and VWN wines incubated with same amount of AgNSs (bottom left) and Raman spectra for MWA, MWD and VWN wines in absence of AgNSs. Collected with 633 nm laser.

The spectra shown in figure 4.14, for the same samples, but collected with 633 nm laser, reveal the same behaviour already observed with the 532 nm laser, *i.e.*, (i) samples prepared with a 1:20 silver nanostars to wine volume ratio lack some peaks, as it can be seen in the two top charts in figure 4.14, (ii) samples prepared with a 4:20 ratio can be distinguished from each other, although the difference between the two *Maduro* wines seem to be more evident with the 532 nm laser and (iii) the Raman spectra (shown at the bottom right chart) of the three different wines are indistinguishable.

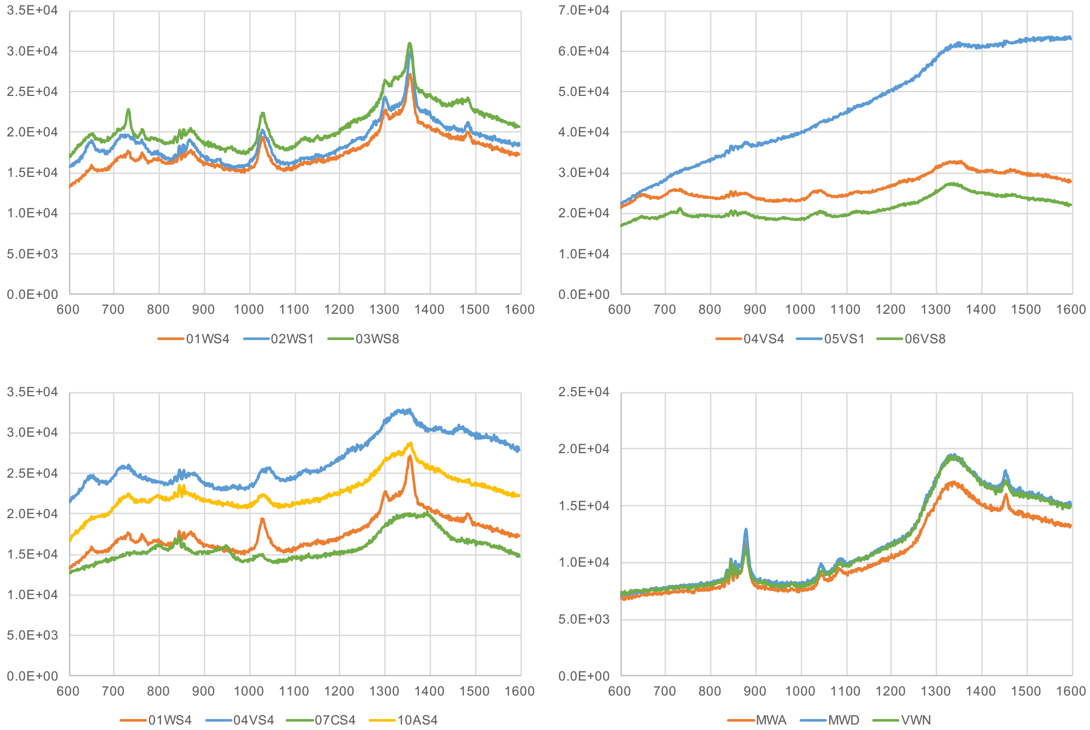

Figure 4.15 – SERS spectra for MWD (top left) and VWN (top right) wines incubated with different amounts of AgNSs; for MWA, MWD and VWN wines incubated with same amount of AgNSs (bottom left) and Raman spectra for MWA, MWD and VWN wines in absence of AgNSs. Collected with 785 nm laser.

The spectra acquired with the near infrared (785 nm) laser, although for the MWD still present sharp peaks, for MWA and VWN present broad peaks leading to a less defined spectra.

The following set of spectra compares the four lasers for the same wine in order to better visualise which laser can be the best for wine fingerprinting.

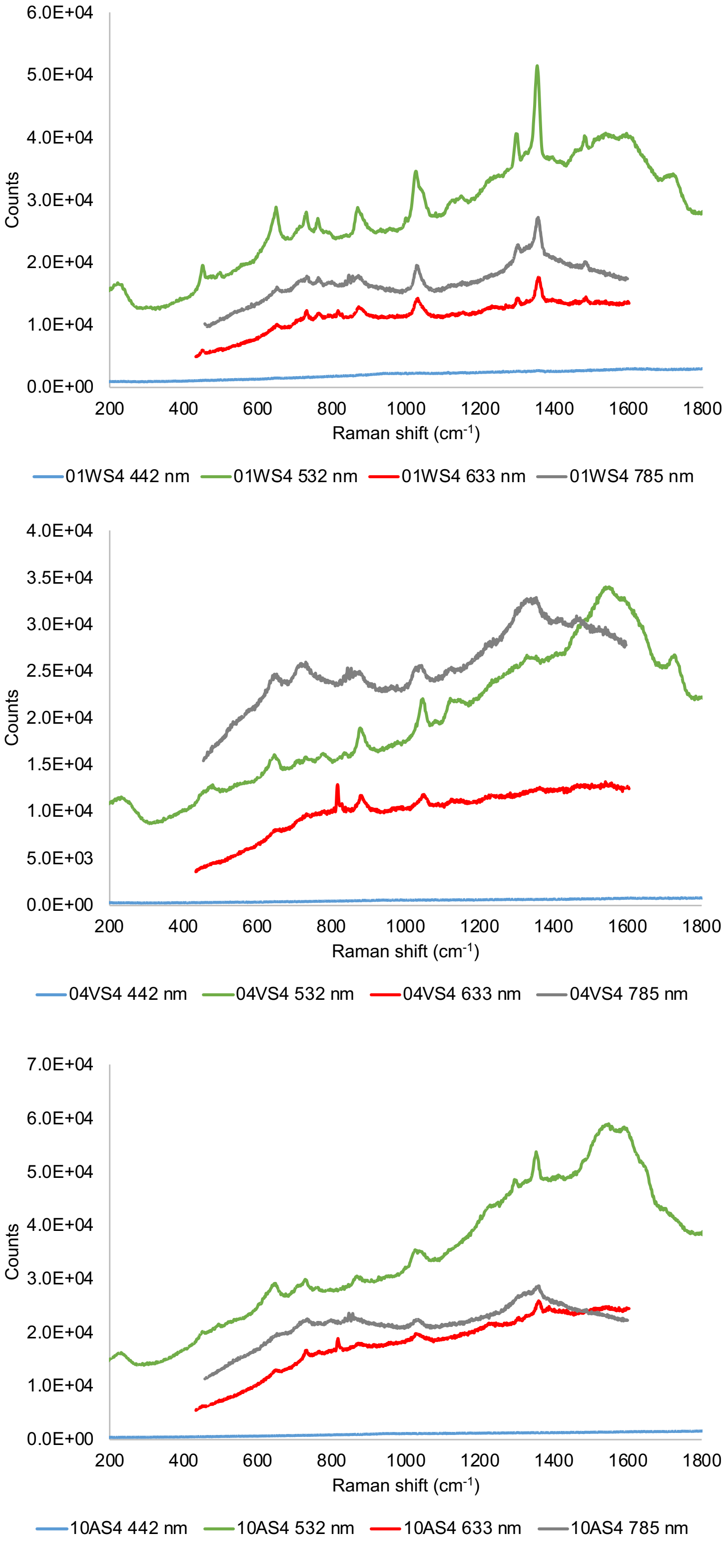

Figure 4.16 – SERS spectra for MWD (top), VWN (middle) and MWA (bottom) wines, acquired with four lasers.

Spectra obtained with 532 nm laser seem to be the most structured and, therefore, richer in information. Data acquired with 785 nm laser present broader bands than the 633 nm. Also, using the 532 nm laser enables the possibility of collecting data, in single measurement mode, in a larger range (~1750 units of Raman shift) than 633 nm or 785 nm lasers (~1150 units of Raman shift). However, the lower resolution for the 532 nm laser does not seem to compromise data quality. The 442 nm laser is capable of covering a large range (~2580 units of Raman shift), but it keeps showing its unfitting for these samples, though silver nanostars have a higher extinction peak at 442 nm that at other lasers wavelengths, so a surface-enhanced resonance Raman scattering (SERRS) phenomenon is probably discarded.

Finally, it was analysed the interference of the support in spectra profile for each laser. The collected spectra are shown below in figure 4.17.

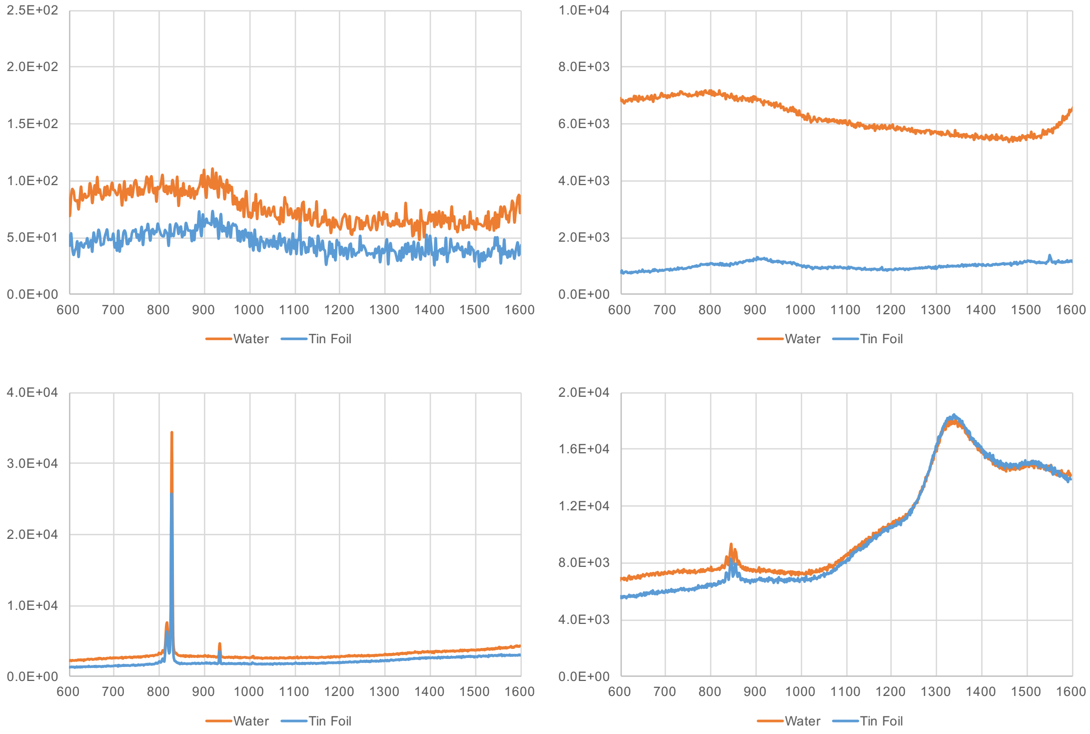

Figure 4.17 – Raman spectra for water and sample support (tin foil) obtained with 442 nm (top left), 532 nm (top right), 633 nm (bottom left) and 785 nm (bottom right) lasers.

The sharp peaks at 825-830 cm^{-1} and 930-935 cm^{-1} regions, visible in spectra collected with the 633 nm laser and depicted on figure 4.14, do not have their origin in wines, since they also appear in water and support (tin foil) controls, as seen in figure 4.18 at the bottom left chart.

Also, for data collected using the 785 nm laser, there is a set of peaks in the 830-870 cm^{-1} that appear in wine samples it is but also visible in controls. A broad band in the 1230-1430 cm^{-1} region, with two less intense bands in its vicinity are also very clear in control samples.

Regarding the interference of the laser with the support, the 442 nm and 532 nm lasers seem to be the best options.

4.3.2.4. Silver nanostars functionalization by wine compounds without incubation

The following data resulted from the evaluation of a quick method (without incubation steps) for wine fingerprinting.

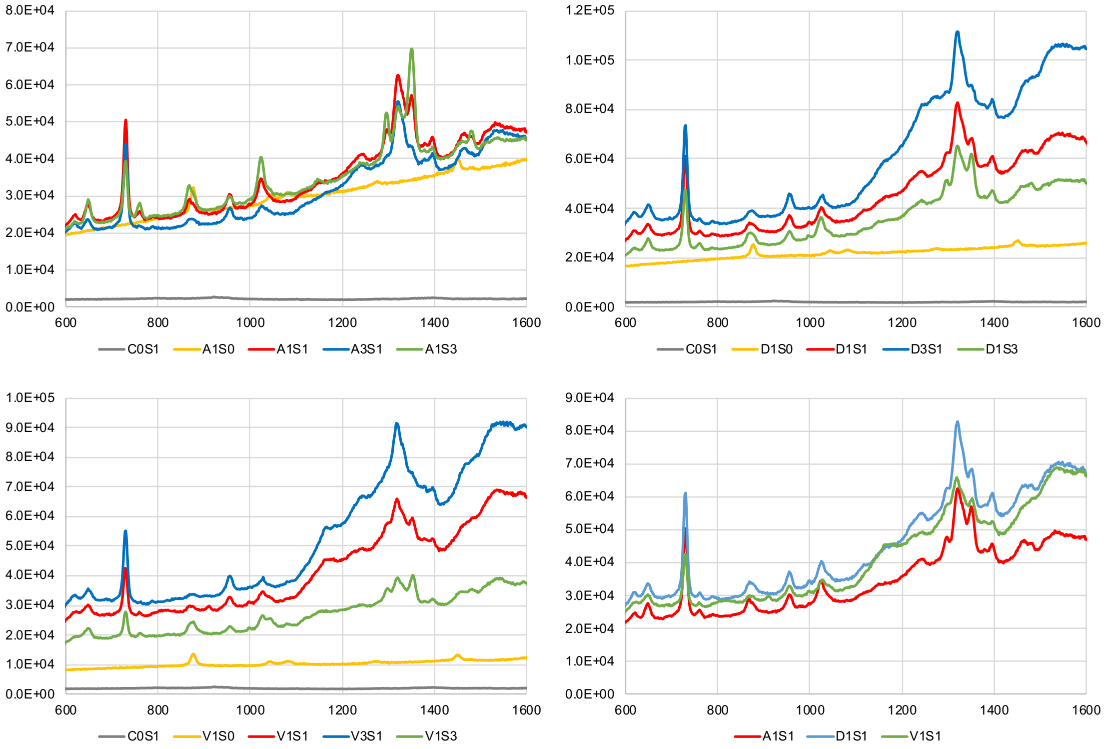

Figure 4.18 – Spectra for MWA (top left), MWD (top right) and VWN (bottom left) mixed in different proportions of wine to nanostars and for the three wines under the same conditions (bottom right). Acquired with 532 nm laser.

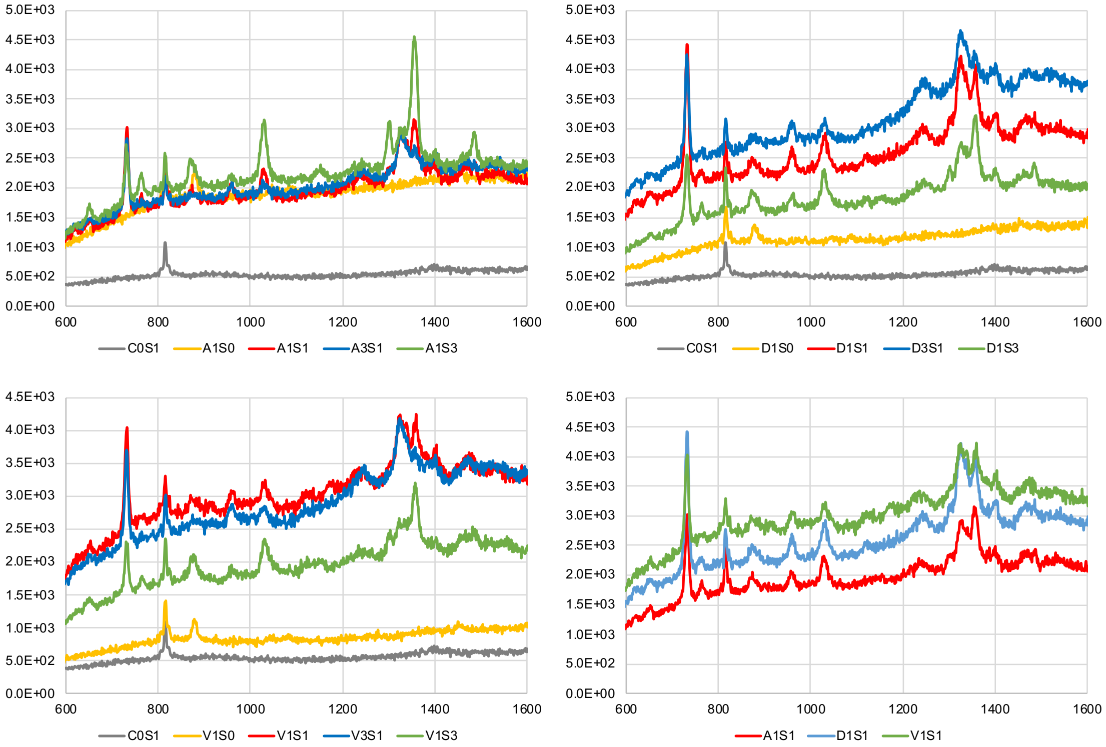

Figure 4.19 – Spectra for MWA (top left), MWD (top right) and VWN (bottom left) mixed in different proportions of wine to nanostars and for the three wines under the same conditions (bottom right). Acquired with 633 nm laser.

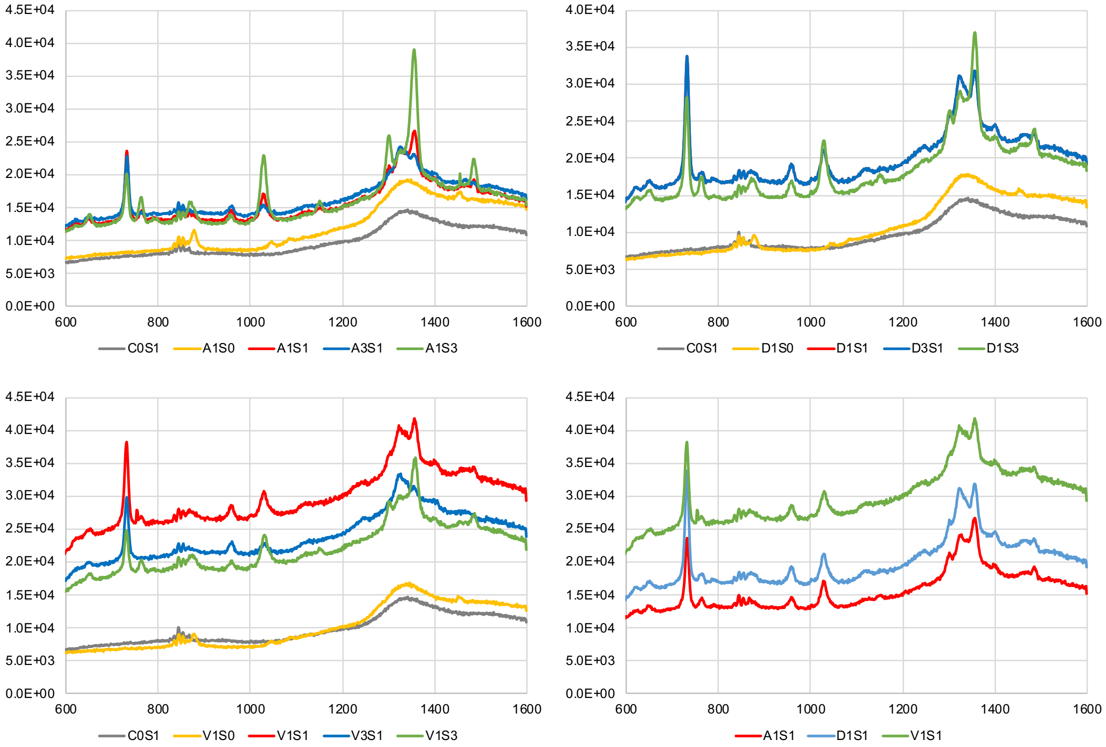

Figure 4.20 – Spectra for MWA (top left), MWD (top right) and VWN (bottom left) mixed in different proportions of wine to nanostars and for the three wines under the same conditions (bottom right). Acquired with 785 nm laser.

In the right bottom chart of each one of the figures 4.18, 4.19 and 4.20, acquired with three different lasers, it is possible to observe the similarity of the spectra of the three wines under the same conditions. It is also possible to observe in the remaining charts that some peaks change with the concentration of silver nanostars, namely the relative intensities between the peaks at 1325 cm^{-1} and at 1350 cm^{-1} for each wine, under different wine to silver nanostars ratios.

Either the silver nanostars are functionalised quickly by the most abundant compounds in wine, that should be quite transversal to every wine (e.g. ethanol), or they act as regular Raman enhancers, *i.e.*, without nanobioconjugation, with sample components being under the influence of the hotspots electromagnetic field. This also will privilege the most abundant compounds, given the higher probability to be found in higher quantity near the hotspots.

Although no clear differences are clearly distinguishable between the wines, the spectra are very structured. The results obtained by this protocol were submitted to statistical analysis (section 4.3), since this can reveal differences that are barely noticeable.

4.3.3. Wine fingerprinting

The ten spectra collected per sample and per protocol are presented bellow as an average spectrum, since the spectra for the same sample are quite similar. All the original data is shown in appendix.

Figure 4.21 shows the average spectra for the three wines submitted to the three different protocols.

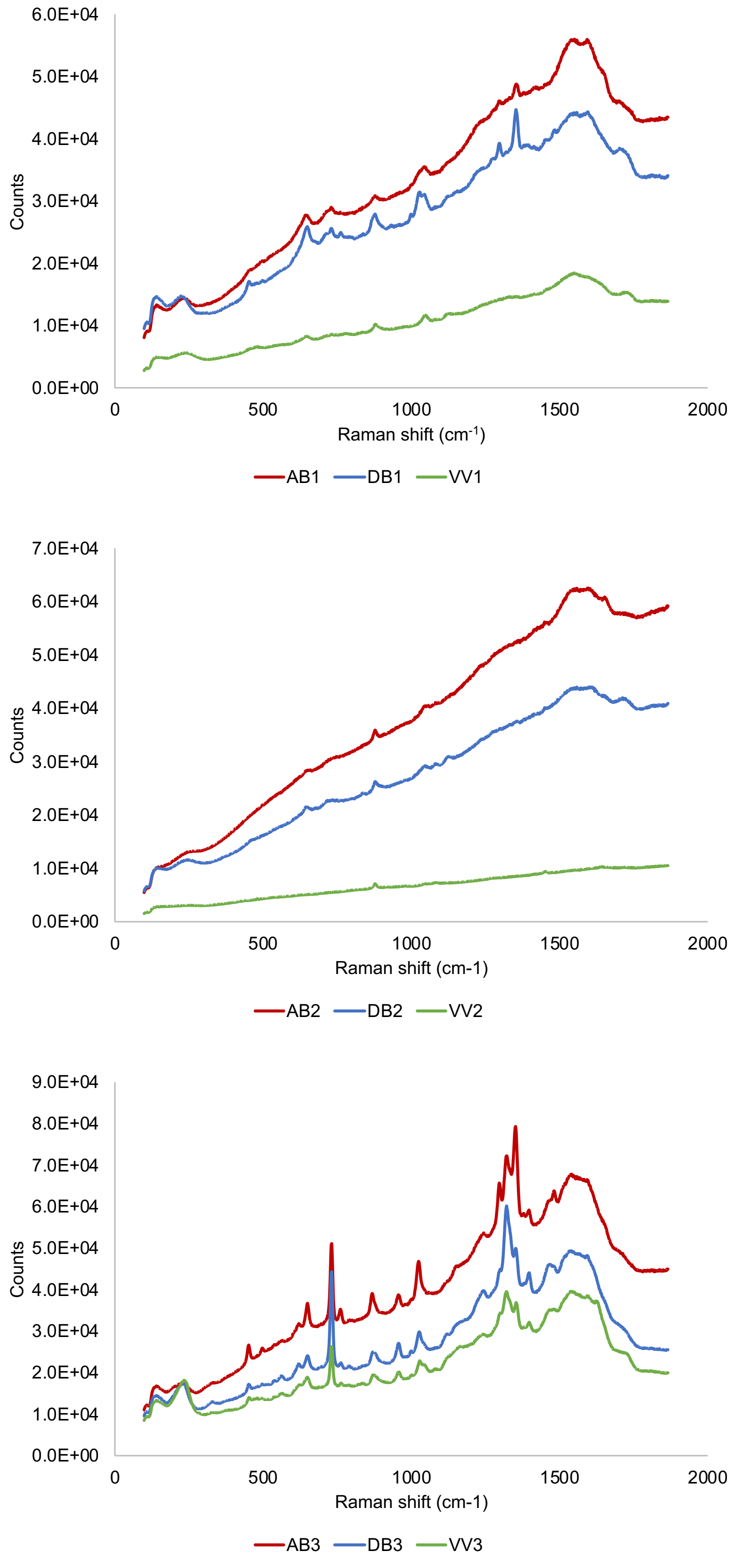

Figure 4.21 – Spectra of the three wines (AB*, DB* and VV*) prepared by the three different protocols (grouped as **1, **2 or **3 samples). Data collected with 532 nm laser.

All the results are in line with what was seen and discussed before. Spectra of samples with incubation period (figure 4.21 top) have a higher number of differences regarding the number of peaks and their relative intensity. Samples immediately read after the addition of silver nanostars (figure 4.21 bottom) are richer in number of peaks and definition, however all the peaks are transversal to all wines, despite some relative intensities are different.

Protocol 2 was never studied before, and it shows a peak profile closer to protocol 1 however with less intense peaks. Since this protocol 2 has the incubation time of protocol 1 but silver nanostars amount used in protocol 3, the presented spectra seem reasonable.

All of this data was processed statistically by principal component analysis (PCA), with the results shown in figures 4.22 to 4.28.

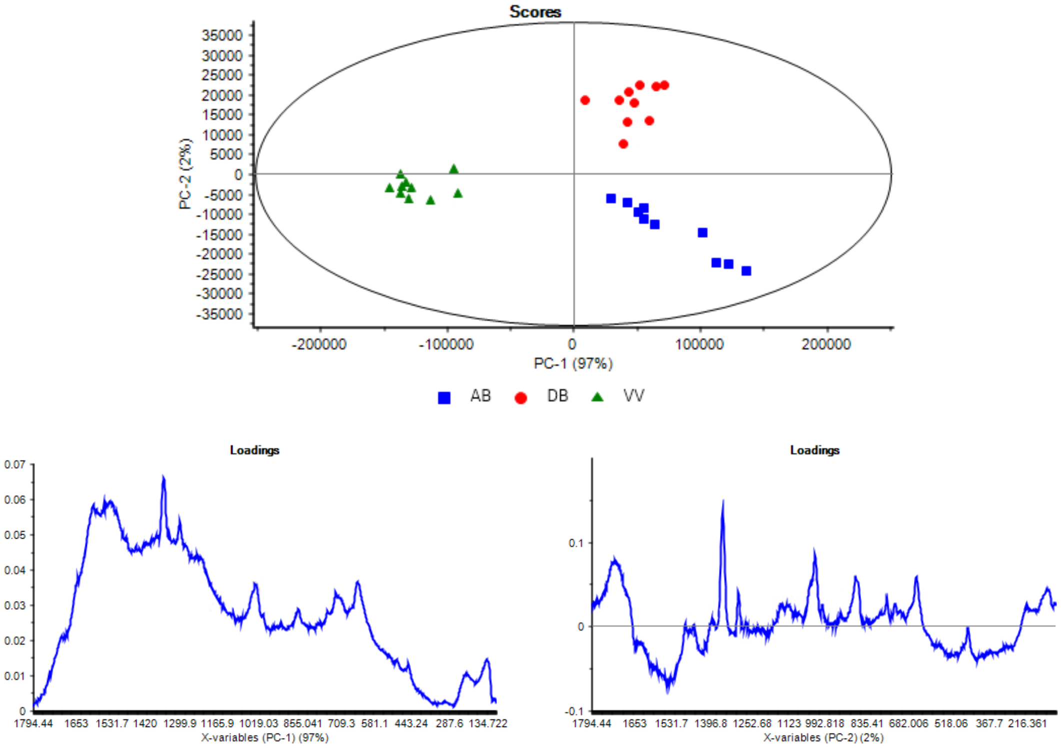

Figure 4.22 – Scores plot depicting PC1 and PC2 (top) and loadings plot for the two PC (bottom). Applied to protocol 1, with data pre-treatment by BLC.

Both score plots for protocol 1, depicted in figures 4.22 and 4.23, show three clearly distinct groups corresponding to the three different wines.

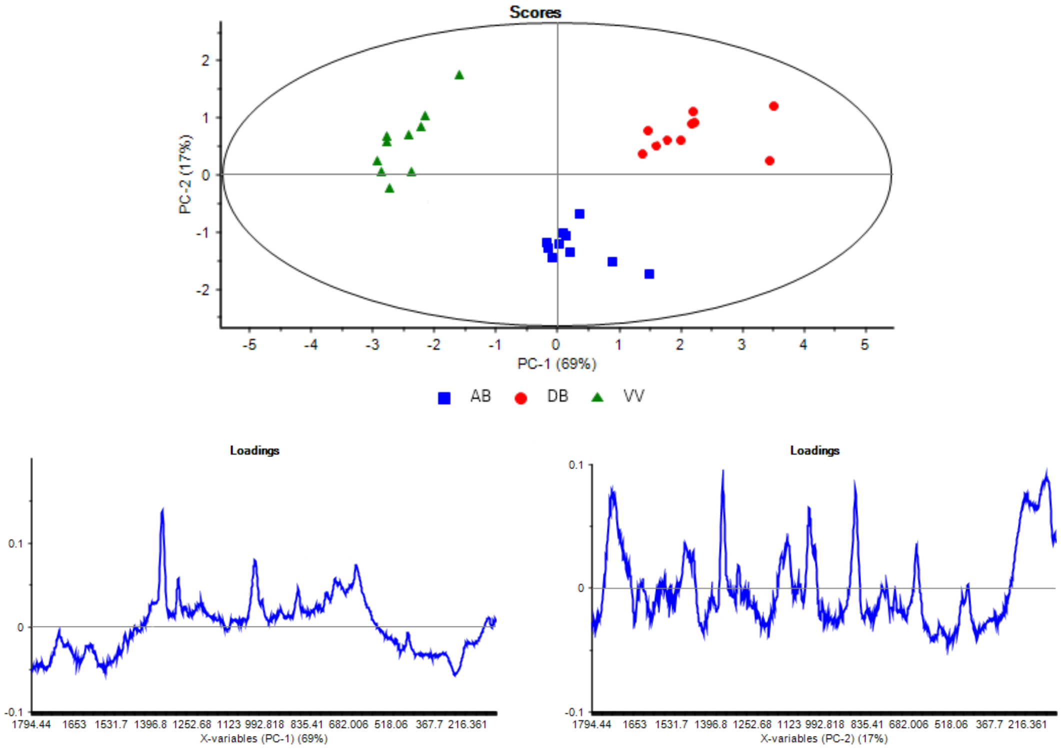

Figure 4.23 – Scores plot depicting PC1 and PC2 (top) and loadings plot for the two PC (bottom). Applied to protocol 1, with data pre-treatment by SNV.

For the data with a baseline linear correction (BLC) pre-treatment (figure 4.22) the elevated and increasing baseline seem to be a major characteristic that enables the distinction between *Verde* and *Maduro* wines, since it is related to principal component 1 (PC1), which has a 97% of weight. The second principal component seems to essentially distinguish between the two regions of *Maduro* wine.

Data pre-processed by standard normal variate (SNV) reduces the weight of the baseline arch, by opposition to BLC that only “rotates”, lowering the higher end of the spectra by subtracting a calculated linear baseline. Keeping the three clear groups, it is not easy to rationalize the position of the groups in the scores plot.

Back to the plots in figure 4.22, it is normal that baseline arch makes the distinction between *Maduro* (positive section of PC1 axis) and *Verde* (negative section of PC1 axis) wines since, since *Maduro* type is richer in compounds that may work as fluorophores, influencing the baseline in this way.

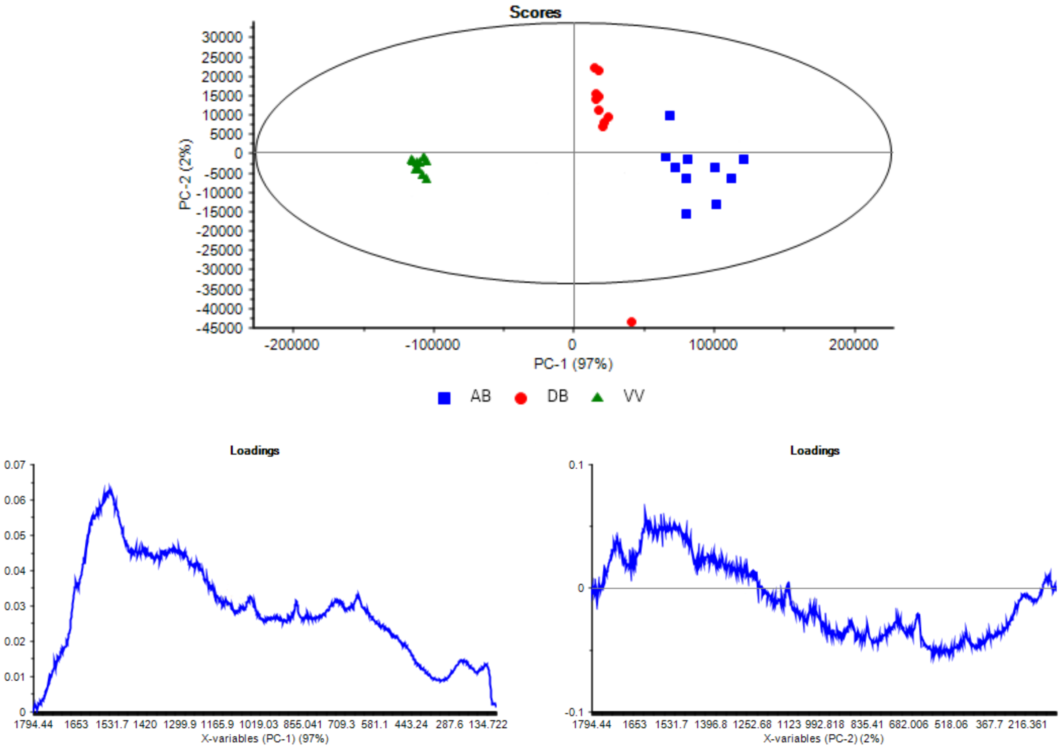

Figure 4.24 – Scores plot depicting PC1 and PC2 (top) and loadings plot for the two PC (bottom). Applied to protocol 2, with data pre-treatment by BLC.

The baseline distinction criteria, principal components weight, distribution of the wine groups across PC1 and PC2, except for one aberrant for MWD wine, are in line with was observed for protocol 1 under the same data processing conditions.

The main change is that in figure 4.24 loadings charts the peaks are less sharp than the ones in figure 4.22, which naturally arises from the original data (figure 4.21 middle).

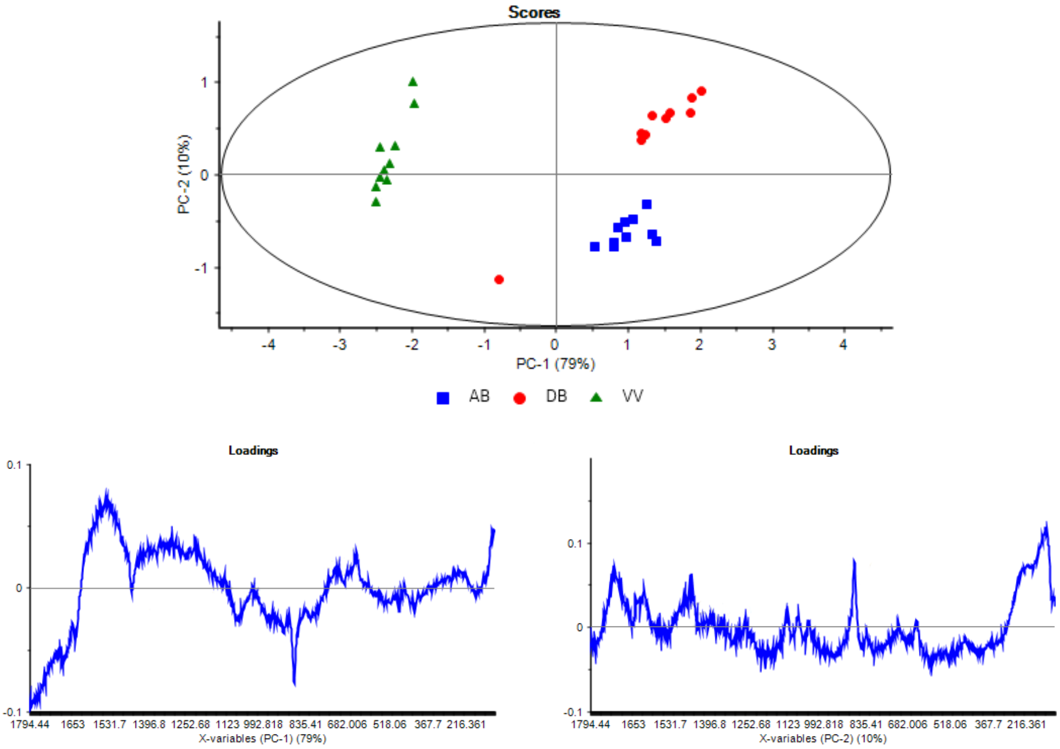

Figure 4.25 – Scores plot depicting PC1 and PC2 (top) and loadings plot for the two PC (bottom). Applied to protocol 2, with data pre-treatment by SNV.

The same is applicable to figure 4.25 *vs.* figure 4.23.

Although protocol 2 shares the incubation time with protocol 1, a significantly lower amount of silver nanostars is used. Despite the less intense spectra, PCA manages to distinguish the spectra in three different groups.

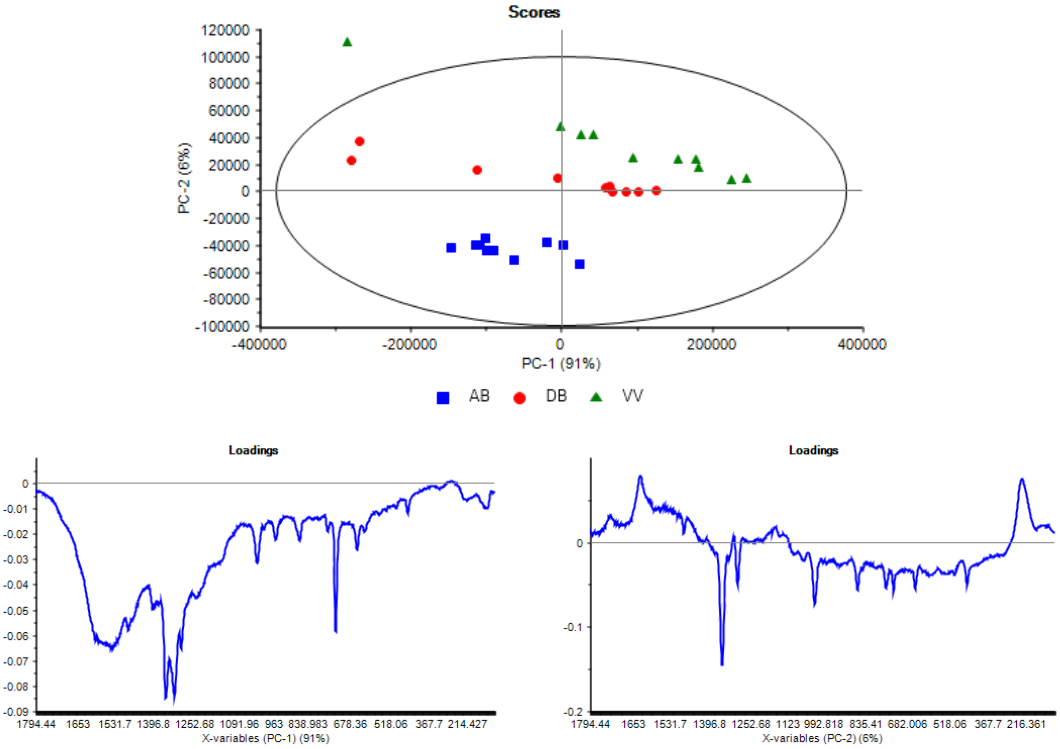

Figure 4.26 – Scores plot depicting PC1 and PC2 (top) and loadings plot for the two PC (bottom). Applied to protocol 3, with data pre-treatment by BLC.

In data obtained for protocol 3, and depicted above in figure 4.26, shows a great weight (91%) for principal component 1, however the samples score points are quite dispersed across PC1 axis, being both in positive and negative regions. It is possible although to recognize groups organised in horizontal layers, so PC2 seems to distinguish the three wines.

Plotting the scores of PC2 against to PC3 can be useful to evaluate if those are the components that really differentiate the wines.

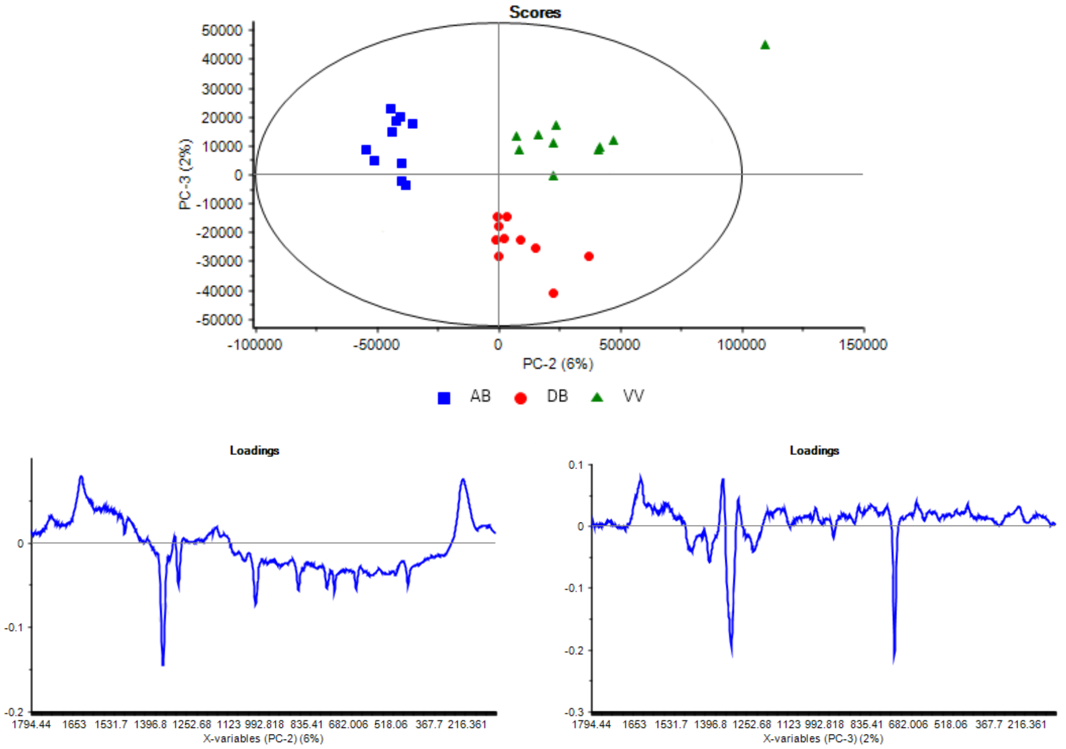

Figure 4.27 – Scores plot depicting PC2 and PC3 (top) and loadings plot for the two PC (bottom). Applied to protocol 3, with data pre-treatment by BLC.

Although principal components 2 and 3 only have a total a weight of 8% (PC1 has 91%) their score plot clearly isolates three groups corresponding to three different wines.

This is the first case where PC1 loses relevance and PC3 helps to differentiate wines. This is in line with what it was already discussed for this approach, specifically the huge role of abundant and transversal wine compounds in SERS signal. These common and abundant compounds are probably the main contributor for PC1, therefore a big distribution across PC1 axis and its high weight.

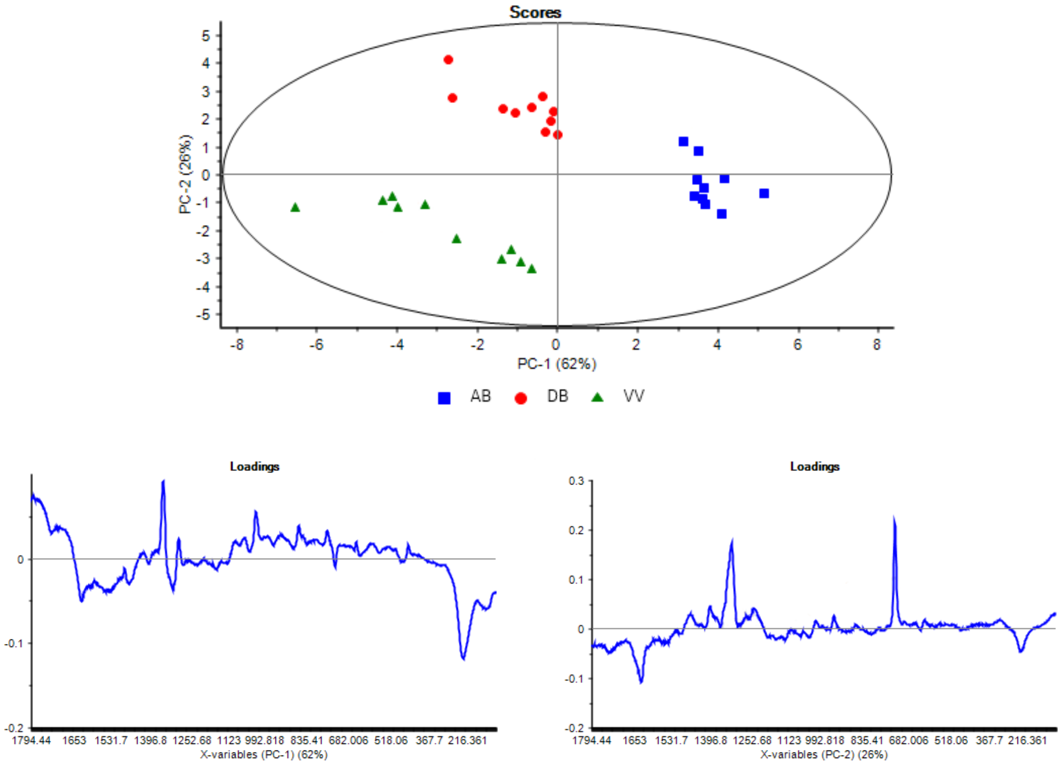

Figure 4.28 – Scores plot depicting PC1 and PC2 (top) and loadings plot for the two PC (bottom). Applied to protocol 3, with data pre-treatment by SNV.

With the SNV data pre-treatment, the groups are well defined in the PC1 and PC2 scores plot, as seen in figure 4.28. The compounds that are more abundant are probably components acting as fluorophores, since when spectra arch shape is removed, by using SNV data, or not using PC1 data in BLC data, the discrimination is better.

4.3.4. Band assignments

In the following figure 4.29 are highlighted the main differences in spectra from the three wines and a tentative band assignment.

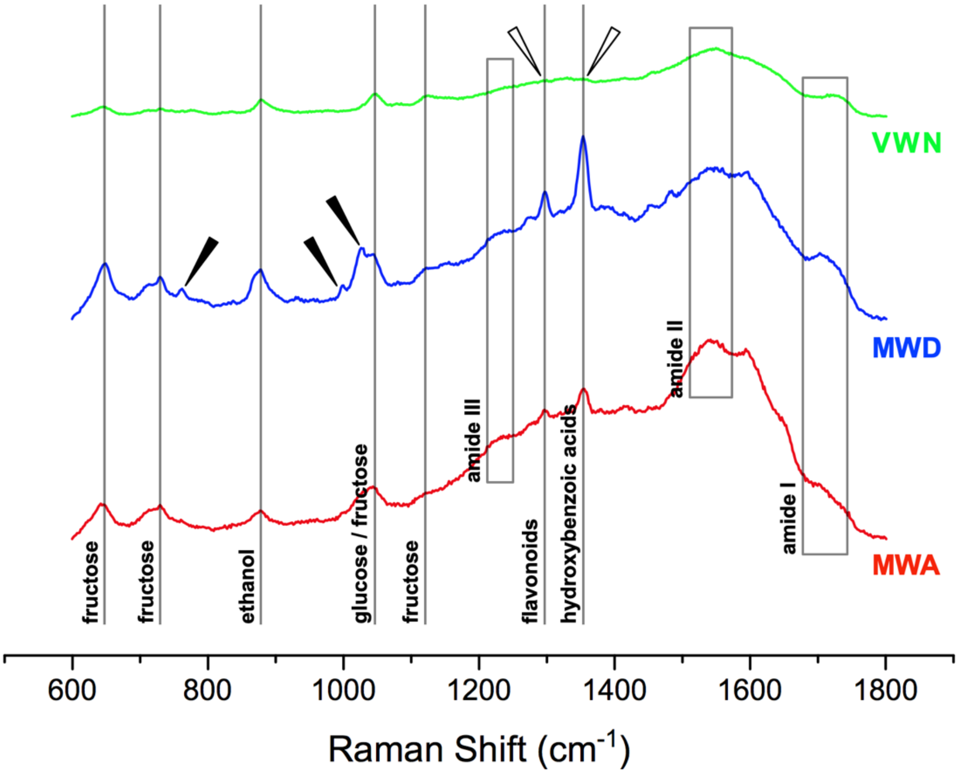

Figure 4.29 – Raman spectra for the three different wines, with some proposed assignments for common wine components. Black arrows: exclusive peaks; White arrows: relevant missing peaks.

In figure 4.29, several peaks are lacking (white arrows) in the VWN spectrum in the 1250-1350 cm^{-1} region, when compared to the other type of wine (MW*). Peaks in this region can be attributed to vibrations from phenolic compounds, namely from multiple types of bonds involving carbon and oxygen.[16-17] The black arrows show peaks that are exclusive to MWD or present a different relative intensity. These peaks (750, 1000, 1020 cm^{-1}) can be attributed to vibrations from rings, like aromatic rings from phenolic compounds (in line with the previous observations) or from other type of rings present in some amino acids.[18] Other strong bands in the spectra can be attributed to wine sugars and ethanol[19] and some weaker bands to amide groups[18] from the conjugation of amino acids in peptides or with phenolic compounds[17].

It is important to notice that bands from some groups of the identified molecules can be missing or have very weak intensities, since SERS is a short-distance effect, so, depending on the size and orientation of the molecules, these groups can be no longer under the influence of a strong electromagnetic field created on the hotspots.

4.4. Conclusions

The use of silver nanostars for wine fingerprinting was proven possible with these three wines. The possibility of silver colloids synthesis in wine revealed to be not suitable for this purpose since none of the attempts provided satisfactory results. However, the option of decorating the silver nanostars with wine compounds revealed to be the key to fingerprinting. These compounds exchanged with citrate, and presumably started to work as new capping agents. A capping agent is as close as possible to any nanoparticle surface, so the new capping comprised by wine molecules will be greatly enhanced by AgNSs hotspots.

It important to notice that a typical “add colloid and read” approach can be misleading, probably due to the emphasis given to abundant compounds in wine, that are not so specific from wine to wine. If the silver nanostars are added and are left to incubate in wine, after a period of time (*e.g.* 20 hours) the compounds with higher affinity to silver surfaces will replace the abundant compounds. These low quantity compounds are probably more characteristic of each wine.

However, since the objective of this work was to find a fast, yet effective, method for wine fingerprinting, protocol 3 should be considered. If the weight of the most abundant species is somehow discarded (*e.g.* ignoring the principal component 1 from principal component analysis), it could be possible to fully achieve the objective of getting results in easy and fast way.

Studies adding more (Portuguese) wine samples will help to validate this method in a larger range. This will confirm the need of using a protocol focused in high affinity compounds or if a fast protocol is suitable for the purpose. These additional wine samples should probably be from more regions (and more than one sample per region), including Madeira and Azores. Besides different regions, different wine years can also be tested as a discrimination factor. With data from different years, it will be also possible to evaluate if there are some tendencies regarding a possible convergence or divergence of wine properties from different regions due to climate changes.[12]

It would be also interesting to confirm which kind of compounds are present on silver nanostars surface and are the main responsible for wine differentiation, either in a “high-affinity” protocol or in fast protocol.

Extending this method to Red wines would be a big challenge due to their high content in fluorescent compounds but finding a combination of colloids suitable for SERS and colloids appropriate for fluorescence quenching can be a research direction in the future.

4.5. References

1. A Carpentieri, G Marino, A Amoresano. Rapid fingerprinting of red wines by MALDI mass spectrometry. *Analytical and Bioanalytical Chemistry* **2007,** *389* (3), 969-82.

2. N Paixão, R Perestrelo, J Marques, J Câmara. Relationship between antioxidant capacity and total phenolic content of red, rosé and white wines. *Food Chemistry* **2007,** *105* (1), 204-214.

3. D Airado-Rodriguez, T Galeano-Diaz, I Duran-Meras, JP Wold. Usefulness of fluorescence excitation-emission matrices in combination with PARAFAC, as fingerprints of red wines. *Journal of Agricultural and Food Chemistry* **2009,** *57* (5), 1711-20.

4. CJ Bevin, AJ Fergusson, WB Perry, LJ Janik, D Cozzolino. Development of a rapid "fingerprinting" system for wine authenticity by mid-infrared spectroscopy. *Journal of Agricultural and Food Chemistry* **2006,** *54* (26), 9713-8.

5. M Casale, P Oliveri, C Armanino, S Lanteri, M Forina. NIR and UV-vis spectroscopy, artificial nose and tongue: comparison of four fingerprinting techniques for the characterisation of Italian red wines. *Analytica Chimica Acta* **2010,** *668* (2), 143-8.

6. S Agatonovic-Kustrin, D Milojković-Opsenica, DW Morton, P Ristivojević. Chemometric characterization of wines according to their HPTLC fingerprints. *European Food Research and Technology* **2016,** *243* (4), 659-667.

7. S Marchionni, E Braschi, S Tommasini, A Bollati, F Cifelli, N Mulinacci, M Mattei, S Conticelli. High-precision 87Sr/86Sr analyses in wines and their use as a geological fingerprint for tracing geographic provenance. *Journal of Agricultural and Food Chemistry* **2013,** *61* (28), 6822-31.

8. OR Dinca, RE Ionete, D Costinel, IE Geana, R Popescu, I Stefanescu, GL Radu. Regional and Vintage Discrimination of Romanian Wines Based on Elemental and Isotopic Fingerprinting. *Food Analytical Methods* **2016,** *9* (8), 2406-2417.

9. D Rešetar, M Marchetti-Deschmann, G Allmaier, JP Katalinić, S Kraljević Pavelić. Matrix assisted laser desorption ionization mass spectrometry linear time-of-flight method for white wine fingerprinting and classification. *Food Control* **2016,** *64*, 157-164.

10. CA Teixeira dos Santos, R Pascoa, MC Sarraguca, P Porto, AL Cerdeira, JM Gonzalez-Saiz, C Pizarro, JA Lopes. Merging vibrational spectroscopic data for wine classification according to the geographic origin. *Food Research International* **2017,** *102*, 504-510.

11. H Fraga, AC Malheiro, J Moutinho-Pereira, JA Santos. Climate factors driving wine production in the Portuguese Minho region. *Agricultural and Forest Meteorology* **2014,** *185*, 26-36.

12. M Cunha, C Richter. The impact of climate change on the winegrape vineyards of the Portuguese Douro region. *Climatic Change* **2016,** *138* (1-2), 239-251.

13. H Fraga, JA Santos, J Moutinho-Pereira, C Carlos, J Silvestre, J Eiras-Dias, T Mota, AC Malheiro. Statistical modelling of grapevine phenology in Portuguese wine regions: observed trends and climate change projections. *The Journal of Agricultural Science* **2015,** *154* (05), 795-811.

14. A Garcia-Leis, JV Garcia-Ramos, S Sanchez-Cortes. Silver Nanostars with High SERS Performance. *The Journal of Physical Chemistry C* **2013,** *117* (15), 7791-7795.

15. F Zapata, C Garcia-Ruiz. The discrimination of 72 nitrate, chlorate and perchlorate salts using IR and Raman spectroscopy. *Spectrochimica Acta Part A: Molecular and Biomolecular Spectroscopy* **2018,** *189*, 535-542.

16. C Martin, JL Bruneel, F Guyon, B Medina, M Jourdes, PL Teissedre, F Guillaume. Raman spectroscopy of white wines. *Food Chemistry* **2015,** *181*, 235-40.

17. A Edelmann, B Lendl. Toward the Optical Tongue: Flow-Through Sensing of Tannin−Protein Interactions Based on FTIR Spectroscopy. *Journal of the American Chemical Society* **2002,** *124* (49), 14741-14747.

18. G Zhu, X Zhu, Q Fan, X Wan. Raman spectra of amino acids and their aqueous solutions. *Spectrochimica Acta Part A: Molecular and Biomolecular Spectroscopy* **2011,** *78* (3), 1187-95.

19. K Ilaslan, IH Boyaci, A Topcu. Rapid analysis of glucose, fructose and sucrose contents of commercial soft drinks using Raman spectroscopy. *Food Control* **2015,** *48*, 56-61.

Nanobioconjugates for Bacteria Fingerprinting by Surface-Enhanced Raman Spectroscopy

5

5.1. Introduction

Results from the previous chapter were promising regarding the use of silver nanostars (AgNSs) as a key element for wine fingerprinting by surface-enhanced Raman spectroscopy (SERS). In this chapter, fingerprinting by SERS using AgNSs was also pursued, but this time for more complex systems – bacteria and their structural components and metabolites.

5.1.1. Antibiotic-resistant bacteria

One of the most critical issues in public health is the crescent number of resistance to antibiotics, that has made diseases that were once easily treatable deadly again.[1] World Health Organization (WHO) acknowledges this problem and issued the "Global priority list of antibiotic-resistant bacteria to guide research, discovery, and development of new antibiotics".[2] This list establishes three priority groups each one comprised by several species: Critical – *Acinetobacter baumannii*, *Pseudomonas aeruginosa*, *Klebsiella pneumonia*, *Escherichia coli*, *Enterobacter spp.*, *Serratia spp.*, *Proteus spp.*, *Providencia spp.*, and *Morganella spp.*; High – *Enterococcus faecium*, *Staphylococcus aureus*, *Helicobacter pylori*, *Campylobacter*, *Salmonella enterica*, and *Neisseria gonorrhoeae*; Medium – *Streptococcus pneumoniae*, *Haemophilus influenzae*, and *Shigella spp.* Additionally, these bacteria, when in biofilms, show different proprieties than the free-living cells.[3]

Concerning the work described in this chapter, we selected two species from the "critical priority group" – *Acinetobacter baumannii* and *Klebsiella pneumonia* – and two species from the "high priority group" – *Salmonella enterica* and *Enterococcus faecium*. Despite of the research going on, currently, when these infections are found in a patient, the earlier the treatment the better. Since targeted antibiotics are more efficient than large spectrum antibiotics, an early identification of the species causing the infection can be crucial for the success of the treatment.

Reports about the discrimination of species mentioned in the previous paragraph down to the intraspecies level are quite recent (2017 and 2018)[4-6]. There is however a considerable advance, since in the beginning of this decade the focus was yet a Gram-positive *vs.* Gram-negative discrimination.[7]

5.1.2. Common method for bacteria identification

Bacteria identification was based on morphological and biochemical analysis for a while, but the methods associated to this type of analysis are often stepwise, tedious and time consuming.[8]

Nowadays, the gold standard to identify bacteria species is mass spectrometry (MS), namely matrix-assisted laser desorption/ionization (MALDI) time-of-flight (TOF) mass spectrometry (MALDI–TOF–MS).[8-10] This method has several advantages, with emphasis on a fast analysis of microbiological biomarkers, providing reliable information on bacteria characterization even at the intraspecies level.[10] Alternatives to MALDI–TOF–MS have then to, at least, keep this two advantages and preferably adding others.

5.1.3. Raman spectroscopy for bacteria identification

Raman spectroscopy is reported in the literature as an important whole-organism fingerprinting technique, used to characterise, discriminate and identify microorganisms.[11] However, the Raman effect is so weak that acquisition times can go for several minutes per sample, limiting its usefulness in laboratories where high-throughput analyses are needed.[12]

The use of surface enhanced Raman spectroscopy (SERS) for bacteria fingerprinting allow to reduce the acquisition time drastically[13], from several minutes to a few seconds, avoiding the biological sample deterioration by exposure to the laser, besides speeding the overall process. The first report of SERS for bacteria fingerprinting is from 2004, when it was demonstrated that it was possible to distinguish the microorganism species, including discrimination down to strain level.[13] Later reports achieved similar results.[12] The two main advantages of the gold standard MALDI–TOF–MS, *i.e.* fast analysis and discrimination down to intraspecies level, are equalled by SERS-based bacteria fingerprinting. An additional advantage of Raman equipment is its cost when compared to mass spectrometry apparatus.

Gold[14-15] and silver[13, 16-18] nanoparticles are often used for SERS, especially aggregates from the latter, successfully. There is no report so far concerning the use of silver nanostars for this purpose.

The main objective of the work described in this chapter is to develop an easy method for conjugate silver nanostars and bacteria capable of discriminating microorganisms down to intraspecies, especially bacteria from the WHO critical and priority groups[2].

5.2. Methods

In surface-enhanced Raman spectroscopy measurements, a Renishaw InVia Raman microscope, coupled with 442 nm 80 mW (He-Cd), 532 nm 200 mW (diode), 633 nm 17 mW (He-Ne), 785/830 nm 300 mW (diode) lasers was used, focused with a 50x objective. This equipment was operated at *Facultatea de Fizică* from *Universitatea Babeș-Bolyai* (*FFUBB*).

Raman spectroscopy apparatus used in *Departamento de Conservação e Restauro* at *Faculdade de Ciências e Tecnologia da Universidade Nova de Lisboa* (*FCTUNL*) was a Labram 300 Horiba Jobin Yvon spectrometer equipped with a laser of 633 nm (He-Ne), focused with a 50x objective.

5.2.1. Synthesis of silver nanostars

The star-shaped silver nanoparticles were synthesised as described in section 4.2.1., from chapter 4.

5.2.2. Microbiologic material

Bacterial growth was performed at *Faculdade de Farmácia da Universidade do Porto* (*FFUP*), by Dr. Filipa Grosso and Dr. Carla Rodrigues, from Dr. Luísa Peixe research group. There were used both liquid (Luria Bertani broth) and solid (Luria Bertani agar) media for bacterial growth. The protocol using liquid media was adapted from elsewhere[19], while the one using solid media is one well stablished on that research group. The incubations were performed at 37 ºC and the microorganisms were collected when they were on their exponential phase.

The species studied were *Acinetobacter baumannii*, *Klebsiella pneumoniae*, *Salmonella enterica*, and *Enterococcus spp.* (two distinct isolates). *Acinetobacter baumannii* and *Klebsiella pneumoniae* were used both for interspecies and intraspecie discrimination. Regarding the sequence types belonging to the same species used in the first phase of this work, they are listed in table 5.1 below.

Table 5.1. – *Acinetobacter baumannii* and *Klebsiella pneumoniae* sequence types.

Isolate	Specie	Sequence Type
Ab1 – Ab2	*Acinetobacter baumannii*	103
Ab3 – Ab4		98
Ab5 – Ab6		208
Ab7 – Ab8		218
Ab9		1000
Ab10		515
Kp1 – Kp6	*Klebsiella pneumoniae*	15
Kp7 – Kp8		14
Kp9 – Kp10		147

In a final experiment, *Klebsiella pneumoniae* sequence types 11, 101 and 258 were additionally used, in a new fresh set of samples, also including the previously used sequence types 14, 15 and 147. This set of samples is summarised in table 5.2.

Table 5.2. – *Klebsiella pneumoniae* sequence types.

Isolate	Specie	Sequence Type
Kp11 – Kp18	*Klebsiella pneumoniae*	11
Kp19 – Kp21		14
Kp22 – Kp29		15
Kp30 – Kp34		101
Kp35 – Kp40		147
Kp41 – Kp46		258

5.2.3. Nanobioconjugation between silver nanostars and bacteria

The nanobioconjugation was performed using five different protocols, varying (i) the combination method, (ii) amount of biologic material and (iii) capping agent of the nanoparticles, in the following manner:

i. Combination of the nanoparticles: (a) the pellet from the centrifugation (5 min at 4000 rpm) of liquid growth medium was resuspended in 50 µl of 0.1 nM solution of silver nanostars and left to incubate for 30 minutes, (b) one colony was resuspended in 50 µl of a 0.1 nM solution of silver nanostars and left to incubate for 30 minutes, and (c) one colony was mixed with 10 µl of a 0.5 nM silver nanostars and immediately deposited on the support.

ii. Amount of biologic materials: (a) 1 McF, (b) 2 McF and (c) 5 McF.

iii. Capping agents: (a) citrate and (b) cysteamine. The molecular structures of these two capping molecules are depicted in figure 5.1.

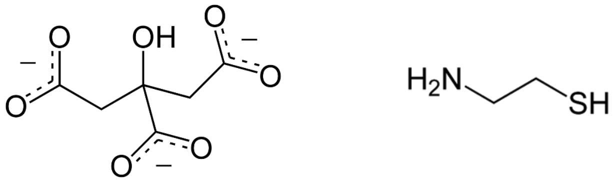

Figure 5.1 – Molecular structures of citrate (left) and cysteamine (right).

Five different protocols were tested, as summarized below in table 5.3.

Table 5.3. – Silver nanostars and bacteria nanobioconjugation protocols.

Protocol	AgNSs Bacteria Mixing (i)	Bacteria Amount (ii)	AgNSs Capping (iii)
1	a	a	b
2	b	b	b
3	c	b	b
4	c	b	a
5	b	c	b

Each one of five protocols were tested with *Acinetobacter baumannii* (A1-A5), *Klebsiella pneumoniae* (B1-B5), *Salmonella enterica* (C1-C5) and *Enterococcus spp.* (D1-D5 and E1-E5).

5.2.4. Preparation of the nanobioconjugates for SERS measurements

After nanobioconjugation, the resultant volume is drop-casted in filter paper (Whatman Grade 1) at well identified spots. Successive 10 µl portions (1 to 5) are deposited on the filter paper, with drying steps (undisturbed, room temperature) between additions. This enables the formation of a spot rich in nanobioconjugates, as observed before for silver nanostars deposited in office paper under similar conditions[20].

In this particular case, besides the low cost of a filter paper support, it is also a material easily incinerated.

5.2.5. SERS measurements

Raman spectra were acquired in a 7 x 3 matrix, in total of 21 different and not overlapping spots, for *Acinetobacter baumannii* and *Klebsiella pneumoniae* (at *FFUBB*). For the extended experiments with *Acinetobacter baumannii*, *Klebsiella pneumoniae*, *Salmonella enterica* and *Enterococcus spp.* at least 3 spectra were manually (not as pre-set matrix) acquired at *FCTUNL*. The acquisition times varied from 4 to 20 seconds, depending on laser, Raman spectrophotometer and sample.

5.2.6. Data analysis

Data processing – principal component analysis (PCA) and partial least squares discriminant analysis (PLS-DA) – was performed at *FFUP*, by Dr. Carla Rodrigues and Dr. Ângela Novais, from Dr. Luísa Peixe research group, using MatLab software.

5.3. Results and Discussion

Results come from two main groups of experiments. Firstly, only two species (*Acinetobacter baumannii* and *Klebsiella pneumoniae*) and one base nanobioconjugation protocol (protocol 1, from table 5.3) were used. With these two species they were found the most appropriate nanobioconjugation media (PBS *vs.* UW) and the most appropriate measurement laser (532 nm *vs.* 633 nm *vs.* 785 nm). The best results, for these two species, were further studied for interspecies discrimination but also for intraspecies discrimination. This first part of the work was developed at *FCUP*, *FFUP* and *FFUBB*.

Secondly, the experiments were extended to *Salmonella enterica* and *Enterococcus spp.*, in addition to the first two species above. With the previously evaluated parameters already stablished, other protocols were tried. Despite the success of the first protocol, these additional four protocols aimed to simplify the preparation of the nanobioconjugates either by using the AgNSs as synthesised or by a "mix and read" approach. This second part of the work was developed at *FCUP*, *FFUP* and *FCTUNL*.

5.3.1. Nanobioconjugation protocols

Although the data in this section is regarding the second group of results described above (5.3), the data only concerns the macroscopic and microscopic observations of the nanobioconjugates. The ability of differentiate microorganisms at interspecies level is described in section 5.3.2, together with other data from the results of the first group of experiments mentioned in the point 5.3.

At a macroscopic level, the nanobioconjugation seemed to occur successfully. The control samples showed a white spot, barely distinguishable from the paper support, for the deposited biologic material, with no added AgNSs. In the other hand, the AgNSs deposition, with no added biologic material, dispersed easily across the filter paper by capillarity. The nanobioconjugates, independently the preparation method, assured a very dark and localized spot on the support. Optical microscopy showed a fully covered support, as depicted in figure 5.2.

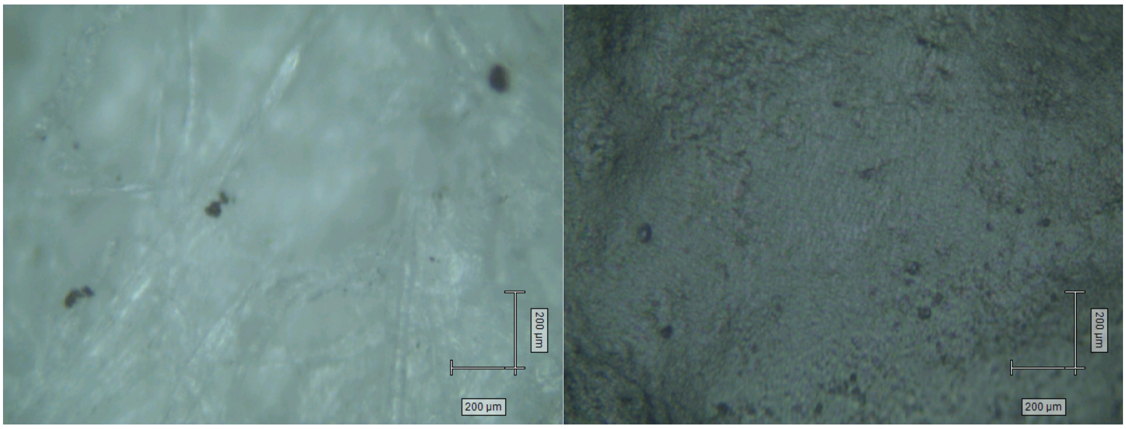

Figure 5.2 – Micrographs of the original filter paper support (left) and of the nanobioconjugates spot (right) – 50x magnification.

Compared to the bare support (figure 5.2, left) the nanobioconjugates spot (figure 5.2, right) does not show any paper fibres. At this magnification, it is possible to see that nanobioconjugates mass completely covers the paper surface, in a way that looks very homogeneous.

With the help of scanning electron microscopy (SEM), it is possible to achieve magnifications capable of showing the relative position of the silver nanostars and bacteria. The SEM results are depicted next in figure 5.3, for all protocols described in section 5.2.3, applied to one of the *Enterococcus spp*. isolates.

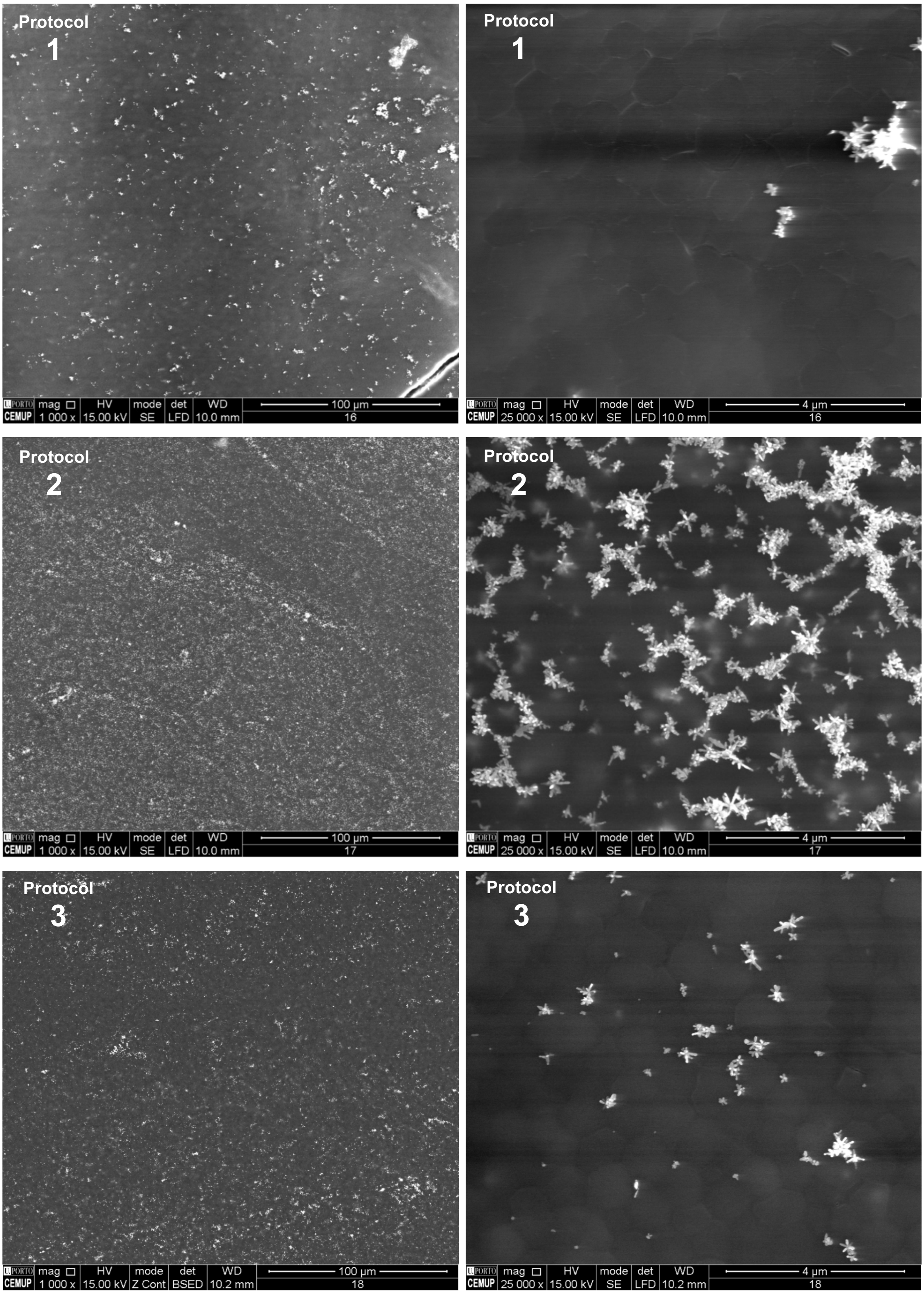
Protocol 1
Protocol 1
mag HV mode det WD 100 µm
1 000 x 15.00 kV SE LFD 10.0 mm 16
mag HV mode det WD 4 µm
25 000 x 15.00 kV SE LFD 10.0 mm 16
Protocol 2
Protocol 2
mag HV mode det WD 100 µm
1 000 x 15.00 kV SE LFD 10.0 mm 17
mag HV mode det WD 4 µm
25 000 x 15.00 kV SE LFD 10.0 mm 17
Protocol 3
Protocol 3
mag HV mode det WD 100 µm
1 000 x 15.00 kV Z Cont BSED 10.2 mm 18
mag HV mode det WD 4 µm
25 000 x 15.00 kV SE LFD 10.2 mm 18
CEMUP

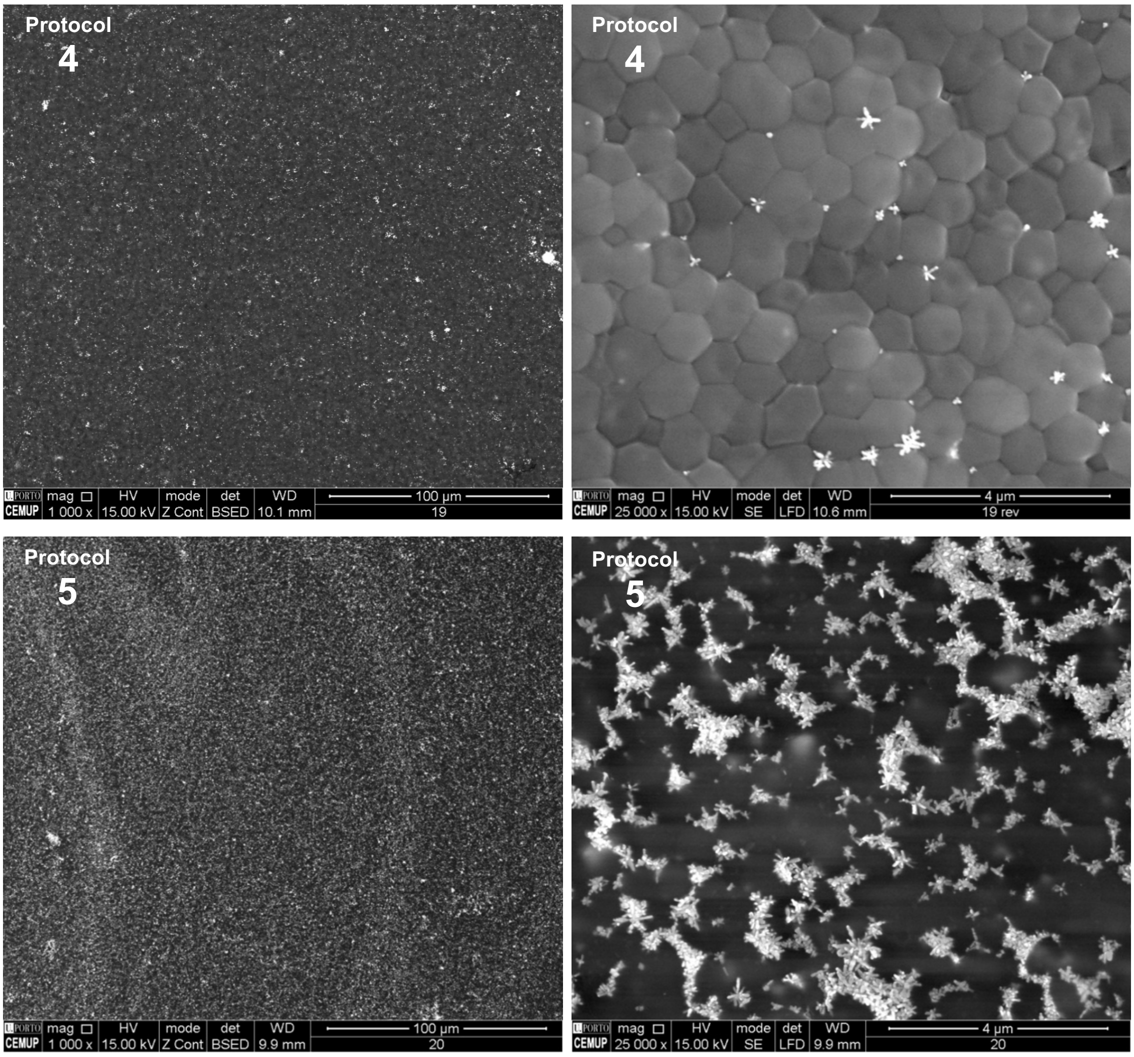

Figure 5.3 – SEM micrographs of *Enterococcus spp.* (bacteria D) prepared for SERS, accordingly to protocols 1-5 (from top to bottom rows), shown in 1000x (left) and 25000x (right) magnifications.

Although all samples had a similar macroscopic appearance, evident differences between the samples were detected by SEM. Samples prepared by protocols 2 and 5 show a large amount of silver nanostars on the surface and it is possible to detect bacteria shapes delimited by the AgNSs at a 25000x magnification. At the 1000x magnification, both samples present an evenly distributed high load of AgNSs. Samples prepared by protocols 1, 3 and 4 have a lower amount of AgNSs on the surface compared to the previous samples. Despite the lower loading, the global AgNSs distribution (1000x magnification) are evenly distributed in samples obtained by protocols 3 and 4, especially for protocol 4, which present a lower amount of aggregates than protocol 3. From these three protocols, protocol 1 has the worst AgNSs loading and distribution. Bacteria in all these five samples are not covered by the nanoparticles, which instead are entrapped between the cells.

Protocols 2 and 5 are the only ones that combine the use of one colony dispersed in 50 µl of 0.1 nM AgNSs. In protocols 3 and 4 one colony was also used, but the concentration of AgNSs used was higher (0.5 nM), reducing the added volume to 10 µl in order to maintain the amount of AgNSs the same for all protocols. The role of extra 40 µl of UW and 30 minutes incubation period probably allowed a better mixing of the components, due to less physical constraints assured by higher dispersant volume and also due to a higher time available to the nanobioconjugates formation.

Protocol 5 used 2.5x the amount of biologic material than protocol 2, but that does not seem to influence the final sample, as evaluated by SEM. Protocol 4 used AgNSs as synthesised (citrate capping) while all other protocols, namely protocol 3, used cysteamine-capped AgNSs. This citrate capping can justify the lower number of aggregates observed in sample prepared by protocol 4 in opposition to the sample prepared by protocol 3.

Finally, protocol 1, the only one using bacteria grown in liquid medium, has its poor AgNSs distribution probably due to remaining amounts of culture medium, that can originate AgNSs aggregation, with loss of particles at the recipient walls or fast deposition even for the short period of sample drying time.

5.3.2. Interspecies bacteria discrimination

The first step to discriminate as much as possible different bacteria is to differentiate the bacteria species. In the following subsections the results towards parameters optimization are described. Data for interspecies discrimination was analysed by principal component analysis (PCA).

5.3.2.1. Laser selection

Since different lasers are appropriate for different types of molecules[21], and at this stage there was not information about the bacterial compounds that would be SERS active, several lasers were tried to differentiate between *Acinetobacter baumannii* and *Klebsiella pneumoniae* species.

In figure 5.4 is depicted a score plot resulting from principal component analysis (PCA), plotting 10 different isolates of each species, regarding SERS average spectra obtained using the 532 nm green laser. Scores calculated from data collected with this nm laser show extensive overlapping, both for principal components 1 (PC1) and 2 (PC2) scores. There is no clear separation between both groups of samples. The fact of PC1 has a big weight (> 90%) between principal components, indicates that there was not a lot of specific information of each species.

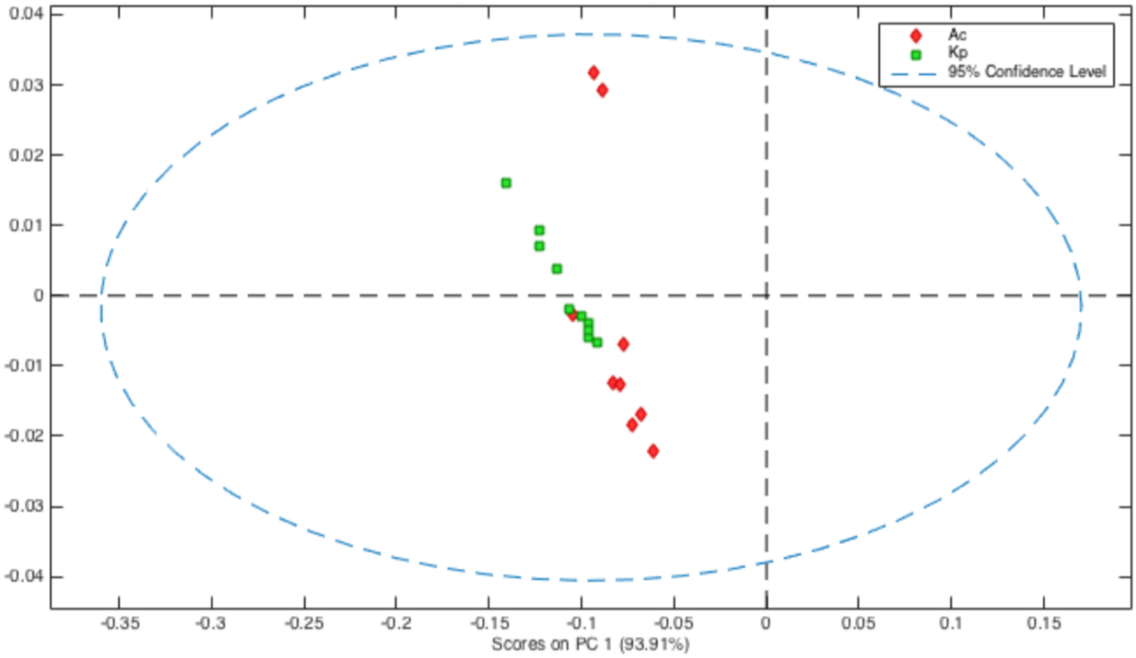

Figure 5.4 – PCA score plot for nanobioconjugates with *Acinetobacter baumannii* (◆) and with *Klebsiella pneumoniae* (■), prepared in UW – data collected with the 532 nm laser.

A similar analysis was performed with data collected with 633 nm red laser, originating the score plot in figure 5.5 below. In this case there is no overlapping in PC1 and PC2. Two distinct groups of points are clearly visible in this plot. In this case, other principal components than PC1 have more weight (64% for PC1 and 13% for PC2), which contributes for a better separation.

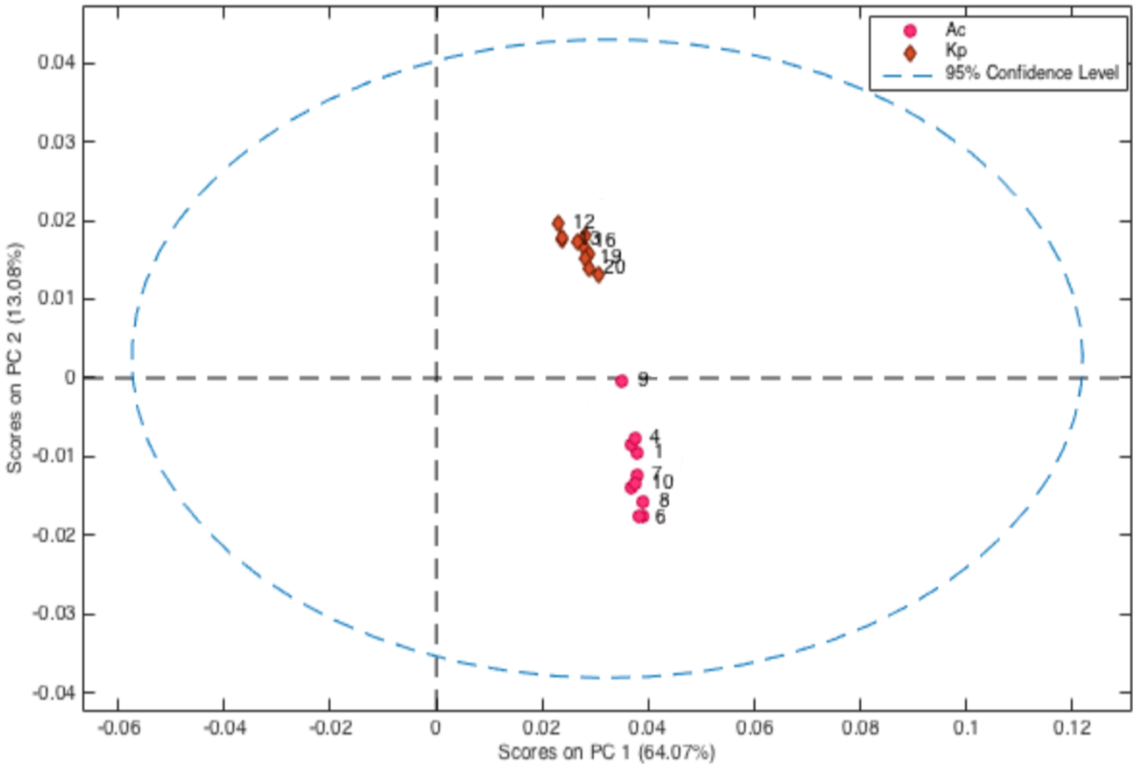

Figure 5.5 – PCA score plot for nanobioconjugates with *Acinetobacter baumannii* (●) and with *Klebsiella pneumoniae* (◆), prepared in UW – data collected with the 633 nm laser.

Finally, the analysis was performed with data collected with 785 nm infrared laser, originating the score plot in figure 5.6 below. In this case, PC2 scores present no overlapping, but a poor group separation. For PC1 scores, overlapping is observed. Especially for *Acinetobacter baumannii*, the score dispersion is quite high. PC1 contribution is again quite high (99%).

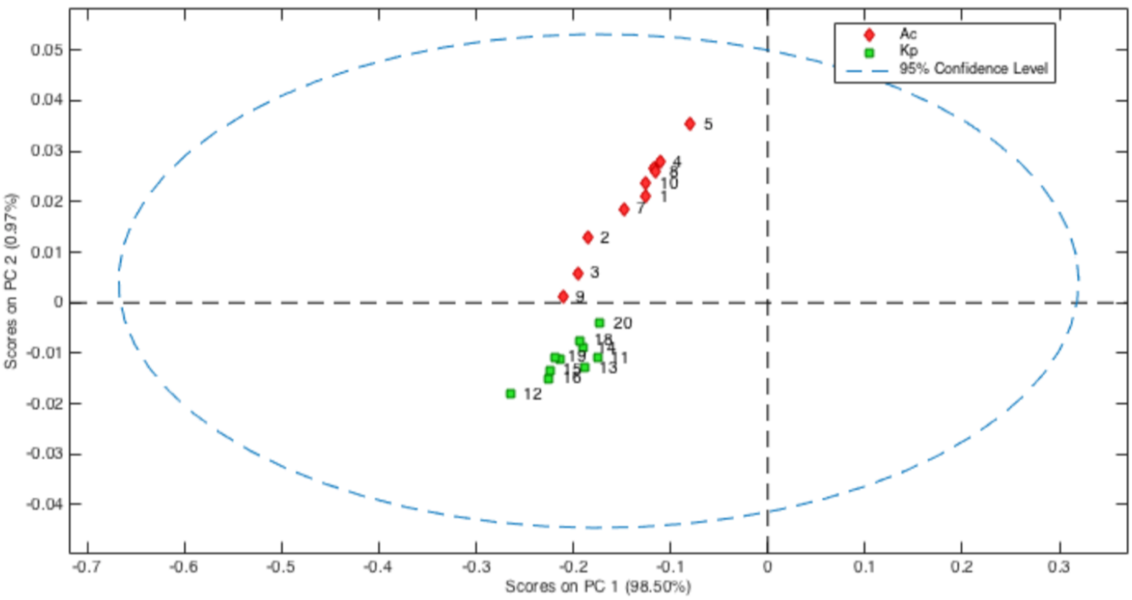

Figure 5.6 – PCA score plot for nanobioconjugates with *Acinetobacter baumannii* (◆) and with *Klebsiella pneumoniae* (■), prepared in UW – data collected with the 785 nm laser.

In sum, the lasers that assure a best discrimination are, from the better to the worst: 633 nm, 785 nm and 532 nm. The use of the first two lasers is usually less prone to fluorescence emission from the sample.[21] Fluorescence is a huge shortcoming for Raman spectroscopy, since it can hide several peaks rich in information. Although IR lasers are usually better to avoid fluorescence interferences, the lasers with lower wavelengths usually provide better resolution of the spectra. It is probable that for these biological samples, 633 nm laser is the best compromise, at least for interspecies discrimination. Since 785 nm also enable species discrimination (despite only by PC2), it should be also taken into account to an intraspecies discrimination, described on section 5.3.3 later in this chapter.

5.3.2.2. Selection of nanobioconjugation media

Other of the preliminary assessments concerned the media where the nanobioconjugates should be assembled. Two sets were tested: the media where the silver nanostars are typically manipulated – ultrapure water (UW) – and the media where the bacteria are typically manipulated – phosphate buffer saline (PBS).

Acinetobacter baumannii and *Klebsiella pneumoniae* samples were prepared accordingly to protocol 1, and their spectra are respectively depicted in figures 5.7 and 5.8, either using UW or PBS.

This experiment was also used to evaluate the influence of cysteamine capping on spectra.

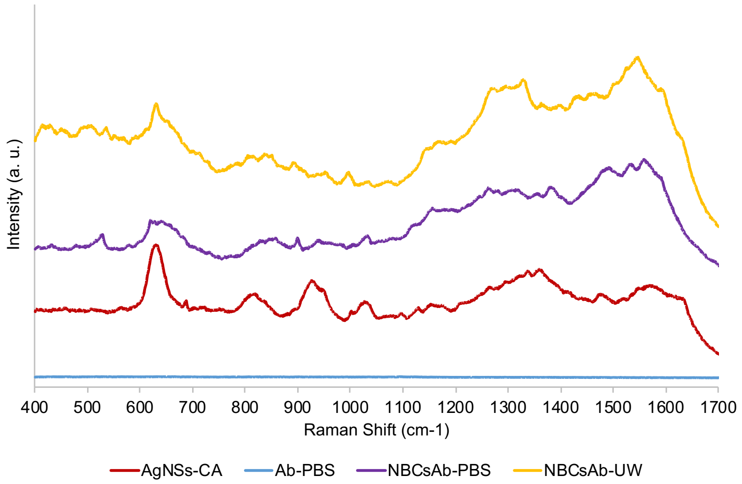

Figure 5.7 – Spectra of cysteamine-capped AgNSs (red), free *Acinetobacter baumannii* (blue) and nanobioconjugates with *Acinetobacter baumannii* prepared in PBS (purple) and UW (yellow) – acquired with 633 nm laser.

For *Acinetobacter baumannii* nanobioconjugates, the samples prepared in ultrapure water (NBCsAb-UW, figure 5.7) present a higher number of peaks than the nanobioconjugates prepared in phosphate buffer saline (NBCsAb-PBS, figure 5.7). Several new peaks are observed in NBC samples compared to the bare cysteamine-functionalised silver nanostars (AgNSs-CA) and peaks from the last are missing or attenuated in the NBC samples. It was also confirmed that, as expected, Raman signal from *Acinetobacter baumannii* alone (Ab-PBS) is negligible.

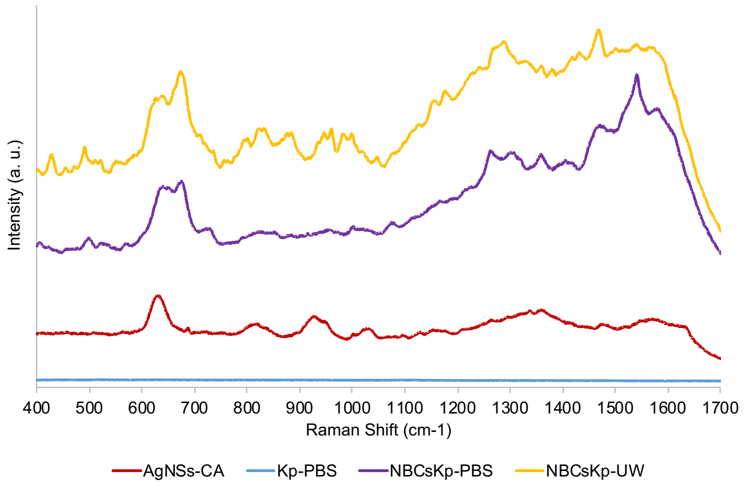

Figure 5.8 – Spectra of cysteamine-capped AgNSs (red), free *Klebsiella pneumoniae* (blue) and nanobioconjugates with *Klebsiella pneumoniae* prepared in PBS (purple) and UW (red) – acquired with 633 nm laser.

The behaviour depicted in figure 5.7 and described above, is similar to the one in figure 5.8. The NBCsKp-UW spectrum is richer in information than NBCsKp-PBS spectrum, peaks from AgNSs-CA are missing or attenuated in NBC samples and the bacteria alone (Kp-PBS) present a negligible spectrum.

In figures 5.7 and 5.8, they are noticeable regions with new peaks associated to the samples with bacteria conjugated with silver nanostars (NBCsAb and NBCsKp), not present in AgNSs spectra alone. The following assignments are proposed:[22]

There are shifted peaks (compared to cysteamine-functionalized nanoparticles) and new peaks at ~650 cm^{-1} associated to C–S bonds with different environments. A band at ~730 cm^{-1} can be due to the presence of glyosidic rings. Peaks at ~900 cm^{-1}, ~1020 cm^{-1}, ~1320–1380 cm^{-1} region and ~1460 cm^{-1} are typically associated to proteins, namely C–C stretching, phenylalanine residues, C–H bending and CH_2 bending, respectively. This last CH_2 bending is also found in lipids. Finally, the information in ~1550–1600 cm^{-1} region can be attributed to C=C in lipids. All the listed compounds are typically found or associated to bacteria membranes, but a lot of them can also be found in the cytoplasm.

Although the data is restricted to just one sample per condition, spectra were processed by principal component analysis, resulting in the score plot depicted in figure 5.9.

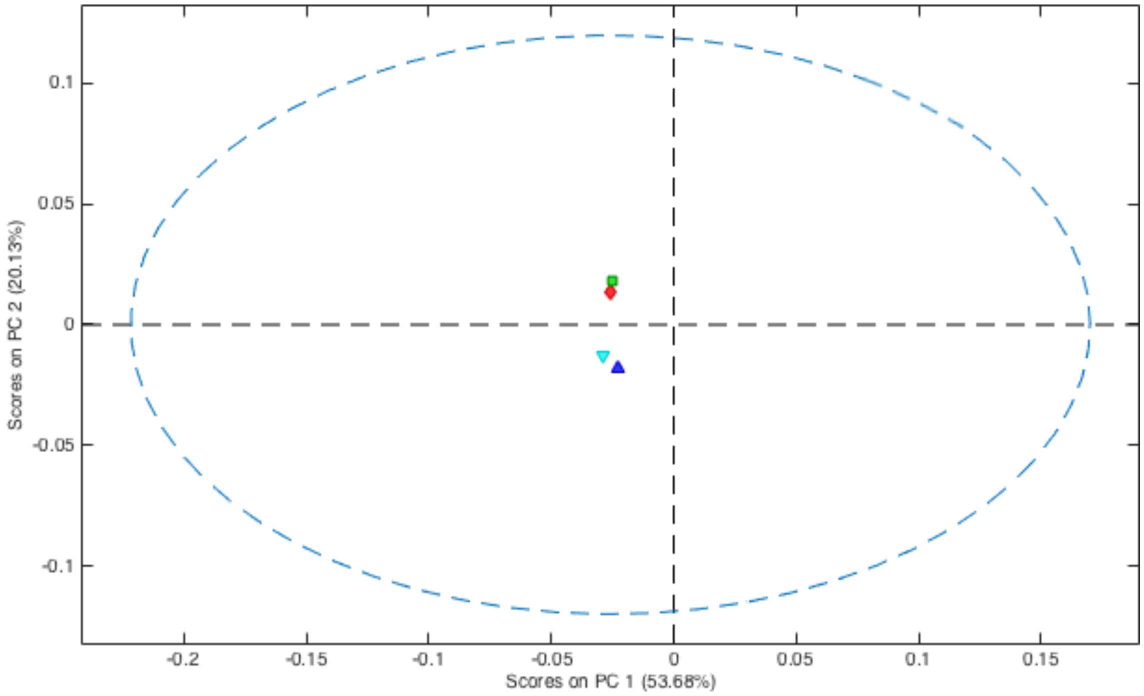

Figure 5.9 – PCA score plot for nanobioconjugates with *Acinetobacter baumannii* prepared in PBS (■) and UW (◆) and with *Klebsiella pneumoniae* prepared in PBS (▼) and UW (▲).

The samples can be distinguished by their principal component 2 (PC2), with positive scores for *Acinetobacter baumannii* and negative scores for *Klebsiella pneumoniae*, independently of the nanobioconjugation being made using PBS or UW media. Given the low number of points (samples) and the lack of discrimination in PC1, further assessments were made regarding the media selection subject.

The two score plots below (figures 5.10 and 5.11) depict the discrimination between *Acinetobacter baumannii* and *Klebsiella pneumoniae* species, with data collected with 633 nm and 785 nm lasers, using nanobioconjugates assembled in PBS. The respective score plots for nanobioconjugates assembled in UW are depicted in figures 5.5 and 5.6, back in section 5.3.2.1 (laser selection).

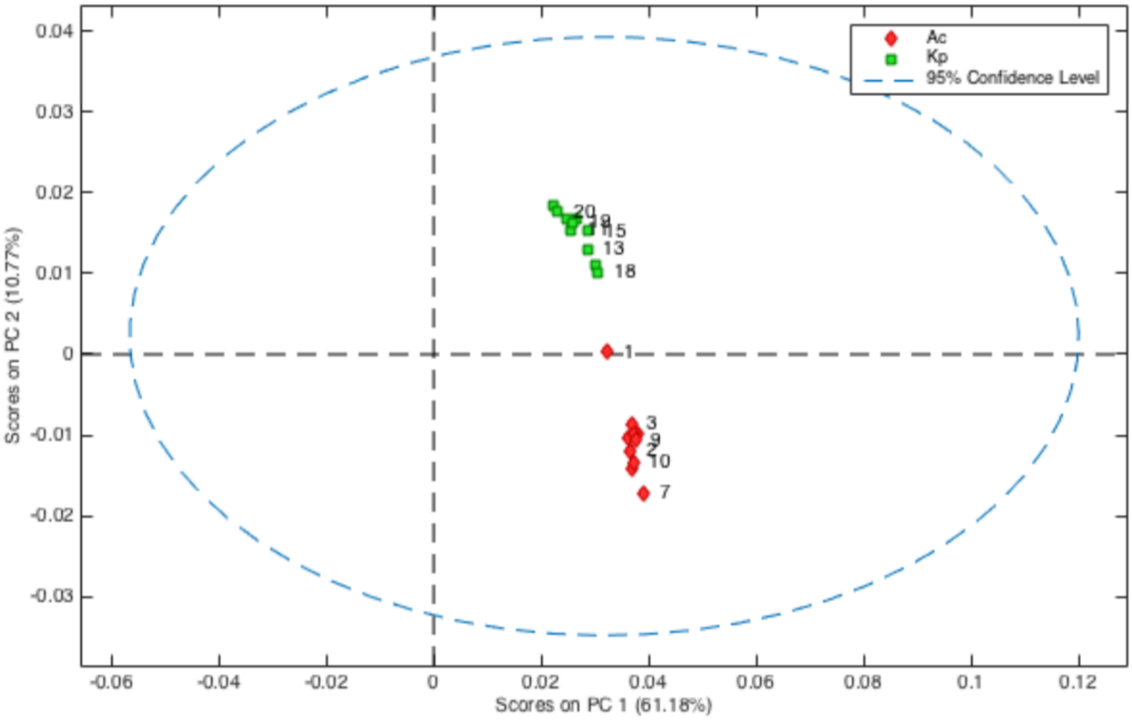

Figure 5.10 – PCA score plot for nanobioconjugates with *Acinetobacter baumannii* (◆) and with *Klebsiella pneumoniae* (■), prepared in PBS – data collected with the 633 nm laser.

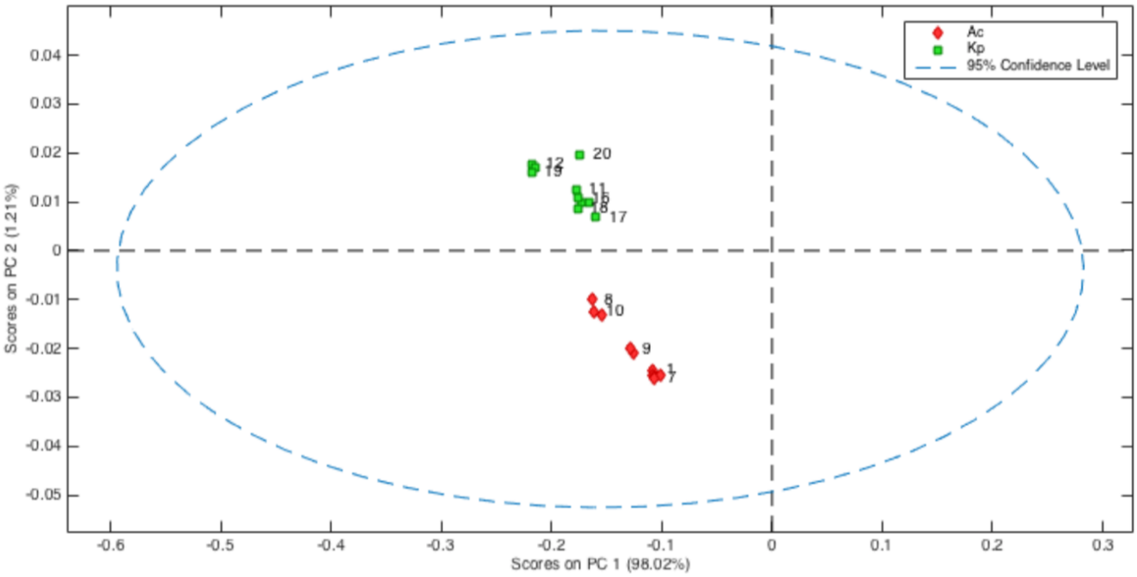

Figure 5.11 – PCA score plot for nanobioconjugates with *Acinetobacter baumannii* (◆) and with *Klebsiella pneumoniae* (■), prepared in PBS – data collected with the 785 nm laser.

Nanobioconjugates prepared in phosphate buffer saline medium present a good discrimination between the two species, as observed before to nanobioconjugates prepared in ultrapure water. Again, like the 633 nm and 785 nm laser option, both nanobioconjugation in PBS and UW deserve to be taken into account for intraspecies discrimination, explored later in section 5.3.3. Principal components 1 (PC1) weight for both scores are quite different – 61% for 633 nm data and 98% for 785 nm data. As stated before, a better weigh distribution between principal components can help the discrimination.

Data from these last two figures corroborate the previous conclusion that 633 nm laser is a slightly better fit to discriminate bacteria species, not excluding completely the 785 nm laser.

5.3.2.3. Protocol selection

When the protocol 1 (table 5.3) was considered satisfactorily established for discrimination between *Acinetobacter baumannii* and *Klebsiella pneumoniae*, more species were added to the study, namely Gram-positive *Enterococcus spp*. Protocols 2 to 5 aimed to be simplifications of protocol 1, either by eliminating the nanoparticle functionalization step, by establishing a “mix and read” procedure and/or by bringing the method closer to the typical laboratory procedures which rely in Petri dish based cultures.

The following five score plots (figures 5.12 to 5.16) depict the discrimination between four species – *Klebsiella pneumoniae*, *Salmonella enterica* and two *Enterococcus spp.* – in nanobioconjugates prepared in ultrapure water, using SERS spectra acquired using a 633 nm laser. Some key points of each the protocol are also rememberd.

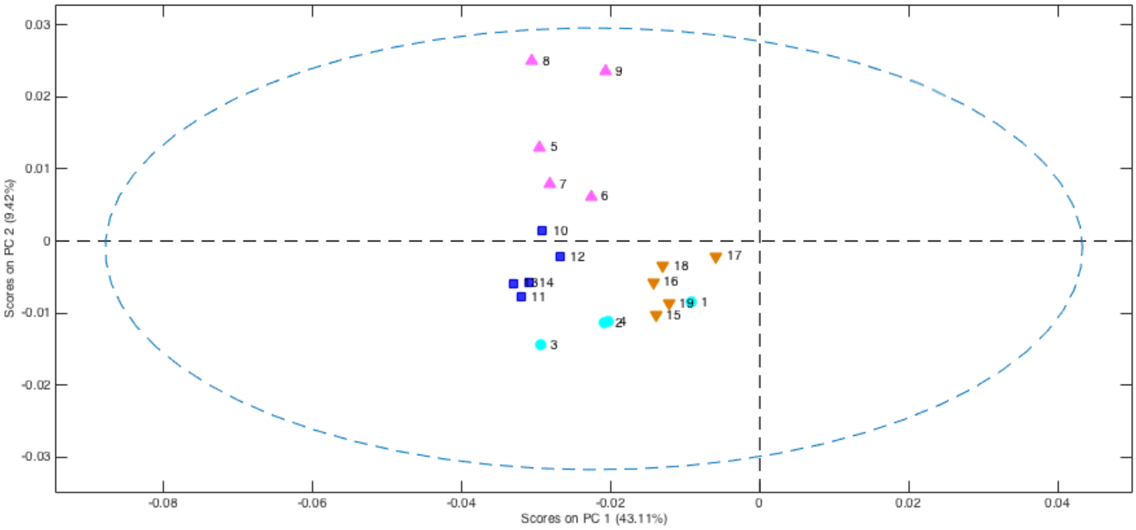

Figure 5.12 – PCA score plot for *Klebsiella pneumoniae* (▼), *Salmonella enterica* (●) and *Enterococcus spp.* (▲ and ■) samples, prepared accordingly protocol 1.

The score plot above shows that each one of the *Enterococcus spp.* can be distinguished from all the other species. Both can even be distinguished from each other in PC2. *Klebsiella pneumoniae* and *Salmonella enterica* can be distinguished from the other two species but not from each other due to overlapping points.

Protocol 1 (the only one using cultures in liquid media) can eventually be a protocol for discrimination between Gram-positive (GP) – *Enterococcus spp.* – and Gram-negative (GN) – *Klebsiella pneumoniae* and *Salmonella enterica* – bacteria groups.

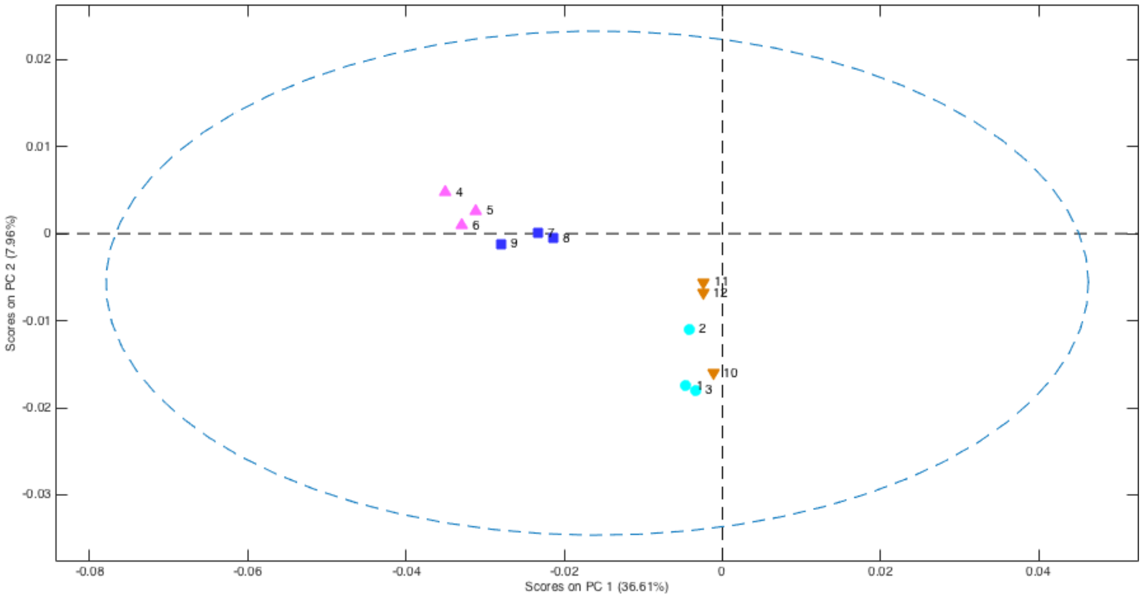

Figure 5.13 – PCA score plot for *Klebsiella pneumoniae* (▼), *Salmonella enterica* (●) and *Enterococcus spp.* (▲ and ■) samples, prepared accordingly protocol 2.

Protocol 2 (cultures in solid media, with twice the amount of biologic material used in protocol 1) also enabled the discrimination between Gram-positive (GP) – *Enterococcus spp.* – and Gram-negative (GN) – *Klebsiella pneumoniae* and *Salmonella enterica* – bacteria groups, in a more evident way that the on provided by protocol 1. In figure 5.13 is shown a distinction between GP and GN species both in PC1 and PC2, while in figure 5.12 this distinction is not clear both in PC1 and PC2.

The discrimination between both GP bacteria is more evident, due the absence of overlapping scores, than the discrimination between both GN bacteria, which showed some overlapped points from the two groups of scores.

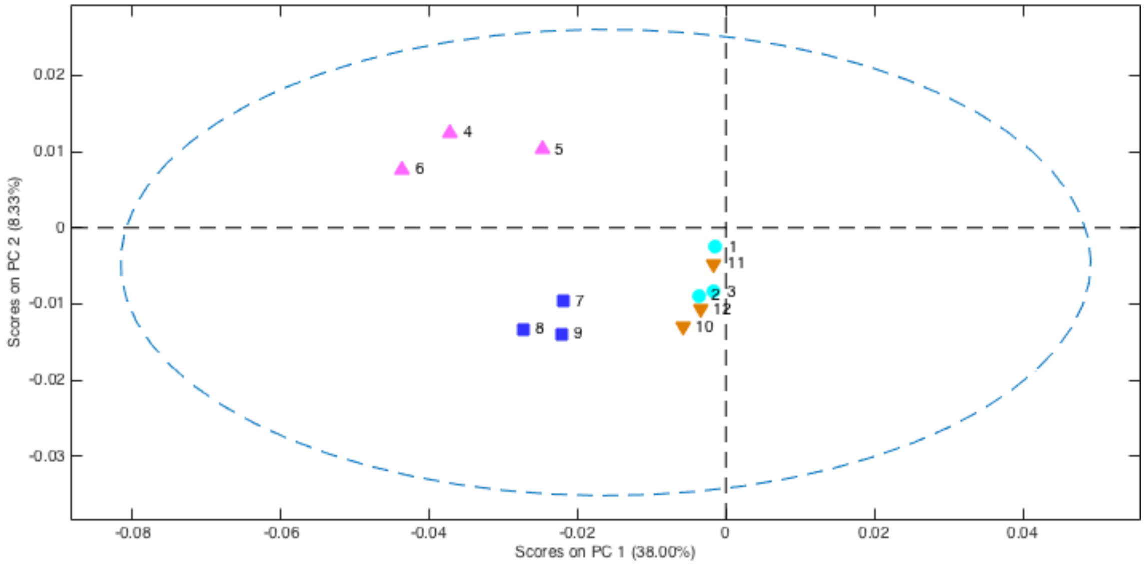

Figure 5.14 – PCA score plot for *Klebsiella pneumoniae* (▼), *Salmonella enterica* (●) and *Enterococcus spp.* (▲ and ■) samples, prepared accordingly protocol 3.

Protocol 3 (equivalent to protocol 2, but with an immediate deposition of the nanobioconjugates on the support) also enabled the discrimination between Gram-positive (GP) – *Enterococcus spp.* – and Gram-negative (GN) – *Klebsiella pneumoniae* and *Salmonella enterica* – bacteria groups, taking in to account PC1 scores.

The discrimination between both GP bacteria was the most evident between all five protocols, with positive scores in PC2 for one species and negative scores in for the other. In the other hand, scores for both GN bacteria, can easily be considered as just one group, with their similar PC1 and PC2 scores.

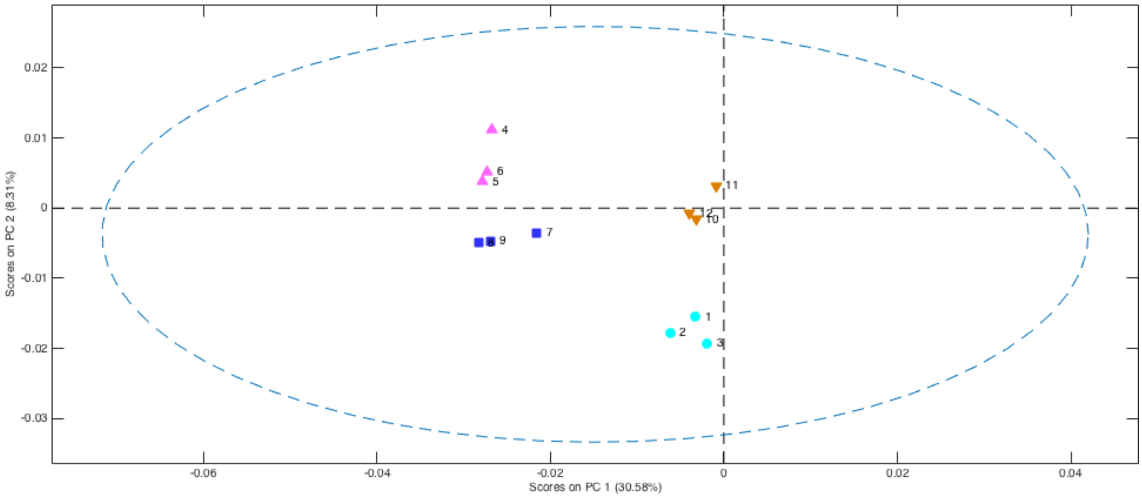

Figure 5.15 – PCA score plot for *Klebsiella pneumoniae* (▼), *Salmonella enterica* (●) and *Enterococcus spp.* (▲ and ■) samples, prepared accordingly protocol 4.

In the score plot above, the two GN and GP major groups are clearly distinguished in PC1. The two species belonging to each GN and GP groups are distinguished from each other in PC2.

So, protocol 4 (equivalent to protocol 3, but using citrate-capped silver nanostars, in opposite to all other protocols) enabled the discrimination between all four species, being the best of all five protocols in this matter. The use of citrate can have a role on this better discrimination, since is more labile than cysteamine. This probably allows that citrate is replaced by compounds than can assure discrimination between the two Gram negative bacteria - *Klebsiella pneumoniae* and *Salmonella enterica*

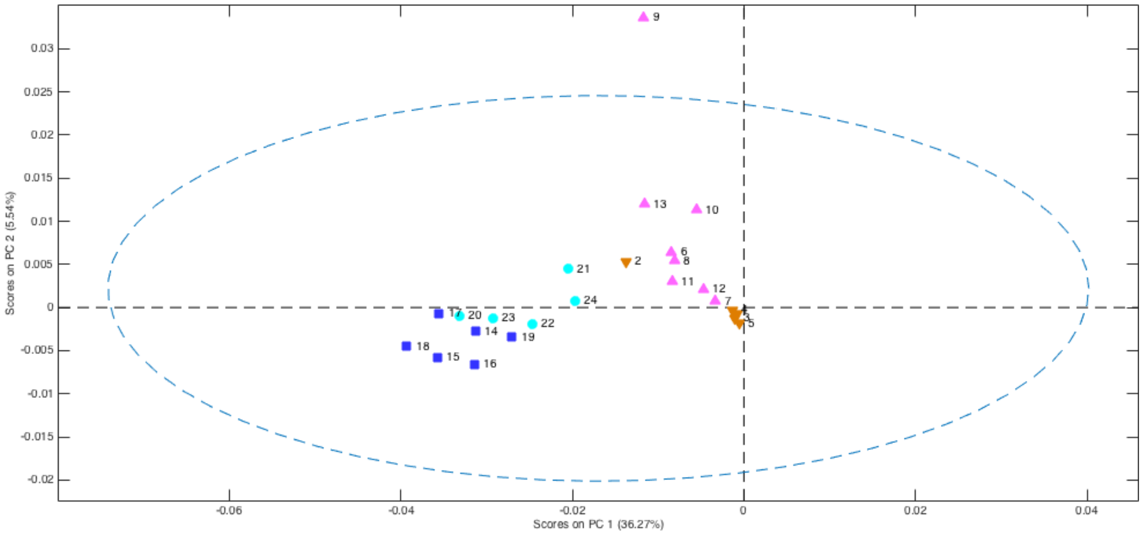

Figure 5.16 – PCA score plot for *Klebsiella pneumoniae* (▼), *Salmonella enterica* (●) and *Enterococcus spp.* (▲ and ■) samples, prepared accordingly protocol 5.

Protocol 5 (equivalent to protocol 2, but with 2.5 times more microbiologic material) originated a very poor discrimination between the Gram groups, and consequently between any of the analysed species. There are PC2 scores common to all species and in PC1 there also values common to two species, however each one belonging a different GP or GN groups.

Analysing both the data in this section and the SEM data in section 5.3.1, it was expected that, for example, protocol 5 could originate good results given the high load and uniformity of the AgNSs on the surface. On the other hand, SEM micrographs obtained for protocol 4 indicated a not so promising method, given the lower load of AgNSs, however, this protocol gave origin to the better discrimination data, as stated before. There are phenomena that can overlap the importance of AgNSs distribution across the sample, such as the decoration of these nanoparticles by relevant and specific compounds for bacteria discrimination.

This protocol comparison still has some gaps to be filled in. Two of the major needs are the use of multiple isolates per sample and the acquisition of a higher number of spectra per sample.

5.3.3. Intraspecies discrimination

After a successful interspecies discrimination between *Acinetobacter baumannii* and *Klebsiella pneumoniae*, a more detailed (intraspecies) discrimination was attempted.

The discrimination was based in different sequence types for the same species. Both lasers (633 nm and 785 nm) and both nanobioconjugation media (PBS and UW) that were successfully able to discriminate these two species were again tested, in order to evaluate their suitability also for intraspecies discrimination.

Data for intraspecies discrimination was analysed by partial least squares discriminant analysis (PLS-DA) in order to sharpen the separation between groups of observations. Data presented in two-dimensional score plots did not show better discrimination when plotted in three-dimensional score plots (data not shown).

5.3.3.1. Laser selection

Six sequence types listed for *Acinetobacter baumannii* in table 5.1 – 98, 103, 208, 218, 515 and 1000 – were analysed. Latent variables (LV) scores resulting from PLS-DA are plotted in figures 5.17 and 5.18. Spectra were acquired with 633 nm and 785 nm lasers, respectively.

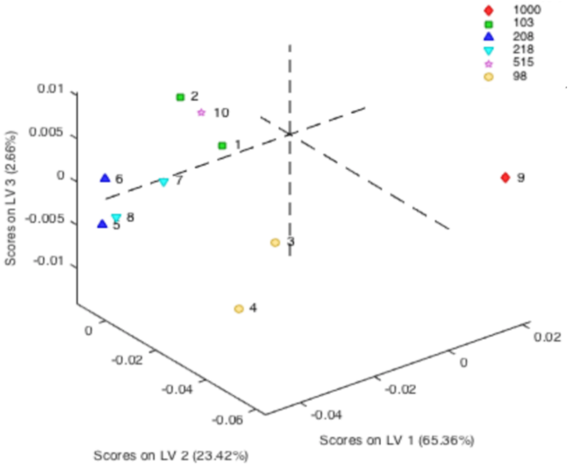

Figure 5.17 – PLS-DA score plot for nanobioconjugates with *Acinetobacter baumannii* sequence types 98 (●), 103 (■), 208 (▲), 218 (▼), 515 (★) and 1000 (◆), prepared in UW – data collected with the 633 nm laser.

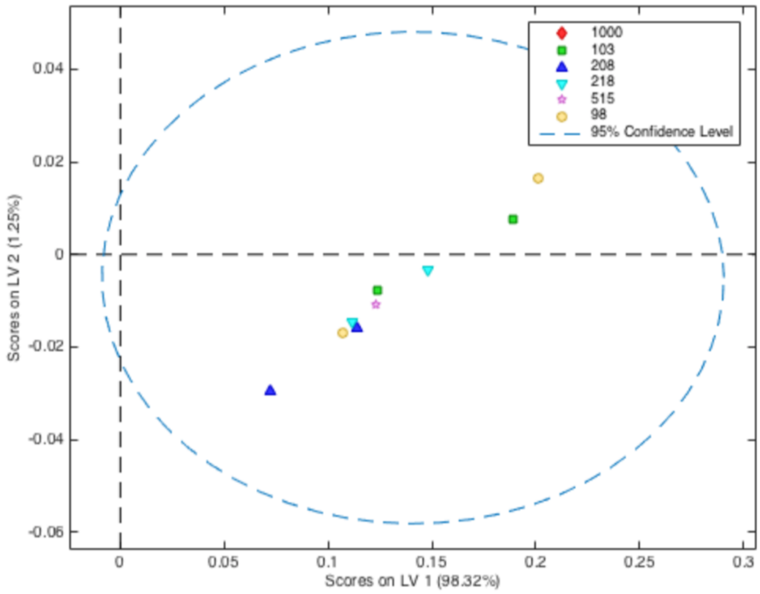

Figure 5.18 – PLS-DA score plot for nanobioconjugates with *Acinetobacter baumannii* sequence types 98 (●), 103 (■), 208 (▲), 218 (▼), 515 (★) and 1000 (◆), prepared in UW – data collected with the 785 nm laser.

Results for discrimination by sequence type for *Acinetobacter baumannii* were not satisfactory. Data extracted from spectra collected with the 633 nm laser, when plotted in a three-dimensional score plot (figure 5.17) can better discriminate sequence types 98 and 1000, but there are overlapping scores for the other sequence types.

The scenario obtained with data from 785 nm laser is worse (figure 5.18), with scores from the same sequence type always overlapped with other scores. Like PC in PCA plots in other sections, here LV1 has a high weigh in opposition to others, compromising sample differentiation.

Three sequence types listed for *Klebsiella pneumoniae* in table 5.1 – 14, 15 and 147 – were analysed. Latent variables (LV) scores resulting from PLS-DA are plotted in figures 5.19 and 5.20. Spectra were acquired with 633 nm and 785 nm lasers, respectively.

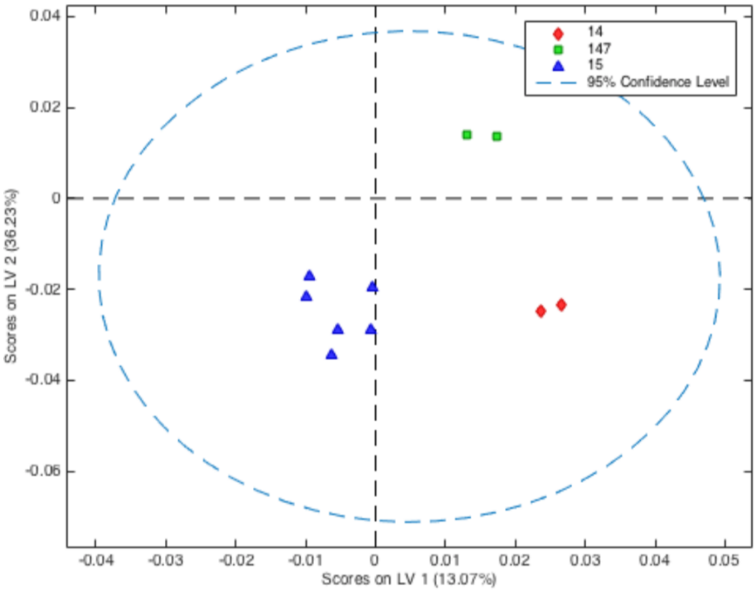

Figure 5.19 – PLS-DA score plot for nanobioconjugates with *Klebsiella pneumoniae* sequence types 14 (◆), 15 (▲), and 147 (■), prepared in UW – data collected with the 633 nm laser.

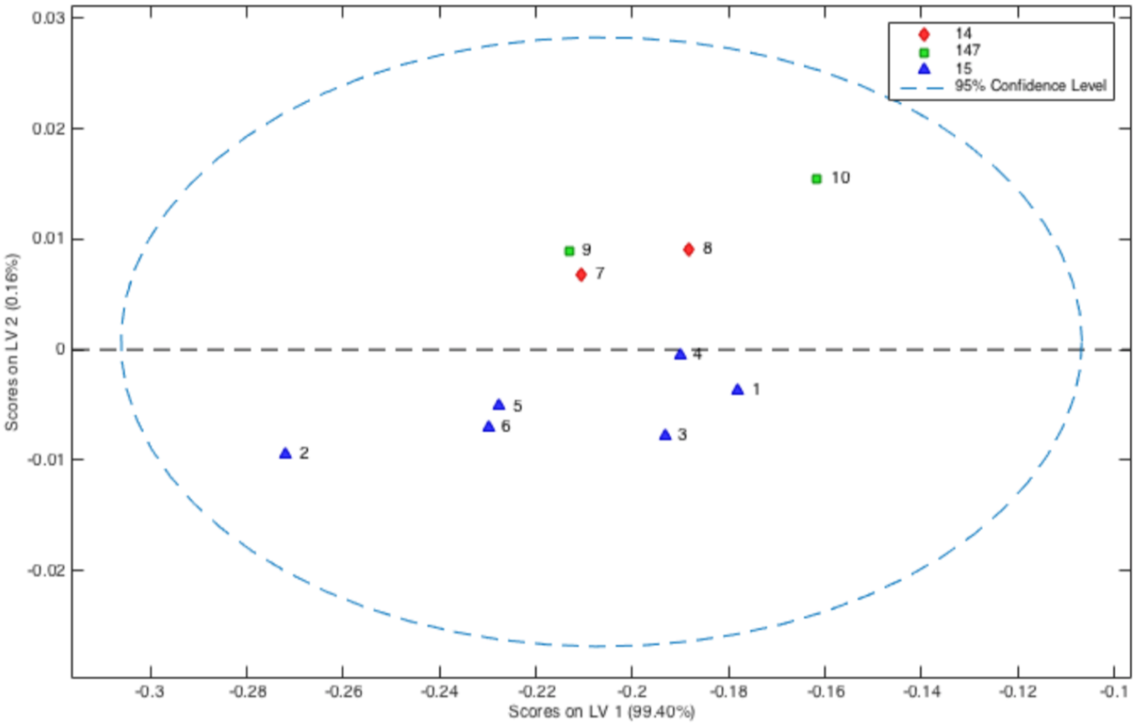

Figure 5.20 – PLS-DA score plot for nanobioconjugates with *Klebsiella pneumoniae* sequence types 14 (◆), 15 (▲), and 147 (■), prepared in UW – data collected with the 785 nm laser.

For *Klebsiella pneumoniae*, the intraspecies discrimination was better, especially considering the spectra obtained with 633 nm laser. In PLS-DA score plot depicted in figure 5.19 are clearly visible three groups corresponding to the three different sequence types.

In figure 5.20, with data from experiments with the 785 nm laser, the distinction between sequence types 14 and 147 was not possible. Like the results depicted in figure 5.18, the same LV1 high weigh in opposition to others seems to compromise sample differentiation.

5.3.3.2. Nanobioconjugation media selection

Klebsiella pneumoniae served as an intraspecies model for evaluating phosphate buffer saline as other possible conjugation media. Figures 5.21 and 5.22 below depict score plots equivalent to figures 5.19 and 5.20 from last section, with the latter relative to an ultrapure water medium.

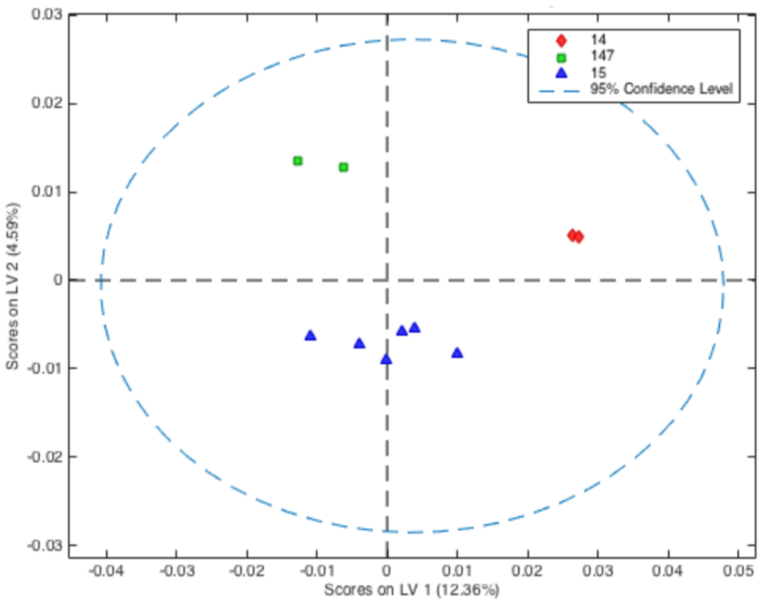

Figure 5.21 – PLS-DA score plot for nanobioconjugates with *Klebsiella pneumoniae* sequence types 14 (◆), 15 (▲), and 147 (■), prepared in PBS – data collected with the 633 nm laser.

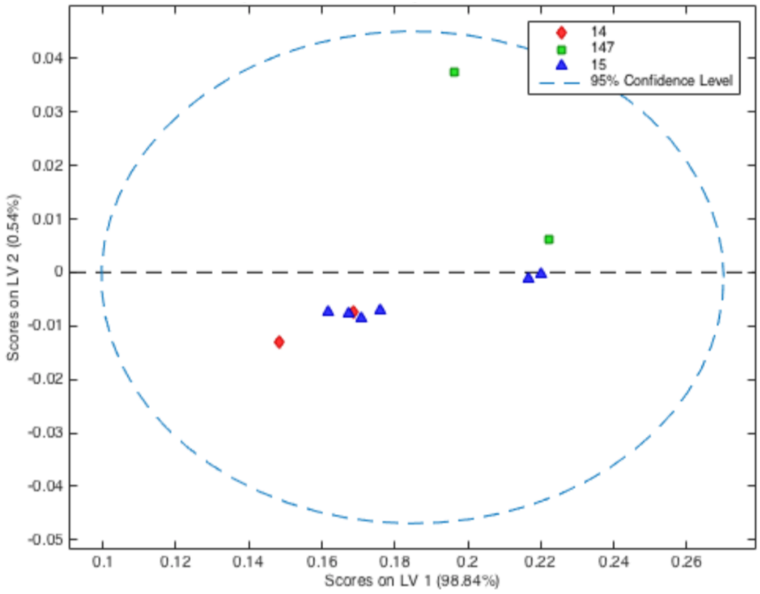

Figure 5.22 – PLS-DA score plot for nanobioconjugates with *Klebsiella pneumoniae* sequence types 14 (◆), 15 (▲), and 147 (■), prepared in PBS – data collected with the 785 nm laser.

The discrimination of nanobioconjugates assembled in PBS, with their SERS spectra collected using the 633 nm laser, was satisfactory, since it is possible two observe three well defined groups. However, when compared with figure 5.19 (data obtained from the same experimental conditions, except for nanobioconjugation medium that was water) the discrimination is better, since sequence type 15 scores are only negative in LV1, and in the case of figure 5.20 they show both positive and negative scores, not evidencing a discrimination in LV1. Scores in the nanobioconjugates assembled in PBS score plot (figure 5.22), resulting from 785 nm laser experiments, can be considered overlapped.

After all the data and analysis presented before, the use of a 633 nm for SERS spectra acquisition and an ultrapure water as nanobioconjugation medium were found to be the most appropriate for a bacteria fingerprinting protocol. As already discussed, the 633 nm laser seem to be the best compromise between fluorescence effect attenuation and resolution. Regarding phosphate saline buffer *vs.* ultrapure water, the latter causes bacteria stress and osmotic lysis, leading to the production and/or release of metabolites or biomolecules that can help to identify a specific species or sequence type.

With the chosen laser (633 nm) and nanobioconjugation media (UW), extra measurements were made for a new set of samples. This set increases the number of *Klebsiella pneumoniae* sequence types and also the number of samples per sequence type. The data obtained is plotted in the three-dimensional score plot depicted in figure 5.23.

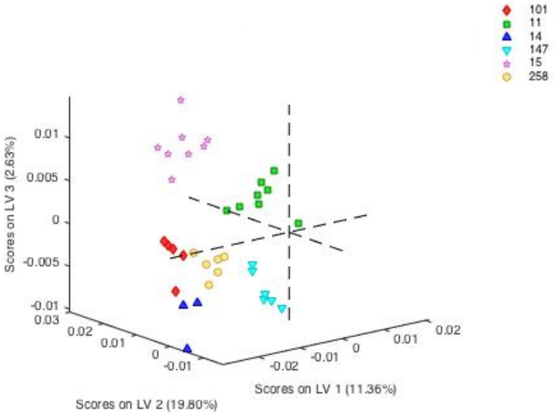

Figure 5.23 – PLS-DA score plot for nanobioconjugates with *Klebsiella pneumoniae* sequence types 11 (■), 14 (▲), 15 (★), 101 (◆), 147 (▼) and 258 (●), prepared in UW – data collected with the 633 nm laser.

Observing the plot in figure 5.23 here are different sequence types with similar scores in LV1 (*e.g.* 11 and 15), LV2 (*e.g.* 14 and 147) and LV3 (*e.g.* 101 and 258). However, the six sequence types – 11, 14, 15, 101, 147 and 258 – clearly form six different groups in the three-dimensional space of the score plot, since each one of them have unique LV1–LV2–LV3 scores combination.

5.4. Conclusions

There is a lot of concern regarding antibiotic-resistant bacteria and for a prompt response to the infections they cause. A crucial point is to get early results regarding the infectious species (and regarding other intraspecies data, if possible).[1] In this work, surface-enhanced Raman spectroscopy was explored as a technique capable of this differentiation. The use of silver nanostars, nanobioconjugated with bacteria from the WHO critical and high priority groups[2] and the use of easily disposable support, were here described.

Several parameters like the capping of silver nanostars, nanobioconjugation media, incubation time, biomaterial amount or laser wavelength were studied. The final criterion was if a set of conditions enabled or not a good discrimination in principal component analysis or score plots.

Regarding the capping of silver nanostars, where cysteamine or citrate were tested, citrate was found be better, possibly due to its lability. Because it is easily exchanged with other molecules (in opposition to cysteamine), these other molecules can be closer to hotspots and consequently under the influence of a stronger magnetic field.

For nanobioconjugation media ultrapure water and phosphate buffer saline were tested. Experiments using water gave better results, probably by the stress caused to the bacteria that can origin the production of stress metabolites that can be released due to cell lysis.

For incubation time (in nanobioconjugation step), no special difference was found. Probably the period when the sample is still drying is enough to cause bacterial stress and lysis.

The worst results for interspecies differentiation, were obtained with the highest loading of biomaterial on the support, proving the lower amounts tested are enough for obtain a good signal.

Regarding the most appropriate laser wavelength, the green (532 nm) laser was excluded right on interspecies discrimination. Red (633 nm) and infrared (785 nm) lasers were used down to intraspecies discrimination, since they have lower fluorescence interferences. Infrared was even better to avoid fluorescence phenomena, but probably due to its lower spectral resolution when compared to the red laser, the results obtained using 633 nm laser provided a better discrimination.

The objective of quickly and accurately discriminate different species and different sequence types belonging to the same species was achieved. It was possible to differentiate *Acinetobacter baumannii*, *Klebsiella pneumoniae*, *Salmonella enterica* and *Enterococcus spp.* species and 11, 14, 15, 101, 147 and 258 sequence types from *Klebsiella pneumoniae*. These are promising results for a quick and cost-effective protocol for bacteria fingerprinting.

The collection of data from additional species can help to consolidate these results. This larger batch of samples can also help to tune even more the protocol in order to establish a large spectrum protocol as a primary approach. Additional and alternative protocols can also be developed for results confirmation, fitted to a special group of microorganisms (Gram negative *vs.* Gram positive) or even fitted to specific species, for intraspecies discrimination. The methods here described still imply incubation periods for bacterial growth. The possibility of using the advantage of surface-enhanced Raman spectroscopy provided by the silver nanostars can eventually allow to do direct analyses on biological fluids. This could be an interesting application to be explored.

5.5. References

1. ED Brown, GD Wright. Antibacterial drug discovery in the resistance era. *Nature* **2016,** *529* (7586), 336-43.

2. WH Organization WHO publishes list of bacteria for which new antibiotics are urgently needed. http://www.who.int/news-room/detail/27-02-2017-who-publishes-list-of-bacteria-for-which-new-antibiotics-are-urgently-needed (accessed 21 May 2018).

3. HC Flemming, J Wingender, U Szewzyk, P Steinberg, SA Rice, S Kjelleberg. Biofilms: an emergent form of bacterial life. *Nature Reviews Microbiology* **2016,** *14* (9), 563-75.

4. M Ghebremedhin, R Heitkamp, S Yesupriya, B Clay, NJ Crane. Accurate and Rapid Differentiation of *Acinetobacter baumannii* Strains by Raman Spectroscopy: a Comparative Study. *Journal of Clinical Microbiology* **2017,** *55* (8), 2480-2490.

5. Y Cheong, YJ Kim, H Kang, S Choi, HJ Lee. Rapid label-free identification of *Klebsiella pneumoniae* antibiotic resistant strains by the drop-coating deposition surface-enhanced Raman scattering method. *Spectrochimica Acta Part A: Molecular and Biomolecular Spectroscopy* **2017,** *183*, 53-59.

6. C-C Lin, C-Y Lin, C-J Kao, C-H Hung. High efficiency SERS detection of clinical microorganism by AgNPs-decorated filter membrane and pattern recognition techniques. *Sensors and Actuators B: Chemical* **2017,** *241*, 513-521.

7. R Prucek, V Ranc, L Kvitek, A Panacek, R Zboril, M Kolar. Reproducible discrimination between gram-positive and gram-negative bacteria using surface enhanced Raman spectroscopy with infrared excitation. *Analyst* **2012,** *137* (12), 2866-70.

8. PAC Braga, A Tata, V Gonçalves dos Santos, JR Barreiro, NV Schwab, M Veiga dos Santos, MN Eberlin, CR Ferreira. Bacterial identification: from the agar plate to the mass spectrometer. *RSC Advances* **2013,** *3* (4), 994-1008.

9. K Cheng, H Chui, L Domish, D Hernandez, G Wang. Recent development of mass spectrometry and proteomics applications in identification and typing of bacteria. *Proteomics Clinical Applications* **2016,** *10* (4), 346-57.

10. L Krásný, R Hynek, I Hochel. Identification of bacteria using mass spectrometry techniques. *International Journal of Mass Spectrometry* **2013,** *353*, 67-79.

11. RM Jarvis, R Goodacre. Characterisation and identification of bacteria using SERS. *Chemical Society Reviews* **2008,** *37* (5), 931-6.

12. RM Jarvis, A Brooker, R Goodacre. Surface-enhanced Raman scattering for the rapid discrimination of bacteria. *Faraday Discussions* **2006,** *132*, 281-292.

13. RM Jarvis, R Goodacre. Discrimination of bacteria using surface-enhanced Raman spectroscopy. *Analytical Chemistry* **2004,** *76* (1), 40-7.

14. IS Patel, WR Premasiri, DT Moir, LD Ziegler. Barcoding bacterial cells: A SERS based methodology for pathogen identification. *Journal of Raman Spectroscopy* **2008,** *39* (11), 1660-1672.

15. WR Premasiri, DT Moir, MS Klempner, N Krieger, G Jones, 2nd, LD Ziegler. Characterization of the surface enhanced raman scattering (SERS) of bacteria. *The Journal of Physical Chemistry B* **2005,** *109* (1), 312-20.

16. D Yang, H Zhou, C Haisch, R Niessner, Y Ying. Reproducible E. coli detection based on label-free SERS and mapping. *Talanta* **2016,** *146*, 457-63.

17. Y Liu, YR Chen, X Nou, K Chao. Potential of surface-enhanced Raman spectroscopy for the rapid identification of Escherichia coli and Listeria monocytogenes cultures on silver colloidal nanoparticles. *Applied Spectroscopy* **2007,** *61* (8), 824-31.

18. M Knauer, NP Ivleva, R Niessner, C Haisch. Optimized Surface-enhanced Raman Scattering (SERS) Colloids for the Characterization of Microorganisms. *Analytical Sciences* **2010,** *26* (7), 761-766.

19. WR Premasiri, JC Lee, A Sauer-Budge, R Theberge, CE Costello, LD Ziegler. The biochemical origins of the surface-enhanced Raman spectra of bacteria: a metabolomics profiling by SERS. *Analytical and Bioanalytical Chemistry* **2016,** *408* (17), 4631-47.

20. MJ Oliveira, P Quaresma, M Peixoto de Almeida, A Araújo, E Pereira, E Fortunato, R Martins, R Franco, H Águas. Office paper decorated with silver nanostars - an alternative cost effective platform for trace analyte detection by SERS. *Scientific Reports* **2017,** *7* (1), 2480.

21. D Tuschel. Selecting an Excitation Wavelength for Raman Spectroscopy. *Spectroscopy* **2016,** *31* (3), 14–23.

22. NE Dina, AMR Gherman, V Chis, C Sarbu, A Wieser, D Bauer, C Haisch. Characterization of Clinically Relevant Fungi via SERS Fingerprinting Assisted by Novel Chemometric Models. *Analytical Chemistry* **2018,** *90* (4), 2484-2492.

Nanostructured surfaces for Surface-Enhanced Raman Spectroscopy

6

6.1. Introduction

In the previous two chapters silver nanostars were conjugated with molecules from real samples for a fingerprinting purpose. In the work described in this chapter, the objective was to obtain a surface, rich in silver nanostars, that can be ready for reading different analytes of interest.

Given the affinity of nitrogen to silver surfaces[1-2], one possible application of this method could be the detection of biogenic amines like putrescine and cadaverine, associated with poor sanitary conditions, or tyramine and histamine, suspected to cause a toxicological effect.[3]

6.1.1. Nanostructured silver surfaces for SERS

Typically, the silver "ready to use" for surface-enhanced Raman spectroscopy (SERS) is under the form of silver colloids, used with or without induced aggregation.[4-8] In these type of analysis, the silver colloid, and eventually the aggregation agent, work like a reagent to be added to the media containing the analyte.

Nanostructured surfaces using silver nanoparticles have considerably less reports. The most commonly reported way of creating a support rich in silver for SERS is through the silver mirror reaction[9-11]. These reactions were already described for less conventional supports like a melamine sponge[10] or filter paper[11]. Other works report the use of templates on top of flat surfaces (*e.g.* glass), using latex/polystyrene particles that are later coated with silver[12-13], nanoparticle synthesis on top of the substrate[14] or nanoparticle immobilization by means of a chemical agent linking both substrate and silver nanoparticles[15]. In this last case, enhancement factors in the 10^7 range were observed.

Given the lack of reports of fine-tuned nanostructured SERS substrates in the literature, the work described in this chapter aimed to produce a support containing highly SERS-efficient silver nanostars, evenly distributed, preferentially as a monolayer. This type of organization will assure a better reproducibility across the same support and between supports. Variability is expected from colloids that undergo aggregation – a highly unpredictable phenomenon – and randomly organized supports.

6.1.2. Amine-functionalized glass supports

If the affinity of nitrogen to silver surfaces[1-2] make silver nanoparticles able to bind analytes, especially the ones with nitrogen atoms in their composition, substrates with exposed chemical groups like amines can also be excellent to immobilize silver nanoparticles.

The functionalization of available silanol groups in glass, exposed usually by a piranha solution treatment[16], by (3-aminopropyl)triethoxysilane (APTES), enables the formation of a surface rich in amine groups[17]. The hydrolysis followed by condensation between silanol groups and APTES is depicted below (reaction scheme 6.1).

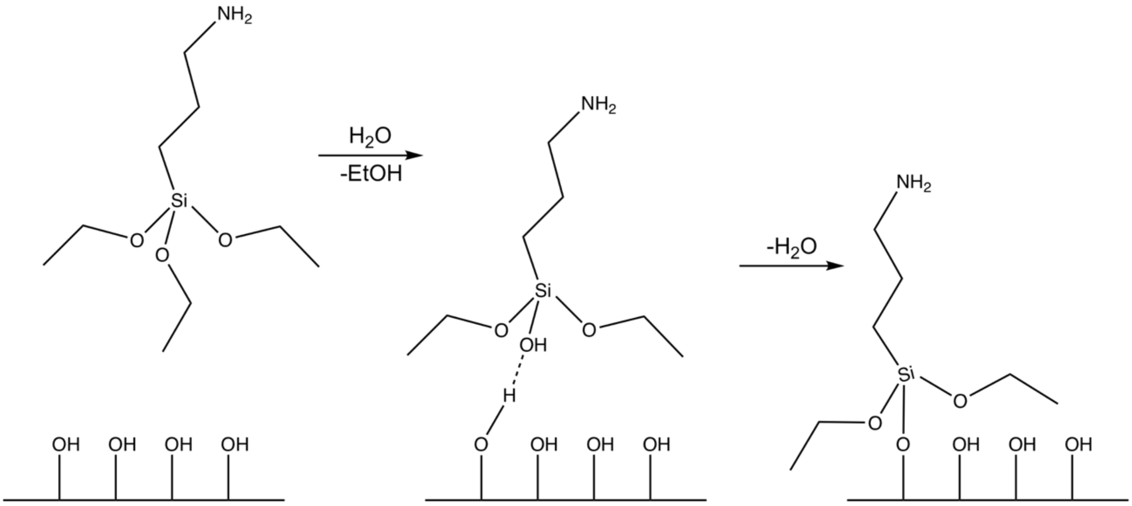

Reaction Scheme 6.1 – APTES hydrolysis followed by condensation for silica surface amination.

Reports on APTES-functionalized glass surfaces as support of silver nanoparticles are scarce and they are used in other applications beside SERS.[18-19]

Other surfaces like the already mentioned silver mirrors or others covered with silver nanoparticles, can also be a good support to immobilize silver nanostars trough a molecular linker, with groups with affinity for silver in both ends.

6.2. Methods

This section enlists the main equipment, the reagents and the experimental procedures. All the reagents were used as purchased, with no further steps of purification. Equipment and reagents used in protocols listed in this section but described in other chapters, are omitted.

Supports and samples dry or curation, were done in an oven Memmert UF30. Samples were sonicated in a Bandelin Sonorex Digitec DT 100 H ultrasonic bath. The orbital shaker used was a Digisystem Laboratory Instruments DSR-2800V.

Raman/SERS spectra were acquired using a Labram 300 Horiba Jobin Yvon spectrometer and a Renishaw inVia Qontor, both equipped with a 633 nm laser (HeNe) and a 50x objective, for a 1000-1700 cm^{-1} window. Both were operated by Maria João Oliveira at *Departamento de Conservação e Restauro da Faculdade de Ciências e Tecnologia da Universidade Nova de Lisboa* (*FCTUNL*) and *CENIMAT|i3N*, respectively.

Scanning electron microscopy (SEM) was performed in a Carl Zeiss AURIGA Crossbeam (focused ion beam SEM) Workstation microscope, operated by Maria João Oliveira at *CENIMAT|i3N*.

The following reagents were used: absolute ethanol (Fisher), (3-aminopropyl)triethoxysilane 98% (TCI), ammonium hydroxide 25% (Merck), hydrogen peroxide 30% (Fisher), potassium hydrogenophosphate 98% (Sigma-Aldrich), potassium di-hydrogenophosphate 99% (Sigma-Aldrich), silver nitrate 99.9999% (Aldrich), sodium hydroxide 99% (Fisher), sulfuric acid 95-97% (Fluka), phosphoric acid and tetraethylrhodamine hydrochloride (rhodamine 6G) 95% (Sigma-Aldrich).

6.2.1. Synthesis of silver nanostars

The synthesis of silver nanostars (AgNSs) was performed by the protocol described in chapter 4, section 4.2.1.

6.2.2. Decorated silicon-based supports

Silicon wafers decorated with a layer of silver nanoparticles with a 6 nm thickness, deposited using an electron gun-assisted thermal evaporation technique[20] were used as substrates. The preparation of these modified silicon wafers was performed at *CENIMAT|i3N* by Dr. Andreia Araújo.

The silver layer on the silicon substrate was then functionalised with a bifunctional linker with a thiol group in one end and an amine group in the other end. For this functionalisation, square-shape silicon wafers with the silver layer, with 2 cm side length, were immersed in 5 mL of a 10 μM ethanol solution of the bifunctional linker for 30 minutes and then washed twice with 5 mL of absolute ethanol. Adsorption by immersion was chosen instead of drop casting to avoid drying effects like a "coffee ring gradient".

After these steps, common to all samples except some control samples, the conditions to immobilize silver nanostars on this substrate were varied according to table 6.1.

Table 6.1 – Silicon based supports.

Sample ID	[AgNS] (nM)	Shaking[a]
SS.C1–2	n.a.	n.a.
SS.10.UUa–c	0.10	UU
SS.05.UUa–c	0.05*	UU
SS.05.UUd–f	0.05*	UU
SS.05.USa–c	0.05	US

Notes n.a.: not applicable; * – different AgNSs batches; [a] – UU: undisturbed, US: assisted by ultra-sounds.

All samples were prepared in triplicate, with an adsorption time of 30 minutes, also by immersion in an AgNSs media. Concentration of silver nanostars in the media was 0.05 or 0.10 nM. Samples SS.C1–2 were controls, *i.e.* surfaces as prepared at *CENIMAT|i3N*. In samples with their incubation assisted by ultra-sounds (SS.05.US), the vessel was in an ultra-sounds bath for the 30 minutes of adsorption time. Every sample was washed with ultrapure water and dried before storage for SERS readings.

6.2.3. Functionalized glass-based supports

Prior to use, all glassware was washed by immersion in piranha solution[16] for 1 hour, in order to remove any contaminants from glass surface and to expose the silanol groups[21] for further reaction. *Attention: This piranha solution is highly corrosive and should be manipulated with extreme care.*

The amine functionalization of the glass, according to the reaction scheme 6.1 (section 6.1.3), is performed as follows, based on a well stablished protocol[22]. Clean and dry glass slides were placed in a jar filled with a 2% (v/v) ethanolic solution of (3-aminopropyl)triethoxysilane (APTES). After 30 minutes, the slides were removed and washed with absolute ethanol and then dried for 100 °C for 30 minutes. After this period the glasses were ready to be stored for further use.

The functionalized supports were prepared by immersion in a colloidal solution of silver nanostars, like for the silicon substrates. However, the total number of the experiments was larger for glass substrate samples.

The concentration range studied was from 0.1 to 0.8 nM, with adsorption time of 60 or 120 minutes. The solution was left undisturbed (UU), in the ultrasonic bath (US) or under orbital shaking at 100 rpm (OS). The pH ranged from 6.0 to 11.0, including the usual pH (slightly basic) of the silver nanostars solution (S). Every sample was washed with ultrapure water and dried before storage for SERS experiments. Detailed information about the samples is summarized in table 6.2.

Table 6.2 – Functionalised glass-based supports.

Sample ID	[AgNS] (nM)	Adsorption Time^{a} (min)	Shaking^{b}	pH^{c}
GS.10.OS.60.085$_{a-c}$	0.1	60	OS	8.5
GS.20.OS.60.085$_{a-c}$	0.2	60	OS	8.5
GS.10.US.60.085$_{a-c}$	0.1	60	US	8.5
GS.10.OS.60.060$_{a-c}$	0.1	60	OS	6.0
GS.10.OS.60.110$_{a-c}$	0.1	60	OS	11.0
GS.10.OS.60.085	0.1	60	OS	8.5
GS.20.OS.60.085	0.2	60	OS	8.5
GS.30.OS.60.085	0.3	60	OS	8.5
GS.50.OS.60.085	0.5	60	OS	8.5
GS.80.OS.60.085	0.8	60	OS	8.5
GS.1010.OS.3030.085	0.1 + 0.1	30 + 30	OS	8.5
GS.10.OS.120.00	0.1	120	OS	S
GS.20.OS.120.00	0.2	120	OS	S
GS.1010.OS.6060.00	0.1 + 0.1	60 + 60	OS	S
GS.1020.OS.6060.00	0.1 + 0.2	60 + 60	OS	S
GS.2010.OS.6060.00	0.2 + 0.1	60 + 60	OS	S

Notes a – ON: overnight; b – OS: orbital shaking; US: assisted by ultra-sounds; c – S: same as synthesis.

6.2.4. Decorated cardboard-based supports

The substrate for these supports is a cardboard with an aluminium layer finish. This aluminium surface is decorated with a layer of silver nanoparticles with a 6 nm thickness, deposited using an electron gun-assisted thermal evaporation technique[20] – the same method applied to subtracts described in section 6.2.2.

The silver layer on the silicon substrate was then functionalised with the aminothiol linker, as described for decorated silicon-based supports. However, instead of immersion, 2 mL of a 10 μM ethanolic solution of the linker was drop-casted on top of the aluminium face of the support and left undisturbed for 30 minutes. Finally, the support was washed with absolute ethanol.

The deposition of silver nanostars was done by drop-casting 2 mL of a 0.05 nM silver nanostars solution on top of the functionalised surface, for 30 minutes. Then, the support was washed with ultrapure water (samples CBa–c).

6.2.5. Silver mirror-based supports

Silver mirrors were prepared based on Tollens reagent reaction with reducing sugars, a widely known protocol that can be also used with the purpose of depositing a metallic silver film on a surface[23-24], following the reaction scheme 6.2 (section 6.1.2).

Ammonium hydroxide (NH_4OH) was added dropwise to 50 mL of 0.1 M $AgNO_3$ and a brown precipitate started to form. Additional NH_4OH led to the disappearance of this precipitate and the solution became clear. A potassium hydroxide (KOH) solution was added upon the formation of the same brown precipitate. Then NH_4OH was added until the solution is clear again. The glass slides were introduced in the reaction vessel and a D-glucose solution was added to the media. After 5-10 minutes the glass slides were covered with a silver film.

The six samples listed in table 6.3 were prepared in order to evaluate the usefulness of the silver film on the glass slide. Every glass slide was previously treated with piranha solution, as described in section 6.2.4.

Table 6.3 – Silver mirror-based supports.

Sample ID	Surface[a]	[AgNS] (nM)	Adsorption Time[b] (min)	Temperature[c] (°C)	Acid Washing[d]
SM.00.60.RT.Y	M	-	60	RT	Y
SM.05.ON.RT.N	M	0.05	ON	RT	N
SM.C1	G	0.05	ON	RT	N
SM.05.30.100.Y	M	0.05	30	100	Y
SM.05.60.50.N	M	0.05	60	50	N
SM.C2	G	0.05	60	50	N

a – M: silver mirror, G: glass; b – ON: overnight; c – RT: room temperature; d – Y: yes, N: no.

The glass slides were either covered with a silver mirror or as bare glass control. Concentration of silver nanostars was 0.05 nM, deposited on the supports for 30 minutes to overnight (~18 hours), without shaking. The drying temperature for AgNSs ranged from room temperature to 100 °C. In those cases, where an acid washing was performed, a phosphoric acid (H_3PO_4) 0.01 M solution was used. The pH was not adjusted. Every sample was washed with ultrapure water and dried before storage for SERS readings.

6.2.6. Zinc oxide nanorods-based supports

Zinc oxide (ZnO) nanorods were grown on top of a glass slide, by a method of hydrothermal synthesis assisted by microwave radiation method[25]. For the nanorods with silver nanoparticles cover, the deposition was done by the electron gun-assisted thermal evaporation process[20], equal to the ones applied in sections 6.2.2 and 6.2.4. These processes were performed at *CENIMAT|i3N* by Dr. Andreia Araújo. There were two pairs of samples: one with the bare ZnO nanorods and other with the nanorods covered with silver nanoparticles, as described for the silicon-based and cardboard-based supports. These conditions are summarised below in table 6.4.

Table 6.4 – Zinc oxide nanorods-based supports.

Sample ID	Surface[a]	[AgNS] (nM)	Adsorption Time (min)
ZS.S.05.30	S	0.05	30
ZS.Z.05.30	Z		
ZS.S.05.60	S		60
ZS.Z.05.60	Z		

Note a – S: silver nanoparticles on zinc oxide, Z: APTES-functionalised zinc oxide.

The pair of samples with ZnO nanorods covered with silver nanoparticles, followed the same treatment of 6.2.2 supports, *i.e.* functionalization with linker.

The pair of samples with bare ZnO nanorods, followed the same treatment of 6.2.3 supports, *i.e.* functionalization with APTES.

One sample from each pair was dipped for 30 minutes under orbital shaking in a 0.05 nM AgNSs solution and then washed with ultrapure water.

Other sample from each pair was dipped for 60 minutes in a 0.05 nM AgNSs solution (without shaking) and then washed with ultrapure water.

A total of four samples (ZS.S.05.30, ZS.S.05.60, ZS.Z.05.30 and ZS.Z.05.30) were prepared.

6.2.7. SERS measurements and data analysis

SERS measurements were performed using 2 µL of rhodamine 6G (R6G) solution drop-casted onto the nanostructure surface. Concentrations of the R6G solution were in the range 10^{-3}–10^{-12} M.

In figure 6.1 are depicted a Raman spectrum for R6G and a SERS spectrum for the same analyte. The concentration of R6G for spectra acquisition was 10^{-3} M and 10^{-6} M, respectively.

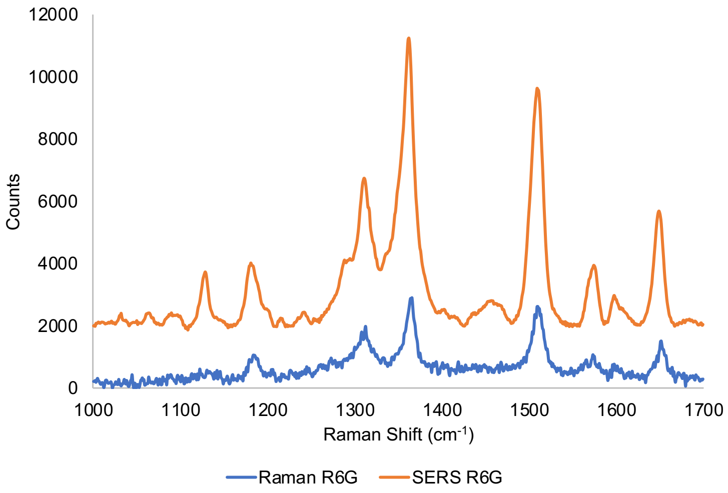

Figure 6.1 – Raman (blue trace) and SERS (orange trace) spectra of rhodamine 6G (10^{-3} M and 10^{-6} M, respectively).

The areas of the vibrational Raman lines at 1360 cm^{-1} and 1509 cm^{-1} were used to calculate spectral intensity using the curve-fitting program Peakfit v4.12 (Seasolve Software Inc.). After linear baseline subtraction, Lorentzian decomposition of spectra was performed to identify peak parameters (height, area, centre, and width) associated with selected Raman lines.

The average SERS enhancement factor (EF) was calculated using the following equation 6.1:

$$EF = \frac{A_{SERS} \times N_{SERS}}{A_{Raman} \times N_{Raman}} \qquad \text{(Eq. 6.1)}$$

where, A_{SERS} is the SERS peak area of a R6G spectrum (1360 cm^{-1} or 1509 cm^{-1}) and A_{Raman} is the peak area of a (not enhanced) Raman R6G spectrum measured over a non-plasmonic substrate. N_{SERS} corresponds to the estimated number of molecules contributing to the SERS signal, while N_{Raman} is the number of molecules contributing to the not enhanced Raman signal.

The Raman/SERS spectra and SEM images were obtained by Maria João Oliveira, at *CENIMAT|i3N* and *Departamento de Conservação e Restauro* from *Faculdade de Ciências e Tecnologia da Universidade Nova de Lisboa*.

6.3. Results and Analysis

The following sections describe the results obtained in the study of the influence of silver nanostars concentration, pH and shaking type for three different supports: silicon wafers, cardboard and glass. For the latter support, results for different surface modifications are also described.

6.3.1. Silicon-based supports

These supports already start with a silver nanoparticles film, where the AgNSs were deposited.

6.3.1.1. Influence of silver nanostars concentration

The beforehand functionalized silicon wafers were immersed in star-shaped silver nanoparticles (AgNSs) solution with two different concentrations – 0.05 and 0.10 nM. The figure 6.2 below depicts the calculated enhancement factor for two different concentrations of AgNSs (0.10 nM: SS.10.UU and 0.05 nM: SS.05.UU) and respective controls (SS.C1 and SS.C2). On the right, the triplicate SS.05.UU$_{a–c}$ is compared with another triplicate (SS.05.UU$_{d–f}$), prepared under the same conditions, but with a different batch of silver nanostars.

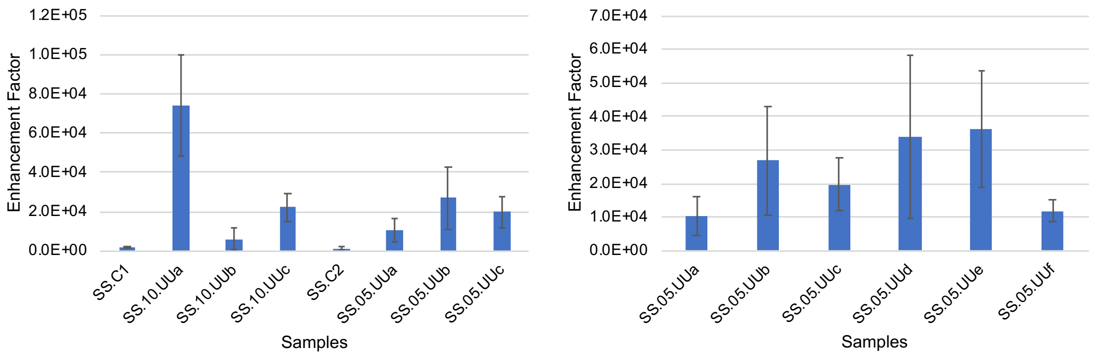

Figure 6.2 – Enhancement factors (blue columns) and standard error (black lines) for samples prepared using 0.05 nM (SS.05.UU), 0.10 nM (SS.10.UU) and no (SS.C1 and SS.C2) silver nanostars solutions. Calculated based on R6G 1360 cm^{-1} band.

The enhancement factors for the control samples SS.C1 and SS.C2 – silicon wafer with silver nanoparticles produced by PVD – are the lowest in all the experiment, with an EF in the 1.2–1.8 x 10^3 range. The presence of silver nanostars in samples SS.10.UU and SS.05.UU increases the enhancement factor (EF) to the 0.6–7.4 x 10^4 range. Despite this increase for all samples, the intra and inter sample standard deviation (SD) and relative standard deviation (RSD), respectively, are both high.

The samples with higher concentration (SS.10.UU) present higher variation of EF than the samples SS.05.UU, prepared with half the concentration of the previous. The set SS.10.UU comprises both the higher (7.4 x 10^4) and the lowest (6.1 x 10^3) EF values and present an RSD value of 85%. The sets SS.05.UU$_{a\text{–}c}$ and SS.05.UU$_{d\text{–}f}$ present RSD values of 36% and 40%, respectively. Taking in consideration the two sets of triplicates together (SS.05.UU), the RSD value is 43%. This last RSD is slightly higher, which was expected due to an introduction of an extra variable, *i.e.* the different AgNSs batches.

Despite the increase of the SERS effect in all samples containing silver nanostars, this method of preparing surfaces does not present the desired repeatability. The produced surfaces are probably quite heterogenous regarding the nanostars distribution but also regarding the presence of single particles *vs*. aggregates.

The samples prepared with the higher concentration do not seem to necessarily assure a higher density of hotspots on the surface. The higher concentration can induce the formation of a higher number of aggregates. In theory, aggregates have higher EF, since the contact points between AgNSs originates extra and stronger magnetic fields working as hotspots. Since the drop of analyte solution is randomly placed on the surface, the laser will also focus in a random spot on the surface. Therefore, it can hit a spot with a single particle organization, an aggregate or even only the primary surface. The SERS effect generated by an aggregate, a region rich in single particles, a single particle or the bare primary surface is sequentially decrescent, so surfaces that can contain the both extremes present higher variability. Therefore, due to a high variation in EF value between spots from the same sample in case of the presence of aggregates, an evenly dispersed and dense monolayer of AgNSs is desirable.

6.3.1.2. Influence of the shaking method

Since the major issue reported in last section was the possible aggregate formation, an ultrasound assisted deposition (adsorption reaction vessel in an ultrasounds bath) was tested. The aim of the introduction of ultrasounds in the deposition procedure was to keep the AgNSs individualised so they can be adsorbed as single particles instead of aggregates.

Figure 6.3 below depicts the enhancement factors for samples with an undisturbed adsorption process (SS.05.UU$_{d–f}$) and an adsorption step assisted by ultrasounds (SS.05.US).

From this point, most of the experiments show the enhancement factors calculated from both 1360 cm^{-1} and 1509 cm^{-1} bands. This due to citrate (AgNSs capping agent) band overlap the 1360 cm^{-1} band, so it can interfere with the calculations.

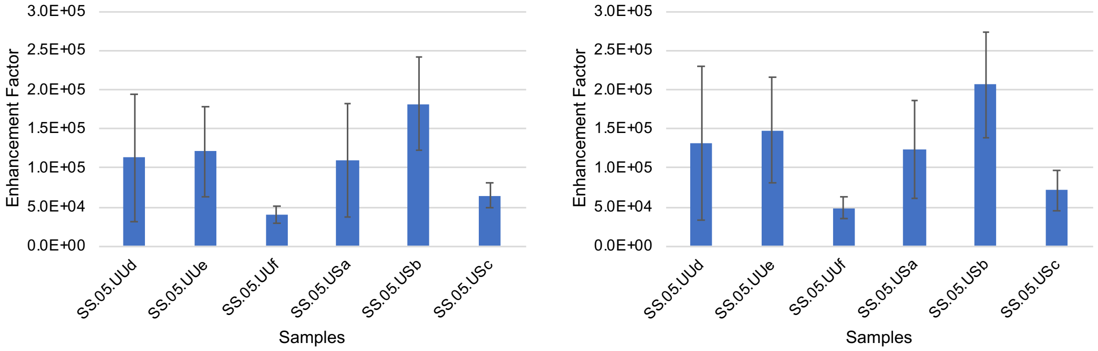

Figure 6.3 – Enhancement factors (blue columns) and standard error (black lines) calculated from the 1360 cm^{-1} (left) and 1509 cm^{-1} (right) bands, for samples prepared without shaking (SS.05.UUd–f) and assisted by ultrasounds (SS.05.US).

Globally, samples prepared in ultrasounds (SS.05.US), present higher enhancement factors, with ranges of 0.4–1.2 x 10^{5} (EF, 1360 cm^{-1} band) and 0.5–1.5 x 10^{5} (EF, 1509 cm^{-1} band), in opposition to samples prepared without shaking (SS.05.UU$_{d–f}$) that registered 0.7–1.8 x 10^{5} and 0.7–2.1 x 10^{5}, respectively. The last set of samples present however an RSD value (41%) of the same order of magnitude than the one from first set (40%).

In order to better understand the differences between supports, scanning electron microscopy micrographs were obtained for samples SS.05.UU$_{d}$ and SS.05.US$_{a}$, prepared without shaking and with the help of ultrasounds, respectively. They are depicted in figure 6.4.

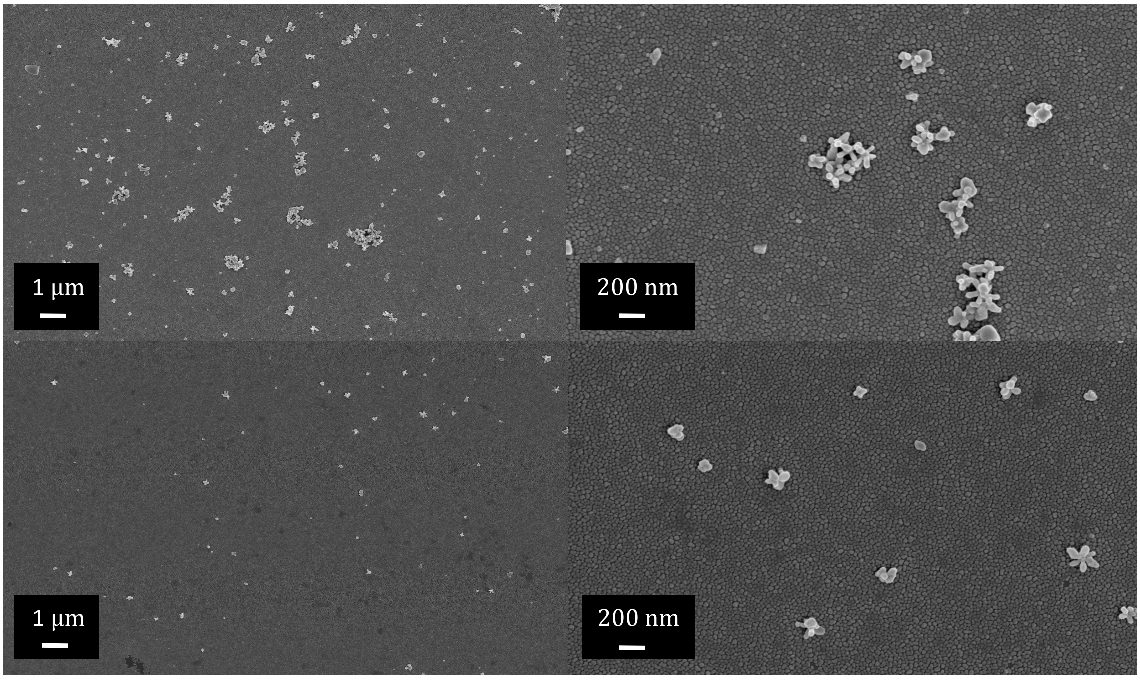

Figure 6.4 – Scanning electron microscopy micrographs of samples SS.05.UUd (top), with an undisturbed adsorption process and SS.05.USa (bottom), with the adsorption process assisted by ultrasounds.

In both samples the area without silver nanostars is much higher than the area covered with these nanoparticles. The sample prepared without shaking (SS.05.UU$_d$, top) shows both well-dispersed nanoparticles and aggregates, in opposition to sample SS.05.US$_a$ (bottom) prepared under sonication, that only show well-dispersed particles. The sonication process seems to work as intended.

In terms of probability of the laser hitting the surface, for sample SS.05.US$_a$ it can hit mostly space without any silver nanostars, but it can also hit a single nanoparticle, up to a few of them. The scenario is the same for sample SS.05.UU$_d$, but the laser can additionally hit aggregates, known for their high enhancement factors. However, for the experiments with the EF depicted in figure 6.4, this not seemed to be the case, since the average EF for both sets of samples and their RDS values are quite similar.

6.3.2. Glass-based supports

Since the results with silicon-based supports never presented a satisfactory repeatability, other type of support was considered – glass. By functionalizing the surface of commercial microscope slides and coverslips, it was possible to use well-established protocols, like glass functionalization with (3-aminopropyl)triethoxysilane (APTES), minimizing variations in the surface itself.

Before starting this section analysis, it is important to notice that control samples – APTES-functionalised glass with no contact with AgNSs and bare glass with contact with AgNSs – showed no signal at all, showing that APTES is not an interference in SERS measurements however is essential to glass decoration with AgNSs (data not shown).

6.3.2.1. Influence of the concentration

In figure 6.5, are presented, for the same set of samples, the enhancement factors determined by 1360 cm^{-1} and 1509 cm^{-1} bands analysis. This time they were used 0.10 nM (GS.10.OS.60.085) and 0.20 nM (GS.20.OS.60.085) silver nanostars solutions. Relative to the previous set of experiments, several changes were introduced in order to improve the reproducibility. Samples A15-A20 had a 60 minutes adsorption time, controlled pH (8.5), and orbital shaking (100 rpm).

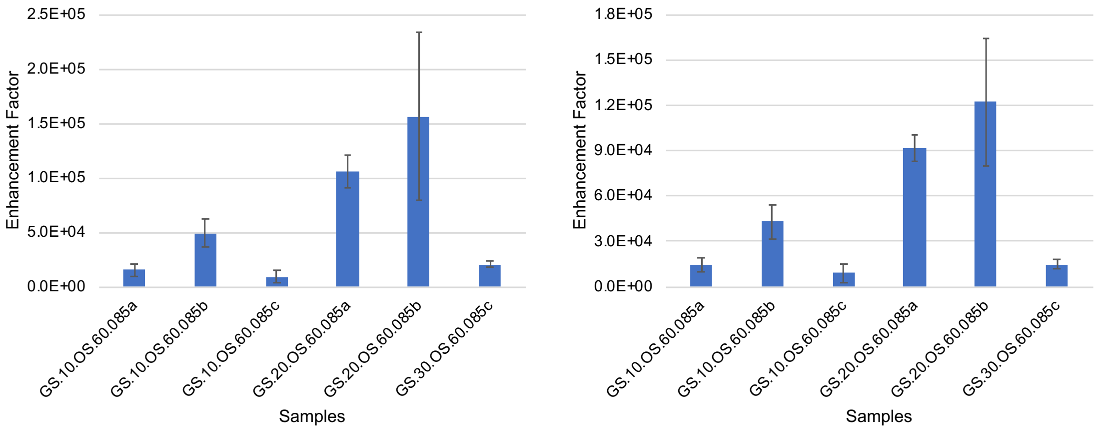

Figure 6.5 – Enhancement factors (blue columns) and standard error (black lines) calculated from the 1360 cm^{-1} (left) and 1509 cm^{-1} (right) bands, for samples prepared using 0.10 nM (GS.10.OS.60.085) and 0.20 nM (GS.20.OS.60.085) silver nanostars solutions.

The samples prepared with a higher concentration of silver nanostars (0.20 nM, GS.20.OS.60.085) reached EF in the 0.2–1.6 x 10^{5} range (1360 cm^{-1} band) and in the 0.2–1.2 x 10^{5} range (1509 cm^{-1} band). In all cases GS.20.OS.60.085 set reveal better enhancements than the GS.10.OS.60.085 set, that reached EF in the 0.9–4.9 x 10^{4}

range (1360 cm^{-1} band) and in the 0.9–4.3 x 10^4 range (1509 cm^{-1} band). The inter sample variations are also lower for the GS.20.OS.60.085 (59% for both bands) when compared to GS.10.OS.60.085 (~69% for both bands). However, these RSD values are still high.

This time, the higher number of nanoparticles in the medium seem to increase the probability of the analyte in the sample drop being under the SERS effect, in opposition to what happened in the previous experiment (SS.05.UU *vs.* SS.10.UU) studying this parameter. There are naturally more silver nanostars available to cover the surface, and probably the introduction of orbital shaking, for twice the adsorption time, increases the adsorption of the nanostars. If in one way the high concentration favours the amount of adsorbed AgNSs and orbital shaking favours the mass transport (so the adsorption), in other way it can favour also the aggregation (even more than an undisturbed solution).

Additionally, the pH was controlled (8.5), although the value is not far from the typical values of the AgNSs solution (7-8). Further shaking and pH studies will be described in the following sections.

With the results available so far from other nanostars-functionalized supports, despite we observed an increase in EF values for all samples, the variation of these values obtained in measurements at different spots in the same sample, was quite considerable. As discussed before, this could be due to the analyte and laser focus being in a region with single nanostars, several isolated nanostars or an aggregate. The focus changed then to optimize the uniformity of the surface.

Since the AgNSs concentration increase from 0.1 nM to 0.2 nM originated better results for the latter condition and assuming that glass functionalization with APTES assures an even and dense availability of amino groups across the surface, the initial approach was to provide increasing amounts of nanostars to the supports, by increasing the concentration of the immersion solution (even above the 0.2 nM).

In figure 6.6 there is a set of SEM micrographs obtained from samples GS.10.OS.60.085, GS.20.OS.60.085, GS.30.OS.60.085, GS.50.OS.60.085, and GS.80.OS.60.085, covering concentrations from 0.1 nM to 0.8 nM. Additionally, a sample prepared in two cycles of 30 minutes, using a fresh AgNSs solution for the second cycle of 30 minutes – GS.1010.OS.3030.085.

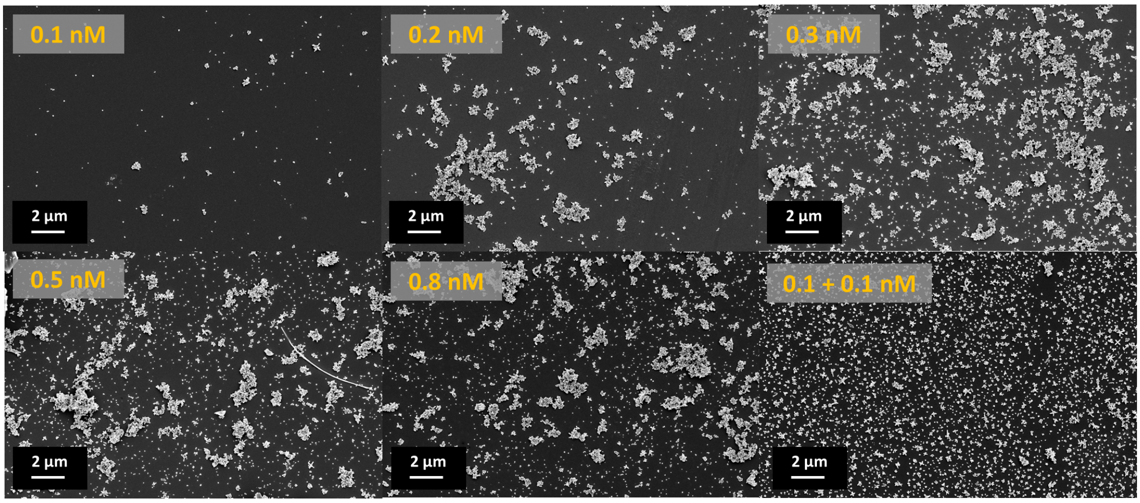

Figure 6.6 – Samples prepared over orbital shaking for 60 minutes at pH 8.5, using immersion solutions with silver nanostars concentrations of 0.1 nM, 0.2 nM, 0.3 nM, 0.5 nM, 0.8 nM and 0.1 + 0.1 nM (two 30 minutes cycles at 0.1 nM) – samples GS.10.OS.60.085, GS.20.OS.60.085, GS.30.OS.60.085, GS.50.OS.60.085, GS.80.OS.60.085, and GS.1010.OS.3030.085, respectively.

The aggregation issue was still present, however this time it was also possible to identify some degradation of the silver nanostars. They were found fractions of these characteristic nanostructures, like single arms and cores. A micrograph with a higher amplification for a sample representative of all samples using phosphate buffer clearly show these fragments, together with very few intact silver nanostars, and is depicted below in figure 6.7.

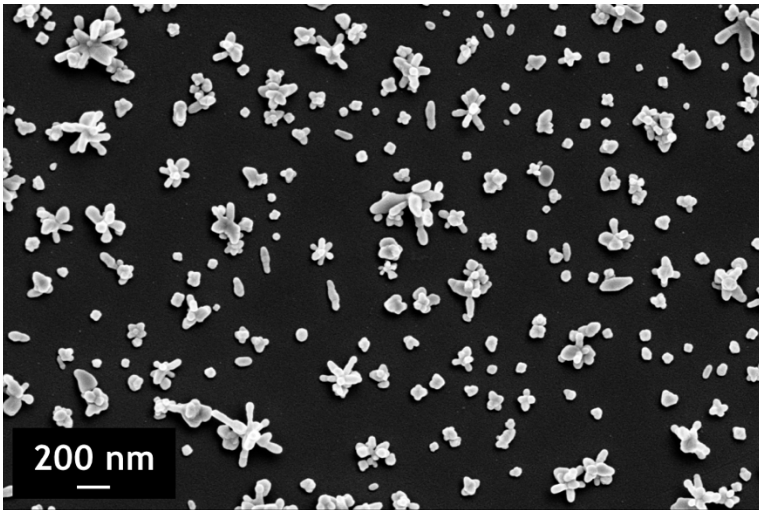

Figure 6.7 – SEM micrograph of fragmented silver nanostars representing the set samples GS.10.OS.60.085, GS.20.OS.60.085, GS.30.OS.60.085, GS.50.OS.60.085, GS.80.OS.60.085, and GS.1010.OS.3030.085.

This fragmentation was never observed before controlling the pH with buffer (phosphate buffer 10 mM). The microscopic behaviour seen in figure 6.7 but also the macroscopically visible aggregation of part of the remaining nanostars in the immersion media, also never seen before, led us to conclude that the higher ionic strength of the nanoparticle solution destabilized the nanoparticle solution.

It was also observed that, generically, as the concentration increases, the size of the aggregates also increases. In figure 6.8, it can be seen big aggregates in the sample prepared under the highest concentration (0.8 nM, left) in opposition to the lower concentration (in two cycles of 0.1 nM, right).

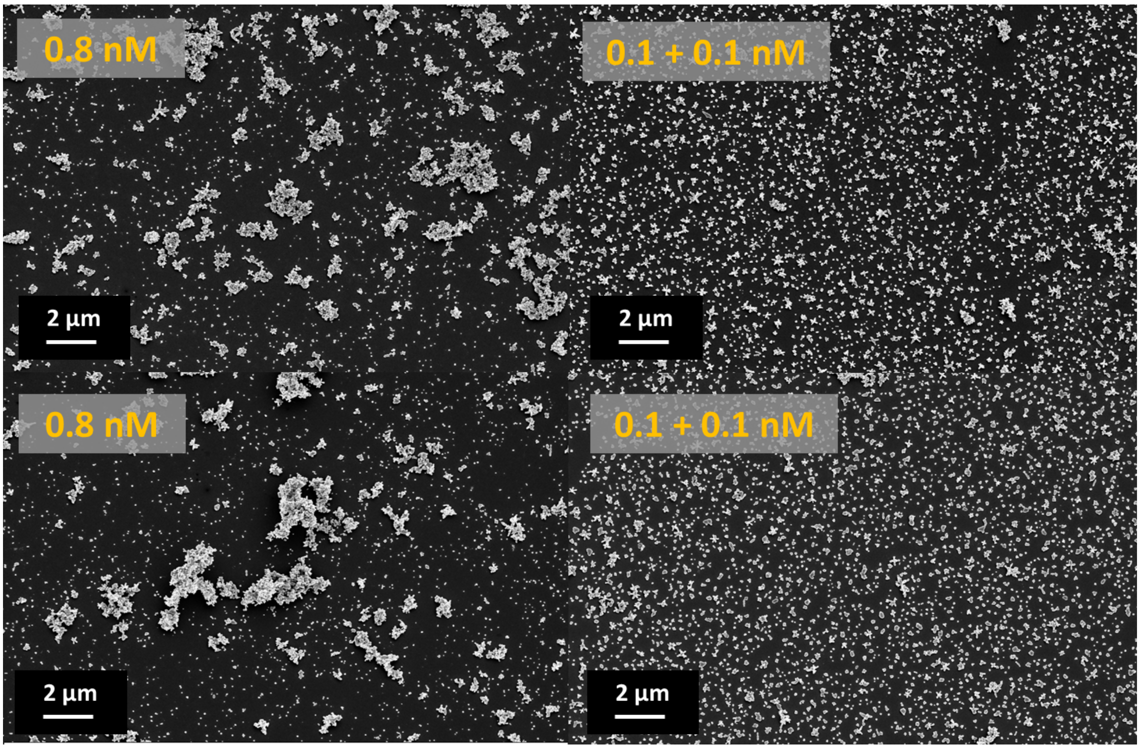

Figure 6.8 – SEM micrographs obtained in two different regions from samples GS.80.OS.60.085 (left) and GS.1010.OS.3030.085 (right).

The sample prepared by immersion in a 0.8 nM silver nanostars solution, as representative of samples with aggregates in this experiment, is consistently uneven across the surface, demonstrated in figure 6.8 (left) by two micrographs obtained from two random spots in the sample. In opposition, the sample prepared by immersion (two cycles) in a 0.1 nM silver nanostars solution shows a much more uniform nanostars distribution (figure 6.8, right).

Below in figure 6.9 are plotted the EF values for these samples.

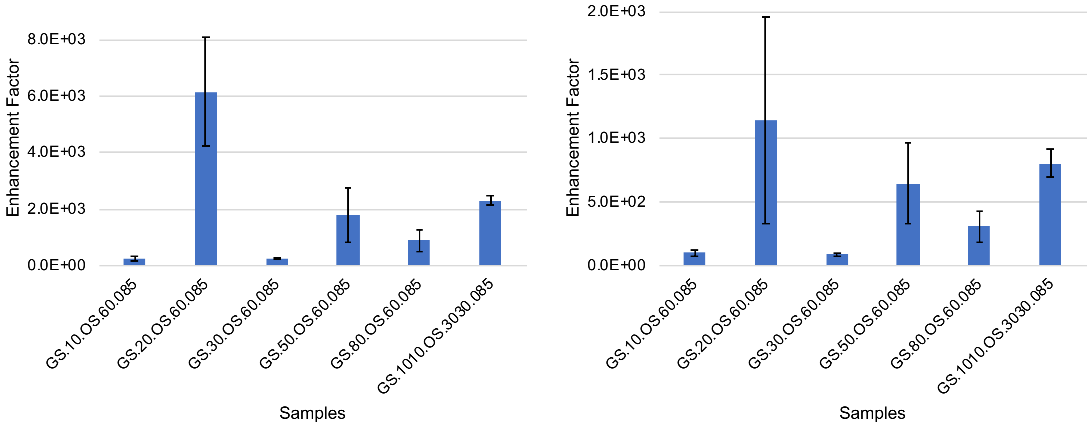

Figure 6.9 – Enhancement factors (blue columns) and standard error (black lines) calculated from the 1360 cm^{-1} (left) and 1509 cm^{-1} (right) bands, for samples using immersion solutions with silver nanostars concentrations of 0.1 nM, 0.2 nM, 0.3 nM, 0.5 nM, 0.8 nM and 0.1 + 0.1 nM (two 30 minutes cycles at 0.1 nM) – samples GS.10.OS.60.085, GS.20.OS.60.085, GS.30.OS.60.085, GS.50.OS.60.085, GS.80.OS.60.085, and GS.1010.OS.3030.085, respectively.

The samples with aggregates (0.2-0.8 nM) led to the already mentioned typical problems, namely high intrasample variability and lack of correlation between crescent concentrations and respective EF, both depicted in figure 6.9. The sample without aggregates (0.1 + 0.1 nM), assured a lower variability, depicted above in the same chart (figure 6.9). This last sample seem to be a good step towards a lower variability, however the presence of silver nanostars fragments can compromise the enhancement factor values, since spheres and rods have a lower number of hotspots compared to the star-shaped nanoparticles[26].

As stated before, the presence of phosphate buffer is probably detrimental for the nanostars morphology, so in the next set of samples several concentrations were again tested, but this time without pH adjustments. Scanning electron microscopy micrographs from the resultant samples are depicted below in figure 6.10.

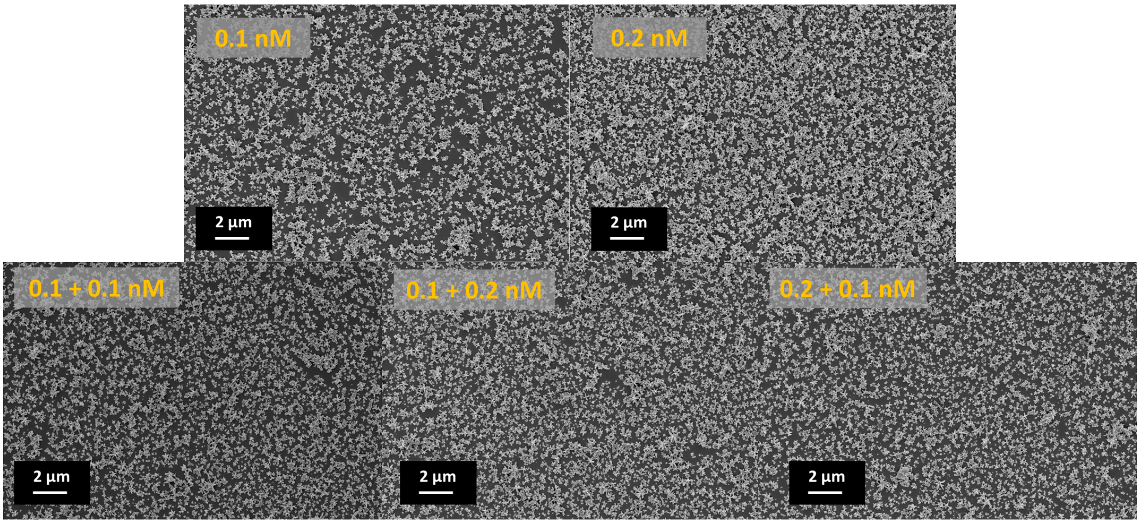

Figure 6.10 – SEM micrographs using immersion solutions with silver nanostars concentrations 0.1 nM, 0.2 nM, 0.1 + 0.1 nM, 0.1 + 0.2 nM nM and 0.2 + 0.1 nM (two 60 minutes cycles) – samples GS.10.OS.120.00, GS.20.OS.120.00, GS.1010.OS.6060.00, GS.1020.OS.6060.00, and GS.2010.OS.6060.00, respectively.

All the samples depicted above show no clear evidence of the presence of aggregates. For sample GS.10.OS.120.00, prepared in 0.1 nM nanostars solution, some gaps are observed along the surface, which seem to be filled with a second cycle, specially using a 0.2 nM nanostars solution in a second step. However, sample GS.20.OS.120.00 is highly densely packed after a single step.

Micrographs of five different random spots from each sample shown in figure 6.11 showed that each one of the five random spots are perfectly similar to the other four (data not shown).

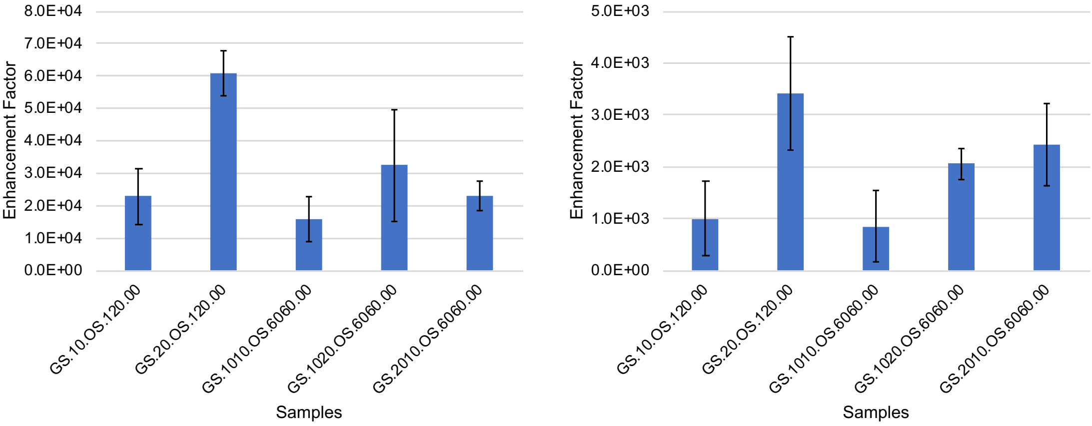

Figure 6.11 – Enhancement factors (blue columns) and standard error (black lines) calculated from the 1360 cm^{-1} (left) and 1509 cm^{-1} (right) bands, for samples using immersion solutions with silver nanostars concentrations of 0.1 nM, 0.2 nM, 0.1 + 0.1 nM, 0.1 + 0.2 nM nM and 0.2 + 0.1 nM (two 60 minutes cycles) – samples GS.10.OS.120.00, GS.20.OS.120.00, GS.1010.OS.6060.00, GS.1020.OS.6060.00, and GS.2010.OS.6060.00, respectively.

The sample providing the highest enhancement factor in this last set (GS.20.OS.120.00) presents an EF of 6.1 x 10^4, a tenfold increase relative to the sample with highest EF (6.1 x 10^3) from the set prepared with buffer (GS.20.OS.60.085), where degradation of the nanostars was detected. In both cases the sample best EF performance was the one using a 0.2 nM AgNSs solution, but the organised and dense distribution of AgNSs positively affects the SERS effect.

6.3.2.2. Influence of shaking

Equally for the functionalised glass supports, the ultrasounds assisted adsorption was studied, however compared to orbital shaking. The EF of these samples is depicted in figure 6.12.

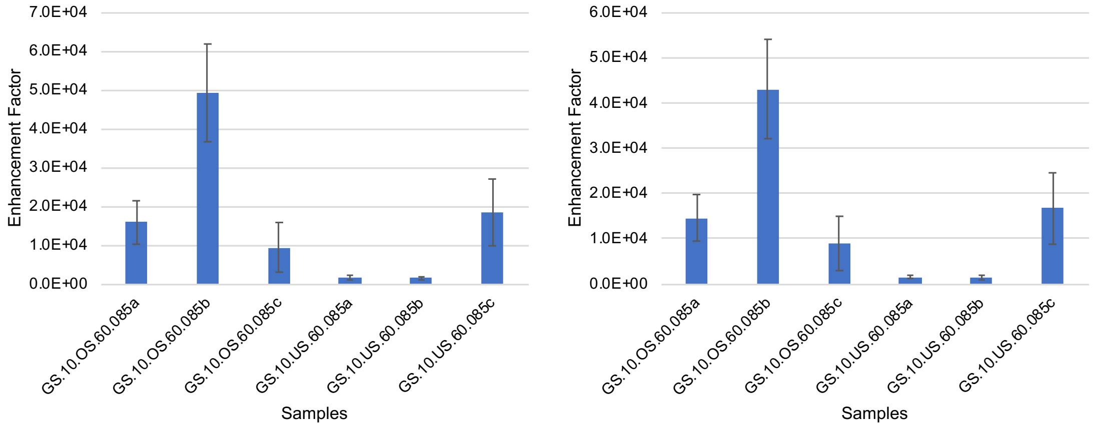

Figure 6.12 – Enhancement factors (blue columns) and standard error (black lines) calculated from the 1360 cm^{-1} (left) and 1509 cm^{-1} (right) bands, for samples prepared with orbital shaking (GS.10.OS.60.085) and assisted by ultrasounds (GS.10.OS.60.085).

In this case the lowest enhancements arise from glass supports functionalized under sonication. The best enhancement was observed in a sample prepared under orbital shaking (GS.10.OS.60.085$_{b}$) – 4.9 x 10^{4} (1360 cm^{-1} band) and 4.3 x 10^{4} (1509 cm^{-1} band) –, however the second best comes from a sample prepared by the other method (GS.10.US.60.085$_{c}$) – 1.8 x 10^{4} (1360 cm^{-1} band) and 1.7 x 10^{4} (1509 cm^{-1} band). Two of the lowest results so far were observed in samples GS.10.US.60.085$_{a-b}$, prepared under sonication, with EF values of 1.6–1.7 x 10^{3} (1360 cm^{-1} band) and 1.4–1.5 x 10^{3} (1509 cm^{-1} band). RSD for GS.10.OS.60.085 and GS.10.US.60.085 were respectively and ~69% (both bands) and 110% (both bands).

Finally, it is important to notice that these experiments were performed with controlled pH, which has been demonstrated before to be detrimental for AgNSs integrity.

6.3.2.3. Influence of media pH

Finally, the effect of the pH was evaluated, with pH values below, slightly above and above the pKa of the amine groups on the surface. A value typically considered for amines pKa is 9,[27] however for immobilised APTES the value is around 7.6.[28] The results are shown in figure 6.13 below.

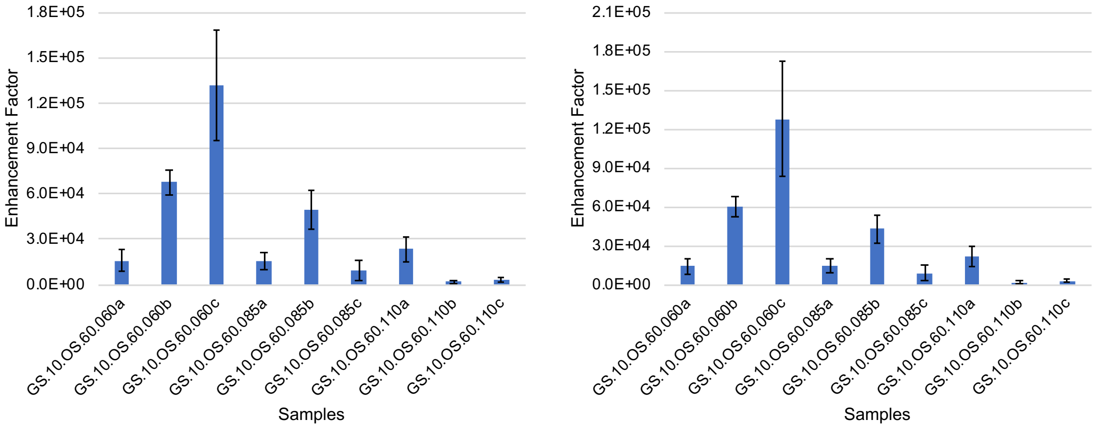

Figure 6.13 – Enhancement factors (blue columns) and standard error (black lines) calculated from the 1360 cm^{-1} (left) and 1509 cm^{-1} (right) bands, for samples prepared at pH 6.0 (GS.10.OS.60.060), pH 8.5 (GS.10.OS.60.085), and pH 11.0 (GS.10.OS.60.110).

The two highest EF values belong to samples functionalized at pH 6.0 – 0.7–1.3 x 10^{5} (1360 cm^{-1} band), 0.6–1.3 x 10^{5} (1509 cm^{-1} band). In the other hand, the two lowest values were observed in samples functionalized at pH 11.0 – 2.1–3.0 x 10^{3} (1360 cm^{-1} band), 1.8–2.7 x 10^{3} (1509 cm^{-1} band). Once again, the repeatability is not quite satisfactory, with RSD values of ~68% (pH 6.0), ~69% (pH 8.5), and ~105% (pH 11.0).

It is important to remember that the silver nanostars employed in these experiments are citrate-capped, *i.e.* they are negatively charged. A surface positively charged, like the one with the aminothiol linker at pH 6.0, where mostly the amine groups are expected to be protonated, can more easily attract and capture the negatively charged nanoparticles. For pH 8.5, where a lower fraction of amine groups is protonated, and for pH 11.0, where mostly the amine groups are expected to be deprotonated, this electrostatic attraction is disfavoured. This data points to pH 6.0 as the better value for AgNSs media, however the effect of phosphate buffer on AgNSs integrity has to be solved first.

6.3.3. Other supports

In addition to silicon bases decorated with silver nanoparticles and APTES-functionalized glass, four other supports were used for small sets of experiments. These four other supports can be considered variations of the supports analysed in section 6.3.1 and 6.3.2. Both cardboard aluminium layer and zinc oxide nanorods (on glass) were decorated with silver nanoparticles. These two supports together with silver mirrors (on glass) represent metallic silver finishes to deposit the silver nanostars. Bare zinc oxide nanorods (on glass), represent other metal oxide surface (additionally to SiO_2).

6.3.3.1. Cardboard-based surfaces

Regarding the cardboard-based surfaces, the EF results have significative variations intrasample and intersample (CBa–c are triplicates), as can be seen in figure 6.14 below. RSD for samples CBa–c is ~61%. However, this was the first sample where an EF value of 10^6 was observed.

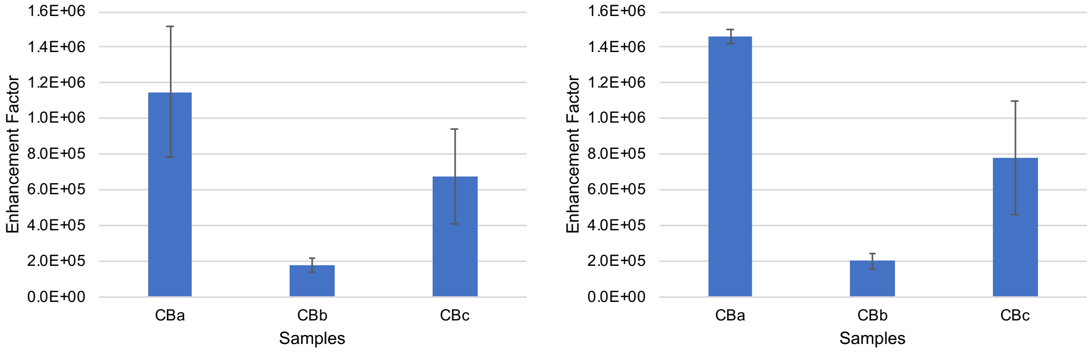

Figure 6.14 – Enhancement factors (blue columns) and standard error (black lines) calculated from the 1360 cm^{-1} (left) and 1509 cm^{-1} (right) bands, for samples CBa–c.

. Again, scanning electron microscopy can help to explain this behaviour. Micrographs captured from sample CBc are depicted in figure 6.15.

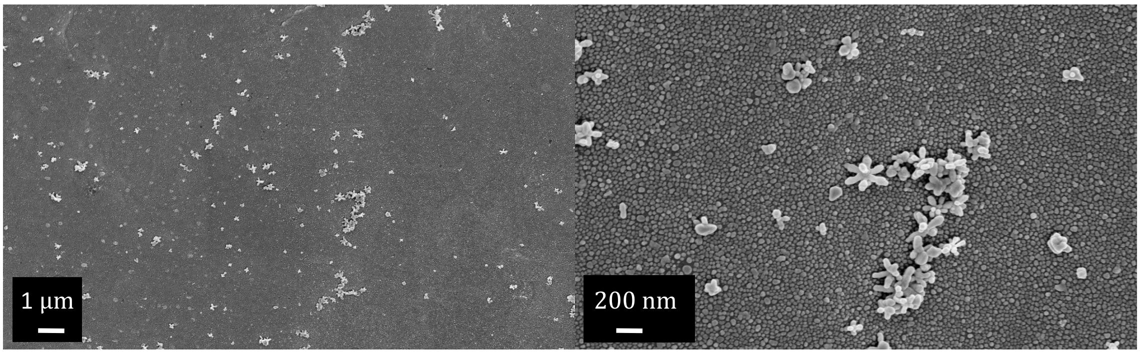

Figure 6.15 – SEM micrographs obtained from sample CBc.

AgNSs quantity and distribution uniformity are very poor in this samples as seen in the micrographs in figure 6.15. This explains the variability of the results. In one way, the nanostars seem to improve the signal despite the variations. Sample CBb can eventually represent a sample with no nanostars given the lower EF values but also the very low standard deviation associated to the measurements. CBb was not prepared as a negative control, however the laser could possibly hit regions with no AgNSs or something went wrong with this sample regarding AgNSs deposition.

Due to this poor behaviour and some difficulties in keeping the shape of the support – cardboard reacts to environment humidity levels, gaining some curvature – this support was abandoned.

6.3.3.2. Silver mirror-based surfaces

The possibility of using a silver film as a good support to AgNSs, playing or not an additional enhancement role due to the nanodefects on its surface, was also explored. In figure 6.16 are plotted the EF values for the six samples prepared for this study.

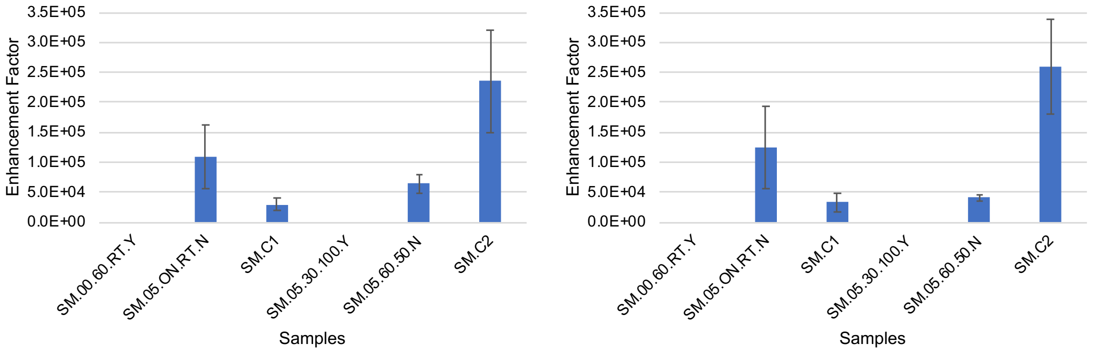

Figure 6.16 – Enhancement factors calculated from the 1360 cm^{-1} (left) and 1509 cm^{-1} (right) bands, for samples using a silver mirror and controls.

Samples where no SERS effect was observed (SM.00.60.RT.Y and SM.05.30.100.Y) have in common an acid (H_3PO_4 0.01 M) washing step that disrupts the silver surface either with (SM.05.30.100.Y) and without (SM.00.60.RT.Y) deposited AgNSs.

The two samples with lowest EF (SM.C1 and SM.05.60.50.N) differ in the absence (SM.C1) or presence (SM.05.60.50.N) of a silver mirror base and also the drying temperature and time – overnight (ON) at room temperature (RT) for SM.C1 and 30 minutes at 50 °C for SM.05.60.50.N. If SM.C1 must have some AgNSs, since bare glass does not generate any enhancement (control not shown), SM.05.60.50.N seem to have a contribution from the silver film, since its SEM images (figure 6.17, top) reveal no AgNSs along the surface. Their enhancements seem to be however equivalent.

For the sample with higher enhancement (SM.C2) the only difference for sample SM.05.60.50.N is that SM.C2 does not have the silver film. In opposition to SM.05.60.50.N, D6 has a considerable loading of AgNSs, as it can be seen in figure 6.17, bottom. If this data suggests that the silver film is detrimental for AgNSs immobilization, the D2–SM.C1 pair of samples suggests otherwise, since the highest enhancement is observed for the sample with the silver film (D2). There is a difference of drying temperature and duration between pairs D2–SM.C1 (RT, ON) and SM.05.60.50.N–SM.C2 (100 °C, 30 minutes).

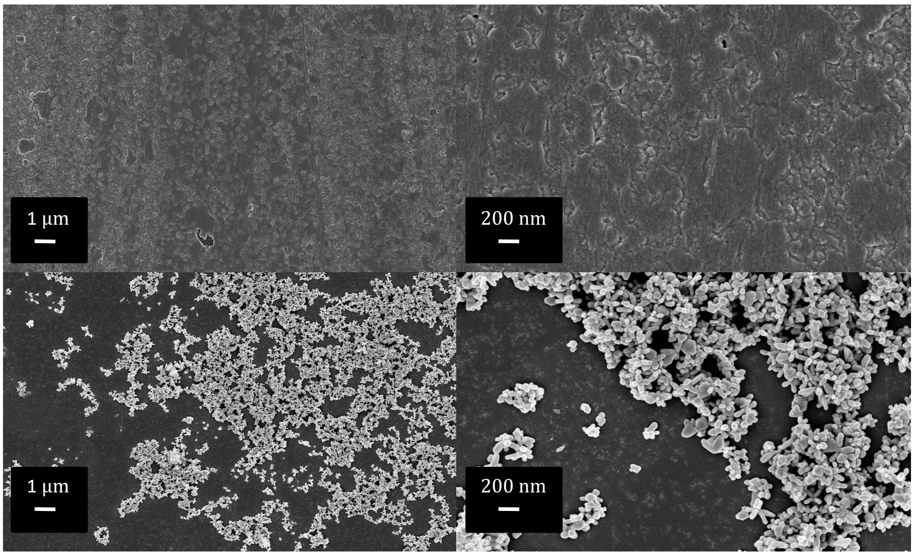

Figure 6.17 – SEM micrographs for samples (SM.05.60.50.N, top) and (SM.C2, bottom).

Given that produced supports do not present a fine nanostructuration, *i.e.* an even AgNSs monolayer surface, neither opens perspectives for that goal, the method was abandoned. Supports with a high load in AgNSs, not focused in fine nanostructuration, were objective of other work[29], not included in this thesis.

6.3.3.3. Zinc oxide nanorods-based surfaces

Finally, supports with zinc oxide (ZnO) nanorods were screened for the purpose of creating good nanostructured SERS substrates. Either silver nanospheres-decorated ZnO nanorods (figure 6.18) and bare ZnO nanorods (figure 6.19) were tested.

Despite different incubation times, none of the four samples was efficiently decorated with silver nanostars, as seen in the SEM micrographs below. The rough surface could be helpful to a physical entrapment, but it revealed to be more an obstacle.

Samples ZS.S.05.30 and ZS.S.05.60 presented higher enhancement factors, however because of the silver nanospheres deposition rather than AgNSs decoration (data not shown).

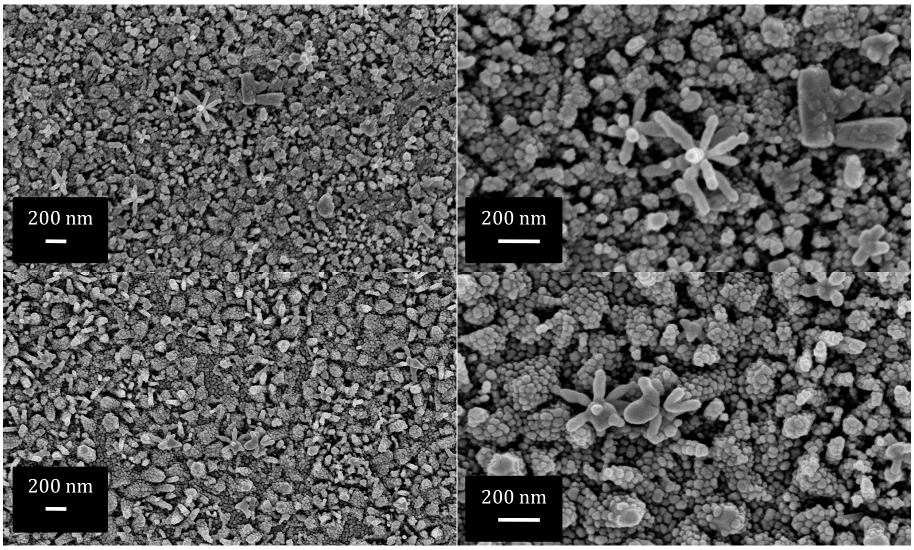

Figure 6.18 – SEM micrographs of silver nanospheres-decorated zinc oxide nanorods tentatively decorated with silver nanostars.

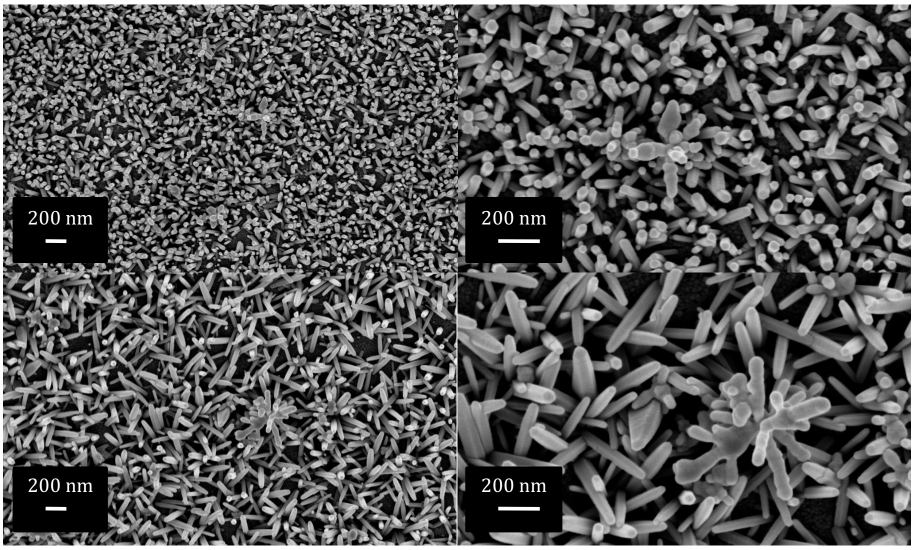

Figure 6.19 – SEM micrographs of bare zinc oxide nanorods tentatively decorated with silver nanostars.

Given the laborious preparation of substrates like these, with no gain regarding AgNSs immobilization, these supports were also abandoned.

6.4. Conclusions

The availability of supports ready for SERS measurements can be useful for a quick and simple analysis. Silver nanostars proved to be a good element to be included in these supports, since all samples containing these nanoparticles shown improved enhancement factors.

Experiments using different supports, different AgNSs media concentrations and pH, and adsorption under different shaking conditions were explored to find the best final material.

Silver nanostars were not successfully supported onto glass functionalised with zinc oxide nanorods, so no improvements in Raman signal were observed. One of the samples of cardboard with pre-deposited silver nanospheres by PVD presented the highest EF between all samples, however only three samples (with a high RSD) were tested since cardboard tends to gain curvature across time. After these results the two supports were discarded. None of the 17 samples prepared with silicon bases with pre-deposited silver nanospheres by PVD was produced with a dense and even monolayer of silver nanostars. The same was verified for silver mirror surfaces. The only supports where a dense and even monolayer of silver nanostars was observed were APTES-functionalised glass.

From all the concentrations tested (from 0.05 nM up to 0.8 nM), the 0.2 nM was proven to be enough to an almost full-coverage. The pH of the media seemed to be related to adsorption efficiency, with the lowest pH (higher percentage of protonated amine in APTES) showing best results. However, since the buffer causes some aggregation and destruction of AgNSs, the pH after synthesis (already below APTES pKa) was proven to be more advantageous.

The adsorption under the influence of the ultrasounds solved aggregation phenomena seen in samples with an undisturbed adsorption. However, the best results were obtained under orbital shaking.

In the end, it was found that an APTES-functionalised glass support, prepared by immersion in a 0.2 nM AgNSs solution, under orbital agitation with no pH control after synthesis produced a dense and even monolayer of silver nanostars on the surface. The EF obtained (for R6G 1350 cm^{-1} band) using this support was 6.1 x 10^{4}. This value is half of the EF of the best results for silicon supports and up to 20 times lower than samples prepared on cardboard. However, none of the silicon or cardboard samples presented a surface so homogenous like the one mentioned above. Maybe a compromise between higher enhancement factors and surface topology is needed.

The EF for the support described in the last paragraph should be further improved, since higher EF were found in other samples, however with huge variations from spot to spot within the same sample. After this improvement, if possible, without compromising reproducibility intra and intersample, analytes of interest, like biologic amines such has epinephrine, dopamine, histamine, norepinephrine and serotonin, could be tested.

6.5. References

1. Maiti, N; Chadha, R; Das, A; Kapoor, S, Surface selective binding of 2,5-dimercapto-1,3,4-thiadiazole (dmtd) on silver and gold nanoparticles: A raman and dft study. *RSC Advances* **2016,** *6* (67), 62529-62539.

2. Al-Shalalfeh, MM; Saleh, TA; Al-Saadi, AA, Silver colloid and film substrates in surface-enhanced raman scattering for 2-thiouracil detection. *RSC Advances* **2016,** *6* (79), 75282-75292.

3. Leitão, MC; Marques, AP; San Romão, MV, A survey of biogenic amines in commercial portuguese wines. *Food Control* **2005,** *16* (3), 199-204.

4. Janči, T; Mikac, L; Ivanda, M; Marušić Radovčić, N; Medić, H; Vidaček, S, Optimization of parameters for histamine detection in fish muscle extracts by surface-enhanced raman spectroscopy using silver colloid sers substrates. *Journal of Raman Spectroscopy* **2017,** *48* (1), 64-72.

5. Turley, HK; Hu, Z; Jensen, L; Camden, JP, Surface-enhanced resonance hyper-raman scattering elucidates the molecular orientation of rhodamine 6g on silver colloids. *The Journal of Physical Chemistry Letters* **2017,** *8* (8), 1819-1823.

6. Lanzarotta, A; Lorenz, L; Batson, JS; Flurer, C, Development and implementation of a pass/fail field-friendly method for detecting sildenafil in suspect pharmaceutical tablets using a handheld raman spectrometer and silver colloids. *Journal of Pharmaceutical and Biomedical Analysis* **2017,** *146*, 420-425.

7. Anastasopoulos, JA; Soto Beobide, A; Manikas, AC; Voyiatzis, GA, Quantitative surface-enhanced resonance raman scattering analysis of methylene blue using silver colloid. *Journal of Raman Spectroscopy* **2017,** *48* (12), 1762-1770.

8. Janci, T; Valinger, D; Gajdos Kljusuric, J; Mikac, L; Vidacek, S; Ivanda, M, Determination of histamine in fish by surface enhanced raman spectroscopy using silver colloid sers substrates. *Food Chemistry* **2017,** *224*, 48-54.

9. Hu, J; Zhao, B; Xu, W; Li, B; Fan, Y, Surface-enhanced raman spectroscopy study on the structure changes of 4-mercaptopyridine adsorbed on silver substrates and silver colloids. *Spectrochimica Acta Part A: Molecular and Biomolecular Spectroscopy* **2002,** *58* (13), 2827-2834.

10. Zhou, N; Meng, G; Zhu, C; Chen, B; Zhou, Q; Ke, Y; Huo, D, A silver-grafted sponge as an effective surface-enhanced raman scattering substrate. *Sensors and Actuators B: Chemical* **2018,** *258*, 56-63.

11. Weatherston, JD; Seguban, RKO; Hunt, D; Wu, HJ, Low-cost and simple fabrication of nanoplasmonic paper for coupled chromatography separation and surface enhanced raman detection. *ACS Sensors* **2018,** *3* (4), 852-857.

12. Mikac, L; Ivanda, M; Gotić, M; Janicki, V; Zorc, H; Janči, T; Vidaček, S, Surface-enhanced raman spectroscopy substrate based on ag-coated self-assembled polystyrene spheres. *Journal of Molecular Structure* **2017,** *1146*, 530-535.

13. Kahraman, M; Ozbay, A; Yuksel, H; Solmaz, R; Demir, B; Caglayan, H, Tunable plasmonic silver nanodomes for surface-enhanced raman scattering. *Plasmonics* **2017,** *13* (3), 785-795.

14. Suchomel, P; Prucek, R; Cerna, K; Fargasova, A; Panacek, A; Gedanken, A; Zboril, R; Kvitek, L, Highly efficient silver particle layers on glass substrate synthesized by the sonochemical method for surface enhanced raman spectroscopy purposes. *Ultrasonics Sonochemistry* **2016,** *32*, 165-172.

15. Yoon, H; Suh, JS, Simple and efficient fabrication of dimers of silver colloidal particles for surface-enhanced raman scattering. *Journal of Raman Spectroscopy* **2018,** *49* (4), 651-658.

16. Kim, N; Kim, CT; Cho, YJ; Kim, CJ, Development of an immobilized-antigen immunofluorescence glass slide system that exploits fluorescent silica nanoparticles. *Sensors and Actuators B: Chemical* **2011,** *160* (1), 563-570.

17. Howarter, JA; Youngblood, JP, Optimization of silica silanization by 3-aminopropyltriethoxysilane. *Langmuir* **2006,** *22* (26), 11142-7.

18. Zhu, S; Fan, C; Wang, J; He, J; Liang, E, Self-assembled ag nanoparticles for surface enhanced raman scattering. *Optical Review* **2013,** *20* (5), 361-366.

19. Taglietti, A; Arciola, CR; D'Agostino, A; Dacarro, G; Montanaro, L; Campoccia, D; Cucca, L; Vercellino, M; Poggi, A; Pallavicini, P; Visai, L, Antibiofilm activity of a monolayer of silver nanoparticles anchored to an amino-silanized glass surface. *Biomaterials* **2014,** *35* (6), 1779-88.

20. Araújo, A; Mendes, MJ; Mateus, T; Vicente, A; Nunes, D; Calmeiro, T; Fortunato, E; Águas, H; Martins, R, Influence of the substrate on the morphology of self-assembled silver nanoparticles by rapid thermal annealing. *The Journal of Physical Chemistry C* **2016,** *120* (32), 18235-18242.

21. Szunerits, S; Boukherroub, R, Preparation and characterization of thin films of sio(x) on gold substrates for surface plasmon resonance studies. *Langmuir* **2006,** *22* (4), 1660-3.

22. Sang, CH; Chou, SJ; Pan, FM; Sheu, JT, Fluorescence enhancement and multiple protein detection in zno nanostructure microfluidic devices. *Biosensors and Bioelectronics* **2016,** *75*, 285-92.

23. Wang, Z; Pan, S; Krauss, TD; Du, H; Rothberg, LJ, The structural basis for giant enhancement enabling single-molecule raman scattering. *Proceedings of the National Academy of Sciences of the United States of America* **2003,** *100* (15), 8638-43.

24. Leona, M; Stenger, J; Ferloni, E, Application of surface-enhanced raman scattering techniques to the ultrasensitive identification of natural dyes in works of art. *Journal of Raman Spectroscopy* **2006,** *37* (10), 981-992.

25. Pimentel, A; Araújo, A; Coelho, BJ; Nunes, D; Oliveira, MJ; Mendes, MJ; Águas, H; Martins, R; Fortunato, E, 3d zno/ag surface-enhanced raman scattering on disposable and flexible cardboard platforms. *Materials* **2017,** *10* (12).

26. Garcia-Leis, A; Garcia-Ramos, JV; Sanchez-Cortes, S, Silver nanostars with high sers performance. *The Journal of Physical Chemistry C* **2013,** *117* (15), 7791-7795.

27. Fox, MA; Whitesell, JK, *Organic chemistry*. 3rd ed.; Jones & Bartlett Publishers: 2004.

28. Bhat, RR; Genzer, J, Tuning the number density of nanoparticles by multivariant tailoring of attachment points on flat substrates. *Nanotechnology* **2007,** *18* (2).

29. Oliveira, MJ; Quaresma, P; Peixoto de Almeida, M; Araújo, A; Pereira, E; Fortunato, E; Martins, R; Franco, R; Águas, H, Office paper decorated with silver nanostars - an alternative cost effective platform for trace analyte detection by sers. *Scientific Reports* **2017,** *7* (1), 2480.

General Conclusion

7

The main objective of the present work was to use the optical and electronic properties of metal nanoparticles in the improvement of useful characteristics of adsorbed biomolecules, for sensing and fingerprinting applications.

Firstly, 15 nm gold nanospheres were used as activity enhancers of laccase from *Toxicodendron verniciflua* (*Tov*L). Spherical gold nanoparticles (AuNPs), functionalised with the pentapeptide CALNN, were electrostatically conjugated with laccase biomolecules. The adsorption process was studied by four different techniques: dynamic light scattering (DLS), electrophoretic light scattering (ELS), agarose gel electrophoresis (AGE) and fluorescence quenching. Adsorption constants were obtained from each one of the methods, with log *K* values within the 6.8–8.9 range. This range of values demonstrated a strong binding between AuNPs–CALNN and *T. verniciflua* laccase, and also a discrepancy between the constants that emphasises the necessity of using several methods to get reliable information about the binding between nanoparticles and biomolecules. Furthermore, these AuNPs–CALNN–*Tov*L nanobioconjugates (NBCs) were tested for their enzymatic activities. For all the assays, the NBCs showed higher enzymatic activities than the respective amount of free enzyme (up to 9 times higher). The pH profile for these NBCs showed the highest increases for lower pH values (6.5–7.0), which can be interesting for industrial applications.

Secondly, this activity enhancement effect of gold nanoparticles was evaluated for a different laccase from *Trametes versicolor*. In addition to the 15 nm gold nanospheres, 40 nm gold nanospheres and gold nanostars were also tested. DLS and NTA studies showed that this enzyme does not form NBCs in solution with the selected nanoparticles. In order to ascertain if the activity enhancement effect occurs even when the enzyme is not adsorbed to the nanoparticle surface, immobilization of the enzyme and nanoparticles in several membrane-like supports were tested, namely nitrocellulose, hydrophilic mixed esters cellulose and filter paper. Given the loading of each one the nanoparticle types on each supporting materials, mechanical resistance, cost and ability to bind proteins, nitrocellulose was chosen as support for NBCs assembling. The 15 nm gold nanospheres were also found to be the ones with better impregnation yield, probably due their spherical shape and small size. Every nanoparticle-enriched nitrocellulose enzymatic disks (except for the ones where no thiol was used as AuNPs capping) showed increased enzymatic activity when compared to the respective control disk (just laccase on nitrocellulose). It was not clear which (thiol) capping was the best for enzymatic performance, however it was clear the need of thiol, otherwise the enzyme probably randomly folds around the AuNP available surface. The possibility of having supported laccase, with its activity enhanced, is exciting since these disks can be included in a biosensor in the future.

In the second part of this work, star-shaped silver nanoparticles (AgNSs) were used as a key component for surface-enhanced Raman spectroscopy (SERS) in fingerprinting applications.

Silver nanostars were mixed with three Portuguese wines representing different types and regions of production – *Verde*, *Alentejo Maduro* and *Douro Maduro*. This enabled the collection of SERS spectra for all of them, in different conditions. Data from SERS was then analysed by principal component analysis (PCA) and procedure for sample preparation was optimized in order to achieve discrimination (fingerprinting) between the three wines. For an overnight incubation of AgNSs, principal components (PC) 1 and 2 plotted against each other showed three distinct groups of scores. This long incubation step is expected to favour the binding of compounds that have a strong affinity for the nanoparticles relative to other compounds that have lower affinity constants, but that are present at higher concentrations. Possibly, these high affinity, low concentration compounds are characteristic of each wine allowing a complete discrimination between the three wines studied. In a “mix and read” approach, the overnight incubation was skipped. The collected spectra for the three wines were very similar, possibly due to a fast adsorption of compounds abundant in wines and therefore less specific. In PCA analysis, when PC1 and PC2 were plotted against each other, the discrimination was poor. PC1 encompassed contributions from the more abundant compounds, less specific as stated before, so no discrimination information was provided by this parameter. However, when PC2 and PC3 are plotted against each other, the weight of the most abundant compounds (PC1) is lost. In this case, although spectra were very similar to the naked eye, discrimination was possible, so a fast method is also possible to be used. This should not discard the method with overnight incubation, since it could be helpful for cases where the discrimination by the quick method is poor.

Using a similar principle, but with more complex samples, bacteria from groups indicated by World Health Organization as critical and high priority for research (to combat their resistance to antibiotics) were chosen for fingerprinting – *Acinetobacter baumannii*, *Klebsiella pneumoniae*, *Salmonella enterica*, and *Enterococcus spp*. (two isolates). Several protocols were tested in order to get the best nanobioconjugation between bacteria and AgNSs. Part of the samples resulting from these protocols were analysed by scanning electron microscopy (SEM), however the samples that show no evidence for aggregates and an even distribution of the particles, were not the ones with the best SERS performance. The ultimate criterion was then the PCA analysis of the spectra collected in several conditions. One of the tested protocols – mix of a colony collected from an agar plate with citrate-capped silver nanostars – enabled the distinction between the four species tested for that conditions – *Klebsiella pneumoniae*, *Salmonella enterica*, and *Enterococcus spp*. (two isolates). Further studies with *Klebsiella pneumoniae* showed that fingerprinting can go down to the sequence type level. This work revealed the possibility of using SERS for bacteria discrimination, in a quick analysis and most cost-effective than mass spectrometry, typically used for this purpose.

Finally, in view of the high success in the use of silver nanostars for SERS, a simple method to produce ready-to-use SERS supports was pursued. As base material, glass, silicon wafer and cardboard were tested. Some surface modifications were also tested, like aminothiol or (3-aminopropyl)triethoxysilane (APTES) functionalisation, and silver mirrors. Also, AgNSs media concentration and pH were taken into account. A surface densely covered with AgNSs, with no aggregates, was achieved using APTES-functionalised glass with AgNSs deposited under orbital agitation using a concentration of 0.2 nM and pH not adjusted with buffer. The enhancement factor (EF) achieved with this support – 6.1 x 10^4 – is not as high as the ones verified for some measurements in surfaces with a first layer of silver nanospheres (below the deposited nanostars), that showed EF within 10^5–10^6 range. However, measurements with this latter samples were inconsistent across the sample, probably because the distribution of AgNSs was also uneven. For the surface densely covered with AgNSs, with no aggregates, these variations were less important.

The global objectives for this thesis were achieved, with successful production of nanobioconjugates of laccases with gold nanoparticles (in solution or immobilised), nanobioconjugates of silver nanostars with wine or bacteria compounds for their fingerprinting and to obtain a ready-to use surface for SERS. The results presented here constitute a proof-of concept that the approaches and materials used are promising, but further research into use of these findings in devices for technological applications should be pursued in the future.